# A versatile toolbox for the comprehensive analysis of nervous tissue organization with light microscopy

by

Julia Magdalena Michalska

December 2022

*A thesis submitted to the*
*Graduate School*
*of the*
*Institute of Science and Technology Austria*
*in partial fulfillment of the requirements*
*for the degree of*
*Doctor of Philosophy*

Committee in charge:

Beatriz Vicoso, Chair
Johann Georg Danzl
Peter Jonas
Stephan Sigrist

The thesis of Julia Magdalena Michalska, titled 'A versatile toolbox for the comprehensive analysis of nervous tissue organization with light microscopy', is approved by:

**Supervisor:** Johann Georg Danzl, ISTA, Klosterneuburg, Austria

Signature: _____

**Committee Member:** Peter Jonas, ISTA, Klosterneuburg, Austria

Signature: _____

**Committee Member:** Stephan Sigrist, FU Berlin, Berlin, Germany

Signature: _____

**Defense Chair:** Beatriz Vicoso, ISTA, Klosterneuburg, Austria

Signature: _____

Signed page is on file

ISTA Thesis, ISSN: 2663-337X

ISBN: 978-3-99078-026-8

I hereby declare that this thesis is my own work and that it does not contain other people's work without this being so stated; this thesis does not contain my previous work without this being stated, and the bibliography contains all the literature that I used in writing the dissertation.

I declare that this is a true copy of my thesis, including any final revisions, as approved by my thesis committee, and that this thesis has not been submitted for a higher degree to any other university or institution.

I certify that any republication of materials presented in this thesis has been approved by the relevant publishers and co-authors.

Signature: _____

Julia Magdalena Michalska

December 2022

Signed page is on file

# Abstract

The brain is an exceptionally sophisticated organ consisting of billions of cells and trillions of connections that orchestrate our cognition and behavior. To decode its complex connectivity, it is pivotal to disentangle its intricate architecture spanning from cm-sized circuits down to tens of nm-small synapses.

To achieve this goal, I developed CATS – Comprehensive Analysis of nervous Tissue across Scales, a versatile toolbox for obtaining a holistic view of nervous tissue context with (super-resolution) fluorescence microscopy. CATS combines comprehensive labeling of the extracellular space, that is compatible with chemical fixation, with information on molecular markers, super-resolved data acquisition and machine-learning based data analysis for segmentation and synapse identification.

I used CATS to analyze key features of nervous tissue connectivity, ranging from whole tissue architecture, neuronal in- and output-fields, down to synapse morphology.

Focusing on the hippocampal circuitry, I quantified synaptic transmission properties of mossy fiber boutons and analyzed the connectivity pattern of dentate gyrus granule cells with CA3 pyramidal neurons. This shows that CATS is a viable tool to study hallmarks of neuronal connectivity with light microscopy.

# About the author

Julia Magdalena Michalska is an interdisciplinary life scientist focusing on neurobiology and biophysics.
She started her academic career by studying Molecular Biotechnology at the Bielefeld University in Germany, followed by a master's education in Molecular Bioengineering at the BIOTEC, Technical University Dresden in Germany. She performed her master's thesis at the Karolinska Institute in Stockholm, Sweden, where she studied genetic factors underlying the neurological disorder Cluster Headache. After continuing this research for another year, she started her PhD training at the Institute of Science and Technology Austria in Klosterneuburg, Austria, in late 2017. She developed technologies for the visualization and interrogation of brain tissue with super-resolution light microscopy under the supervision of Johann G. Danzl.
Julia is an advocate of science communication, haven taken part in various scientific outreach events, including Pint of Science 2022. She is an enthusiastic outdoor person, who spends her free time climbing and hiking.

# Acknowledgements

First, I would like to thank my PhD committee, consisting of my supervisor Johann G. Danzl, Peter Jonas and Stephan Sigrist, for guiding me through this journey to obtaining my PhD.

This work was supported by funding from the European Union's Horizon 2020 Programme for Research and Innovation (Marie-Skłodowska Curie grant agreement no. 665385), as well as funding from the Austrian Research Fund (FWF MolTag DK, W1232).

Next, I would like to acknowledge the work of all of my colleagues, who have been vital in shaping and elevating this project:

Hana Štefaničková, Jake Watson, Alban Cenameri and Alessandro Venturino for performing experiments.

Nathalie Agudelo-Dueñas, Jakob Vorlaufer and Andreas Wartak for expertly maintaining the optical systems and enduring all my optics-related questions.

Christoph Sommer, Marek Šuplata, Eder Miguel and especially Julia Lyudchik for making my life easier through their computational support.

ISTA's imaging and optics facility, life science facility, preclinical facility, electron microscopy facility, MIBA machine shop, IT and scientific computing for their assistance.

I am especially grateful for having had the opportunity to work with and learn from Philipp Velicky, Sven Truckenbrodt and Wiebke Jahr, who have not just been colleagues, but also mentors and friends to me. I will dearly miss the discussions over many cups of coffee with our lab-angel Caroline Kreuzinger.

I want to express my gratitude to my family for always rooting for me. My mother, Maria Poznysz-Michalska, whose endless curiosity encouraged me to never stop discovering and developing ideas. My father, Ryszard Michalski, whose grit taught me that I could be whoever I want to be, as long as I worked hard for it. And my sister, Sarah Michalska, who showed me that there are many, sometimes seemingly unconventional ways, to personal success.

Further, I would like to thank my friend, Hannah Wurzer, who always knows how to pick me up after a hard day.

Most importantly, I want to say thank you to my partner, Neville Junkin, for always being by my side and endlessly supporting me.

# Danksagung

Als Erstes möchte ich mich bei meinem PhD Kommittee, bestehend aus meinem Betreuer Johann G. Danzl, Peter Jonas und Stephan Sigrist, bedanken. Sie haben mich durch diese Reise zur Erlangung meines Doktortitels geleitet.

Diese Arbeit wurde unterstützt durch Finanzierung des European Union's Horizon 2020 Programme for Research and Innovation (Marie-Skłodowska Curie grant agreement no. 665385), sowie durch Finanzierung des FWF Wissenschaftsfonds (MolTag DK, W1232).

Als Nächstes möchte ich die Unterstützung aller meiner Arbeitskollegen anerkennen. Ihre Arbeit hat wesentlich dazu beigetragen dieses Projekt zu formen und zu verbessern:

Hana Štefaničková, Jake Watson, Alban Cenameri und Alessandro Venturino für die Durchführung von Experimenten.

Nathalie Agudelo-Dueñas, Jakob Vorlaufer and Andreas Wartak für die fachmännische Instandhaltung der Mikroskope und dafür, dass sie alle meine Optik-Fragen ertragen haben.

Christoph Sommer, Marek Suplata, Eder Miguel, aber vor Allem Julia Lyudchik, für ihre technische Unterstützung in jeglichen Computer-Anliegen, die mein Leben vereinfacht haben.

ISTA's imaging & optics facility, life science facility, preclinical facility, electron microscopy facility, MIBA machine shop, IT und scientific computing für ihre Mitwirkung.

Ich bin besonders dankbar dafür die Gelegenheit erhalten zu haben mit Philipp Velicky, Sven Truckenbrodt und Wiebke Jahre zu arbeiten und von ihnen zu lernen. Sie waren nicht nur Arbeitskollegen, sondern vielmehr Mentoren und Freunde. Ich werde auch die vielen Gespräche und Kaffees mit unserem Labor-Engel Caroline Kreuzinger vermissen.

Ich möchte meine Dankbarkeit gegenüber meiner Familie ausdrücken, die mich immer unterstützt haben. Gegenüber meiner Mutter, Maria Poznysz-Michalska, deren endlose Neugier mich dazu ermutigt hat nie damit aufzuhören, Neues zu entdecken und Ideen zu entwickeln. Gegenüber meinem Vater, Ryszard Michalski, dessen Entschlossenheit mir beigebracht hat, dass ich selbst darüber bestimmen kann, wer ich sein möchte, solange ich hart dafür arbeite. Und gegenüber meiner Schwester, Sarah Michalska, die mir gezeigt hat, dass viele Wege, auch scheinbar unkonventionelle, zu persönlichem Erfolg führen.

Ich möchte mich auch bei meiner Freundin Hannah Wurzer bedanken. Sie weiß genau wie man mir nach einem harten Tag Mut macht.

Vor allem aber möchte ich mich bei meinem Partner Neville Junkin bedanken, der mir immer zur Seite gestanden ist und mich stehts unterstützt hat.

# List of publications

Uncovering brain tissue architecture across scales with super-resolution light microscopy

**Michalska JM**, Lyudchik J, Velicky P, Štefaničková H, Watson JF, Cenameri A,. Sommer C, Venturino A, Roessler K, Czech T, Siegert S, Novarino G, Jonas P, Danzl JG; bioRxiv (2022); DOI: 10.1101/2022.08.17.504272

Saturated reconstruction of living brain tissue

Velicky P, Miguel E, **Michalska JM**, Wei D, Lin Z, Watson JF, Troidl J, Beyer J, Ben-Simon Y, Sommer C, Jahr W, Cenameri A, Broichhagen J, Grant SGN, Jonas P, Novarino G, Pfister HP, Bickel B, Danzl JG; bioRxiv (2022); DOI: 10.1101/2022.03.16.484431

# Table of contents

# List of abbreviations

| | |
|---|---|
| A | Area |
| $A_{pSCR/MFB}$ | Absolute MFB surface area occupied by pSCRs |
| $A_{pSCR}/A_{MFB}$ | Relative MFB surface area occupied by pSCRs |
| AA | Acrylamide |
| ACSF | Artificial cerebrospinal fluid |
| AcX | Acryloyl-X |
| AZ | Active zone |
| BCN | Bicyclononyne |
| BSA | Bovine serum albumin |
| CA | *Cornu ammonis* |
| CARE | Content-aware image restoration |
| CATS | Comprehensive analysis of nervous tissue across scales |
| coCATS | Compartment CATS |
| rCATS | Resident CATS |
| DAPI | 4',6-diaminidino-phenylindole (marker for nuclei) |
| DBCO | Dibenzocyclooctin |
| $ddH_2O$ | Double-distilled water |
| DG | Dentate gyrus |
| DIV | Days *in vitro* |
| DMSO | Dimethyl sulfoxide |
| ECM | Extracellular matrix |
| ECS | Extracellular space |
| EGFP | Enhanced green fluorescent protein |
| EM | Electron microscopy |
| EtOH | Ethanol |
| ExM | Expansion microscopy |
| FA | Formaldehyde |
| FP | Fluorescent protein |
| FWHM | Full width at half maximum |
| GABA | γ-aminobutyric acid |
| GC | Granule cell |
| GFAP | Glial fibrillary acidic protein (marker for astrocytes) |
| GFP | Green fluorescent protein |
| HBSS | Hank's Balanced Salt Solution |
| HOMER1 | Homer scaffold protein 1 (marker for excitatory postsynapses) |
| ICS | Intracellular space |
| l | Length |
| LEL | Lycopersicon esculentum lectin |
| LIONESS | Live Information-Optimized Nanoscopy Enabling Saturated Segmentation |
| LUT | Lookup table |
| LV | Lateral ventricle |
| MAP | Magnified analysis of the proteome |
| MAP2 | Microtubule-associated protein 2 (marker for neuronal dendrites and soma) |
| MFB | Mossy fiber bouton |
| MIP | Maximum intensity projection |
| MW | Molecular weight |
| n | Number |
| NA | Numerical aperture |
| NAS | Acrylic acid N-hydroxysuccinimide ester |
| NGS | Normal goat serum |
| NHS | N-hydroxysuccinimide ester |
| N2V | Noise2Void |

| | |
|---|---|
| ON | Over night |
| P | Post-natal day |
| PLL | Poly-l-lysine |
| PB | Phosphate buffer |
| PBS | Phosphate buffered saline |
| PEG | Polyethyleneglycol |
| PFP | Pentafluorophenyl |
| PHA-E | Phaseolus vulgaris erythroagglutinin |
| PHA-L | Phaseolus vulgaris leucoagglutinin |
| PN | Pyramidal neuron |
| proExM | Protein-retention expansion microscopy |
| pSCR | Putative synaptic cleft region |
| PSD | Postsynaptic density |
| PSF | Point-spread function |
| r | Pearson correlation coefficient |
| $R^2$ | R-squared |
| RESCue | Reduction of state transition cycles |
| RT | Room temperature |
| SBEM | Serial block-face scanning electron microscopy |
| SHANK2 | Proline-rich synapse associated protein-1 (marker for excitatory postsynapses) |
| SLM | Spatial light modulator |
| SMLM | Single-molecule localization microscopy |
| SNR | Signal-to-noise ratio |
| STED | Stimulated emission depletion |
| SUSHI | Super resolution shadow imaging |
| $S_0$ | Singlet ground state |
| $S_1$ | First excited state |
| s.d. | Standard deviation |
| TE | Thorny excrescence |
| TEM | Transmission electron microscopy |
| TFP | Tetrafluorophenyl |
| TX | Triton X-100 |
| U | unit |
| V | Volume |
| VGAT | Vesicular gamma-aminobutyric acid transporter (marker for inhibitory synapses) |
| VGLUT1 | Vesicular glutamate transporter 1 (marker for excitatory synapses) |
| VVL | Vicia villosa lectin |
| wt | Wild type |
| v/v | Volume per volume |
| WD | Working distance |
| WFL | Wisteria floribunda lectin |
| WGA | Wheat germ agglutinin |
| w/v | Weight per volume |
| 3D | Three-dimensional |
| $\Delta q$ | Electrical charge |
| $\lambda$ | Wavelength |
| $\lambda_{ex}$ | Longest-wavelength absorption maximum |
| $\lambda_{em}$ | Fluorescence maximum |

# List of figures

# List of tables

# 1 Introduction

The brain is an exceptionally sophisticated organ consisting of billions of cells and trillions of connections that orchestrate our cognition and behavior. To decode its complex connectivity, it is pivotal to disentangle its intricate architecture spanning from cm-sized circuits down to tens of nm-small synapses.
Light microscopy is an exquisite tool to study brain tissue organization, as it provides access to nearly all spatial scales of the brain, ranging from whole-tissue to sub-cellular scale. Super-resolution microscopy techniques, including stimulated emission depletion (STED) microscopy[1,2] and expansion microscopy (ExM)[3,4], are capable of resolving structures down to tens of nm, enabling the visualization of neuronal connections established by chemical synapses. In addition, structural interrogation of brain tissue with light microscopy is easily paired with readouts for neuronal activity, such as electrophysiological recordings or calcium imaging.
Currently, one of the major limitations for studying brain tissue organization with light microscopy is the lack of a labeling strategy that elucidates tissue structure in an unbiased fashion.

For my PhD project, my main goal was to establish a technology that enables researchers to study the organization of brain tissue in an unbiased fashion across multiple spatial scales, ranging from brain regions down to synapses. This included:

- The development of two labeling approaches, which fluorescently highlight the extracellular space (ECS) and are compatible with chemical fixation
- The combination with two super-resolution readout strategies (STED, ExM)
- The optimization of imaging parameters for isotropic super-resolution imaging, as well as large scale tissue imaging
- The development and adaptation of (deep learning) algorithms for the detection of synapse location
- The establishment of data analysis pipelines for the study of structural characteristics and connectivity

As the main application of this technology, I chose the hippocampal circuitry, mainly focusing on the connectivity established between the dentate gyrus (DG) and the CA3. This circuitry has been extensively characterized with electron microscopy (EM), giving me the possibility to validate my findings.

This section provides an overview of the landscape of super-resolution microscopy, current methods for studying brain tissue organization and an introduction of the structural characteristics of the hippocampal circuitry. Section 2 guides the reader through all stages of the development of the technology, starting with the introduction of an extracellular contrast into fixed brain tissue specimens, followed by protocols for super-resolution imaging and analysis strategies for studying neuronal properties. Section 3 provides a summary of the main biological findings, focusing on the hippocampal circuitry. Section 4 offers an outlook, discussing the potential of the technology for future (neuro-) biological studies.

## 1.1 Optical super-resolution microscopy

Light microscopy has been a powerful tool for attaining biological insights for hundreds of years. All light microscopy methods are constrained by the 'diffraction limit of light' as described by Abbe in 1837.[5] This limit, which arises from the wave nature of light, imposes a fundamental constraint on the obtainable spatial resolution in light microscopy. As a result, features residing closer to one another than the diffraction limit cannot be discriminated, thus severely hampering the study of fine structures in biological specimens.[6,7] For fluorescence microscopes using light in the visible wavelength range and high-numerical aperture (NA) objectives, the resolution limit is ~200-300 nm in the lateral (*xy*) direction and 700-800 nm in the axial (*z*) direction. This constraint especially impedes the study of the brain, an organ known for its complex composition and intricate structures, such as axons with down to ~100 nm thickness[8] and 20 nm wide synaptic clefts[9], with light microscopy.

The desire to overcome this constraint has driven the development of novel optical technologies resulting in ~2-fold resolution improvement, such as structured illumination microscopy for widefield microscopy[10,11] and airyscan detection for confocal imaging[12,13]. The resolution-limit was ultimately broken by the advent of optical super-resolution microscopy, also called 'nanoscopy' techniques. These techniques achieve diffraction-unlimited resolution by putting fluorophores in a diffraction-limited spot into distinguishable states, a fluorescent ON-state and a non-fluorescent OFF-state (Figure 1a).[14] Nanoscopy techniques are broadly classified in two groups: single-molecule localization microscopy (SMLM) and coordinate-targeted fluorescence nanoscopy.

SMLM techniques are based on the stochastic activation and localization of individual fluorophores. The resulting super-resolved image is created by superimposing many imaging frames containing sparse fluorophore localizations.[15] Variants of SMLM include photo-activated localization microscopy[15,16], stochastic optical reconstruction microscopy[17,18] and ground-state depletion followed by individual molecule return[19], differentiated by the use of fluorescent proteins (FPs) and fluorophores, respectively. Point accumulation for imaging in nanoscale topography, another SMLM technique, relies on stochastic, reversible binding of freely diffusing fluorescent ligands to a target.[20,21]

Coordinate-targeted fluorescence nanoscopy techniques use patterns of light to control the state (ON- or OFF) of fluorophores, thus making them distinguishable at the time point of detection.[14] The most commonly used form of coordinate-targeted fluorescence nanoscopy is STED microscopy. Here, stimulated emission is used to switch fluorophores into the OFF-state. The STED beam, which is overlaid with an excitation beam, features an intensity minimum, ideally of zero intensity. Fluorophores residing at this minimum remain in the ON-state and are detected (see Section 1.1.1).[1,2]

In recent years, the concepts of SMLM and coordinate-targeted nanoscopy have been combined to create a novel nanoscopy techniques yielding resolution down to single nm. These techniques utilize a two-step concept. First, sparse fluorophores in the ON-state are localized in a diffraction-limited fashion. Then, either a STED beam[22,23] or an excitation beam[24], both featuring an intensity minimum, is used to probe the position of the fluorophore.

### 1.1.1 Stimulated emission depletion microscopy

In fluorescence microscopy, a fluorophore is excited from the singlet ground state ($S_0$) into the first excited state ($S_1$) by an excitation laser beam. It will return to the $S_0$ state after ~1-4 ns, thereby emitting a single photon of a slightly longer wavelength. This phenomenon is called 'Stokes shift' and occurs due to energy loss caused by vibrational transitions.[25] In the excited state, the fluorophore can interact with an incoming photon resulting in stimulated emission. In this case, the fluorophore will emit a photon of the same wavelength as the incoming photon while returning to the $S_0$ state (Figure 1b, top). The wavelength of the STED laser is chosen such that it lays at the

tail of the fluorophore emission spectrum, to avoid excitation by the STED beam (Figure 1b, bottom).[2,14]

STED microscopy utilizes the concept of stimulated emission to distinguish fluorophores between ON-state (emission) and OFF-state (stimulated emission). An excitation beam is overlaid with a second (STED) beam that turns excited fluorophores into the OFF-state via stimulated emission. Fluorophores in the ON-state are confined to a small area in the immediate vicinity of the intensity minimum of the STED beam (Figure 1c).[1,2]

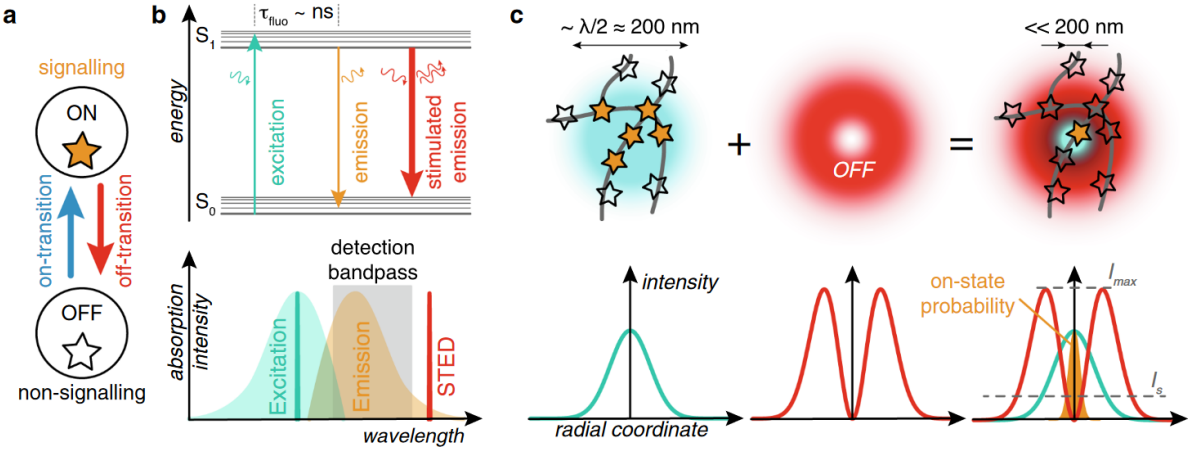


**Figure 1: Schematic of STED microscopy.** a) Schematic of molecular states needed for super-resolution microscopy. b) (Top) Energy diagram of fluorophore excitation (green), emission (yellow) and stimulated emission (red). (Bottom) Excitation (green) and emission (yellow) spectra of a typical STED fluorophore, including detection window (grey) and wavelengths for excitation (green) and STED (red) laser beams. c) Lateral views and intensity distribution of excitation and *xy*-STED beam. Fluorophores (stars) are excited (orange stars) in a diffraction-limited spot upon confocal excitation. When superimposing the excitation beam with a STED beam, only fluorophores located at the STED intensity zero are excited. $\tau_{fluo}$=fluorescence lifetime; λ=wavelength; $I_{max}$=maximum STED intensity; $I_S$=saturation intensity. Adapted with permission from Jahr *et al.*, 2019[14].

The shape of the STED beam governs the effective point-spread function (PSF) of the emitted light (Figure 2).

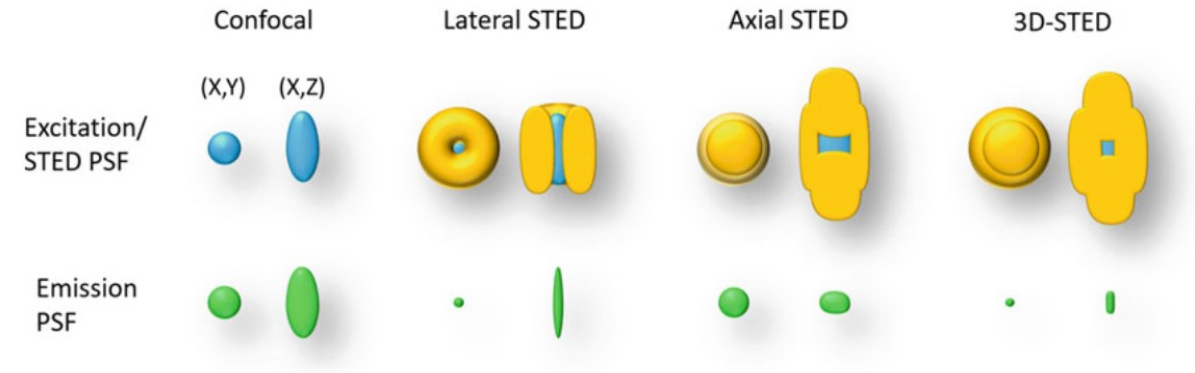


**Figure 2: Excitation and emission PSFs in confocal and STED microscopy.** Shapes of the excitation (blue), STED (yellow) and emission (green) PSFs in lateral (*xy*) and axial (*xz*) direction. The STED beam pattern influences the shape of the emission PSF. Reproduced with permission (Springer Nature, Methods Mol. Biol.) from Lenz & Tønnesen, 2019[26].

The most commonly used STED beam (*xy*-STED or lateral STED) resembles the shape of a donut and is commonly achieved via 2π-helical phase modulation of the STED beam.[26,27] This beam shape greatly enhances resolution in the lateral, but not in the axial direction. To improve resolution along the axial imaging axis, an alternative STED beam is created by a π–top-hat phase modulation (also called *z*-STED or axial STED). This modulation results in a beam with lobes

above and below the imaging plane, as well as a faint donut. As the resolution is mainly increased in the axial direction with a minor increase along the lateral axes, using axial STED enables near-isotropic resolution.[2] Lateral and axial STED beams can be combined to create a three dimensional (3D)-STED (or *xyz*-STED) beam[28], which allows for tuning of resolution increase in lateral and axial direction by varying the ratio of laser power between the *xy*- and the *z*-STED beam.

Overlaying the intensity minima of the two STED beams can be tricky, especially in scattering samples, such as tissues. A bigger *xy*-STED donut shape with a wider intensity minimum can be created by using a 4π-helical phase modulation, instead of the classical 2π. This facilitates overlaying the intensity minima of the *xy*- and *z*-STED beams and optimizes fluorescence quenching outside the central minimum. Fully isotropic resolution is achieved when using a 80:20 ratio between 4π-helical phase modulated *xy*-STED and *z*-STED beams.[29]
The resolution scales with the inverse square root of the power of the depletion laser.[30] As such, in theory there is no limit to the resolution that can be obtained with STED microscopy. However, increasing resolution by increasing STED power becomes progressively harder, as practical limitations, such as photobleaching, come into play.[1,14]
STED microscopy provides a direct, all optical strategy to read out fluorescence in a diffraction-unlimited fashion without the need for complex data post-processing. It can be advantageously combined with confocal detection to provide optical sectioning, such that volumetric imaging can be performed without the need for sample sectioning. Compared to other nanoscopy techniques, it excels at providing isotropic resolution in complex sample types, such as brain tissue. The major drawbacks are the need for specialized equipment and the use of high (STED) laser powers, which can result in phototoxicity and photobleaching.[31]

STED for tissue imaging
The performance of all light microscopy methods is affected by system- and sample-induced aberrations. In STED microscopy, loss of performance results from scattering and aberration-induced distortions of the depletion beam. These obscure the beam's intensity minimum, which is the critical component for maintaining the super-resolution properties of a STED microscope.[32,33] To achieve high quality super-resolved imaging data in tissue samples beyond a few μm in depth, it is therefore necessary to account for these aberrations.
Multiple studies have shown that the use of a sample refractive index (RI)-matched objective is beneficial for tissue imaging, as it minimizes spherical aberrations resulting from changes in the RI.[34,35] To this end, water (RI=1.33) objectives or glycerol objectives (RI=1.45) are commonly used. The RI of human and rodent brain tissue is estimated to be 1.37-1.47, dependent on the brain area.[36–38] This value is closely matched by silicone oil objectives using immersion oils with an RI of 1.41. In addition, an objective correction collar can greatly improve the penetration depth of the STED beam, as it can be used to compensate for RI-mismatches between the immersion medium of the lens and the sample.[39] Further adaptive elements can be employed to correct for sample-induced aberrations. As biological samples are optically heterogeneous, sample-induced aberrations cannot be easily estimated and pre-corrected. Therefore, adjustments need to be made through a feedback loop. This can be achieved by using a device that modulates the laser beam on the fly, such as a spatial light modulator (SLM). The SLM is utilized to create a desired STED beam pattern and alter its shape (while imaging the sample) to compensate for sample-induced aberrations.[35,40,41]

## 1.1.2 Expansion microscopy

ExM enhances resolution by embedding a sample into a swellable hydrogel, resulting in the sample's physical magnification.[3] The expansion factor, meaning the extent of expansion, directly translates into an effective resolution enhancement, thus providing super-resolution with a diffraction-limited imaging setup.
The principle of ExM is to create a polyelectrolyte gel within a biological sample with the goal of covalently linking molecules to be retained, such as proteins of interest or labels (e.g. antibodies), within the gel network. To achieve this, target molecules of interest are populated with an anchor. Then, the sample is infused with a hydrogel monomer solution. Due to the small size of the monomers, they permeate into the intracellular space (ICS) of the sample. Polymerization of the hydrogel monomers by a cross-linker is initiated. During this process, the target molecules are incorporated into the hydrogel via the anchoring moiety. Next, the mechanical cohesiveness of the tissue is disrupted in a homogenization step to allow for its isotropic expansion. Previously anchored molecules remain immobilized in the gel network and thus faithfully retained. The gelled sample is then placed into deionized water, leading to the swelling of the gel due to the charge repulsion of the polymer chains.[42]
During the expansion process, the sample is cleared and its RI is homogenized and matched to the RI of water, thus diminishing aberrations and scattering. This greatly facilitates deep tissue imaging, making ExM an excellent tool for the visualization and study of large tissue volumes with high resolution.[43] Yet, one should be aware that sample expansion leads to a drastic increase in sample volume. For example, 10-fold expansion leads to a 1000-fold increase in sample volume, thus resulting in an increased acquisition time and data volume.
Since its invention in 2015[3], a plethora of ExM protocols has been developed. They differ in their hydrogel compositions, strategies to anchor target molecules into the hydrogel, target molecule labeling approaches and mechanisms of homogenization.

Hydrogel composition: Most ExM hydrogels are acrylamide (AA)-acrylate co-polymers created by free radical polymerization. The first hydrogels of this type, some of which are still widely used, provide ~4-fold expansion.[3,44–46] Various modifications to the polymer chemistry and expansion procedure have been introduced to increase the expansion factor and thus the attainable resolution. Iterative ExM uses two consecutive rounds of hydrogel embedding and expansion, resulting in 20-fold expansion.[47,48] In X10 microscopy[49,50] and MAGNIFY[51], the hydrogel composition has been altered to provide ~10-fold expansion in a single expansion step. ZOOM utilizes a hydrogel-conversion based expansion strategy, which introduces ionic residues into the gel network by alkaline hydrolysis, resulting in a tunable, up to 10-fold expansion.[52] Gao *et al.*[53] proposed a hydrogel consisting of tetrahedral monomers, which assemble via non-radical linking, to achieve a more homogeneous network structure.

Anchoring approaches: Many ExM variants comprise a dedicated anchoring step after the fixation procedure. An anchoring moiety, such as Acryloyl-X (AcX)[44] or (meth)acrylic acid N-hydroxy succinimidyl ester (NAS)[45], covalently binds to primary amines in the sample to incorporate acryloyl moieties, which then copolymerize with the hydrogel. Alternatively, acryloyl moieties can be added to primary amines directly during the fixation procedure by using a formaldehyde (FA)-acrylamide mixture during fixation.[46,54] Both approaches lead to the incorporation of the majority of proteins into the hydrogel. In addition, there are dedicated strategies, involving the use of click-chemistry[55] and multifunctional anchors[56–58], to optimize the retention of specific biomolecular groups, such as lipids[59,60] and nucleic acids[61].

Target molecule labeling: Molecules of interest can be labeled before or after the expansion procedure. Introducing the label, e.g. in form of an immunostaining, before the gelation procedure,

is a straightforward way to achieve a fluorescent readout[44,45,49]. However, this approach suffers from various drawbacks, such as loss of fluorescent signal during the gelation and homogenization procedure, introduction of a linkage error - the displacement of the imaging probe to the actual target - and potentially limited labeling efficiency in the crowded pre-expansion environment. The loss of fluorescent signal can be mitigated by using labeling approaches, which allow for the addition of a fluorescent readout-probe after the expansion procedure, such as click chemistry[55] or strong non-covalent interactions (e.g. biotin-avidin interactions)[62] and/or by using signal amplification strategies. In the super-resolution field, efforts are underway to address the linkage error and issue of crowding by using small molecule probes, such as nanobodies.[63] ExM offers the possibility to mitigate this problem by post-expansion labeling.[46] Various publications have shown that decrowding of the environment by expansion before target labeling results in an increase in epitope accessibility, thus improving labeling density.[48,54,64]

Sample homogenization: There are two commonly used mechanisms to homogenize the biological sample after gelation: enzymatic digestion and heat/chemical denaturation. To achieve enzymatic digestion, a nonspecific proteinase, such as proteinase K, is utilized to disrupt the tissue.[3] In this case, it is common to label proteins of interest before the homogenization procedure, as the digestion disrupts epitopes (Figure 3a). Alternatively, the sample can be homogenized by the use of high temperatures paired with denaturation agents, such as surfactants, thereby dissociating and denaturing protein complexes and clearing the samples from lipids.[46] As the primary structure of proteins remains intact, immunostainings can be performed after the homogenization procedure (Figure 3b). Yet, because of the denaturation of the epitopes, only antibodies, whose binding is not dependent on intact protein folding, will perform well.

Based on the recent developments of the ExM technology, further advancements can be expected in the near future.

The two ExM protocols used in this study are protein-retention expansion microscopy (proExM)[44] and magnified analysis of the proteome (MAP)[46]. Both protocols are based on AA-acrylate copolymers resulting in ~4-fold expansion, but utilize different anchoring and homogenization mechanisms. For proExM, a commonly fixed sample is first labeled with fluorescent molecules, such as antibodies. The sample proteins and antibodies are anchored into the hydrogel with AcX.[44] The sample is then digested with proteinase K and expanded (Figure 3a). MAP requires a fixation or post-fixation step with a FA-AA mixture for anchoring. The hydrogel is cast directly after this procedure and sample cohesiveness is disrupted by heat/chemical denaturation. Staining of proteins is performed after expansion (Figure 3b).[46]

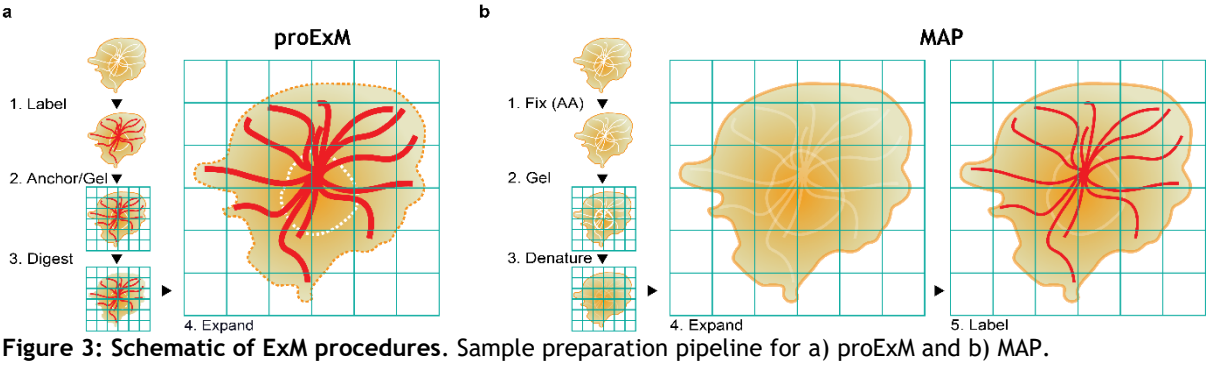


**Figure 3: Schematic of ExM procedures.** Sample preparation pipeline for a) proExM and b) MAP.

## 1.2 Visualizing brain tissue organization across scales

Visualizing the architecture that underlies the complex organization of the brain has been a major goal in the field of neuroscience for decades, spearheaded by Ramon y Cajal's insights into the microscopic structure of neural circuitry.[65] Disentangling the precise relationships between the brain's copious cellular components is fundamental to understanding how it develops, functions in a healthy state and malfunctions in disease. The challenge lies in the visualization of the brain across its many spatial scales, ranging from mm-cm sized circuits to tens of nm-sized synaptic connections. EM is one of the most common tools for the analysis of nervous tissue organization down to synapse level to date, as it provides exquisite spatial resolution and structural contrast. EM has been widely used to reconstruct nervous tissue from human[66–68], mouse[66,69–72], zebrafish[73–75], nematode[76–78] and fruit fly[79] specimens to analyze their connectivity. Nowadays, serial block-face (SBEM)[80], focused ion beam[81] or gas cluster ion beam[82] scanning EM are then utilized for acquiring volumetric datasets, as they combine sectioning and data acquisition with minimal need for data alignment. Yet, these methods are technically challenging, laborious and difficult to combine with molecular stainings. While the resolution and thus detail obtainable with EM is unrivaled, it also results in large amounts of data that are tedious to handle computationally. For example, a 1 $mm^3$ tissue volume amounts to ~1.4 petabytes of data.[68] This amount of data requires a lot of storage space, as well as powerful machinery for visualization, data processing and analysis. Hence, upscaling EM workflows to access bigger spatial scales remains challenging. One way to address this challenge is the use of correlative multimodal imaging approaches. These involve multiple imaging modalities, each of which is optimized for the visualization of a different spatial (or temporal) scale.[83–85] In many cases, correlative approaches combine structural and functional data with the aim of gaining a mechanistic understanding of neural circuitry from its architecture and activity.[86–90] In addition, correlative light electron microscopy can be used to underpin structural EM data with molecular information obtained from light microscopy.[91,92] In principle, correlative approaches simplify computational efforts, as they generate lower amounts of data compared to pure EM-studies. Yet, registration of imaging data from different imaging modalities poses a serious computational challenge. Additionally, correlative approaches are limited to sample preparation protocols that ensure compatibility with all imaging modalities.
In summary, currently no single imaging method exists that is capable of spanning all spatial scales needed to map the brain from whole tissue to single synapse.

### 1.2.1 Creating tissue contrast for visualizing brain tissue architecture

Visualizing the structure of the brain is fundamental to understanding how composition and activity act in concert to direct all its functions. In fluorescence microscopy, this is typically achieved by labeling certain molecules, for example a particular protein species, with high specificity, to study it. This provides information about the abundance and location of this protein species in the sample. Yet, as long as other components of the sample remain unlabeled, it is not possible to place the labeled structure in its structural context. To elucidate structural context, it is necessary to introduce contrast, which makes it possible to demarcate the biological components that make up the tissue. Most imaging methods necessitate a dedicated labeling procedure to introduce such a contrast.
In EM, heavy metal stains, often based on osmium, uranium and lead, are used to visualize proteins and lipids by increasing their electron-density.[93–96] This **membrane/protein contrast** (Figure 4a) permits the identification of cellular and subcellular structures, including the cytoskeleton and organelles, as well as the distinction of the intra- and extracellular environment via cell membranes. Many cellular structures, including synapses, can be clearly identified based on their location, architecture, as well as their lipid and protein content, even in the absence of specific molecular stainings. Recently, membrane/protein contrasting has been paired with other imaging strategies,

such as X-ray holographic nano-tomography, to achieve dense reconstruction of brain tissue.[97] To create similar structural contrast for light microscopy-approaches, comprehensive staining of various molecule groups, including lipids, proteins and carbohydrates, has been utilized.[55,59,98,99] Alternative imaging technologies, such as nonlinear stimulated Raman scattering, achieve high protein contrast without the need for a dedicated staining step (label-free imaging), and have been paired with ExM to visualize the structure of cultured cells and brain slices.[100,101]

The standard tool for visualizing and tracing cellular structures with light microscopy is to create **intracellular contrast** (Figure 4b) by introducing fluorescent molecules into the cell interior of a sparse subset of cells. This is commonly achieved by genetically encoded or virally induced expression of FPs, such as green fluorescent protein (GFP), in the ICS, or by manual filling of individual cells.[102–105] FPs can also be guided to cellular compartments, e.g. the plasma membrane or organelles, if needed. Combinatorial approaches, such as Brainbow[106], Confetti[107,108], Tetbow[109] and Bitbow[110], utilize the stochastic combined expression of multiple FPs to barcode individual cells in different colors. The main advantage of intracellular labeling is the high specificity achieved by targeting specific cell populations based on their genetic or spatial characteristics. Yet, this specificity proves to be a disadvantage for creating tissue contrast in a comprehensive fashion, as in most cases only a subset of cells is labeled. In addition, despite the introduction of various colors, it is challenging to distinguish complex cellular structures when the labeling becomes too dense.

A less targeted approach to visualize tissue context involves the labeling of the extracellular compartment, thereby creating **extracellular contrast** (Figure 4c). By keeping the ICS unlabeled, a 'negative image' of cellular structures independent of their identity is created. This strategy was introduced in early EM-connectomics studies of the mouse retina.[89] Here, acute, living retina samples were bathed in a horseradish peroxidase-containing solution and chemically fixed directly thereafter, thus immobilizing the peroxidase in the ECS and on cell surfaces. Horseradish peroxidase retains its enzymatic activity upon FA-fixation. It was used to deposit electron-dense material in its close proximity by oxidizing diaminobenzidine. This resulted in a 'negative image' of the extracellular environment that could be read out with EM. In the field of light microscopy, extracellular contrast is created by bathing living samples in a solution of membrane-impermeant fluorophores, which freely diffuse through the ECS, and imaging in the living state.[111] Large-molecular weight molecules comprised of dextran have also been used to study the flow of soluble factors in lymph nodes and the brain.[112,113] A different approach is to track the diffusion of single carbon nanotubes in intact ECS to analyze the dimension and local viscosity of the extracellular compartment.[114]

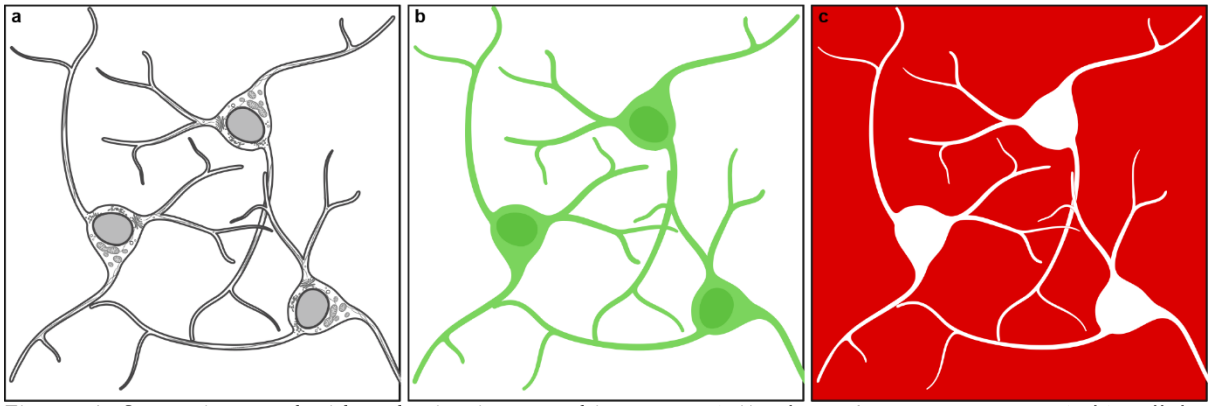


**Figure 4: Strategies to elucidate brain tissue architecture.** a) Membrane/protein contrast: (sub) cellular structures become visible by labeling of specific molecule groups, such as lipids and/or proteins. b) Intracellular contrast: cellular structures are outlined by the presence of fluorescent molecules in the ICS. c) Extracellular contrast: cellular structures are demarcated by labeling the extracellular compartment, thus creating a 'negative image' of the intracellular compartment. Created with BioRender (biorender.com).

### 1.2.2 Studying brain organization with super-resolution light microscopy

The advent of nanoscopy marked the start of a revolution for the study of brain organization with light microscopy. Once the resolution limit was lifted, super-resolution microscopy was used to study the molecular organization of complex brain structures that lay beneath the diffraction limit of light, including synapses[39,115–121], the neuronal cytoskeleton[122–124], neuronal structure-function relationships[125–129] and synaptic connectivity[43,130]. However, in all these cases information about tissue context was missing, as the analysis was limited to specific molecular targets or a subset of labeled cells. To overcome this limitation, super-resolution-compatible labeling paradigms for creating tissue contrast were developed and applied to get insights into brain tissue architecture and connectivity.

Various ExM approaches have achieved comprehensive labeling of brain tissue by targeting molecule groups, such as lipids, proteins or carbohydrates. Localizing membrane structures with ExM is difficult, as permeabilization and homogenization steps lead to the extraction of lipids. This problem was addressed by developing multifunctional anchors that consist of moieties for lipid recognition, hydrogel incorporation and fluorescent readout.[58,59] M'Saad *et al.*[98] and Mao *et al.*[99] have shown that fluorescent dyes, which are coupled with reactive groups covalently binding to primary amines or thiols, label proteins in cultured cells and tissues in a comprehensive fashion. Similarly, carbohydrates, which are enriched in the ECS, were visualized.[99] While diffraction-limited light microscopy is sufficient to visualize tissue organization at regional scale, these studies have shown that resolution beyond the diffraction limit is necessary to elucidate cellular ultrastructure.[98] Combined with high expansion factors (~24-fold) for improved resolution, protein-contrasting in combination with synaptic markers has created insights into brain tissue ultrastructure, including the architecture of the synaptic scaffold.[131] Whilst revealing intracellular complexity by total protein staining is beneficial for studying cellular ultrastructure, the labeling of all cellular structures complicates the identification of cellular outlines in complex tissue environments. Hence, even though these approaches optically yield staining patterns similar to the membrane/protein contrasting commonly used in EM, they have not yet been successfully applied to analyze tissue connectivity.

ExM has also been used to simultaneously interrogate cellular morphology, identity and connectivity at super-resolution by multiplexed readout of intracellular Brainbow labeling and molecular markers for excitatory and inhibitory neurons.[132] This approach proved to be useful for the study of synaptic profiles of Brainbow-expressing neuronal cell populations, but could not provide unbiased insights into the structure and connectivity of non-labeled cells. Hypothetically, an unbiased representation of tissue structure can be achieved by intracellularly labeling all cells in a given tissue. Yet, this approach would necessitate extremely high resolution to distinguish cellular structures labeled with the same FP from one another, as borders between structures, which are smaller than the effective resolution, would be obscured. This is especially problematic when studying nervous tissue, because it features an intricate extracellular environment including synaptic clefts, which are a mere 20 nm wide.[9] Combinatorial labeling aims at alleviating this caveat by providing every cell with an individual color code, but its potential to comprehensively disentangle intricate neuronal networks has yet to be demonstrated.

An elegant approach to circumvent the obstruction of cellular borders is by labeling the structures in question. This can be achieved by targeting the ECS, which comprises the space between all cellular structures and thus creates a natural border that demarcates cellular structures. This has two major advantages. Firstly, the resulting data remains free of intracellular complexity, thus facilitating manual and automated segmentation tasks. Secondly, labeling the extracellular borders between cellular structures enables the distinction of cellular compartments even at low resolution. The main disadvantage is that cellular structures considerably smaller than the effective resolution are lost. Tønnesen *et al.*[133] demonstrated the power of extracellular labeling for the study of brain

organization by developing and applying a method called super-resolution shadow imaging (SUSHI). Here, freely diffusing, membrane-impermeant fluorophores are applied extracellularly and super-resolved with STED microscopy in living brain tissue. SUSHI enabled the unbiased visualization of unlabeled brain cells in their anatomical context. This opens the door to study tissue structure and dynamics at high resolution with light microscopy, as shown by imaging microglia cell migration, structural changes in neurons and glia resulting from osmolality changes and reconstruction of major cellular structures.[133,134] Building on the method, we have recently demonstrated that dense, synapse-level reconstruction of living brain tissue is possible with light microscopy.[29] We achieved this by applying extracellular contrast to intact brain samples and reading it out with a specifically engineered 3D-STED imaging approach. We used a deep learning algorithm for image restoration[135] to decrease the light burden on the sample. We then reconstructed cellular structures with a machine learning pipeline for automated segmentation[136].
To increase imaging volume, as well as imaging depth, diffraction-limited shadow imaging has recently been combined with light sheet microscopy and two-photon microscopy in brain slices and intact brain.[137] However, all shadow imaging approaches, including SUSHI and LIONESS, are only amenable to living, intact specimens. This creates limitations in terms of sample type, addressable tissue volumes and molecular labeling options. Live imaging does not lend itself to the acquisition of large tissue volumes, as this requires extensive imaging time. In addition, the axial extent of imaging volumes is limited by sample-induced optical aberrations. Therefore, these approaches are not suitable for the study of brain organization across spatial scales.
Thus, there is an unmet need for an optical technology enabling the unbiased visualization and quantification of brain tissue organization across spatial scales, ranging from regional to single-synapse level.
For my PhD project, my goal was to address this need by developing a technology that enables the visualization of brain tissue architecture across several spatial scales, in conjunction with accessing molecular and functional information.

# 1.3 Hippocampal circuitry

The hippocampal formation is one of the most thoroughly studied brain regions of the mammalian central nervous system. It is part of the limbic system and plays a fundamental role in learning and memory formation. It is involved in the processing, storage and recall of spatial information, as well as the formation of episodic memory.[138,139]

The hippocampal formation consists of the DG, the hippocampus (proper), the subiculum, presubiculum, parasubiculum and the entorhinal cortex (Figure 5). The DG is populated by granule cells (GCs) whose cell bodies form the DG granule cell layer. Their dendrites are located in the molecular layer, while their axons run through the polymorphic layer, also called hilus, where they contact mossy cells and inhibitory neurons. The hippocampus is separated into three *cornu ammonis* (CA) subfields – CA1, CA2 and CA3 – based on the morphology and connectivity of its principal cells, the pyramidal neurons (PNs).[140] The CA is divided into four layers. The *stratum pyramidale* (pyramidal layer) is the main cell layer, housing PN cell bodies. The basal dendrites of PNs are located in the the *stratum oriens*, while the apical dendrites extend through the *stratum radiatum* into the *stratum lacunosum-moleculare*. The hippocampal formation receives sensory information via glutamatergic inputs from the entorhinal cortex. These inputs either synapse directly onto CA1 PNs, or relay their information through the trisynaptic path, involving the DG and CA3. In this case, DG GCs receive excitatory input from the entorhinal cortex through the perforant path (Figure 5). The GCs send their axons in the form of bundles, so called mossy fibers, through the DG hilus into the CA3 *stratum lucidum*. Here, they form complex excitatory synaptic connections with CA3 PNs. These CA3 PNs provide strong excitation by projecting to the proximal dendrites of CA1 PNs through the Schaffer collateral pathway.[141–143]

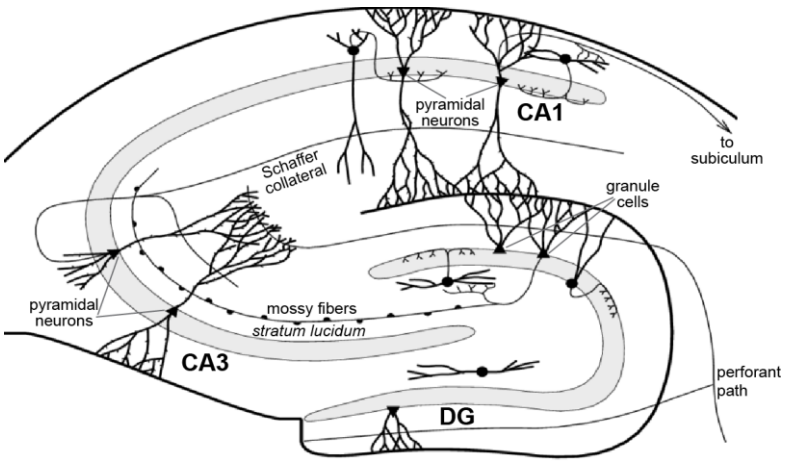


**Figure 5: Schematic diagram of the trisynaptic path.** Mouse hippocampal formation, including cellular components involved in the trisynaptic path. Adapted with permission from Schultz *et al.*, 2000[143].

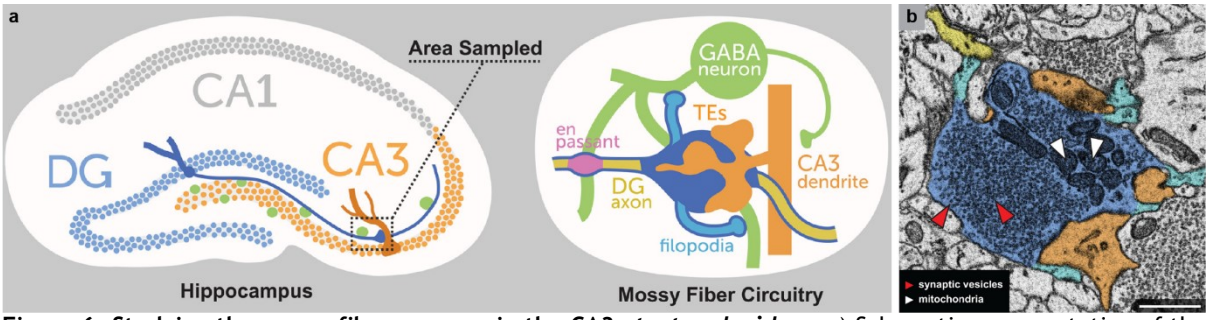


**Figure 6: Studying the mossy fiber synapse in the CA3 *stratum lucidum*.** a) Schematic representation of the cellular structures involved in DG GC-CA3 PN connectivity (also called mossy fiber circuitry). b) Single SBEM section from the CA3 *stratum lucidum* (Area Sampled in a) of an adult wildtype (wt) mouse showing the various components of a DG GC-CA3 PN synapse (blue = mossy fiber bouton (MFB), cyan = filopodia, orange = TE, yellow = DG axon). Adapted from Martin *et al.*, 2017[144].

In this pathway, the synaptic connections formed between the DG GC and the CA3 PN have received particular attention, as they constitute one of the most complex synapses in the brain, providing a unique system for the study of higher order computation. In the CA3 *stratum lucidum*,

incoming DG mossy fibers form big presynaptic structures called giant mossy fiber boutons (MFBs), which innervate complex branched postsynaptic structures on the proximal dendrites of CA3 PNs termed thorny excrescences (TEs) (Figure 6).[145–147]

Thorough morphological characterizations of DG GC-CA3 PN synapses have been mainly performed with transmission EM (TEM) and SBEM (Table 1). These have shown that both giant MFBs and TEs are highly variable in shape and size. Giant MFBs are vesicle-rich and connect to TEs extensively through multiple active zones (AZs) (Figure 6b). In the mature state, they form 2-4 filopodial extensions, which provide feed-forward inhibition by synapsing onto γ-aminobutyric acid (GABA)-producing, interneurons.[144,148–150] Each DG GC forms 10-15 giant, evenly spaced MFBs, as well as 40-50 smaller MFBs, called *en passant* boutons, in the CA3 *stratum lucidum*.[151] In addition, GCs form connections with interneurons and mossy cells in the DG hilus. Here, each GC gives rise to ~10 giant MFBs and 120-150 *en passant* boutons.[152]

**Table 1: Morphological characteristics of pre- and postsynaptic components of the DG GC-CA3 PN synapse.**

| | | Chicurel & Harris (1992)[148] | Rollenhagen *et al.* (2007, 2010)[149,153] | Wilke *et al.* (2013)[150] |
|---|---|---|---|---|
| | Organism | Rat | Rat | Mouse |
| | Age (days) | 70 | 90-120 | 120 |
| | Sample type | Perfused brain | Perfused brain | Perfused brain |
| | Acquisition | TEM | TEM | SBEM |
| MFBs | $n_{MFB}$/cell (-) | - | 15 | 10-15 |
| | $A_{MFB}$ (µm²) | - | 58.50 | 66.53 |
| | $V_{MFB}$ (µm³) | - | 8.24 | 13.51 |
| | $n_{AZ}$/MFB (-) | - | 18 | - |
| | $A_{AZ}$ (µm²) | - | 0.11 | - |
| | $A_{AZ}$/MFB (µm²) | - | 2.10 | - |
| | $A_{AZ}$/MFB (%) | - | 9.70 | - |
| TEs | $n_{filopodium}$/MFB (-) | - | 2-4 | 2.33 |
| | $l_{filopodium}$ (µm) | - | 1.00-5.00 | - |
| | $n_{TE}$/cell (-) | - | - | 46 |
| | $A_{TE}$ (µm²) | 22.65 | 16.03 | 13.85 |
| | $V_{TE}$ (µm³) | 1.83 | - | 1.64 |

n=number, A=area, V=volume, l=length

The DG GC-CA3 PN synapse displays unique structural and functional characteristics, making it an exciting target for further studies.

# 2 Method development: Comprehensive analysis of nervous tissue across scales

The main goal of my project was to develop a toolbox for the investigation of brain tissue organization across spatial scales to uncover tissue architecture and connectivity with light microscopy

The following considerations guided the development of this methodology:

1. Contrasting: A labeling procedure that introduces contrast into the nervous tissue is needed to enable the visualization of morphological context with light microscopy. I decided to develop labeling strategies creating an extracellular contrast, as this delineates all cellular structures, making it useful for image acquisition at various scales and resolutions (e.g. regional, cellular, synaptic scale).
2. Compatibility with fixation: Working with (chemically) fixed tissue implies high flexibility in terms of sample handling, labeling of molecular markers and data acquisition. Fixed specimens allow easier access to multiple spatial scales compared to living ones, as they can be cleared, imaged over long time periods and moved between imaging systems, thus enabling more elaborate data acquisition workflows.
3. Access to molecular information: Compatibility with molecular labeling is needed to probe the sample beyond its structural organization, for example to characterize cellular identities or synaptic locations.
4. Scalability: The method needs to be compatible with the multitude of fluorescent microscopy techniques (e.g. spinning disk, confocal and STED microscopy) to enable imaging at various spatial scales. Additionally, access to deep tissue layers without the need of fine sectioning, e.g. by tissue clearing, is desirable.
5. Adoptability: The method should be accessible and easily adoptable for the scientific community. Hence, I decided to base the toolbox entirely on commercially available chemicals and optical imaging systems, straightforward sample handling workflows and open-source software and scripts for data analysis.

Taking all these considerations into account, I developed a platform called **Comprehensive Analysis of nervous Tissue across Scales** (CATS). The CATS toolbox consists of a modular workflow to ensure high flexibility and versatility for the scientific community (Figure 7).

I developed two labeling paradigms to account for the majority of commonly used brain sample types, including native brain, acute and cultured brain slices, cerebral organoids, primary neuron cultures, perfusion-fixed brains, as well as chemically fixed clinical samples. The compartment CATS (coCATS) labeling paradigm makes use of reactive, membrane-impermeant labeling compounds, which are infused into the ECS of living specimens. There, they covalently bind to proteins and other molecules, making them available for readout after fixation (see Section 2.1.1). Resident CATS (rCATS) is applied after fixation and demarcates the ECS by binding to molecules enriched in the extracellular matrix (ECM) (see Section 2.1.2). CATS labeling is compatible with staining for molecular markers, such as immunostaining approaches. I focused mainly on super-resolution data acquisition schemes, such as STED and ExM, to get access to the synaptic scale. Still, I ensured that tissue context with CATS can be studied with diverse fluorescence microscopy techniques. Lastly, with the help of colleagues, I developed novel and implemented existing data analysis pipelines for the skeletonization and segmentation of neuronal structures, the automated identification of synapse location and the study of local connectivity. This involved deep learning algorithms for denoising of volumetric data and for the prediction of synaptic locations.

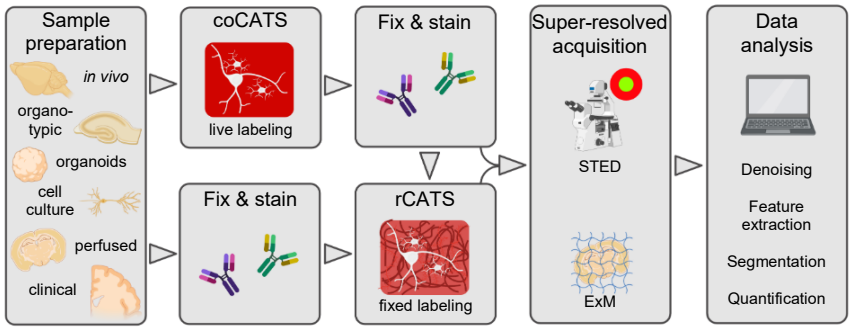


**Figure 7: Toolbox for the Comprehensive Analysis of nervous Tissue across Scales (CATS).** Schematic was created with BioRender (biorender.com).

# 2.1 Tissue labeling

As a first step towards creating a toolbox for the study of brain tissue organization with light microscopy, I needed to develop a labeling paradigm that enables an unbiased distinction of cellular structures in nervous tissue samples.

Labeling the ECS imposes a clear boundary between all cellular structures within the tissue, thus creating an extra- to intracellular contrast. This boundary allows us to distinguish cellular structures that are larger than the resolution utilized for acquiring imaging data. This holds true both for diffraction-limited and super resolution imaging technologies, making CATS a useful tool for visualizing structural context of brain tissue at various spatial scales.

There was no technology available that would reliably label the ECS with fluorescent molecules in fixed nervous tissue specimens. Hence, I set out to create one, based on the following requirements:

1. Contrast: the labeling paradigm has to provide high and homogeneous extracellular contrast
2. Compound binding: the labeling paradigm has to mediate a stable attachment of fluorophores to the sample, via
    a. Covalent attachment or
    b. Attachment with high affinity
3. Fixation: the labeling paradigm has to be compatible with fixation, meaning that it is applied either
    a. in the living specimen and not impacted by the fixation procedure or
    b. after the fixation procedure
4. Tissue penetration: the label has to penetrate the tissue sufficiently
5. Imaging compatibility: the labeling paradigm has to be compatible with downstream (super-resolution) imaging, specifically
    a. STED microscopy and/or
    b. ExM

Based on these premises I developed two labeling paradigms for revealing tissue structure by selective labeling of the extracellular domain: fixable coCATS and fixed-tissue compatible rCATS.

For visualization purposes, the lookup table (LUT) of all CATS images was inverted, if not otherwise stated.

## 2.1.1 Compartment CATS

To demarcate cellular structures within the tissue with high fidelity, it is pivotal to label the ECS with high specificity, homogeneity and signal-to-noise ratio (SNR). Thus, I aimed at creating a labeling paradigm that binds to as many structures within the ECS as possible, with limited specificity for individual molecular identities, while ensuring that it binds exclusively within the ECS.
Inspired by previous approaches for live tissue 'shadow imaging'[111,133], I infused labeling compounds into the ECS of living brain specimens. These compounds feature a reactive group that covalently binds to various structures in the ECS. Extracellular contrast is maintained by the intact cellular membranes of the sample, which constrain the labeling to the ECS and cell surfaces. We termed this labeling paradigm **compartment CATS** (coCATS), as it constrains labeling to the extracellular compartment.

The coCATS labeling paradigm fulfills the requirements stipulated in Section 2.1 as follows:

1. Contrast: Extracellular contrast is achieved by infusing the labeling compound into the ECS of a living specimen with intact membrane boundaries. Compound infusion is performed either by bathing the sample in a solution containing the compound or by injecting the compound directly into the tissue. For direct labeling, fluorescent dyes conjugated to reactive groups are used. To guarantee that they do not pass cellular membranes, hydrophilic, anionic fluorophores were selected. The hydrophilicity of non-fluorescent labeling compounds was increased with a polyethyleneglycol (PEG)-linker. A summary of all tested compounds and their chemical properties can be found in the Appendix Table 1.
2. Compound binding: Stable attachment to structures within the ECS is achieved by covalent binding of the labeling compound via a N-hydroxysuccinimide (NHS)- or tetrafluorophenyl (TFP)-moiety. These moieties react with primary amines, mainly present in proteins, resulting in the formation of a stable amide bond between the protein and the labeling compound (see Appendix Section 6.1).
3. Fixation: Covalent attachment of the labeling compound to structures in the ECS leads to its stable binding before and after fixation. To maintain high labeling intensity after fixation, fixation-compatible fluorophores should be used (direct labeling). Alternatively, non-fluorescent moieties, which are targeted with fluorescent readout probes after fixation, can be used (indirect labeling). For example, labeling compounds containing a biotin moiety are read out with fluorophore-conjugated streptavidin post-fixation.
4. Tissue penetration: All labeling compounds are small (≤1 kDa) and hydrophilic, such that they quickly move through the ECS and penetrate a 100-200 μm thick brain slice within minutes.[133,154] For information on the chemical properties of the probes, see Appendix Table 2.
5. Imaging compatibility
    a. STED: High-performance, far-red, STED-optimized fluorophores, such as **STAR RED-NHS** and **Atto 643-NHS**, are used for direct coCATS labeling. A direct readout strategy bypasses downstream processes, such as permeabilization, that can negatively affect labeling homogeneity and structural preservation.
    b. ExM: **NHS-PEG$_{12}$-biotin** or **TFP-PEG$_{12}$-biotin**, both labeling compounds with an indirect readout strategy, are used for ExM experiments. The PEG-linker imparts hydrophilicity. Using a biotin allows for fluorophore addition post-expansion. This circumvents damage to fluorophores by hydrogel radical chemistry or harsh homogenization steps and provides signal amplification.

The coCATS labeling approach is suitable for all biological sample types that are living and contain intact cellular membranes, including cell cultures, slice cultures, organoid cultures and brain areas labeled *in vivo*.

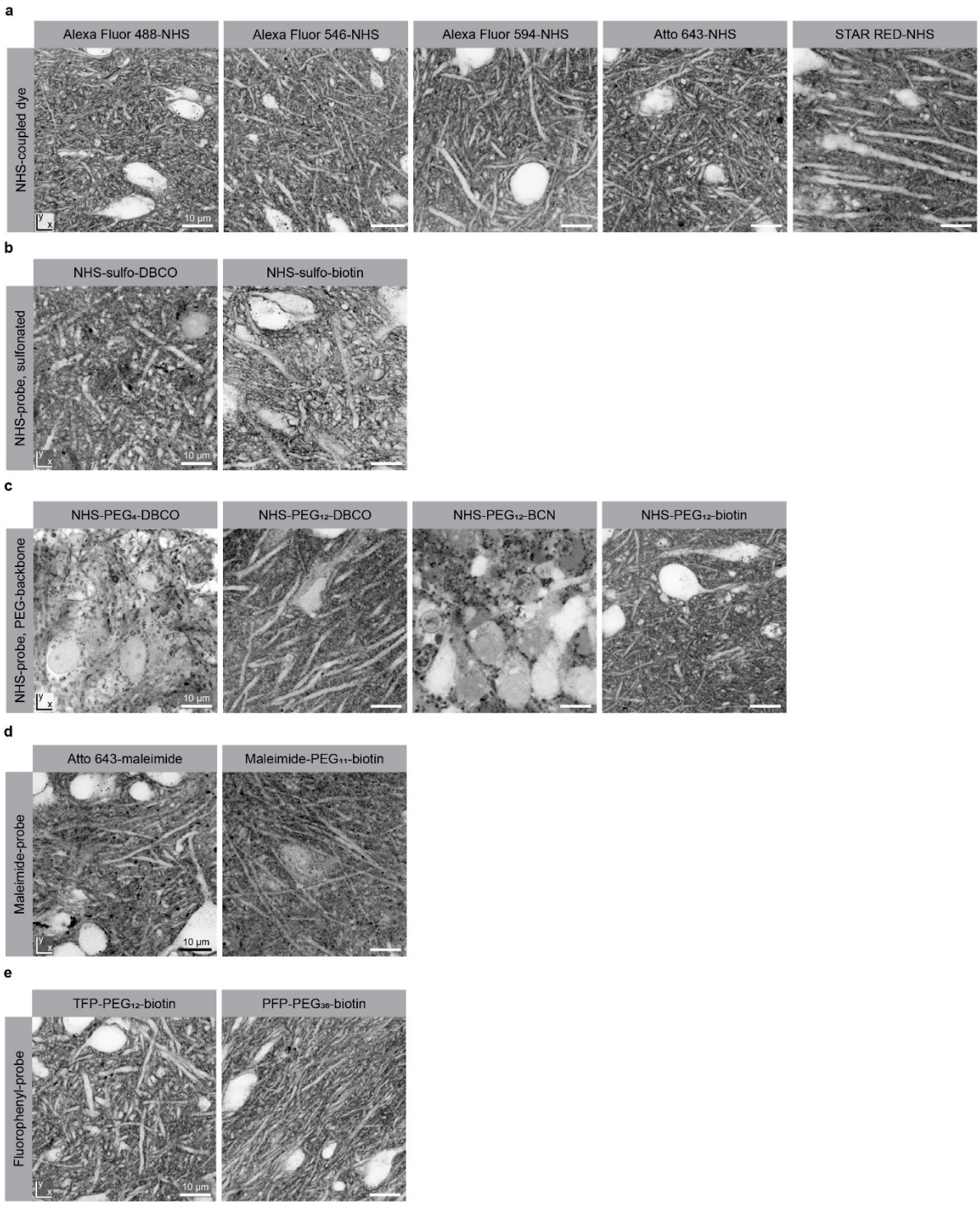


**Figure 8: Screening for coCATS labeling compounds**. 15-30 days *in vitro* (DIV) organotypic hippocampal slice cultures were bathed in coCATS labeling compound in carbogen-equilibrated artificial cerebrospinal fluid (ACSF) for 20-45 min at 37 °C with gentle agitation. The samples were washed and fixed with 4% FA in 0.1 M phosphate buffer (PB) and 0.1 M NaOH for 2 h at room temperature (RT). Biotin- or click chemistry compound-labeled samples were permeabilized with 0.5% Triton X-100 (TX) in 1X phosphate buffered saline (PBS) and incubated with a readout probe. Labeling compounds included a) NHS-coupled dyes, b) sulfonated NHS-probes, c) PEGylated NHS-probes, d) maleimide-probes and e) fluorophenyl-probes. All samples were imaged in confocal mode with a high-magnification objective (100x silicone, NA 1.35). Taken from Michalska *et al.*,2022[155].

I screened a range of labeling compounds in organotypic hippocampal slice cultures to optimize the coCATS labeling conditions (Figure 8).
I mainly focused on NHS esters for covalent binding to ECS-components, as these react with high efficiency at physiological pH (7.4). They bind to primary amines, for example present in the amino acid lysine, which is highly abundant in proteins.[156,157]
For direct fluorophore labeling, I used hydrophilic, anionic fluorophores coupled to an NHS ester (NHS-coupled dyes, Figure 8a). Alexa Fluor 488-NHS, Alexa Fluor 546-NHS, Alexa Fluor 594-NHS, Atto 643-NHS and STAR RED-NHS all resulted in strong, homogeneous labeling of the extracellular compartment when infused into the ECS of living organotypic hippocampal slice cultures and fixed after ~20 min of dye incubation. For STED-imaging, only far-red fluorophores (STAR RED and Atto 643) were used. To allow for fluorescent readout after downstream processing steps, such as fixation, permeabilization and expansion, I tested biotin and click chemistry strategies (dibenzocyclooctin (DBCO) and bicyclononyne (BCN)). Click chemistry encompassed a group of reactions with high selectivity, yield and fast reaction rates.[158] DBCO and BCN are cycloalkanes that react with azides via strain-promoted azide-alkyne cycloaddition (see Appendix Section 6.1). Compared to the click chemistry compounds tested, I found that biotin-containing labeling compounds resulted in more homogeneous extracellular labeling (Figure 8b). This is because biotin is a highly hydrophilic vitamin, while DBCO and BCN are lipophilic compounds, which created aggregates during the live labeling procedure.
The addition of either a sulfo-group (Figure 8b) or a PEG-linker with a chain length of 11-12 PEG molecules (Figure 8c) were suitable strategies for mediating high extracellular contrast. Shorter PEG-chains decreased the hydrophilicity of the probe resulting in aggregate formation, as visible when comparing the staining pattern of NHS-$PEG_4$-DBCO with NHS-$PEG_{12}$-DBCO (Figure 8c).
Further, I tested additional covalent binding strategies for homogeneous labeling of molecules in the ECS. Maleimide probes covalently react with sulfhydryl groups (see Appendix Section 6.1). While the maleimide-probes tested yielded a pronounced extracellular labeling pattern, the staining pattern was less homogeneous compared to the one achieved with NHS esters (Figure 8d). This is likely due to a lower availability of sulfhydryl-groups in the ECS as compared to primary amines.
In contrast, TFP and pentafluorophenyl (PFP) moieties, amine-reactive compounds that are more resistant to hydrolysis than NHS esters, produced a high quality labeling pattern comparable to the one achieved with NHS esters (Figure 8e). For the PFP-probe, I used a longer PEG-linker (36 PEG-molecules) due to the limited availability of PFP probes. A PEG-linker with a chain length of 12 PEG-molecules was sufficient to create high extracellular contrast when paired with a biotin-moiety. A longer PEG chain likely merely increases probe size, potentially hampering tissue penetration.

#### 2.1.1.1 CoCATS visualization of acute and cultured nervous tissue

First, I developed a robust labeling protocol for living *ex vivo* brain samples. These samples include neuron cultures, acute slices and organotypic slice cultures, cultured brain organoids and acute retina (Figure 9). Below is a detailed description of the labeling procedure for direct fluorophore-labeling, using cultured organotypic hippocampal slices as an example.

1. Extract the sample and place it in a well-plate of sufficient size filled with an appropriate buffer.
   *Example: A cultured organotypic hippocampal slice cultured on a membrane insert is cut out of the cell culture insert and immersed in 500 µl of carbogen-equilibrated, pre-warmed ACSF with HEPES (20 mM D-glucose, 4.8 mM KCl, 125 mM NaCl, 26 mM $NaHCO_3$, 1.25 mM $NaHPO_4$* $H_2O$, 2 mM $CaCl_2$, 1.3 mM $MgCl_2$, 7.5 mM HEPES in double-distilled water ($ddH_2O$), pH 7.4) in a 24-well plate.*

2. Prepare the coCATS labeling solution freshly in the same buffer from a highly concentrated labeling compound stock (typically 20-100 mM) in dimethyl sulfoxide (DMSO).
   Note: The amine reactive group spontaneously hydrolyses in aqueous solution, such that it has to be stored in an anhydrous solvent and only diluted just before incubation.
   Note: Use an incubation buffer that does not contain proteins or other primary amine-containing substances, as these will scavenge the coCATS labeling compound.
   Note: The dilution factor for the labeling compound should be as high as possible (at least 1:200) to minimize DMSO toxicity.
   Note: As soon as fluorescent molecules are added to the sample, all incubation steps should be performed in the dark.
   *Example: For direct fluorophore labeling, a 20 mM STAR RED-NHS stock solution in DMSO is diluted 1:400 in pre-warmed carbogen-equilibrated ACSF with HEPES, resulting in a 50 µM STAR RED-NHS labeling solution.*
3. Immerse the sample in coCATS labeling solution and incubate it under physiological temperature with gentle agitation.
   *Example: The slice is immersed in 500 µl coCATS labeling solution and incubated at 37 °C for 20-25 min with gentle agitation.*
4. Wash the sample with an appropriate buffer.
   *Example: The slice is washed twice for 1 min each with 0.5-1.0 ml pre-warmed, carbogen-equilibrated ACSF with HEPES.*
5. Immersion-fix the sample with freshly prepared fixative solution (4% weight per volume (w/v) FA in 0.1 M PB, 0.1 M NaOH, pH 7.4) for at least 1 h at RT with gentle agitation.
   Note: Prepare fixative solution from solid FA, store it at 4 °C and do not use it after more than 7 days of storage.
   Note: Make sure that the fixative solution is warmed up to RT before the fixation to ensure high structural preservation.
   *Example: The solution in the well is exchanged for 500 µl fixative solution and the slice is incubated for at least 1 h at RT with gentle agitation.*
6. Post-fix the sample in the same fixative solution for at least 12 h at 4 °C with gentle agitation.
   *Example: After initial fixation, the sample is moved to 4 °C and post-fixed over night (ON) with gentle agitation.*
7. Thoroughly wash the sample 3 times for 30 min each with 1X PBS at RT with gentle agitation.
8. Optional: Labeling of molecular targets.
   8.1 Mildly permeabilize your sample with a detergent for 12-16 h at 4 °C with gentle agitation.
   *Example: The slice is incubated with 500 µl 0.2% volume per volume (v/v) TX in 1X PBS ON at 4 °C with gentle agitation.*
   8.2 Thoroughly wash the sample 3 times for 30 min each with 1X PBS at RT with gentle agitation.
   8.3 Proceed to label your molecular target(s) of choice, using buffers that do not contain detergents, as these might negatively affect structural preservation.
   *Example: The slice is blocked with blocking solution (5% (w/v) bovine serum albumin (BSA) + 1% (w/v) normal goat serum (NGS) in 1X PBS) for 4 h at RT with gentle agitation. Primary and secondary antibody incubations are performed in blocking solution ON at 4 °C with gentle agitation, followed by 3 washing steps in 1X PBS for 30 min each at RT with gentle agitation.*
9. Image the sample in an imaging chamber containing 1X PBS.

Note: Do not mount the sample in mounting media containing polyvinyl alcohol, as these degrade the coCATS staining pattern quickly (preliminary observation) and can lead to sample shrinkage and flattening.

Modifications to this protocol can and should be made to optimize it for different sample types, especially regarding the live incubation with the coCATS labeling compound. Specifically, incubation buffer, incubation temperature and time can be adjusted accordingly (see Figure 9) for parameters used for different sample types displayed in Figure 9). Physiological pH (7.4) of the buffer is preferable for most nervous tissue specimens, but can be slightly decreased (7.0) to increase the reaction kinetics of the NHS ester (preliminary observation). Highest staining quality is mostly obtained at close-to-physiological temperature, e.g. 35-37 °C for acute and hippocampal slice cultures, but labeling can also be performed at RT, if necessary. The incubation time is mainly dependent on the specimen thickness.

CoCATS labeling can be performed with this protocol in various commonly used brain sample types (Figure 9). Monolayer cultures, such as primary neurons, displayed a membrane-like staining pattern, as they do not produce an extensive 3D-ECM network (Figure 9a). Densely packed cell bodies interspersed with thick processes were visible in a cerebral organoid sample (Figure 9b). In a cultured organotypic slice, coCATS efficiently visualized the CA3 cell body layer consisting of pyramidal neurons, as well as the complex network of processes in the *stratum oriens* (Figure 9c). The cortical area of an acute slice displayed fewer cell bodies with a more pronounced neuropil. Some processes were strongly labeled (dark black) intracellularly, as they had been damaged during the slicing procedure (Figure 9d). In the retina, bundles of nerve fibers meandering through a layer of ganglion cells were visible (Figure 9e).

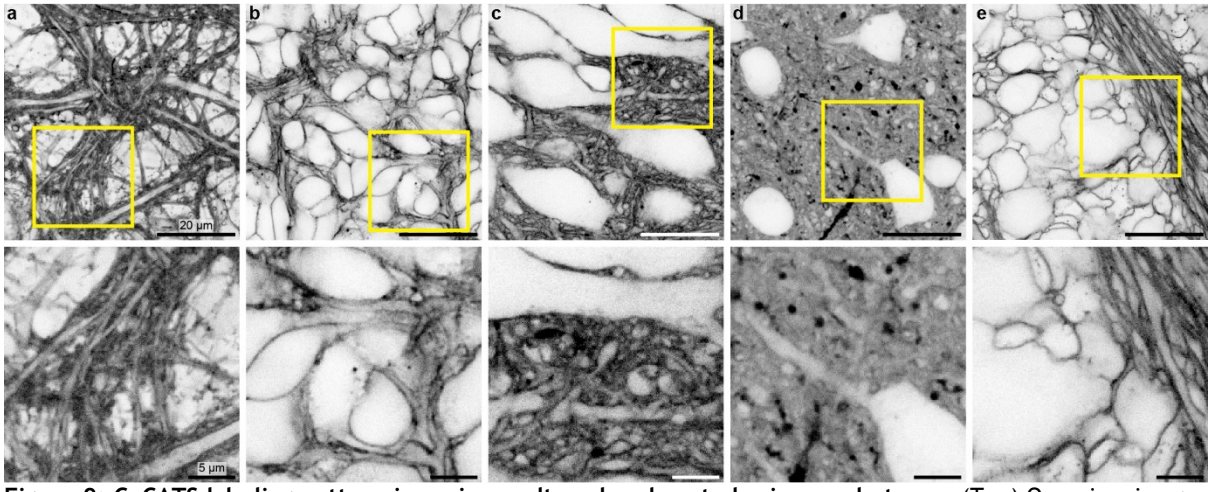


**Figure 9: CoCATS labeling pattern in various cultured and acute brain sample types.** (Top) Overview images and (bottom) zoomed views (yellow squares) of coCATS labeled a) rat primary hippocampal neurons, 16 DIV; b) cerebral organoid, 150 DIV; c) cultured mouse organotypic hippocampal slice, 16 DIV; d) mouse acute brain slice, cortical area, post-natal day (P) 22 (provided by Jonas group); e) mouse acute retina, 3 months. All samples were coCATS labeled by bathing them in a solution containing a NHS-coupled dye, followed by immersion fixation and imaging in confocal mode with a high-magnification objective (100x silicone, NA 1.35 or 60x water, NA 1.2).

Next, I optimized the protocol for combining coCATS labeling of living *ex vivo* brain samples with ExM. Here, I opted for an indirect coCATS labeling strategy by using a biotin-compound. This allowed for post-expansion label readout, thus circumventing damage to the fluorophores by the expansion procedure. In addition, I prolonged the coCATS label incubation step, to ensure homogeneous labeling of thick samples.

2. Prepare a labeling solution of a biotin-compound for coCATS labeling, such as NHS-$PEG_{12}$-biotin or TFP-$PEG_{12}$-biotin.
   *Example: A 100 µM labeling solution is prepared by diluting a 0.1 M NHS-$PEG_{12}$-biotin stock solution in DMSO 1:1000 in pre-warmed, carbogen-equilibrate ACSF.*
3. Immerse the sample in the labeling solution and incubate it for up to 45 min at physiological temperature with gentle agitation.
   Note: If the sample contains fluorescent molecules, such as FPs, all steps until overview imaging should be performed in the dark.
   *Example: The slice is immersed in 500 µl coCATS labeling solution and incubated at 37 °C for 45 min with gentle agitation.*

10. Perform pre-expansion overview-imaging in an imaging chamber in 1X PBS for alignment of pre- and post-expansion images.
    *Example: A cultured organotypic hippocampal slice, coCATS labeled with a biotin-compound, is immunostained for the astrocytic marker glial fibrilliary acidic protein (GFAP). The entire slice is imaged for GFAP signal with a low magnification objective (e.g. 10x air) with a z-step size of 1.5 µm.*
11. Perform ExM procedure according to the desired protocol.
    Note: Biotin-avidin reactivity is maintained after enzymatic digestion, as well as heat/chemical denaturation, such that both homogenization types (e.g. proExM and MAP) can be used.
    Note: A detailed protocol for both proExM and MAP can be found in Appendix Section 6.3.1.2 (III.6.3 Expansion of organotypic slice cultures with coCATS labeling).
12. Excise a fragment of the expanded hydrogel and place it in a well of a 12-well plate. Equilibrate the gel-fragment by incubating it with 1 ml 1X PBS.
    Note: It is easier to handle the gel fragment on a coverslip. Place a coverslip at the bottom of the well before placing the fragment into it. This way, the fragment can be removed from the well by carefully aspirating all aqueous solution and lifting the coverslip with tweezers.
13. Incubate the sample with 1 ml read-out solution (5-10 µg/ml fluorophore-conjugated avidin) for at least 20 h at RT with gentle agitation to read out the coCATS label.
    *Example: The gel fragment is incubated with 5 µg/ml neutravidin STAR635P in 1X PBS for 20 h at RT with gentle agitation.*
    Note: Upon fluorophore incubation, all steps should be performed in the dark.
14. Thoroughly wash and re-expand the sample 3 times for 1 h each with $ddH_2O$ at RT with gentle agitation.
15. Image the sample in an imaging chamber in $ddH_2O$.
    Note: To immobilize the gel fragment, use a poly-L-lysine (PLL)-coated coverslip.

A representative dataset of a coCATS labeled and ~4-fold expanded cultured organotypic hippocampal slice is shown in Figure 10.

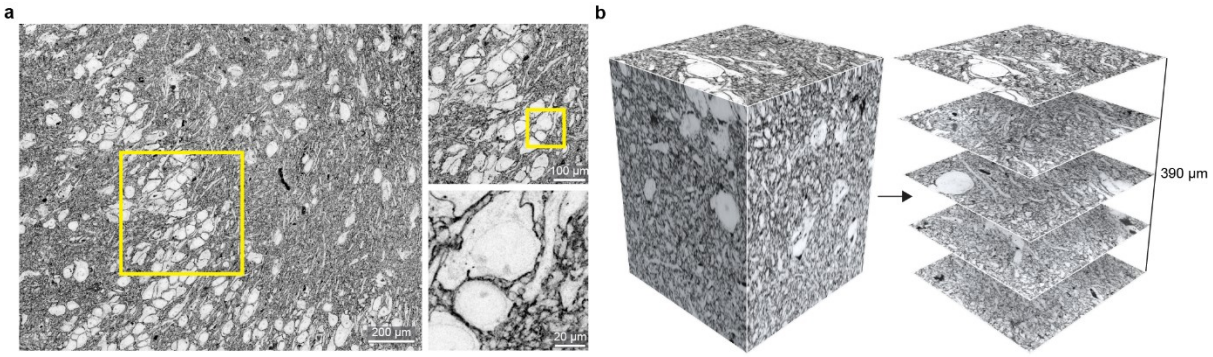


**Figure 10: CoCATS visualization of hippocampal slice architecture with ExM.** A cultured organotypic hippocampal slice was coCATS labeled with NHS-$PEG_{12}$-biotin, immersion-fixed and ~4-fold expanded with MAP. The coCATS label, read out with dye-conjugated streptavidin, was imaged on a confocal microscope with a 40x water objective, NA 1.1. a) Overview image with two progressive zoom-ins. b) (Left) 3D-rendering and (right) single *xy*-planes of a 290 x 290 x 390 $\mu m^3$ sample cube. Scale bars refer to sample size after expansion. Adapted from Michalska *et al.*, 2022[155].

ExM enables the visualization of tissue context from regional to subcellular level (Figure 10a), as well as across extended axial ranges (Figure 10b).

Limitations & future prospects

The *ex vivo* coCATS strategy is limited to a specific group of samples, which are alive and can be immersed in the labeling solution. This includes cultured cells, slices and organoids, as well as some acute preparations, such as retina. Labeling of excised (acute) brain tissue is in principal possible, but impeded by the presence of damaged cells and debris, which decrease the overall quality of the resulting data (Figure 9d). To address this aspect, I developed further labeling paradigms discussed below.

Another limitation is the fixation strategy. Currently, the samples are chemically fixed with FA by immersion fixation. The time it takes for FA to diffuse through the sample has a negative effect on ultrastructural preservation. Previous studies have shown that the ultrastructure of immersion-fixed thick samples is comparable to cryo-fixed samples close to the surface, but substantially altered at greater depths from the surface.[159,160] In addition, FA-fixation is known to be insufficient for the immobilization of lipid molecules, which can decrease the labeling quality upon downstream processing steps, such as detergent permeabilization and sample mounting.[161] Hence, it would be useful to optimize the fixation procedure, focusing on ultrastructural preservation of the ECS, retention of lipids, while preserving the compatibility with readout of molecular markers, e.g. by immunostaining. Here, further chemical fixatives and combinations of those should be evaluated. Inspiration can be taken from EM fixation protocols, as these are optimized for ultrastructural preservation, as well as the retention of lipids, and thus cell surface proteins. Yet, these protocols, which are based on the use of FA and glutaraldehyde, are known to lead to ECS shrinkage.[162,163] Attempts have been made to preserve the ECS by using fixative solutions containing sucrose[164,165] or salts to increase their osmolality[166]. The approaches likely increase the ECS fraction artificially, rather than preserving its native state. Another way to circumvent this problem is by performing cryo-fixation. Many studies have shown that the rapid immobilization of (brain) samples by freezing at high pressure, followed by chemical fixation at low temperatures, results in excellent ultrastructural preservation.[167,168] Current efforts are underway to combine cryo-fixation with light microscopy to decrease artifacts associated with chemical fixation, as shown by a recent study combining plunge freezing with ExM.[169] For thick specimens, cryo-fixation would need to be performed by high-pressure freezing-freeze substitution, as this is currently the only method capable of vitrifying samples of up to 200 µm thickness.[170] As a first step, I have established a protocol for cryo-fixation of cultured organotypic hippocampal slices via HPF-FS combined with fluorescence immunostaining and super-resolution STED imaging. I have also

performed preliminary experiments to combine cryo-fixation by HPF-FS with ExM in monolayer cultures.
In conjunction with optimizing fixation parameters, the permeabilization procedure should continuously be evaluated. I have observed that the coCATS labeling quality can drop significantly after detergent permeabilization dependent on the fixation procedure, especially when using immersion fixation. As structural preservation is a key factor for obtaining reliable results with CATS, one needs to be aware that every sample processing step (fixation, permeabilization, immunostaining, mounting, expansion, etc.) has the potential to impact this factor. The goal should always be to visualize the structure in a state as close to the native state as possible, thus focusing on minimizing the influence of sample processing.
In combination with ExM, signal retention is another crucial factor. To improve the retention of the coCATS label, one can include a moiety into the labeling compound that anchors it directly into the hydrogel. The use of such a multifunctional anchor, harboring a target-binding moiety, an anchoring moiety and a readout-moiety, has been successfully used in the context of ExM.[56,58] These compounds are not commercially available, such that I have not focused on this approach. Still, I recently collaborated with Victor Savic (Marko Mihovilovic group, Technical University of Vienna, Vienna, Austria) who synthesized a trifunctional molecule for the retention of an ECS label in a hydrogel. This molecule features a TFP-group for covalent binding in the ECS, an acrylamide-group for hydrogel anchoring and an azide-group for click chemistry-based readout, all attached to a $PEG_{12}$-backbone mediating hydrophilicity.

#### 2.1.1.2 CoCATS visualization of near-natively preserved brain tissue structure by *in vivo* microinjection

Hana Štefaničková performed all *in vivo* microinjections.

In addition to labeling of *ex vivo* specimens, I developed a protocol for coCATS *in vivo* labeling of brain tissue by stereotactic microinjection. *In vivo* labeling has the advantage that it is compatible with fixation by transcardial perfusion, yielding enhanced, 'near-native' preservation of nervous tissue, especially when compared to immersion fixation. It allows for the study of physiological tissue without the need of processes that can alter its integrity or connectivity, such as tissue extraction and/or culturing. Most importantly, it permits the study of brain regions deep inside the brain, which are difficult to access by *in vivo* live imaging.

The following protocol was developed to achieve reliable *in vivo* coCATS labeling. Direct fluorophore-labeling via *in vivo* microinjection into the lateral ventricle (LV) is used as a showcase.

1. Anesthetize the animal deeply, shave its head and head-fix it in a stereotactic frame. Place the animal on a heating pad under the stereotactic frame.
   *Example: An adult (4 months old) C57BL/6J mouse is used. The aim of the experiment is to visualize mossy fiber boutons (MFBs) in the dorsal hippocampus. The animal is anesthetized by intraperitoneal injection of Ketamine/Xylazine (80-100 mg/kg Ketamine, 10 mg/kg Xylazine). Pain relief is provided by subcutaneous injection of Metamizol (200 mg/kg).*
2. Center and level the skull in the stereotactic frame by aligning bregma and lambda at the same height.
3. Drill a small hole at the injection coordinates.
   *Example: To target the dorsal hippocampus of the adult mouse, specifically the CA3 region, the following coordinates are used: 1.25 mm caudally, +/-2 mm laterally and 2 mm vertically, for injections into the right or left LV.*
4. Fill the injection pipette with undiluted amine reactive dye (stock solution in DMSO).

Note: It is important to use an undiluted stock dilution, as dilution in aqueous solution prior to injection results in spontaneous hydrolysis of the NHS ester, thus decreasing the reactivity of the dye.
*Example: The pipette is filled with 2 µl 20 mM STAR RED-NHS in DMSO.*

5. Lower the injection pipette to the brain surface (used as vertical reference point) and advance it into the tissue. Using a microinjection pump, inject the dye-solution slowly into the tissue.
   Note: For ventricular injections, a flow rate of 50 nl/min is used and a total volume of 500 nl is injected. For injections directly into the tissue, the flow rate and total injection volume should be decreased to 20 nl/min and 200 nl, respectively.
   Note: Make sure to inject the solution slowly, as high local DMSO concentrations from the stock solution can be toxic to the sample, especially when injected directly into the tissue.
   *Example: The pipette is lowered into the tissue. A total volume of 500 nl are injected into the LV over a time course of 10 min with a flow rate of 50 nl/min.*
6. After each injection, leave the pipette in place for 5 min before slowly retracting it over a time course of 1 min to prevent backflow.
7. Place the animal on a heating pad after surgery, until transcardial perfusion (45 min after start of the injection).
8. Confirm the level of anesthesia by toe pinch. If necessary, administer additional anesthesia.
9. Perform transcardial perfusion. The onset of fixative delivery should be 45 min after the start of the dye injection.
   Note: Prepare fixative solution (4% FA (w/v) in 0.1 M PB, 0.1 M NaOH, pH 7.4) from solid FA. It should be freshly prepared on the same day or 1 day before perfusion and stored at 4 °C.
   Note: The quality of the transcardial perfusion procedure has a big effect on tissue preservation. Make sure that the flow rate is steady without pulsation.
   *Example: For transcardial perfusion, the animal is first perfused with 10 ml ice-cold 1X PBS at a flow rate of 7.5 ml/min. This is followed by perfusion with 75 ml ice-cold fixative solution for 10 min with the same flow rate.*
10. Extract the brain and place it in a tube with 10 ml ice-cold fixative solution.
11. Post-fix the brain in fixative solution for 20-24 h at 4 °C with gentle agitation.
12. Wash the brain 3 times for 1 h each with 1X PBS at RT with gentle agitation.
13. Slice the brain according to your needs.
    *Example: The brain is sliced into 100 µm thick coronal slices with a vibratome.*
14. Store the slices in 0.02% (w/v) sodium azide ($NaN_3$) in 1X PBS at 4 °C.
    Note: The slices can be stored for ~1 month in the fridge until the quality of the coCATS staining decreases.
15. Optional: Labeling of molecular targets.
    15.1 Mildly permeabilize your sample with a detergent for 12-16 h at 4 °C with gentle agitation.
    *Example: A slice containing a piece of dorsal hippocampus is chosen. The slice is incubated with 500 µl 0.2% (v/v) TX in 1X PBS ON at 4 °C with gentle agitation.*
    15.2 Thoroughly wash the sample 3 times for 30 min each with 1X PBS at RT with gentle agitation.
    15.3 Proceed to label your molecular target(s) of choice, using buffers that do not contain detergents.
    *Example: The coronal brain slice is blocked with blocking solution (5% (w/v) BSA + 1% (w/v) NGS in 1X PBS) for 4 h at RT with gentle agitation. Primary and secondary antibody incubations are performed in blocking solution ON at 4 °C with gentle agitation, followed by 3 washing steps in 1X PBS for 30 min each at RT with gentle agitation.*

16. Image your sample in an imaging chamber in 1X PBS.
    Note: Do not mount the sample in mounting media containing polyvinyl alcohol, as these degrade the coCATS staining pattern quickly (preliminary observation) and can lead to sample shrinkage and flattening.

Delivering the coCATS labeling compounds by *in vivo* microinjection lead to strong labeling of various brain areas. Figure 11 shows the distribution pattern of the coCATS labeling compound after injection into the LV or cerebral cortex. This highlights the differential organization of the brain areas across multiple spatial scales.
*In vivo* microinjection into the LV elucidated the architecture of tissues lining the lateral, third and fourth ventricles. The organization of parts of the striatum (lateral septal nucleus, caudoputamen), hippocampal area (CA3, CA2 and DG), thalamus (medial habenula), hypothalamus and midbrain (periaqueductal grey) was clearly visible. Injecting into the LV has the advantage that one can study brain areas that are distant from the injection site and therefore do not exhibit injection-induced damage. Yet, not all brain areas can be targeted by ventricular injection.

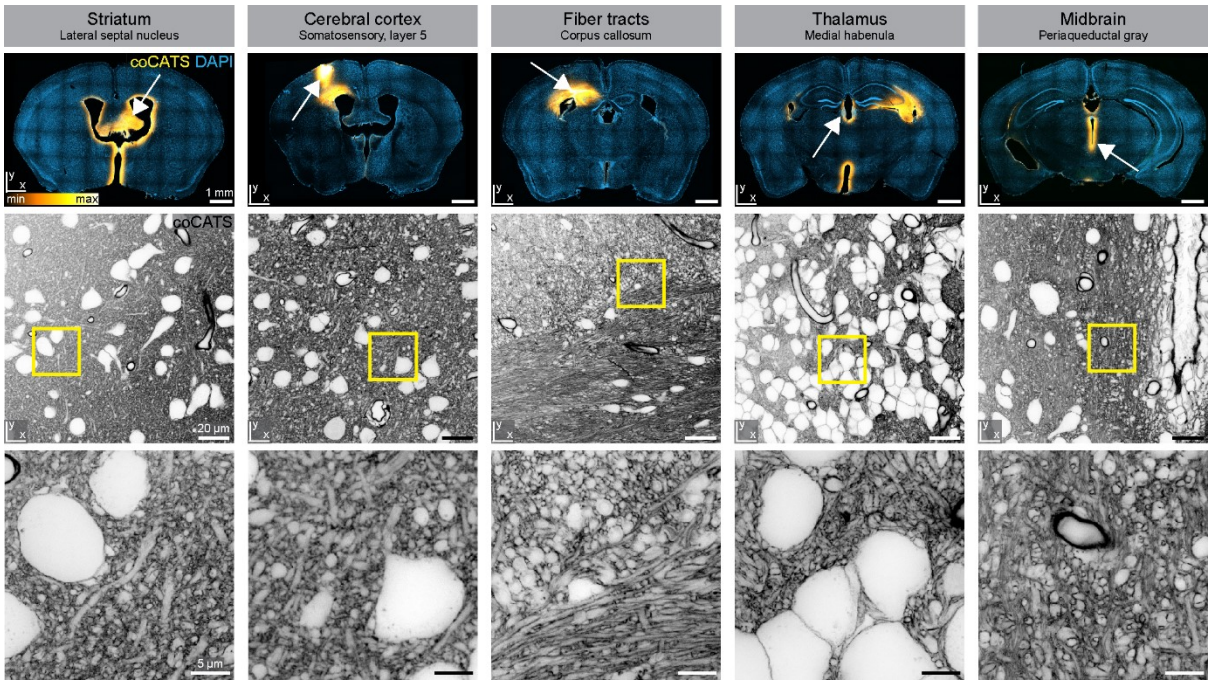


**Figure 11: Labeling pattern of various brain areas after coCATS *in vivo* microinjection.** CoCATS *in vivo* microinjection of STAR RED-NHS was performed either in the LV (striatum, thalamus, midbrain) or in the cortex (cerebral cortex, fiber tracts). (Top) Overview confocal images (spinning disk, 10x air objective, NA 0.45) of whole coronal slices labeled for nuclei (4',6-diaminidino-phenylindole (DAPI), blue), showing the distribution pattern of the coCATS label (yellow, LUT not inverted). White arrows indicate the regions acquired with higher magnification. (Middle) High-resolution confocal images (confocal, 100x silicone objective, NA 1.35) of the coCATS label (grey). (Bottom) Super-resolution STED images (100x silicone objective, NA 1.35) of the yellow-boxed areas. Adapted from Michalska *et al.*, 2022[155].

Alternatively, the labeling compound can be injected directly into the tissue to study areas of interest in close proximity to the injection site. For example, injection into layer 4-5 of the somatosensory cortex lead to reliable labeling surrounding the injection site, as well as the *corpus* callosum (Figure 12a). As CATS elucidates tissue organization, it clearly revealed the extent of tissue damage around the injection site that was introduced by the injection process (Figure 12b). In close proximity to the injection site, ~100 µm away, the tissue appeared disorganized, as many structures were bloated and/or dye-filled (Figure 12c). Damaged cell bodies appeared black, as they had taken up the coCATS dye. These cells exhibited the highest signal intensity of the whole image, as the intracellular milieu is richer in proteins than the extracellular one. Yet, the damage

was spatially confined, meaning that brain areas ~200 µm away from the injection site can be studied. Here, the structure of the tissue was well preserved. Cell bodies and processes were clearly visible, and there were no dye-filled cellular structures (Figure 12d).

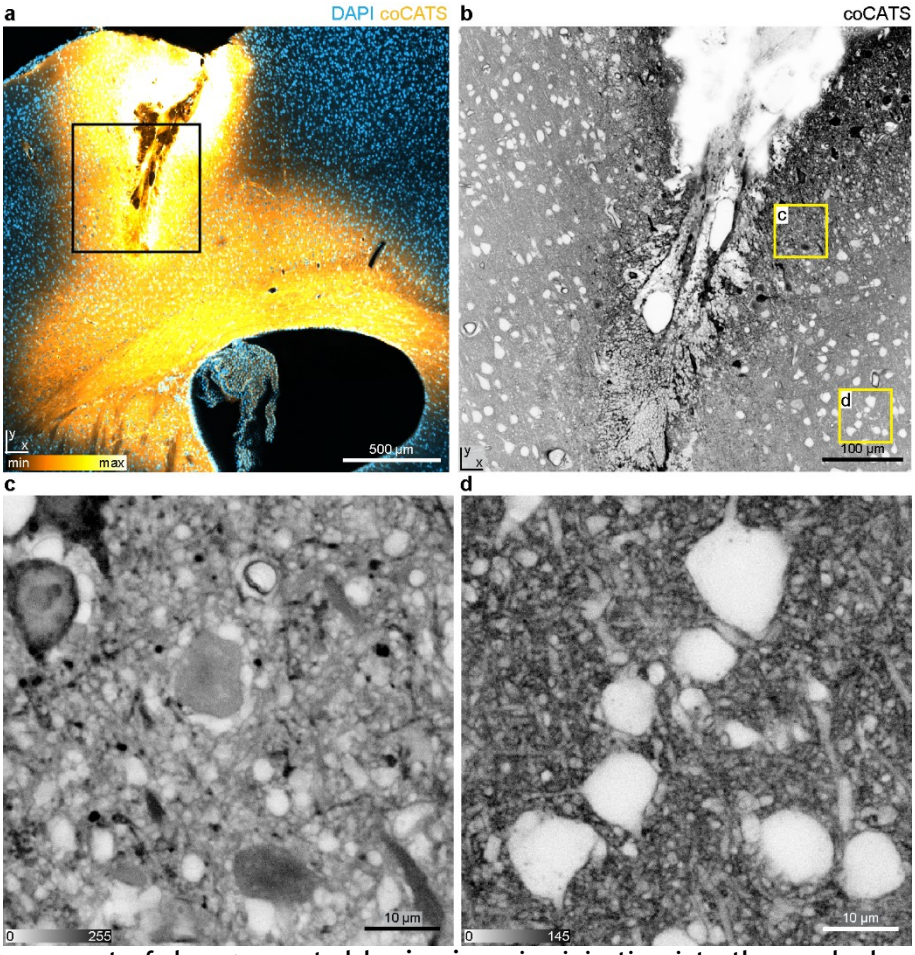


**Figure 12: Assessment of damage created by *in vivo* microinjection into the cerebral cortex.** *In vivo* microinjection was performed with NHS-STAR RED in the somatosensory cortex of an adult wt mouse, followed by transcardial fixative perfusion, slicing, counterstaining with DAPI and imaging. a) Overview confocal image (spinning disk, 10x air objective, NA 0.45) of the injection site, containing coCATS stain (yellow, LUT not inverted) and DAPI (blue). b) Confocal zoom-in (60x water immersion objective, NA 1.2) of coCATS signal (grey) in the black-boxed square. c) Further confocal zoom (yellow box in b) into a region close to the injection site displaying tissue damage. d) Another confocal zoom (yellow box in b) into a region more distant from the injection site, displaying no damage. Photon counts are displayed in the lower left corner of panel c and d. Adapted from Michalska *et al.*, 2022[155].

The coCATS labeling extents at least 500 µm away from the injection site, but can diffuse substantially further from it, depending on the organization of the tissue. This is clearly visible in Figure 12a, where the coCATS labeling compound traveled at least 2 mm away from the injection site along the fiber tracts of the *corpus callosum*.

Figure 13 shows the information that is gained by coCATS over sparse genetic labeling, such as Thy1-enhanced GFP (EGFP) and/or labeling of molecular targets, such as the postsynaptic marker proline-rich synapse associated protein-1 (SHANK2). The mouse line used for this experiment sparsely expresses EGFP in a large population of Thy1-positive projection neurons, including hippocampal GCs in the hippocampus.

While the sparse genetic label pinpointed some DG axons and MFBs in the CA3 *stratum lucidum*, coCATS staining revealed the presence of mossy fiber tracts intermittent with MFBs and PN proximal dendrites (Figure 13a) in proximity to the cell body layer of the CA3 *stratum pyramidale*. Further, combining the genetic label with a synaptic marker elucidated synaptic sites for the

sparsely labeled MFBs. Yet, many postsynaptic structures could not be placed in their structural context. In combination with coCATS labeling, all postsynaptic structures could be associated with MFBs, their presynaptic partners (Figure 13b).

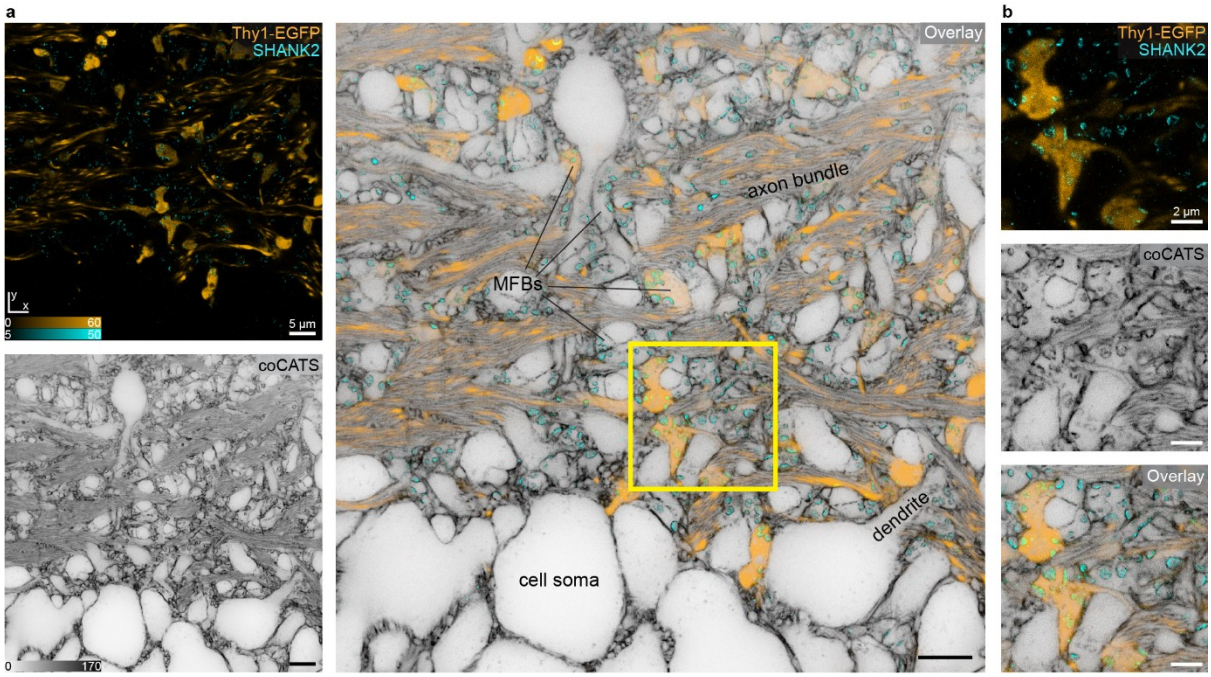


**Figure 13: Combining coCATS labeling with sparse genetic markers and immunostaining.** Super-resolution images in the CA3 *stratum lucidum* of an adult Thy1-EGFP mouse after coCATS (grey, *xy*-STED) *in vivo* microinjection into the LV, transcardial fixative perfusion and immunostaining for GFP (orange, confocal) and SHANK2 (cyan, *xy*-STED). a) Overview and b) zoom-in of the yellow-boxed region, acquired with a high-magnification objective (100x silicone, NA 1.35). Adapted from Michalska *et al.*,2022[155].

Limitations & future prospects

Currently, I have established coCATS *in vivo* microinjection in the adult (3-4 months) mouse LV and cerebral cortex with direct fluorophore readout. The distribution pattern and damage in other brain areas needs to be evaluated. When performing injections with the same parameters into the LV of 1 month old mice, I have found that the distribution pattern of the coCATS labeling compound differs significantly from the one obtained in 3-4 month old mice. Hence, the injection parameters need to be optimized for different developmental stages. In addition, direct injection into highly connected brain areas might be challenging. For example, I tested direct injection into the CA3 of the hippocampus, but found that moving the injection needle through the CA1 to reach the CA3 is problematic. This is because the needle damages and dye-fills Schaffer collaterals projecting from the CA3 into the CA1. The labeling compound travels through the axons back into CA3. There, intracellular labeling of damaged neurons obscures the extracellular contrast provided by the coCATS approach. Hence, the parameters for *in vivo* microinjection need to be optimized for the age of the animal and the region of interest.

Perfusion fixation results in a more homogeneous chemical immobilization compared to immersion fixation. Nevertheless, problems regarding preservation of ultrastructure, specifically the decrease in ECS fraction, remain, as perfusion fixation is also based on the use of aldehydes. Apart from optimizing the fixative solution, one option would be to excise the brain after *in vivo* microinjection, slice it and cryo-fix the acute slices. Yet, this creates substantial experimental overhead and may lead to tissue distortions.

Further, I have so far mainly performed direct fluorophore-injection. Future prospect involve the combination with ExM, which requires an indirect readout strategy involving a biotin-containing coCATS labeling compound. I have performed preliminary experiments, showing that *in vivo* microinjection of NHS-$PEG_{12}$-biotin and TFP-$PEG_{12}$-biotin, followed by a readout with

fluorophore-conjugated streptavidin, highlights tissue structure in the hippocampus. The next step is to combine this strategy with ExM to evaluate the signal retention and homogeneity upon expansion.

## 2.1.2 Resident CATS

My aim was to create a toolbox that is compatible with the majority of brain sample types commonly used in the neuroscientific community. Hence, I developed a second labeling paradigm that enables visualization of brain tissue organization in specimens where live labeling is not possible, for example previously fixed samples. This labeling paradigm is based on the binding of labeling compounds to extracellularly resident molecules, in particular extracellular polysaccharides in the ECM, such that we termed it **resident CATS** (rCATS).

Also here, I assured that the rCATS labeling scheme follows the requirements stipulated in Section 2.1:

1. Contrast: Lectins (carbohydrate-binding proteins) are used to label ECM components that are abundant in rodent and human brain. After performing a screening for suitable lectins, I found that **wheat germ agglutinin** (WGA) provided good extracellular contrast.
2. Compound binding: WGA binds with high affinity to N-acetylglucosamine and sialic acid in the ECM and on cell surfaces.
3. Fixation: WGA can be applied before and after fixation. It stains ECM-resident molecules with high fidelity after chemical fixation with FA.
4. Tissue penetration: WGA is a relatively small protein (~38 kDa). To ensure sufficient penetration of thick samples (>100 μm), they are permeabilized with low concentrations of detergent, such as Triton X-100 (TX) or by repeated freeze-thaw cycles.
5. Imaging compatibility:
    a. STED: Direct labeling is achieved by using a WGA conjugated to a STED-compatible fluorophore, such as AF594 or CF633.
    b. ExM: As WGA contains only few lysines, which mediate incorporation and retention in expansion hydrogels, I developed a retention protocol for the rCATS expansion procedure. This approach is described below (Figure 15).

I conducted a search for labeling compounds that exhibit a homogeneous and strong binding pattern to oligosaccharides resident in the ECS, specifically to ECM components and the cell surface (Figure 14). I mainly screened lectins, as they display a high specificity for glycoproteins[171], which are enriched in the ECM. I found that vicia villosa lectin (VVL) and wisteria floribunda lectin (WFL) staining pattern were restricted to perineuronal nets associated with a sparse subset of neurons in the cerebral cortex and other brain areas. Both lectins bind to N-acetylgalactosamine linked to serine/threonine and galactose, respectively. Lycopersicon esculentum lectin (LEL), which binds to a subset of N-glycans and is used as a vasculature marker, faithfully depicted blood vessels in the cerebral cortex. Phaseolus vulgaris leucoagglutinin (PHA-L) and erythroagglutinin (PHA-E), two members of the same lectin family, created an extracellular contrast in the cerebral cortex and the hippocampus, albeit with a grainy and inhomogeneous labeling pattern. Jacalin is a binder of O-glycosidically-linked oligosaccharides. These are present in perineuronal nets, which were heavily stained, and to a lesser extent in other parts of the ECM, leading to a weak depiction of the extracellular environment in the cerebral cortex. Concanavalin A, which recognizes α-mannose linked to oligosaccharides, bound strongly and homogenously in the ECS, but also displayed intracellular labeling, including labeling of the endoplasmic reticulum and the nuclear envelope, in the cerebral cortex.

I found that the most reliable depiction of the extracellular environment was achieved with the lectin WGA. WGA faithfully delineated cell bodies and cellular processes in various brain areas, including the hippocampus.

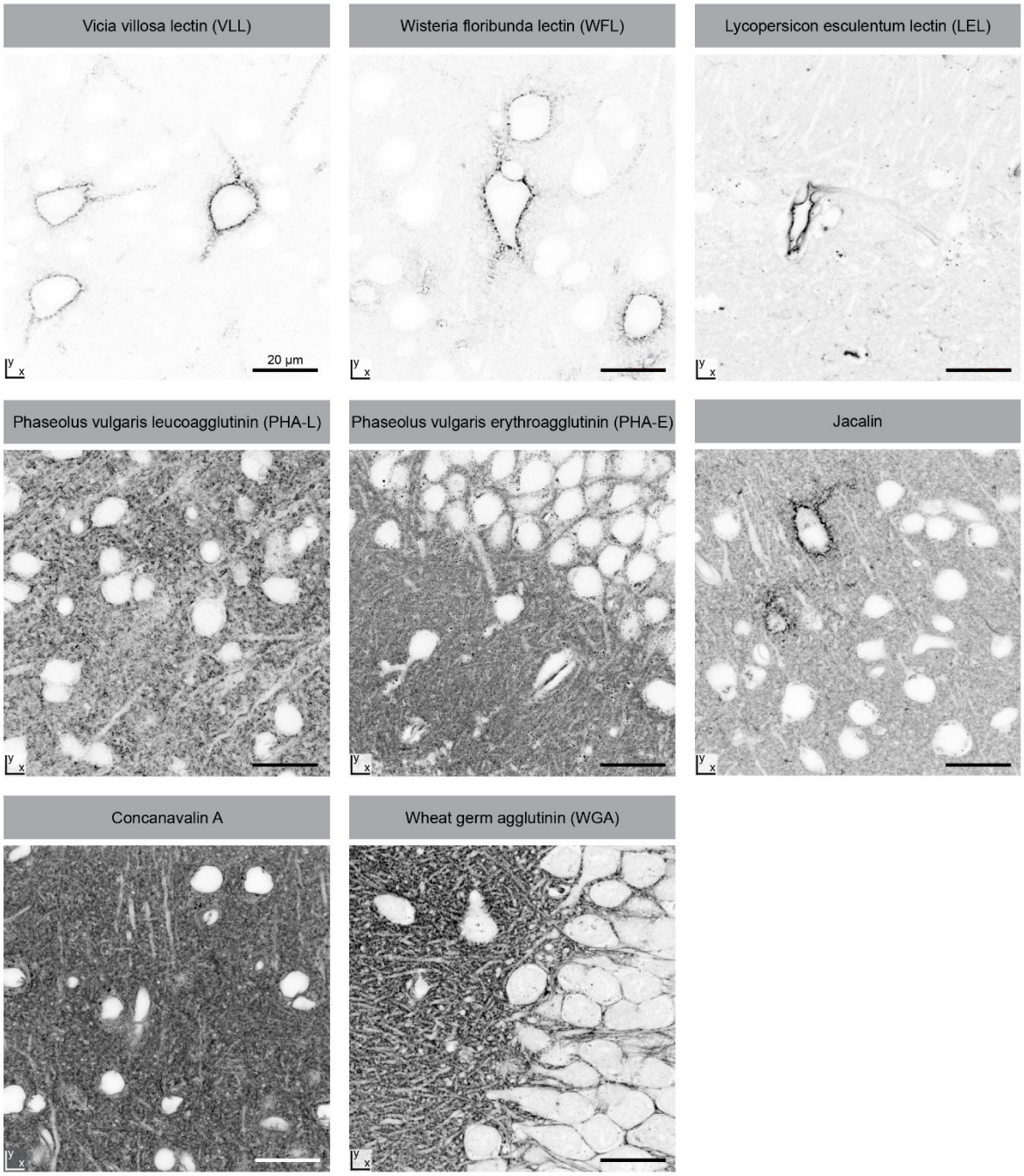


**Figure 14: Screening for affinity binders to reveal tissue architecture with rCATS in rodent brain.** FA perfusion-fixed coronal brain slices from adult mice were used for the experiments. The samples were permeabilized with 0.5% TX in 1x PBS, followed by incubation with a lectin. All lectins, except for LEL, were biotin-conjugated, such that they were read-out with a fluorescently labeled streptavidin. LEL was conjugated with the fluorophore DyLight 594. All imaged were acquired in confocal mode with a high-magnification objective (60x water immersion, NA 1.2). Adapted from Michalska *et al.*,2022[155].

Next, I created a pipeline that ensures the retention of the rCATS label in hydrogels commonly used for ExM. During ExM, molecules are commonly anchored into a hydrogel via a designated anchor, such as AcX or NAS, or via a combined fixation/anchoring strategy, such as using FA

and acrylamide. All these strategies react acrylamide groups to primary amines, mainly present on proteins, such that they are incorporated into the hydrogel during the gelation process. WGA exhibits few lysines and is therefore not faithfully retained in a hydrogel during the expansion procedure (Figure 15b). Hence, it was necessary to develop a designated retention pipeline to ensure that the rCATS information is maintained in the hydrogel and can be read out post-expansion (Figure 15a). First, previously fixed and permeabilized brain samples are incubated with a biotinylated WGA that predominantly binds to extracellularly located glycoproteins. Then, the biotin is detected with streptavidin that is modified with acrylamide-moieties (streptavidin-acrylamide). After this, the sample is infused with a hydrogel monomer solution and the gelation is initiated. Upon gelation, the acrylamide moieties are incorporated into the hydrogel, thus immobilizing the streptavidin. The sample is homogenized by enzymatic digestion or heat/chemical denaturation. Polysaccharides and biotinylated WGA might get lost during this step, but streptavidin-acrylamide is retained in the hydrogel. After expansion, streptavidin is read out with a fluorophore-conjugated biotin.
I tested the compatibility of the retention pipeline with the proExM and MAP expansion protocol. I used adult mouse brain slices that were fixed via transcardial perfusion with FA for both protocols. For MAP, slices were post-fixed with a mixture of FA and AA after slicing (detailed methods in Appendix Section 6.3.1.2).

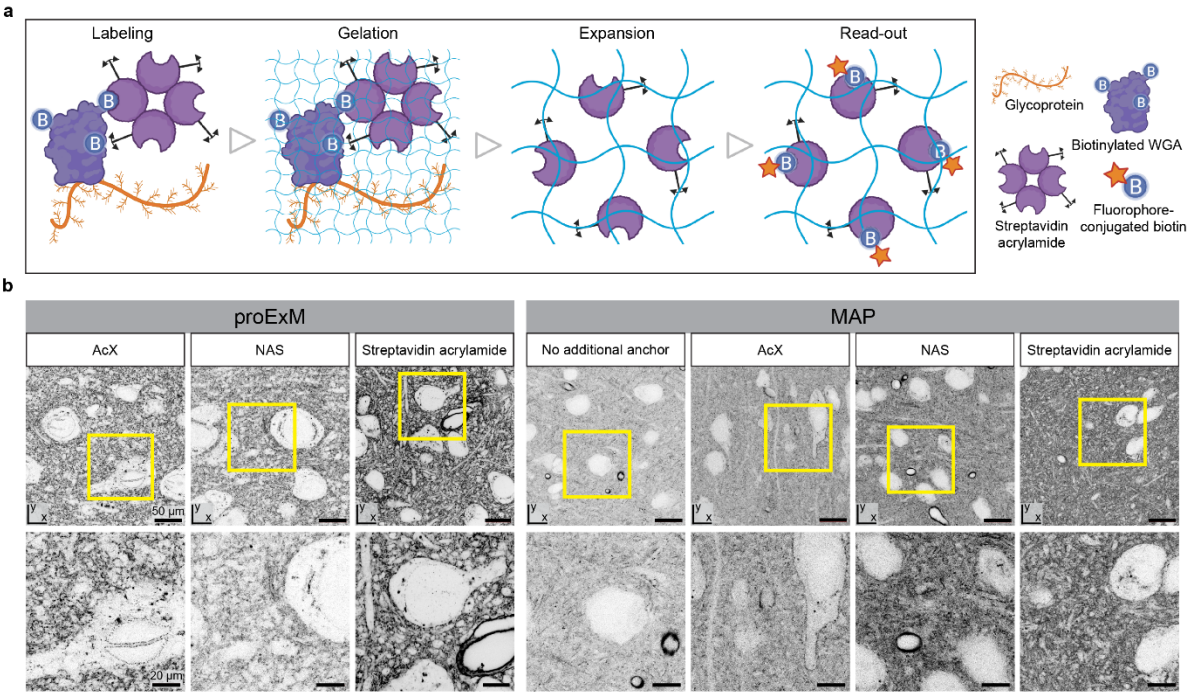


**Figure 15: Pipeline for retention of rCATS-mediated extracellular contrast upon expansion.** a) Schematic of rCATS expansion pipeline ensuring retention of WGA signal. b) Retention of biotinylated WGA in perfusion-fixed adult mouse slices with two common expansion strategies, (left) proExM and (right) MAP, and different anchoring approaches. FA perfusion-fixed adult mouse brain slices were permeabilized and extracellular contrast was introduced with biotinylated WGA. The slices were then incubated with different anchors (AcX, NAS) or streptavidin acrylamide, followed by gelation, expansion and incubation with a read-out probe (fluorophore-conjugated biotin). All images were acquired with a confocal microscope (40x water immersion objective, NA 1.1). Scale bars refer to sample size after expansion. Adapted from Michalska *et al.*,2022[155].

Figure 15b shows that the retention pipeline is compatible with expansion procedures based on either enzymatic digestion, such as proExM, or heat/chemical denaturation, including MAP. WGA was not retained faithfully in the proExM hydrogel when using common anchoring molecules, such as AcX or NAS. The rCATS retention pipeline on the other hand resulted in strong and specific labeling of the extracellular environment and blood vessels post-expansion, corresponding to the expected WGA staining pattern. The MAP expansion strategy does usually not require a

designated anchoring step, as acrylamides are already bound to primary amines during the fixation procedure. Yet, without anchoring the WGA, very low extracellular staining was obtained post-expansion. Including an additional anchoring step with AcX or NAS slightly improved the situation, but the signal was still low and high background was observed. When retaining WGA with streptavidin-acrylamide, I observed a marked increase in specific signal and a decrease in non-specific background post-expansion. Overall, using the proExM approach combined with this pipeline for rCATS signal retention yielded the best results.

#### 2.1.2.1 Visualizing tissue architecture of previously fixed specimens with rCATS

RCATS labeling is a viable alternative for samples for which live labeling is not an option. These include previously perfusion-fixed rodent brain samples and clinical specimens, such as human surgery samples.

I developed the following protocol for the visualization of brain tissue architecture with rCATS. As a showcase, the procedure is explained for an adult mouse brain slice fixed via transcardial perfusion with FA.

1. Wash your previously fixed brain slicess 3 times for 30 min each with 1X PBS at RT with gentle agitation in a well-plate of appropriate size.
   *Example: A 100 µm thick coronal brain slices obtained from a FA fixative-perfused C57BL/6J mouse is used. The slice, previously stored in cryoprotectant solution (60 % (v/v) glycerol in 0.1 M PB) is washed 3 times for 30 min each with 1 ml 1X PBS at RT with gentle agitation.*
2. Incubate the sample with sucrose solution (30% (w/v) sucrose in 1X PBS) ON at 4 °C with gentle agitation or until the sample has sunk to the bottom of the well.
3. Permeabilize the sample by repeated freeze-thaw cycles.
   3.1 Place a drop of sucrose solution onto a microscope slide (e.g. Superfrost slide) and place the sample into the droplet, such that it is immersed in sucrose solution completely.
   3.2 Place the microscope slide on dry ice and wait until the sucrose droplet with the sample is completely frozen. Then remove the microscope slide and let the solution and sample thaw completely at RT.
   3.3 Repeat step 3.2 4 times.
   Note: Samples can also be permeabilized with mild detergents (e.g. ON incubation in 0.5% (v/v) TX in 1X PBS at 4 °C with gentle agitation), although this has a mild negative effect on the rCATS staining quality.
4. Wash the sample 3 times for 30 min each with 1X PBS at RT with gentle agitation.
5. Optional: Labeling of molecular targets.
   Proceed to label your molecular target(s) of choice, using buffers that do not contain detergents.
   *Example: The coronal brain slice is blocked with blocking solution (5% (w/v) BSA + 1% (w/v) NGS in 1X PBS) for 4 h at RT with gentle agitation. Primary and secondary antibody incubations are performed in blocking solution ON at 4 °C with gentle agitation, followed by 3 washing steps 1X PBS for 30 min each at RT with gentle agitation.*
6. Incubate the sample with 5-10 µg/ml WGA conjugated with a readout moiety in 1X PBS for at least 20 h at RT with gentle agitation.
   Note: WGA labeling can also be performed together with primary antibody staining.
   *Example: The coronal brain slice is incubated with 500 µl WGA CF633 in 1X PBS for 20 h at RT with gentle agitation.*
7. Wash the sample 3 times for 30 min each with 1X PBS at RT with gentle agitation.
8. Image your sample in an imaging chamber in 1X PBS.

Note: Do not mount the sample in mounting media containing polyvinyl alcohol, as these can lead to sample shrinkage and flattening.

With this protocol, tissue organization can be visualized in previously fixed tissue, for example in a piece of brain excised from an epilepsy patient and immersion-fixed with FA (Figure 16). At low magnification, the organization of the DG, including its conspicuous GC layer, can be identified easily from the rCATS labeling pattern (Figure 16a). At higher magnification, major processes can be discerned (Figure 16b,c). Zooming in even further, these processes can be identified as neuronal dendrites by co-staining with microtubule-associated protein 2 (MAP2), a marker for neuronal dendrites and somata (Figure 16d). In addition, by using the excitatory postsynaptic marker Homer scaffold protein 1 (HOMER1), synapses become visible and can be placed in their structural context by rCATS. Judging from the morphology of synapses, which are associated with multiple postsynaptic puncta, as well as their location in the DG hilus, many of them likely correspond to MFBs.

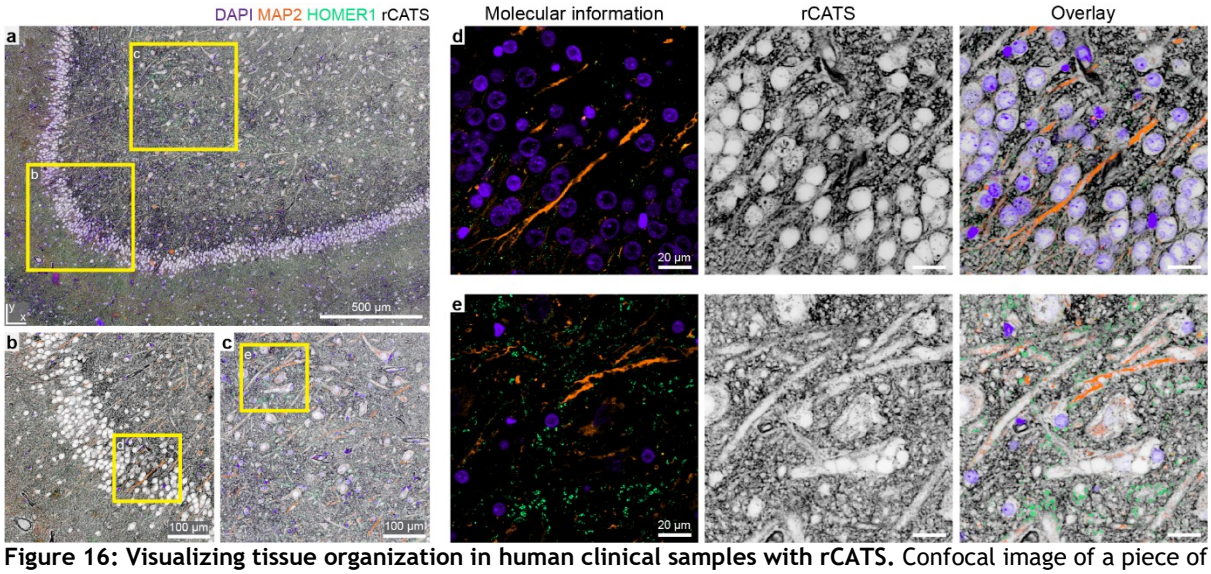


**Figure 16: Visualizing tissue organization in human clinical samples with rCATS.** Confocal image of a piece of immersion-fixed human DG (obtained with informed consent and ethics approval) labeled for MAP2 (orange), HOMER1 (green), nuclei (DAPI, purple) and rCATS (grey) with successive zoom-ins. Data was acquired with a spinning disk confocal microscope, using a 20x air objective, NA 0.75. Adapted from Michalska *et al.*, 2022[155].

To combine rCATS labeling of previously fixed brain samples with ExM, the following changes and additional steps are required:

6. Incubate the sample with 15-20 µg/ml biotinylated WGA in 1X PBS for at least 20 h at RT with gentle agitation.

9. Wash the sample 3 times for 30 min each with 1X PBS at RT with gentle agitation.
10. Incubate the sample with 20 µg/ml streptavidin acrylamide for 20 h at RT with gentle agitation.
    Note: This step can be performed together with secondary antibody incubation.
11. Wash the sample 3 times for 30 min each with 1X PBS at RT with gentle agitation.
12. Perform pre-expansion overview-imaging in an imaging chamber in 1X PBS for alignment of pre- and post-expansion images.
13. Perform ExM procedure according to the desired protocol.
    Note: Biotin-avidin reactivity is maintained after enzymatic digestion, as well as after heat/chemical denaturation.

Note: The rCATS labeling approach works best in combination with expansion protocols that do not require acrylamide-incubation before the gelation procedure (e.g. proExM).
Note: A detailed protocol for both proExM can be found in Appendix Section 6.3.1.2 (III.7.2 rCATS labeling with expansion in previously fixed mouse brain).

14. Excise a fragment of the expanded hydrogel and place it in a well of a 12-well plate. Equilibrate the gel-fragment by incubating it with 1 ml 1X PBS.
    Note: It is easier to handle the gel fragment on a coverslip. Place a coverslip at the bottom of the well before placing the fragment into it. This way, the fragment can be removed from the well by carefully aspirating all aqueous solution and lifting the coverslip with tweezers.
15. Read out the rCATS label by incubating the sample with an appropriate amount of readout solution (5-10 µg/ml fluorophore-conjugated biotin) for at least 20 h at RT with gentle agitation.
    *Example: The gel fragment is incubated with 1 ml 5 µg/ml Atto 643-biotin in 1X PBS for 20 h at RT with gentle agitation.*
16. Thoroughly wash and re-expand the sample 3 times for 1 h each with dd$H_2O$ at RT with gentle agitation.
17. Image the sample in an imaging chamber in dd$H_2O$.
    Note: To immobilize the gel fragment, use a PLL-coated coverslip.

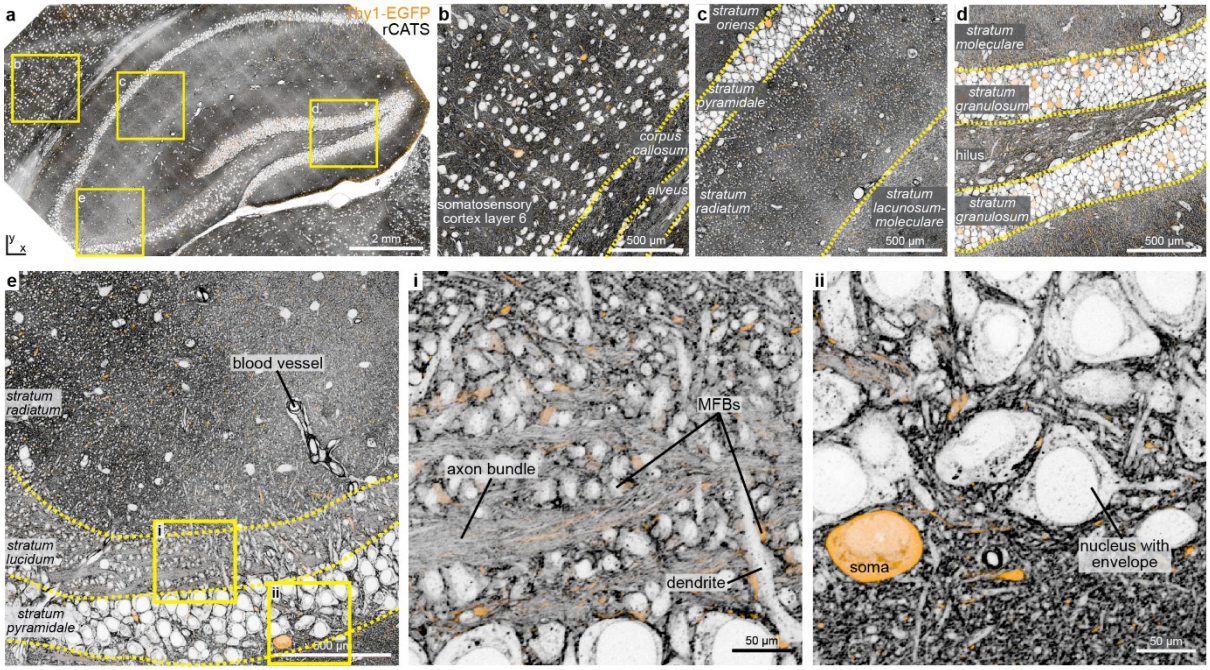


**Figure 17: Studying native brain tissue organization across scales with rCATS and ExM.** a) Confocal overview image and b-e) zoomed views of a piece of previously perfusion-fixed Thy1-EGFP (orange) adult mouse brain slice, ~4-fold expanded with proExM. RCATS labeling (grey) in the b) cerebral cortex, c) CA1, d) DG and e) CA3 elucidates the organization of the tissue. Scale bars refer to sample size after expansion. All images were acquired with a spinning disk confocal microscope (20x water immersion objective, NA 0.95). Adapted from Michalska *et al.*, 2022[155].

Combining rCATS labeling with ExM enables the study of brain tissue across multiple spatial scales with high resolution, using a single imaging set-up. This is demonstrated in Figure 17, showing a 4-fold expanded slice of the hippocampal area of a Thy1-EGFP mouse imaged from regional to subcellular scale with a spinning disk confocal microscope. At regional scale, the gross architecture of the hippocampal area, including the DG blade and the curved hippocampus, can be identified purely from the rCATS labeling pattern (Figure 17a). Focusing on the cerebral cortex (Figure 17b), as well as the different areas of the hippocampal area, including the CA1 (Figure 17c),

the DG (Figure 17d) and the CA3 (Figure 17e), rCATS visualizes their layered organization. WGA is often used as a marker for blood vessels, as it binds to the vasculature with high affinity. After expansion, blood vessels are highlighted brightly, allowing for the study of brain vasculature with rCATS (Figure 17e). Taking advantage of the increased resolution obtained by ExM, subcellular structures, including axon bundles, dendrites and giant MFBs in the CA3 *stratum lucidum* can be studied (Figure 17e). As WGA binds to carbohydrates present in nuclear pores, even nuclei can be identified with rCATS (Figure 17e). In addition, WGA also marks the inner layer of the myelin sheath, as well as nuclear pores (Figure 18). In summary, rCATS with ExM elucidates a multitude of structures in the brain, including the architecture of neuronal and non-neuronal cells, its vasculature and even sub-cellular components (nuclei, myelin). In combination with ExM, which provides clearing and resolution improvement, rCATS facilitates the study of brain organization from whole region down to sub-cellular organization.

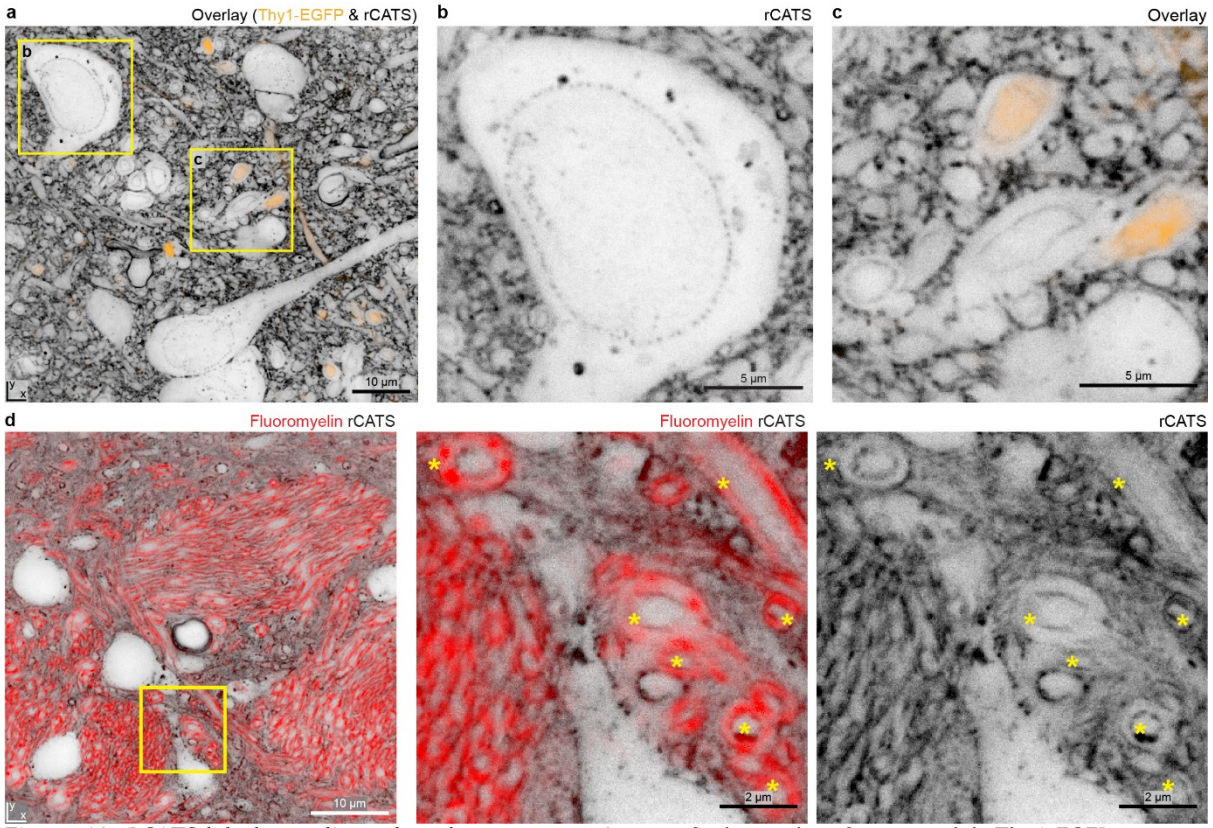


**Figure 18: RCATS labels myelin and nuclear pores.** a) Image of a brain slice from an adult Thy1-EGFP (orange, confocal) mouse brain after perfusion-fixation and rCATS (grey, 20:80 *xy*-STED:*z*-STED ratio) labeling. b) Magnified view of a cell soma, showing its nuclear envelope discernible by rCATS labeling of nuclear pores. c) Magnified view of neuronal processes, some of which show intracellular Thy1-EGFP labeling. RCATS delineates the inner and outer border of the myelin sheath. d) Hypothalamus of an adult mouse after perfusion-fixation, staining for myelin with Fluoromyelin (red, confocal) and rCATS labeling (grey, *z*-STED). Asterisks in magnified view indicate myelin structures. Data was acquired with a high-magnification objective (100x silicone, NA 1.35). Adapted from Michalska *et al.*, 2022[155].

Limitations & future prospects

RCATS provides structural context for samples that do not possess intact membranes, such as previously fixed specimens. The main limitation of this approach is therefore the specificity of the rCATS labeling compound, which must almost exclusively target ECS-resident molecules to create extracellular contrast. While the coCATS labeling approach was optimized to target entire classes of molecules, such as proteins, rCATS is limited to the binding specificity of WGA, mainly N-acetylglucosamine and sialic acid. As a result, the rCATS labeling pattern is likely less homogeneous when compared to the one achieved with coCATS. More importantly, the staining pattern is highly

dependent on the existence and composition of the ECM. I have shown that rCATS reliably demarcates the ECS in adult mouse and human brain tissue. Yet, whether the rCATS labeling paradigm will create extracellular contrast in other species, possibly exhibiting a different ECM composition, is unknown. In addition, the dependency on the ECM organization limits developmental studies. ECM components are known to play a critical role during developmental processes in the brain, including regulation of tissue shape, neural stem cell differentiation, neuronal migration and synapse maturation.[172] To do so, their expression pattern during development is highly dynamic, likely having an effect on the rCATS labeling pattern. Similar issues arise when studying diseased tissue. As the brain ECM provides physical support and assists homeostatic functions of neurons, changes in its composition have been found to be associated with neurodegenerative diseases, including ischemic stroke, multiple sclerosis, dementia and Alzheimer's disease.[173,174] These changes might also be reflected in the rCATS labeling pattern. Whilst this will likely affect labeling homogeneity, it also provides an avenue for utilizing rCATS to identify diseased tissue and study ECM changes therein.

A potential approach for increasing rCATS labeling homogeneity and decreasing its target specificity is to use a cocktail of multiple lectins that bind to different carbohydrates in the ECM. PHA-E, PHA-L and Jacalin all provide extracellular contrast to some extent (Figure 14), such that combining these, in addition to WGA, is a good starting point.

Another challenge is the rCATS SNR and signal homogeneity after the expansion procedure. Increasing the resolution by expanding the tissue results in a grainy staining pattern, which impedes the demarcation of thin structures in the tissue. This issue might be solved by improving lectin retention and/or using signal amplification strategies that deposit fluorophores in close proximity to the rCATS labeling compound. While I have shown that a lectin retention strategy involving biotin-conjugated WGA and streptavidin acrylamide greatly improves signal intensity after expansion, there are alternative options. For example, one could try to directly retain the lectin in the hydrogel by modifying it with an acrylamide moiety. Signal amplification strategies of interest are avidin-biotin complexes[175], hybridization chain reaction[176] and tyramide signal amplification[177], as they are robust and easy to implement.

Increasing the SNR is also crucial to further push the obtainable resolution by increasing the expansion factor. I have combined CATS with two different protocols for 4-fold ExM. This increases the resolution to ~75 nm in the lateral and ~200 nm in the axial direction, when combined with confocal microscopy using a high-NA objective. To be able to reliably study brain connectivity with this approach, one has to be able to resolve even the smallest cellular structures, such as thin axons or spine necks, which can be less than 100 nm in diameter.[8] To achieve sub-100 nm resolution in the axial direction, one needs to at least double the expansion factor (8-fold to 10-fold). Increasing the expansion factor will lead to a further decrease in signal, which in case of the rCATS labeling paradigm is already a limiting factor when combined with 4-fold ExM. Hence, it is crucial to boost signal strength and homogeneity, to ensure that the extracellular contrast used to depict cellular borders is retained sufficiently to delineate all cellular structures.

## 2.2 Data acquisition & processing

### 2.2.1 Super-resolution STED imaging of brain tissue organization

STED microscopy provides a direct, 'all-optical' way to super-resolve structures in CATS-labeled brain tissue samples. Compared to ExM, it requires fewer processing steps, such that there is a lower chance for introducing sample preparation artifacts. Therefore, combining the CATS labeling pipeline with STED microscopy was an obvious choice to study brain tissue organization as close to the native state as possible.

I acquired super-resolved data on an inverted STED microscope (Abberior Instruments Expert Line) with a high-magnification, high-NA objective (100x silicone, NA 1.35, working distance (WD) 0.2 mm) equipped with a correction collar. Using immersion oil with a RI=1.41, I could closely match the RI of brain tissue[36–38]. The STED system comprised three pulsed excitation lasers (485 nm, 561 nm and 633 nm) and one pulsed depletion laser (775 nm). Excitation and stimulated emission in the long visible wavelength range were used to increase tissue penetration. The pulse repetition rate was 40 MHz and fluorescence detection was time gated. Fluorescence was detected by photon counting avalanche photodiodes using bandpass filters at 525/50 nm, 605/50 nm and 685/70 nm. Galvanometric mirrors were used for lateral scanning and a sample piezo stage was used for axial scanning. To obtain STED data of high quality, I used high-performance, far-red STED dyes, such as STAR RED and Atto 643.
To increase STED performance, especially for volumetric imaging, I corrected for RI-mismatches from the tissue sample and the surrounding aqueous mounting medium (1X PBS) in two ways. Firstly, I set the correction collar to ~1.55 to correct for spherical aberrations. Secondly, I used a SLM to compensate for sample-induced aberrations by adjusting the shape of the STED beam in the sample.

I acquired single plane *xy*-STED images, as well as volumetric $z$-STED data.
For single plane STED data, the SLM was used to create a 2π-helical phase modulation (*xy*-STED) to increase lateral resolution. In Figure 19a, the performance of a confocal beam and *xy*-STED in coCATS labeled tissue is shown. The images were acquired in the DG of an adult mouse brain following *in vivo* microinjection of coCATS labeling compound into the LV. The zoom-ins clearly illustrate that the lateral resolution increase achieved by *xy*-STED allows for a more detailed visualization of the tissue organization. For example, only in *xy*-STED mode are individual axons in an axon bundle visible as fine rings. The line profiles in Figure 19b corroborate this finding, as individual axons can only be discerned when using super-resolution microscopy. When using similar imaging parameters as for tissue imaging on bead samples, the resolution increase was clearly visible, with a full width at half maximum (FWHM) of 56 nm with *xy*-STED compared to 261 nm in confocal mode (Figure 19c).

For acquiring volumetric STED data, the SLM was used to generate a π-top-hat phase modulation ($z$-STED), thereby predominantly increasing axial resolution. I compared the performance of an axial confocal vs. $z$-STED scan in the neuropil of a fixed cultured organotypic hippocampal brain slice labeled with coCATS (Figure 19d,e). The zoom-in in Figure 19d and line profiles in Figure 19e show that more details can be resolved with $z$-STED when compared to confocal mode. When using the $z$-STED pattern, the resolution increase is stronger in the axial direction at the STED power used. This results in near-isotropic resolution, which is slightly better in the axial (FWHM=133 nm) compared to the lateral direction (FWHM=159 nm), as can be seen from the images and line profiles of 40 nm Crimson beads (Figure 19f). Near-isotropic resolution greatly improves the study of volumetric brain imaging data, because it facilitates segmentation tasks, which are generally limited by the least-resolved direction.

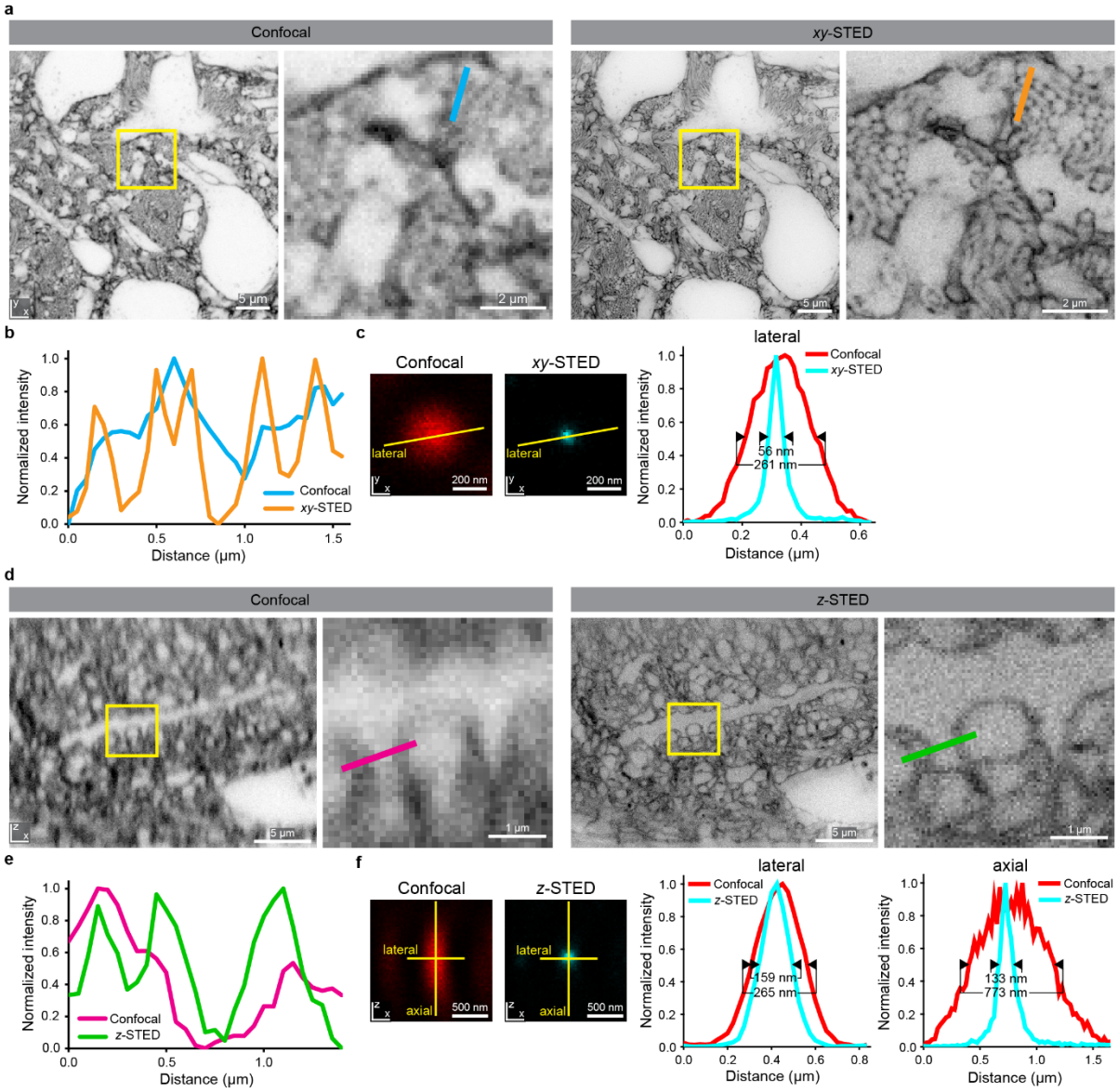


**Figure 19: Effect of STED patterns on lateral and axial resolution.** a) (Left) Confocal and (right) *xy*-STED image of a piece of DG hilus from an adult, perfusion-fixed mouse, labeled via coCATS *in vivo* microinjection of NHS-STAR RED. b) Line profile of the blue (confocal) and orange (*xy*-STED) line as indicated in a. c) Confocal (red) and *xy*-STED (cyan) images of a single 40 nm Crimson bead with line profile and FWHM. d) (Left) Confocal and (right) *z*-STED image in the neuropil of a cultured organotypic hippocampal slice labeled with coCATS. e) Line profile of the magenta (confocal) and orange (*z*-STED) line as indicated in d. f) Confocal (red) and *z*-STED (cyan) images of a single 40 nm Crimson bead with lateral and axial line profiles and FWHM. All images were acquired with a high-magnification objective (100x silicone, NA 1.35). Adapted from Michalska *et al.*, 2022[155].

Limitations & future prospects

The biggest limitation for improving resolution and thus data quality is currently photobleaching. I was able to acquire volumetric datasets (~30 µm x 30 µm x 10 µm) with 2-3 line accumulations, 10-15 µs dwell time and laser powers of max. ~2.0 µW (561 nm excitation laser), ~2.6 µW (640 nm excitation laser) and ~90 mW (775 nm depletion laser) without drastic signal loss. More line accumulations, longer dwell times or higher laser powers resulted in significant photobleaching. Photobleaching especially affected the demarcation of intricate brain structures, such as axon bundles, which exhibited comparatively low labeling intensity. There are multiple ways to decrease photobleaching. Firstly, one can mount the sample in buffers supplemented with reagents that protect fluorophores from photobleaching. These include systems for scavenging reactive oxygen

species, as well as small-molecule protective agents, such as Trolox. The latter have also been shown to have a protective effect when covalently linked to a fluorophore, such that it might be of interest to test these types of molecules.[178] Secondly, one can decrease the light burden on the sample during sample acquisition. This can for example be achieved by reduction of state transition cycles (RESCue) STED. RESCue decreases the photon burden by turning off lasers in cases of very low or very high signal of individual voxels.[179] When a 'lower' threshold of photon counts is not reached within a certain time, the voxel is considered devoid of signal, and all lasers are shut off. Upon reaching an 'upper' threshold, lasers are shut off as well, and the photon counts are extrapolated to the full dwell time.[179] A similar concept, called dynamic intensity minimum, adjusts the STED intensity dynamically at each voxel during the acquisition to decrease photon burden.[180] Alternatively, instead of decreasing photobleaching, one can increase the signal intensity by signal amplification methods, as discussed in Section 2.1.2.1. Another way to reduce light burden is by training a machine learning algorithm to restore high-SNR data from low-SNR data, as recently shown by Velicky *et al.*[29]. Here, one can acquire multiple CATS data pairs with long vs. short dwell time. These pairs can then be used to train a model with the algorithm content-aware image restoration (CARE)[135], which will be capable of restoring the SNR of larger datasets acquired with low light burden.

The axial range in which one can obtain homogeneously super-resolved data in aberrating specimens, such as brain tissue, is limited in STED microscopy. By adjusting the correction collar and the STED beam shape with the SLM, I was able to acquire datasets in an axial range of 10-12 μm with high axial resolution. The easiest way to increase this range further is by adjusting the sample-RI to the objective and decrease sample-induced aberrations. I have tested RI-matched mounting media, such as Fluoromount-G (RI=1.4, ThermoFisher Scientific, 00-4958-02), and have preliminary evidence that these have a positive effect on homogenizing sample-RI and therefore decreasing spherical aberrations. Regardless, one has to evaluate the effect of the mounting medium on sample integrity and staining quality carefully. For example, mounting media containing the polyvinyl alcohol Mowiol, can lead to sample shrinkage and flattening.[181] In addition, I have found that mounting media 'dissolve' the coCATS label, probably due to the extraction of insufficiently immobilized membrane proteins. Similarly, while optical clearing approaches are a great way to reduce sample-induced aberrations, many of them do so by delipidation, which might affect the CATS labeling quality. Here, hydrogel-based clearing approaches, such as CLARITY[182], are an exciting avenue, as they are closely related to the already established ExM. In addition, optimizations of the imaging system, for example by using an automated correction collar that can be adjusted for imaging depth during image acquisition, will also increase the obtainable imaging volumes.

## 2.2.2 Denoising of near-isotropically resolved CATS data

Denoising was performed with the deep-learning (DL)-based algorithm Noise2Void (N2V)[183] on volumetric coCATS data to remove background noise, hence increasing the SNR of the data. This has a positive effect on the outcome of manual segmentation tasks. Automated segmentation tasks have been shown to improve upon denoising as well, especially when the amount of ground truth segmentation data used for training is low.[184,185] N2V is based on an artificial neural network that is trained directly on the data to be denoised, thus circumventing the need to create training pairs. N2V utilizes a 'blind-spot' network, which excludes the central pixel (the pixel to be denoised) from its receptive field. The receptive field is defined as the set of pixels in a square neighborhood influencing the prediction of the central pixel. The exclusion of the central pixel creates a blind spot, meaning that the network prediction will be affected by all pixels in the receptive field, except for the central one. The network estimates the signal of the central pixel based on its surrounding. Pixel-wise independent noise is eliminated, as the surrounding does not carry any information

about its value, such that it cannot be estimated by the network. This way, N2V outperforms traditional denoising techniques.[183]
Volumetric coCATS datasets were denoised with the following parameters: noise2void 3D mode, patch size 16/32 x 32 x 32 (*zyx*), number of patches per image: all, patch augmentation: rotation and axis-mirroring, neighborhood radius: 5, percent pixel manipulation: 1.5, number of epochs: 75-80.

Figure 20 is a comparison between raw and N2V-denoised volumetric coCATS data obtained with *z*-STED in a cultured organotypic hippocampal slice. Raw data (Figure 20a,c,e) displays a stronger salt-and-pepper background and a substantially lower SNR in comparison to the denoised data. Upon N2V-denoising (Figure 20b,d,f), cellular borders are more visible, making it easier to follow structures, for example to annotate them.

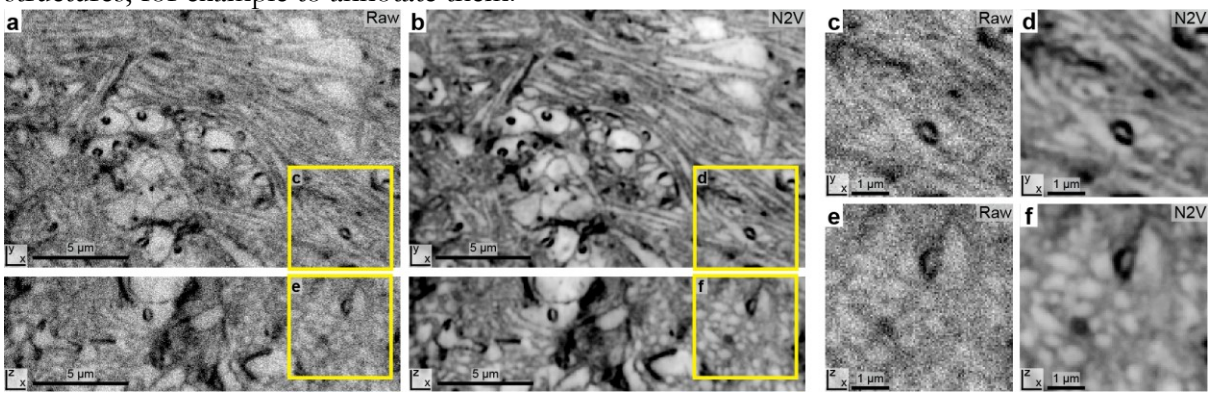


**Figure 20: Comparison of raw and denoised coCATS data.** CoCATS labeling In the DG hilus of a cultured organotypic hippocampal slice, including two zoom-ins. a), c), e) Raw and b), d), f) N2V-denoised data. Data was acquired in *z*-STED mode with a high-magnification objective (100x silicone, NA 1.35). Adapted from Michalska *et al.*, 2022[155].

Limitations & future prospects
Currently, denoised data is mainly used for visualization purposes, as well as for manual segmentation tasks. For automated segmentation of synaptic structures, I have compared the performance of a deep-learning-based algorithm trained on raw and N2V-denoised data, and found the resulting segmentations to be of high similarity.
N2V is based on the assumption that the real signal of a pixel can be predicted from its surrounding. One should be aware of this limitation, and carefully evaluate every denoised dataset for artifacts. In addition, the original implementation of N2V was not capable of eradicating structured noise, as this type of noise is predictable.[183] To solve this issue, a novel implementation of N2V, optimized for the removal of structured noise, was developed.[186]
Instead of simply denoising the data, which will result in a smoothed dataset with lower background, one could use the CARE algorithm, as described in Section 2.2.1. This has the potential to further increase the SNR, which will likely have a positive effect on automated segmentation tasks.[29]

## 2.2.3 Large-scale imaging of brain tissue with ExM

I combined CATS with ExM to demonstrate the capability of the toolbox to analyze brain tissue organization across scales, focusing on regional down to subcellular scales. Therefore, I acquired extended depth and large-scale datasets of ~4-fold expanded brain tissue specimens. I mainly focused on perfusion-fixed mouse brain slices, but this strategy is also compatible with other specimen types, such as organotypic slice cultures (see Michalska *et al.*, 2022[155], Fig. 5a and Suppl. Fig. 10).

Data was acquired on a spinning disk confocal microscope, as it provides high imaging throughput paired with high spatial resolution. I used the Andor Dragonfly imaging platform consisting of a Nikon Ti2E inverted microscope with a motorized stage, a spinning disk with a pinhole diameter of 40 µm and four continuous-wave excitation lasers (405 nm, 488 nm, 561 nm and 637 nm). The signal was detected with an Andor Zyla 4.2 Megapixel sCMOS camera. To achieve high-resolution data, I used a high-magnification, long WD water objective (Nikon Apochromat LWD 40x lambda S/NA 1.15/Water immersion/ WD 0.6 mm). For overview imaging, I used a 10x air objective (Nikon CFI P-Apo 10x λ/NA 0.45/WD 4.0 mm).
Overview imaging was performed to align pre- and post-expansion imaging datasets with the goal of precisely determining the expansion factor and evaluating expansion-induced distortions. Here, the same label has to be acquired before and after the expansion procedure. The rCATS labeling cannot be used, as fluorescent readout is only performed after the expansion procedure. In any case, a sparse label is advantageous for the alignment, as it is easier to identify hallmark features in this type of data. Here, I used the fluorescent signal of a genetic line for sparse labeling of neurons expressing the *Thy1*-gene (Thy1-EGFP) as a marker for alignment. I performed low-magnification overview imaging with a voxel size of 0.3 x 0.3 x 1.5 $\mu m^3$ of the immunostaining-enhanced Thy1-EGFP signal across the entire sample before the start of the ExM procedure.
After expanding the sample, I excised a ~3 cm x 3 cm big piece of expanded hydrogel containing the sample and immobilized it on a PLL-functionalized coverslip in an imaging chamber. The imaging chamber was filled with $ddH_2O$ and a second coverslip was placed on the gel to avoid evaporation during the imaging procedure. Multi-channel imaging was performed ON with a voxel size of 0.15 x 0.15 x 0.30 $\mu m^3$. The imaging data was directly saved on an external hard drive for efficient data transfer.

Limitations & future prospects

The major practical limitation for acquiring large-scale imaging data was the acquisition time.
Even though the spinning disk confocal microscope operates at high speed due to its parallelized excitation, multiple factors increased the imaging time. Firstly, the low signal intensity provided by the expanded sample required the use of long dwell times. As previously stated, enhancing the signal of ExM-treated samples is therefore an avenue for future improvements, not only to increase the quality of the resulting data, but also to decrease imaging time. Further, the use of high-magnification objectives resulted in small fields of view, which also increase imaging time. It was necessary to use a high-magnification objective to push the obtainable resolution, especially in the axial direction. Alternatively, one could increase the obtainable resolution by using a bigger expansion factor, yet the volumetric sample size increase and the dilution of the signal will compete directly with the acquisition time. To address this issue, future experiments using light sheet microscopy for data acquisition are promising, as this imaging technique provides high throughput to capture extended volumes of expanded specimens.[187] Instead of increasing the expansion factor to obtain sufficient resolution in the axial direction, it could be of interest to focus on efforts that push light sheet microscopy towards isotropic resolution.[188–190] Alternatively, lowly expanded gels can be imaged with $z$-STED. For example, the combination of 4-fold ExM, as shown in this work, with $z$-STED, would result in ~50 nm near-isotropic resolution.[191] Yet, if a single-point STED microscope is used, this will greatly impede imaging throughput.
Another practical limit is the sample thickness that can be acquired without slicing. Currently, the limited axial resolution necessitates the use of high NA objectives, which limit their WD. For example, I used a 40x water immersion objective with a WD of 0.6 mm for high-resolution volumetric imaging. In combination with 4-fold expansion, it provides ~75 nm lateral and ~200 nm axial resolution, and is limited to image samples of ~100 µm thickness before expansion. For segmentation tasks, the axial resolution would have to be significantly better, thus necessitating higher expansion factors, which would further decrease the initial sample thickness. To achieve extended depth imaging of thick, expanded samples, using a light sheet microscope, especially one

with an improved axial resolution, would be a possible solution. Another solution would be to combine ExM with serial sectioning, thus providing access to thick, expanded tissue by successively imaging the surface layer and removing it.[192]

### 2.2.4 Large-scale data processing

Christoph Sommer guided me in the development of a pipeline for data handling and data analysis of expanded CATS specimens. He wrote and executed scripts for stitching, denoising and calculation of the expansion factor.

Large-scale imaging of ~4-fold expanded brain tissue specimens resulted in datasets of ~1 TB size (~1.4 x 1.7 x 0.3 $mm^3$ post-expansion). Therefore, it was necessary to develop a pipeline to efficiently handle, visualize and analyze datasets of such a size (and potentially bigger).
Pre-expansion imaging data of the whole brain slice consisted of up to 120 single-channel volumetric tiles. Post-expansion imaging data consisted of up to 36 volumetric tiles containing up to three channels (rCATS, immunostainings). I transferred the imaging data from the hard drive to an internal server. Pre- and post-expansion datasets were transformed into BigStitcher datasets, roughly aligned according to the imaging parameters (10% overlap) and resaved to the chunked, pyramidal image format N5 with 6 pre-computed resolution levels. Data visualization was performed with the ImageJ/Fiji[193] version 1.53f51 plugin BigDataViewer[194]. BigStitcher version 0.8.3[195] was used to align, stitch and fuse the imaging tiles with linear blending and to export the aligned dataset into 16-bit HDF5-BigDataViewer files. Post-expansion datasets were denoised with N2V. For each channel, a N2V model was trained on 6000 randomly selected patches with a size of 64 x 64 x 64 voxels for 60 epochs with 256 steps per epoch. Each channel of the dataset was then denoised with the respective N2V model on a high-performance cluster with GPU-acceleration. Next, I manually aligned the pre- and post-expansion datasets with BigWarp[196] by matching landmarks in the Thy1-EGFP channels in 3D. The expansion factor was extracted from the BigWarp landmark file using a custom script.

Limitations & future prospects
The main practical limitation was the size of the datasets, which made handling and processing challenging. As future developments will lead to a further increase in data volume, this aspect should be further optimized. Transfer of the data and data type transformation steps should be minimized, as these take a lot of time. Sufficient storage space, as well as powerful computational machines, have to be available, to store, process and analyze the data. Here, close collaboration with data analysis and computation experts is necessary.
In addition, there are many recent developments in large-scale ExM imaging, which provide open-source pipelines for data processing that can be taken advantage of, for example the image processing and analysis platform for expanded light sheet data developed by Lillvis *et al.*[197].

# 2.3 Analysis of neuronal properties

While I developed the concepts described in this section, I acknowledge the work of my colleagues who have been involved in this work.
Jake Watson performed all whole-cell patch-clamp experiments, which involved electrophysiological characterization and cell filling.
Eder Miguel installed the software used for skeletonization on our local server. Christoph Sommer transformed the post-expansion dataset into the webKnossos-wrap (WKW) container format for ease of implementation.
Alban Cenameri performed all manual segmentations, which I proofread manually.
Julia Lyudchik wrote and implemented all scripts for the quantification of manually segmented structures. She co-developed the pipelines for the identification of putative synaptic cleft regions (pSCRs). She wrote, adapted and ran all related scripts. Additionally, she created the 3D-visualizations.

## 2.3.1 Analysis of dendritic arborization

I skeletonized single neuronal cells using webKnossos version 22.05.1[198] installed on a local server. The stitched and denoised post-expansion dataset was transformed into 8-bit WKW-format. I then uploaded the dataset into webKnossos on our local server. To create a skeleton, I chose a cell soma situated in the center of the dataset and skeletonized it with the webKnossos skeleton tool with orthogonal views.

*Example:* ***Skeletonization of the dendritic arborization of a DG hilar mossy cell***
*I performed rCATS labeling, as well as immunostaining for GFP and the postsynaptic marker SHANK2 in a 100 µm thick perfusion-fixed coronal brain slice from an adult Thy1-EGFP mouse. After pre-expansion imaging, I expanded the sample with the proExM protocol, using the signal retention pipeline described in Section 2.1.2. After expansion and readout of the rCATS label, I performed ON imaging of the DG. The post-expansion data was processed and denoised. I then aligned pre- and post-expansion datasets to obtain the expansion factor, which was 4.5x. I identified a DG hilar mossy cell lying centrally in the imaging dataset (Figure 21, yellow arrows) by its morphology and the presence of multiple MFBs in contact with its dendrite (Figure 21, yellow asterisks), clearly identifiable via the SHANK2 staining. I skeletonized its major dendritic arborization of this neuron, which was EGFP-negative, from the rCATS signal (Figure 21).*

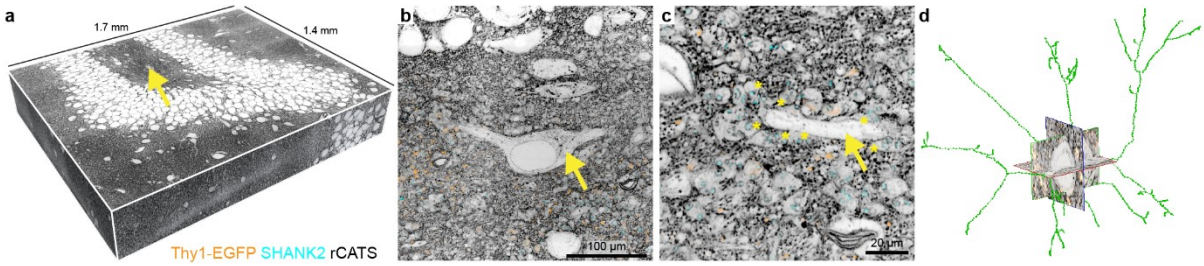


**Figure 21: Large-scale imaging of tissue context with ExM for tracing dendritic arborization.** A 100 µm thick perfusion-fixed brain slice obtained from and adult Thy1-EGFP mouse was 4.5-fold expanded with proExM, labeled with rCATS (grey, N2V), immunostained for GFP (orange, N2V) and SHANK2 (cyan, N2V) and imaged with a spinning disk microscope (40x water immersion objective, NA 1.15). a) 3D-representation of a volume of DG crest. The location of the analyzed hilar mossy cell is denoted with a yellow arrow. b),c) Single slices of the volumetric dataset displaying a close-up of b) the cell body and c) a major dendritic branch of the analyzed hilar mossy cell. MFBs in contact with the mossy cell dendrites are labeled with yellow asterisks. d) Skeletonization of the major branches of the mossy cell in a-c. Scale bars refer to sample size after expansion. Adapted from Michalska *et al.*, 2022[155].

Limitations and future prospects

The tracing of the dendritic arborization of a single mossy cell in Figure 21 shows that CATS can be used to analyze the architecture of complex neurons. The detail of this trace is mainly dependent on the resolution, in this case provided by the expansion factor. Here, I chose a moderate expansion factor (4.5x) to clear the sample and trace the major dendritic processes over an axial range of ~80 µm. Higher resolution, as well as higher signal intensities, are necessary to trace smaller structures, such as thin dendrites, axons and spines. Strategies to address these aspects have been discussed in detail previously (see Section 2.1.2.1 and 2.2.3).

If the aim is to study the architecture of single, predefined neurons, CATS is likely not the best option, as processes smaller than the effective resolution are lost. In this case, an easier approach is to positively label the cell of interest and trace it with the help of the intracellular label. Yet, if one would like to trace cells independent of their cellular identity in the tissue and/or without the availability of a positive label, CATS is a useful approach. At high resolution, and in combination with a synaptic marker, such as SHANK2, it offers not only the possibility trace cells, but also to identify synaptic connections and thus gain information on circuitry.

## 2.3.2 Assessment of cellular structure characteristics

To assess morphological characteristics of cellular structures, they were segmented from super-resolved CATS data. Manual segmentation and proof-reading was performed in VAST v1.4.0[199] in all three dimensions (*xy*, *xz* and *yz*).

Figure 22 shows the dense reconstruction of a volume of human cerebral organoid that was labeled with coCATS and imaged after fixation (Figure 22a,b). A 10 x 10 x 6 µm big volume was manually segmented to map its cellular constituents (Figure 22c).

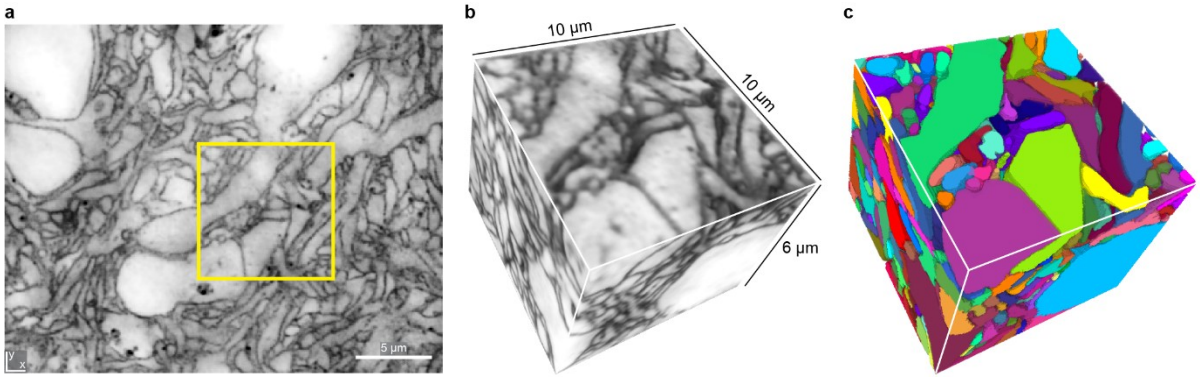


**Figure 22: Reconstruction of a volume of human cerebral organoid.** a) Single plane of a volume of a 150 DIV human cerebral organoid labeled with coCATS and immersion-fixed. b) 3D-represensation of a sub-volume (yellow box) of the data shown in a. The data was acquired in z-STED mode with a high-magnification objective (100x silicone, NA 1.35) and post-processed with N2V and adaptive histogram equalization. c) Dense reconstruction of the sub-volume represented in b. Adapted from Michalska *et al.*, 2022[155].

To quantify structural characteristics of the manually segmented objects, they were turned into 3D-meshes with Blender version 2.92. A custom-written Blender-script was used to calculate surface areas from the 3D-meshes. Blender was also used to compute volumes as the sum of mesh face areas. Custom-written Blender-scripts were further used to extract sub-volumes from segmented cellular structures. MFBs were disconnected from their filopodia and axons to quantify their surface areas and volumes. Complex spines were extracted from a segmented piece of CA3 PN proximal dendrite.

An example for complex spine extraction is displayed in Figure 23. The goal was to extract all spines from the proximal dendrite of a CA3 PN to study their structural characteristics. Single

CA3 PNs in cultured organotypic hippocampal brain slices were whole-cell patch-clamped and filled with Lucifer Yellow. CoCATS labeling was followed by immersion fixation and super-resolution volumetric imaging with STED (Figure 23a). The proximal dendrite was manually segmented from the coCATS channel. Lucifer Yellow, which can only be acquired in confocal mode with our STED microscope, was used as a ground truth for the segmentation. After creating 3D meshes with Blender, all spines were detached from the main dendrite (Figure 23b). To my surprise, I found many small spines emanating from the dendritic shaft alongside big TEs with highly complex structures. The surface area (5.6 ± 11.13 $\mu m^2$) and volume (0.53 ± 1.27$\mu m^3$) were computed. In comparison to previously published EM data (see Table 1), these values are significantly smaller, likely because we included all postsynaptic structures, not just the prominent TEs.

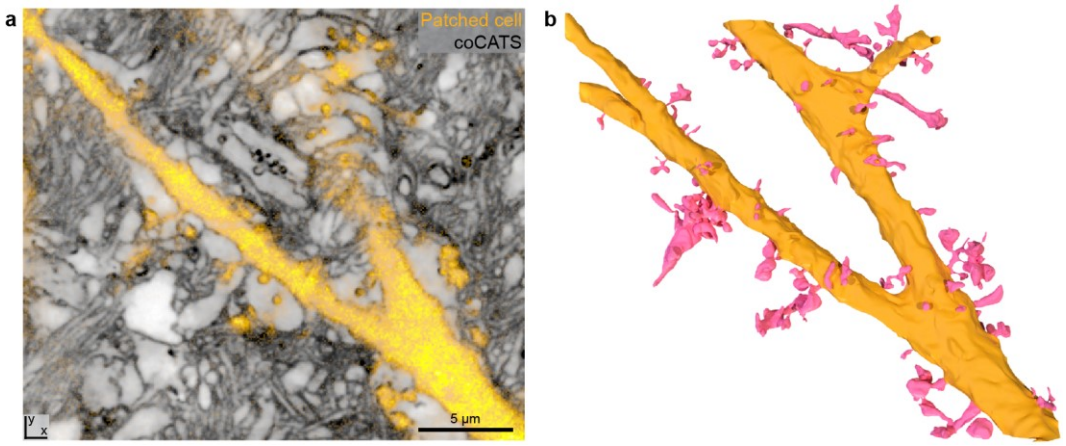


**Figure 23: Spine extraction from a reconstructed CA3 PN proximal dendrite.** a) Single *xy*-plane from a volumetric dataset showing a piece of a positively labeled CA3 PN proximal dendrite (confocal, gold) in its surrounding elucidated via coCATS (grey, z-STED, N2V). Data was acquired from a cultured organotypic hippocampal slice. Single CA3 PNs were whole-cell patch-clamped and dye-filled with Lucifer Yellow to obtain a positive label. The data was acquired with a high-magnification objective (100x silicone, NA 1.35). b) 3D-reconstruction of the positively labeled dendrite (gold) with complex spines (magenta) extracted for quantification. Adapted from Michalska *et al.*, 2022[155].

Limitations & future prospects

Manual segmentation is time-consuming and can thus hardly be upscaled to analyze multiple or large datasets. For example, the reconstruction of a 10 x 10 x 6 $\mu m^3$ cube of coCATS labeled cerebral organoid by a trained segmenter took ~250 h (Figure 22). Yet, it is necessary to analyze a large number of structures in an unbiased fashion to obtain quantitative, and thus meaningful, results. To reach this goal, it will be necessary to automate the segmentation process in the future. Here, one can adapt algorithms for the automated segmentation of EM data for connectomics studies[136,200–203]. In a recent publication introducing LIONESS (see Velicky *et al.*, 2022[29]), we used an iterative training scheme to enable the automated segmentation of extracellular labeling data in living brain specimens by a deep learning algorithm. Initially, the network was trained on a small, manually annotated data volume. The trained model was then applied to larger datasets. The resulting segmentations were manually proofread and fed back into the training, thus extending the training volume, optimizing the model and improving automated segmentation. Adopting this approach to CATS data would greatly reduce the time spent on segmentation, as automated segmentation combined with manual proofreading is substantially less time consuming than manual segmentation. LIONESS uses the SUSHI method to create extracellular contrast in living samples, such that the resulting imaging data exhibits high similarity to CATS, specifically coCATS, data. Thus, it would be exciting to test the performance of the model trained on data obtained from living samples. If it generalizes well, meaning that it provides dense segmentation of coCATS data with limited errors, this initial segmentation could be used as a starting point for the iterative

training scheme to optimize the model for coCATS data. Otherwise, ground truth segmentation of the coCATS data will have to be created manually and used to train an independent model for the automated segmentation of this type of data.

### 2.3.3 Identification of putative synaptic cleft regions

When analyzing images of brain tissue labeled with coCATS and molecular markers for synaptic molecules carefully, I discovered that the coCATS data featured intensely labeled structures tightly sandwiched between pre- and postsynapses. I validated the spatial relationship of these coCATS features with various molecular targets by co-immunostainings with synaptic markers (Figure 24).

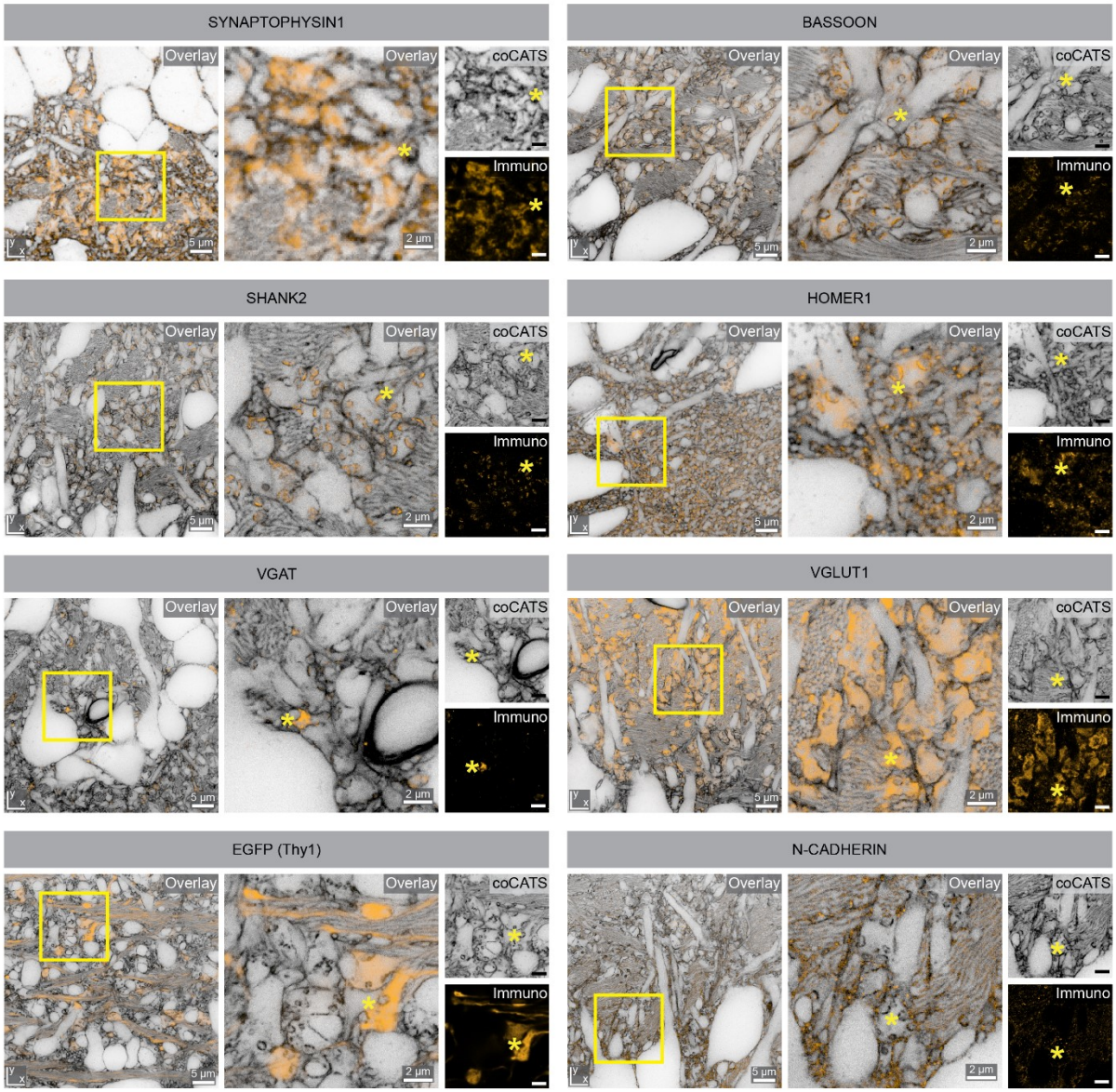


**Figure 24: Validation of the spatial relationship of pSCRs to other synaptic components.** Super-resolved coCATS data (grey) and various immunostainings (orange) adult mouse brain coCATS labeled by *in vivo* microinjection and fixed by transcardial perfusion are shown in an overview image and a zoomed in version. One conspicuous pSCR per dataset is labeled with a yellow asterisk. All images were acquired with a high-magnification objective (100x silicone, NA 1.35) in STED mode, except for SYNAPTOPHYSIN1, which was acquired in confocal mode. Taken from Michalska *et al.*, 2022[155].

I used the following markers: SYNAPTOPHYSIN1 and BASSOON present in presynapses, HOMER1 and SHANK2 present in excitatory postsynapses, vesicular gamma-aminobutyric acid

transporter (VGAT) present in inhibitory synapses, vesicular glutamate transporter 1 (VGLUT1) present in excitatory synapses, sparse cytosolic Thy1-EGFP to test for co-localization with MFBs, and N-CADHERIN, a marker for cell-cell adhesion. I found all markers, except for N-CADHERIN, to be situated in very close proximity to the high-intensity coCATS features in both laterally (*xy*-STED) and axially ($\tilde{z}$-STED) enhanced super-resolution data.
I concluded that high-intensity coCATS features are situated in synaptic cleft regions of both excitatory and inhibitory synapses. They are likely created by strong binding of the coCATS dye to the clefts' protein-rich extracellular environment, such that we termed them 'putative synaptic cleft regions' (pSCRs).
Based on the fact that pSCRs can be clearly identified in coCATS data by eye, with and without the presence of a molecular marker for synapses, I developed two pipelines for their automated detection and segmentation together with my colleague Julia Lyudchik. The first pipeline (automated pSCR segmentation guided by immunostaining) identifies pSCRs in the presence of molecular markers for pre- and postsynapse (Section 2.3.3.1). The second pipeline uses a neural network to locate pSCRs in datasets without additional molecular information (Section 2.3.3.2).

### 2.3.3.1 Automated pSCR segmentation guided by immunostaining

The following steps are performed to detect pSCRs from near-isotropically resolved volumetric coCATS data guided by the presynaptic marker BASSOON and the super-resolved postsynaptic marker SHANK2. A schematic representation, as well as an example with real data, of the process is seen in Figure 25.

1. 3D-data: Volumetric data sets acquired in the CA3 *stratum lucidum* of perfusion-fixed adult mice after coCATS *in vivo* microinjection are used. CoCATS and SHANK2 signals are near-isotropically resolved, while BASSOON is acquired in confocal mode. CoCATS data is enhanced with N2V.
2. BASSOON mask: A binary mask of the BASSOON signal is created by removing background and performing global Otsu thresholding (semantic segmentation).
3. SHANK2 mask + dilation: A binary mask of the SHANK2 signal is created by removing background and performing global Otsu thresholding (semantic segmentation). The SHANK2 mask is dilated to perform a local search in the vicinity of the SHANK2 signal.
4. Local search: The dilated SHANK2 mask is overlaid with the coCATS data to limit the search for pSCRs to regions in the vicinity of the postsynaptic marker.
5. PSCR instance segmentation: A global threshold is applied to the coCATS mask. Then, high-intensity coCATS features are segmented individually (instance segmentation).
6. Triple co-localization: PSCRs co-localizing with an overlap region of the binary BASOON and SHANK2 masks are identified. Segments that do not co-localize with both synaptic markers, are discarded to eliminate false positive synapse identifications.
7. MFB segmentation: Volume segmentations of MFBs from denoised coCATS data are created as described in Section 2.3.2.
8. MFB-pSCR coupling: MFB segmentations are dilated to search for pSCR segments in their vicinity. PSCR segments that display an overlap are extracted and assigned to their respective MFBs.

In the last step, segmented pSCR objects are manually proofread to correct for errors.

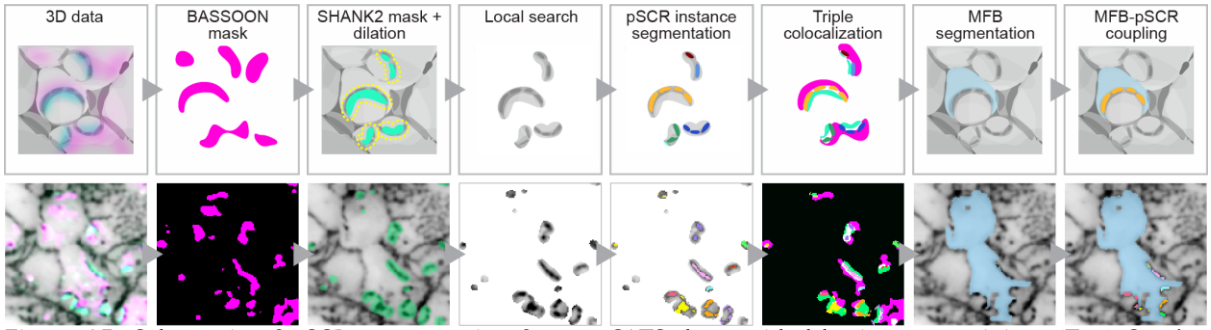


**Figure 25: Schematic of pSCR segmentation from coCATS data guided by immunostaining.** (Top) Graphic representation and (bottom) real data examples depicting the steps to pSCR segmentation from coCATS data (greys) guided by molecular labeling of a pre- (magenta) and postsynaptic (turquoise) marker. Taken from Michalska *et al.*, 2022[155].

An example of the automated pSCR segmentation guided by immunostaining is displayed in Figure 26. Here, I identified pSCRs belonging to MFBs in the CA3 *stratum lucidum* to analyze their synaptic fields. I created extracellular contrast by *in vivo* microinjection of coCATS labeling compound in the LV of adult mice. After perfusion fixation, I stained for BASSOON and SHANK2 to identify excitatory synapses, and acquired super-resolved volumetric datasets (Figure 26a). I used the automated pSCR segmentation pipeline to output pSCR objects, which I proofread manually (Figure 26b). The most common errors I encountered were split-errors (one pSCR identified as two objects) and merge-errors (two pSCRs in close proximity that were identified as one object).

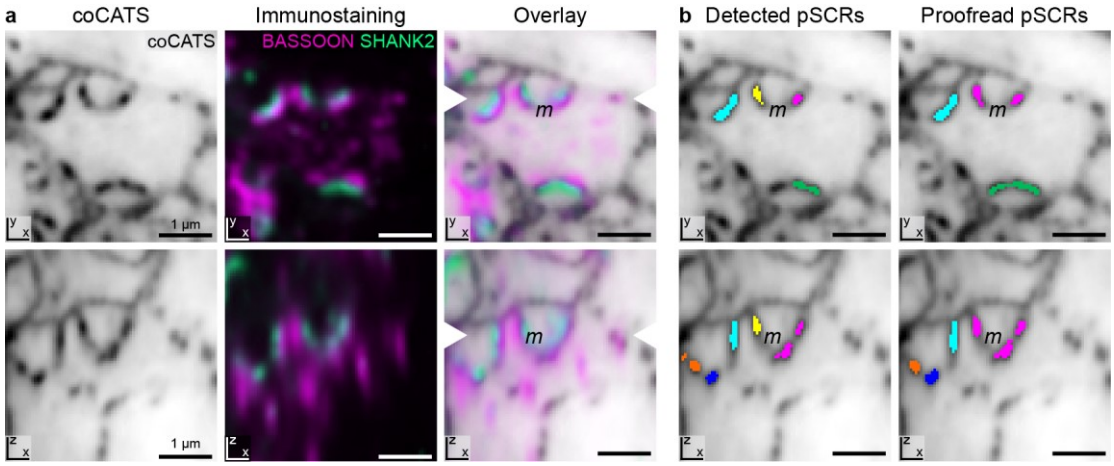


**Figure 26: Automated identification and segmentation of MFB pSCRs guided by immunostaining.** Automated pSCR detection was performed in the CA3 *stratum lucidum* after coCATS *in vivo* microinjection, perfusion fixation and immunostaining for excitatory synapses. a) Single *xy*- and *xz*-image of a volumetric coCATS (grey, *z*-STED), BASSOON (magenta, confocal) and SHANK2 (turquoise, *z*-STED) dataset denoised with N2V. White arrowheads indicate positions of orthogonal views. b) CoCATS data and automatically segmented pSCR objects before (detected pSCRs) and after proofreading (proofread pSCRs). Two objects were merged (*m*) during proofreading. All data was acquired with a high-magnification objective (100x silicone, NA 1.35). Adapted from Michalska *et al.*, 2022[155].

Limitations & future prospects

The pipeline for automated pSCR detection guided by immunostaining utilizes global thresholding of signal intensities, followed by local search in threshold-created binary masks. Currently, this threshold has to be chosen manually to account for variable signal intensities across different imaging volumes. More importantly, even within a single data volume, signal intensities display regional differences, such that a global threshold may not be ideal to distinguish between signal and background across the whole dataset. Therefore, using a local thresholding approach, especially for the pSCR instance segmentation, might improve the shape of the resulting pSCR objects and decrease the amount of split- and merge-errors.

The identification of coCATS high-intensity features is solely based on the proximity to molecular markers, specifically SHANK2. The coCATS and SHANK2 signals are localized using the same STED beam. This is advantageous, as it eliminates system-induced localization errors, such as chromatic aberrations. However, this approach does not make use of the local environmental context, which is elucidated by coCATS. This context might provide information on whether a coCATS high-intensity feature is truly a pSCR. This information might include, especially in the case of MFB synapses: the shape of the coCATS high-intensity feature; the proximity to other coCATS high-intensity features; the positioning of multiple coCATS high-intensity features in relation to one another; the presence of other cellular structures in close proximity, such as proximal dendrites or mossy fibers; etc. To leverage this information, we developed a second automated pSCR segmentation pipeline using deep learning, described in Section 2.3.3.2.

### 2.3.3.2 Deep-learning-assisted prediction of pSCR location

Based on the prominence of pSCRs in coCATS data, I wondered whether it is possible to identify synapses purely from coCATS data without additional molecular information. This would imply that synapse location is directly encoded in the coCATS data, similar to the electron-dense postsynaptic density (PSD) found in electron micrographs.[204] Global thresholding of the coCATS data was not sufficient to identify pSCRs. This is due to the fact that not all high-intensity features in the coCATS data represent synapses, as well as due to regional differences in signal intensities within the datasets.
To overcome this limitation, my colleagues and I adapted a deep learning approach by Ounkomol *et al.*, 2018[205], which was developed to model the relationship between distinct, but correlated imaging modalities, such as EM, brightfield, fluorescence and even stimulated Raman scattering data. A convolutional neural network based on the U-net architecture is trained on paired images of a molecular label and second channel containing structural information. Then, the trained model is used to predict the molecular label from the structural data alone.[100,205]
My goal was to employ this strategy to predict the location of synapses based on the structural information provided by coCATS. I hypothesized that I could leverage the contextual information provided by coCATS data to identify pSCRs. To do so, a deep learning network was trained with super-resolved coCATS data paired with a molecular marker for synapses as ground truth. A schematic of the strategy is displayed in Figure 27a. We used code adapted from Qian *et al.*, 2021[100].

Training
For training, I created coCATS data paired with BASSOON immunostainings, both near-isotropically resolved with $\chi$-STED, to localize excitatory and inhibitory synapses with high precision. Training data was exclusively acquired in the CA3 *stratum lucidum* of coCATS *in vivo* microinjected and perfusion-fixed adult mice. CoCATS data was denoised with N2V and background subtraction was performed for the BASSOON channel. We trained the model with ~85000 $\mu m^3$ of training data.

Prediction
The trained model was used to predict the molecular label (predicted BASSOON) from a previously unseen coCATS dataset. A molecular ground truth in the form of super-resolved BASSOON immunostaining (immuno BASSOON) was also available, but only used for the validation of the model.

pSCR identification & segmentation
The predicted BASSOON label was used to perform pSCR segmentation as described in Section 2.3.3.1. In this case, only one molecular label (predicted BASSOON) was available, which was used as a guide to synaptic sites. The predicted BASSOON signal was turned into a binary mask and

dilated to conduct a local search for pSCRs in the coCATS channel in the vicinity of the molecular marker. Then, instance segmentations of pSCRs were created by global thresholding.

Validation

To validate the accuracy of the molecular label prediction, I first compared the molecular ground truth immunostaining (immuno BASSOON) to the deep learning prediction (predicted BASSOON). Upon visual inspection, I found high similarity between these two labels (Figure 27b). This similarity is corroborated by a high voxel-wise correlation with a Pearson correlation coefficient value of r=0.818. Secondly, we compared the segmentation outcome guided by the immunostaining ($pSCRs_{immuno}$) with the one guided by the deep learning prediction ($pSCRs_{prediction}$) (Figure 27b). Here again, the similarity of the resulting segmentations was high as judged by visual inspection. We further validated the object-based correlation of $pSCR_{immuno}$ and $pSCR_{prediction}$ with the F1 score (Figure 27c), a quality metric widely used in image analysis to evaluate deep learning models.[206] For this, we compared $pSCR_{immuno}$ and $pSCR_{prediction}$ instance segmentations by identifying object-pairs and calculating their intersection over union (IOU; ratio of overlapping volume vs. combined volume). The F1 score as a function of IOU is a number between 0 and 1, where 1 implies perfect correlation. It takes into account precision (number of correctly segmented objects divided by number of all segmented objects) and recall (number of correctly segmented objects divided by number of all true objects). At an IOU=0.5 the F1 score of the deep learning model was 0.73, indicating high correlation. From this we concluded that pSCRs can indeed be reliably identified from the coCATS data only, when using an approach that takes into account the contextual information provided by the coCATS data.

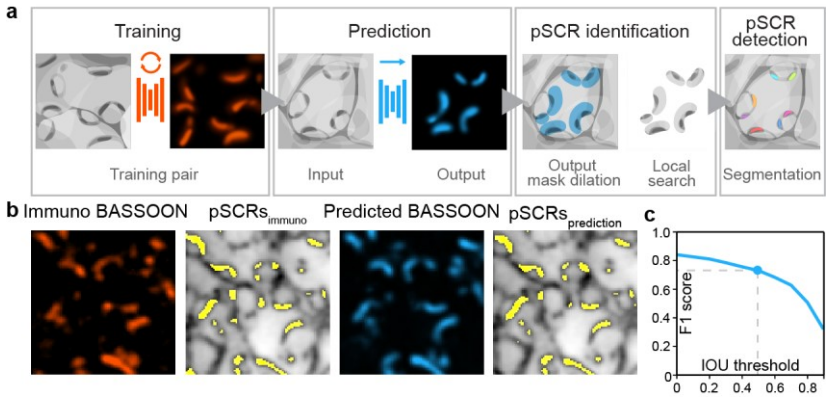


**Figure 27: Deep-learning-assisted identification of synapse location.** a) Scheme of pSCR detection without immunostaining based on a deep-learning network trained on coCATS and matched synaptic marker datasets. b) Comparison of BASSOON immunostaining (orange) and BASSOON predicted by the trained deep learning model (blue), as well as resulting pSCR segmentations (yellow) on coCATS data. c) Quantification of similarity between pSCRs segmention guided by immunostained vs. predicted BASSOON data. Adapted from Michalska *et al.*, 2022[155].

More detailed information on parameters used for the training can be found in Appendix Section 6.3.1.2, IV.7.4 Validation of deep-learning-based synapse prediction.

Labeling of molecular markers in chemically fixed tissue inadvertently leads to additional processing steps, which might negatively affect (ultra-)structural preservation of the tissue, as well as CATS labeling. Specifically, I have found that (detergent) permeabilization markedly decreases the quality of coCATS data. This is likely due to the solubilization and extraction of lipids, and thus membrane-bound proteins, as well as other molecules that are not sufficiently immobilized by FA-fixation.[161,207,208] Hence, being able to reliably identify synapses without the need for molecular labeling, as suggested by this pipeline for deep-learning-assisted prediction of pSCR location, is an exciting avenue to gain insights into the connectivity of well-preserved samples with light microscopy.

To test the pipeline for deep-learning-assisted prediction of pSCR location, we identified pSCRs in the coCATS dataset used for the manual segmentation of the CA3 PN proximal dendrite shown in Figure 23. This dataset did not contain any staining for molecular markers. We used the trained model to predict the molecular marker BASSOON (predicted BASSOON) from the coCATS data. Strong predicted BASSOON signal was visible in MFB structures in close proximity to the PN proximal dendrite and was associated with coCATS high-intensity signals, as expected (Figure 28a). We segmented pSCRs guided by the predicted BASSOON signal (predicted pSCRs) and I proofread them manually (proofread pSCRs) (Figure 28b-d). The most common error was non-detected pSCRs, which were manually added (*a*).

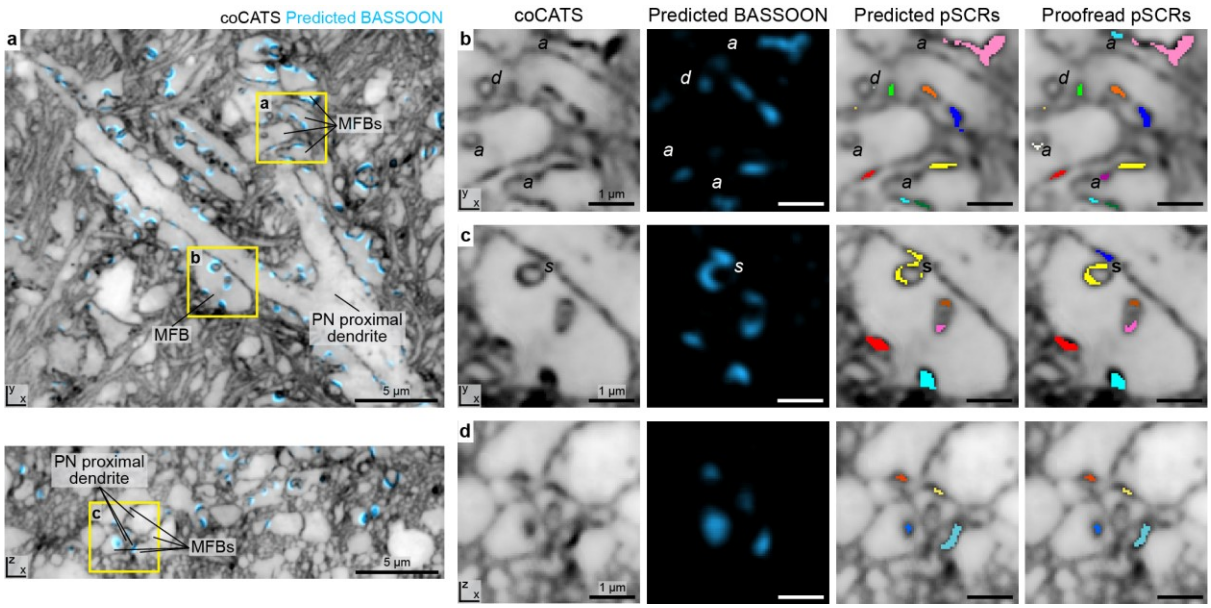


**Figure 28: Automated segmentation of MFB pSCRs without immunostaining.** Data was acquired in a cultured organotypic hippocampal slice, coCATS labeled with NHS-STAR RED, immersion-fixed and super-resolved with STED using a 100x silicone objective, NA 1.35. a) Single *xy*- and *xz*-plane of a volumetric dataset showing a CA3 PN proximal dendrite in its local environment elucidated by coCATS labeling (grey, *z*-STED, N2V). Super-resolved BASSOON signal predicted from the coCATS data by a deep learning model is displayed in cyan. b-d) Zoom-ins on MFBs indicate the association between coCATS high intensity and predicted BASSOON signals. PSCRs were segmented based on the predicted BASSOON signal and manually proofread. Proofreading operations included addition (*a*), deletion (*d*), splitting (*s*) and merging (not shown) of pSCR objects. Adapted from Michalska *et al.*, 2022[155].

Limitations & future prospects

As I was interested in identifying pSCRs associated with the DG GC-CA3 PN synapse, the model for deep-learning-assisted prediction of pSCR location was exclusively trained on datasets from the CA3 *stratum lucidum* of the adult mouse after *in vivo* microinjection of coCATS dye. Figure 28 shows that this model is still capable of predicting pSCRs from coCATS data obtained from coCATS immersion-labeled organotypic slice cultures in the same brain region. This is remarkable, as cultured slices differ from the native brain of an adult mouse in various aspects. Firstly, they display a different developmental stage than adult mouse brains, which likely results in differences in synaptic maturity, as well as ECM composition. Studies have shown that the developmental changes of the mossy fiber circuitry in cultured slices closely resemble those *in vivo*, such that the obtained data would be most comparable to a ~P25 mouse brain.[209] Secondly, cultured slices go through extensive remodeling of their circuitry due to the loss of many natural connections resulting from the excision of the hippocampus. Thirdly, clearing of damaged cells after the cutting procedure, as well as a changed local environment provided by the culture medium, might lead to changes in the ECS distribution of the cultured slice.

As I have mainly focused on the study of the DG GC-CA3 PN synapse, I have not yet established how well the trained model will perform in predicting the location of other types of synapses. The DG GC-CA3 PN synapse exhibits a characteristic shape, size, as well as local environment, such that a model trained on data mostly containing this type of synapse might not generalize to other synaptic structures. Of particular interest here are the excitatory synapses formed between MFB filopodia and GABAergic neurons, as well as inhibitory synapses between CA3 interneurons and CA3 PNs providing feed-forward inhibition. I have established that all of these synapses display pSCRs. As a next step, it would be exciting to test whether models that were trained with data containing molecular markers for excitatory and inhibitory synapses can identify and distinguish the location of these different synapse types.
Further, an exciting avenue is to develop this pipeline further with the aim of accurately predicting synapse locations in brain areas other than the hippocampal CA3 region. As synapses, and therefore also pSCRs, are differentially shaped in other brain areas, for example the cerebral cortex, I expect that the training data would have to be extended to include these structures.

### 2.3.4 Analyzing local connectivity

The existence of synaptic contacts highlights true connections between neurons and is therefore a better predictor of synaptic connectivity than spatial proximity. The coCATS pipeline makes it possible to identify synapse locations via the presence of pSCRs with or without the use of a molecular marker for synapses. Hence, connectivity between neuronal structures can be inferred from coCATS data.

Connectivity can be identified in two ways, by two-way or three-way localization, dependent on the presence of segmented structures.

Two-way localization
This method is used to identify pSCRs associated with a singular previously segmented neuronal structure of interest. In the next step, associated pSCRs are used as a guide to neuronal structures that are synaptically connected with the previously segmented neuron.

First, the neuronal structure of interest is segmented from the coCATS data volume (main object). Then, all pSCRs in that coCATS volume are automatically segmented, as described in Section 2.3.3. The main object is dilated to execute a search in its close proximity. All pSCR segments harboring voxels that overlap with the dilated neuron segment are retained. Manual proofreading is performed to retain only the pSCRs that are directly related to the main object. The main object, the associated pSCR segments and the coCATS data are overlaid. The synaptic partners of the neuronal structure of interest are then identified in the coCATS data by their close proximity to the main object with a pSCR sandwiched in between. They are then manually segmented from the coCATS data.

*Example:* ***Reconstruction of the local output field of a DG granule cell presynapse.***

*I acquired a volumetric dataset in the CA3 stratum lucidum of a cultured organotypic hippocampal slice. A single DG GC was positively labeled by whole-cell patch-clamping and biocytin-filling. The sample was bathed in coCATS labeling solution, followed by immersion fixation, mild permeabilization and incubation with a biocytin readout probe (fluorophore-conjugated streptavidin). I acquired a near-isotropically resolved volumetric dataset containing coCATS and positive label with STED microscopy (z-STED), focusing on a single giant MFB. The MFB was reconstructed from the super-resolved positive label by Otsu thresholding. To identify all postsynaptic partners of the MFB, I performed two-way localization. After automatically segmenting pSCRs with the deep-learning-assisted pipeline described in Section 2.3.3.2, I identified all pSCRs that were associated with the segmented MFB. I then*

*manually identified all neuronal structures connected to the giant MFB by pSCRs. These structures were then manually segmented. This way, I was able to reconstruct the synaptic output field of a single MFB (Figure 29). The main postsynaptic partner of the giant MFB was a CA3 PN (mint color).*

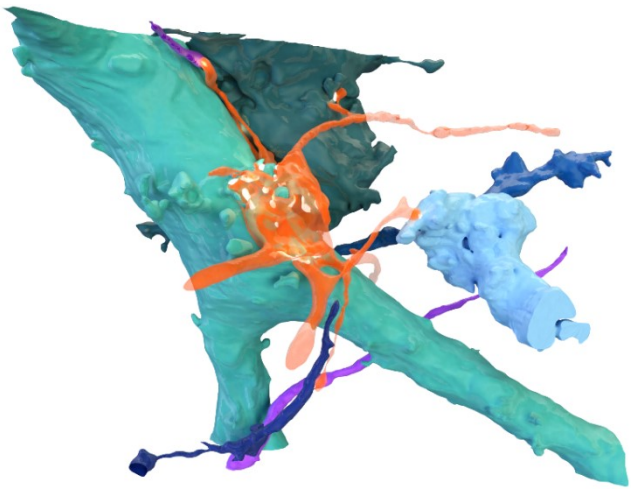

*Multiple PN complex spines were enwrapped by the main body of giant MFB. Filopodia emanating from the MFB body targeted eight additional neuronal structures, including thin processes and complex somatic shapes.*

**Figure 29: Reconstruction of a MFB and its postsynaptic partners.** 3D rendering of a DG granule cell giant MFB (orange) and its nine postsynaptic partners identified by the presence of pSCRs (white) with two-way localization.

Three-way localization

This method is used to clarify the relationship between multiple previously segmented cellular structures via the presence of pSCRs. First, multiple structures are manually segmented from a coCATS dataset (neuron segments). The neuron segments are classified into two groups: presynaptic and postsynaptic. Then, all pSCRs in that dataset are automatically segmented, as described in Section 2.3.3. Next, the pSCR segments are dilated to execute a local search for neuron segments in their close proximity. For each pSCR, a list each of pre- and postsynaptic segments that display a spatial overlap with the dilated pSCR mask is created. If there is more than one overlapping pre- or postsynaptic segment, the segment with the larger overlap is retained. Manual proofreading is performed to verify the alignment of the segments (pre- and postsynaptic segments have to be juxtaposed with a pSCR segment sandwiched in between).

*Example:* ***Identification of synaptic interactions between a CA3 PN proximal dendrite and its presynaptic partners***

*I acquired a volumetric dataset in a cultured organotypic hippocampal slice containing a piece of proximal dendrite of a CA3 PN, which was positively labeled by whole-cell patch-clamping and dye-filling, followed by coCATS labeling and immersion fixation. The coCATS signal was near-isotropically super-resolved (z-STED), while the positive label was acquired in confocal mode. In the coCATS data, I identified the PN and all structures that were synaptically connected to it through pSCRs. The PN was segmented from the coCATS data, whereas the positive label was used for guidance. Presynaptic neuronal structures were segmented purely from the coCATS data. I limited the analysis of presynaptic structures to MFBs. I identified MFBs based on their morphology (bulbous enlargement in close proximity to the proximal dendrite), presence of pSCRs (one or multiple contacts with PN spines) and tissue organization (an axon running alongside other axons in a mossy fiber bundle). Instance segmentations of all complex spines were generated by detaching them from the main PN branch. In the next step, all pSCRs in the dataset were segmented by using the deep-learning-assisted pipeline described in Section 2.3.3.2. Three-way localization was performed to characterize how many MFBs were connected with each complex spine and vice versa. For that, pSCR masks were dilated. A list of all complex spine segments and all MFB segments exhibiting overlap with every single pSCR segment was created. If more than one complex spine or MFB displayed overlap with one pSCR, the structure with the bigger overlap was chosen. This way, I characterized the connectivity pattern between a CA3 PN and its presynaptic partners (Figure 30, top). The displayed giant MFB connected to the CA3 PN through one TE, as*

*well as through a small complex spine in close proximity. While the MFB contacted the TE through 12 pSCRs, only a single synaptic contact was present between the MFB and the small complex spine.*

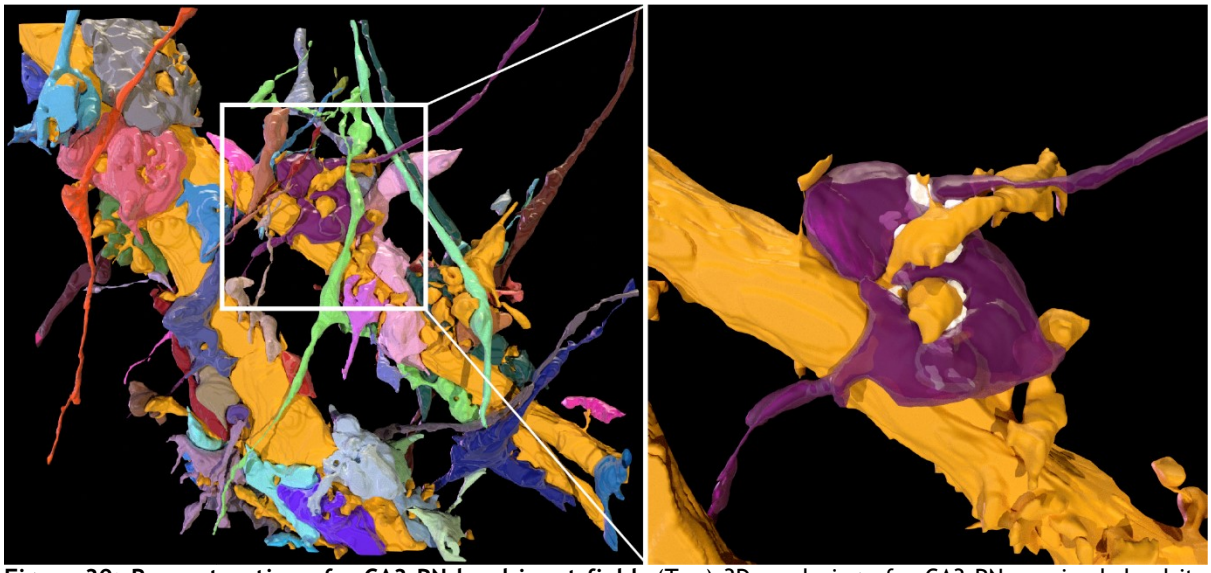

**Figure 30: Reconstruction of a CA3 PN local input field.** (Top) 3D-rendering of a CA3 PN proximal dendrite (yellow) and 56 synaptically connected neuronal structures. (Bottom) Zoom-in on a single MFB (purple) in contact with a PN TE via pSCRs (white).

Limitations & future prospects

Determining neuronal connectivity by automated association of pre- and postsynaptic partners via pSCRs is a powerful step towards being able to study neuronal circuitry in an unbiased fashion with light microscopy.

Currently, the main limitation for achieving this goal is the need for manual segmentation, as previously discussed (see Section 2.3.2). As manual segmentation is time-consuming, I focused on analyzing local connectivity rather than performing dense reconstructions of whole datasets. The study of synaptic input and output fields of single cells was facilitated by their electrophysiological characterization and intracellular labeling. However, a positive label is not necessary to identify synaptically connected structures from coCATS data.

It would be even more exciting to evaluate the connectivity of all neurons in a dataset, without *a priori* focus on a specific cell. To do so, one needs to pair the automated association of pre- and postsynaptic partners via pSCRs with an efficient reconstruction or tracing of all neuronal structures in that dataset.

To my current knowledge, coCATS high-intensity regions only appear in synaptic cleft regions of chemical synapses. To study other types of connections between neurons, including electrical synapses, additional molecular markers are needed.

# 3 Studying the hippocampal circuitry with CATS

Using the tools developed in Section 2, I set out to quantify key parameters of the hippocampal circuitry, mainly focusing on the DG GC-CA3 PN synapse.

## 3.1 Analyzing MFBs synaptic transmission properties

As my first biological application, I focused on studying the architecture and synaptic output structure of giant MFBs with coCATS. I performed *in vivo* microinjections of the coCATS labeling compound into the LV of adult wildtype (wt) mice to introduce extracellular contrast into the CA3 region. After FA-fixation via transcardial perfusion, the brains were sliced and immunostained for the presynaptic marker BASSOON and the postsynaptic marker SHANK2. I acquired 3 volumetric datasets (~30 x 30 x 12 µm$^3$ each, 2 animals) using $z$-STED mode, thus super-resolving the coCATS and SHANK2 signal, and acquiring BASSOON in confocal mode. 10 MFBs per dataset were randomly chosen and manually segmented. Next, I used the pipeline for the automated pSCR segmentation guided by immunostaining (see Section 2.3.3.1) to segment all pSCRs in the volumetric datasets. I identified all pSCR objects associated with the segmented MFBs and proofread them manually. To analyze the dependency between MFBs and pSCRs, I also identified parts of the MFB surface area that are occupied by pSCRs ($A_{pSCR/MFB}$). Figure 31a shows 3D-renderings of all 30 reconstructed MFBs including the $A_{pSCR/MFB}$ in white.

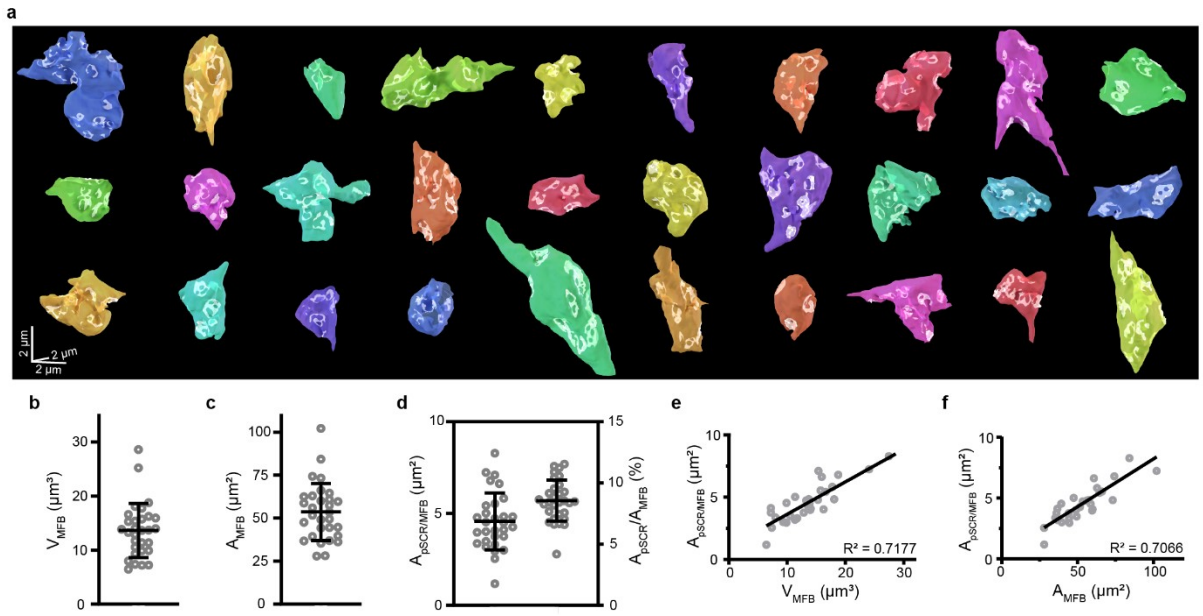


**Figure 31: Quantifying MFB synaptic transmission properties.** 30 MFBs were quantified from 3 near-isotropically resolved volumetric datasets (z-STED) acquired in the CA3 *stratum lucidum* of adult wt mice after coCATS *in vivo* microinjection, perfusion-fixation and immunostaining for pre- and postsynaptic markers. a) 3D-rendering of 30 manually segmented MFBs. MFB surface areas occupied by pSCRs are indicated in white. 3D-scale bar refers to MFB centers. b-d) Quantification of MFB volume ($V_{MFB}$), MFB surface area ($A_{MFB}$), as well as absolute ($A_{pSCR/MFB}$) and relative ($A_{pSCR}/A_{MFB}$) MFB surface area occupied by pSCRs. e,f) $A_{pSCR/MFB}$ as a function of MFB volume and surface area with linear regression. Adapted from Michalska *et al.*, 2022[155].

The volume of the MFBs ($V_{MFB}$) was 13.6±5.0 µm$^3$ (mean ± standard deviation (s.d.), n=30), but MFBs varied substantially in size and shape (Figure 31a,b). This value is in good agreement with data obtained from the adult mouse with SBEM, reporting a mean volume of 13.5 µm$^3$ (see Table

1).[150] Interestingly, another EM study conducted in the adult rat found a significantly smaller mean MFB volume of 8.24 $\mu m^3$ (see Table 1).[149,153] This might be due to studying a different species, difference in area sampled or it might simply reflect the high variability of MFB properties. The MFB surface area ($A_{MFB}$) in this study was 53.5±16.6 $\mu m^2$ (mean ± s.d., n=30) (Figure 31c). This value is also comparable to previously reported numbers (see Table 1), even though it does not take into account the surface area of filopodia, which were not reconstructed. Next, I wondered whether the MFB surface area occupied by pSCRs might resemble the organization of MFB AZs. The mean total MFB surface area occupied by pSCRs ($A_{pSCR/MFB}$) was 4.6±1.6 $\mu m^2$ (Figure 31c). PSCRs exhibited diverse shapes, often forming ring-like or fenestrated structures. A previous study found that the mean MFB surface area occupied by AZs was 2.10 $\mu m^2$, but this study analyzed smaller MFBs.[149] To normalize the results to MFB size, I calculated the fraction of MFB surface area occupied by pSCRs ($A_{pSCR}/A_{MFB}$). I found that on average 8.6±1.7 % (mean ± standard deviation) of the MFB surface area was occupied by pSCRs (Figure 31d). This value displayed smaller spread compared to the total MFB surface area occupied by pSCRs $A_{pSCR/MFB}$, hinting towards a correlation between MFB size and the extent of synaptic release sites. The mean fraction was in good agreement with previous quantifications of MFB surface area occupied by AZs (9.7%) (see Table 1), speaking in favor of a correlation between pSCRs and MFBs.[149] Indeed, when analyzing the relationship between MFB size and $A_{pSCR/MFB}$, I found a strong linear correlation between MFB volume and $A_{pSCR/MFB}$ (Pearson correlation r=0.844, 95% confidence interval: 0.694-0.923, p-value<0.0001, R-squared ($R^2$)=0.72, n=30), as well as between MFB surface area and $A_{pSCR/MFB}$ (Pearson correlation r=0.841, 95% confidence interval: 0.689-0.922, p-value<0.0001, $R^2$=0.71, n=30) (Figure 31d,e). This indicates that larger MFBs engage more extensively in synaptic contacts. These findings are corroborated by a study showing that MFB growth is accompanied by an increase in AZ contents in a linear fashion, both in slice cultures and *in vivo*.[209]

Surprisingly, the correlation between MFB size and pSCR number was markedly lower. The mean pSCR number was 13.0±5.9 (mean ± s.d.), slightly lower than previously reported, and exhibited large variation (3-28 pSCRs per MFB).[149,150] This might indicate that the number of transmission sites per MFB is under less stringent control than the surface area of the MFB used for synaptic transmission. Of note, pSCRs that were located closer to one another than the resolution used in this study were most likely merged, creating a bias towards lower pSCR counts. Still, previous EM studies have found that while the distance between MFB AZs varied widely, it typically exceeded 200 nm. This value is bigger than our estimated resolution, such that we expect to have resolved the majority of pSCRs accurately.[149]

In summary, analyzing the synaptic transmission properties of MFBs in CA3 *stratum lucidum*, I found a correlation between the size of MFBs and their contact area to pSCRs, likely representing a relationship between MFB architecture and synaptic strength.

## 3.2 Studying the connectivity pattern of DG GC-CA3 PN synapses

Moving beyond the characterization of the presynaptic component of the DG GC-CA3 PN synapse, I aimed at analyzing the connectivity pattern between MFBs and their postsynaptic partners. Focusing on a single PN proximal dendrite, we reconstructed its entire local input field, by segmenting all its presynaptic partners (Figure 32a). To do so, single CA3 PNs were whole-cell patch clamped and dye-filled, followed by coCATS labeling and immersion fixation. I super-resolved the local environment of the positively labeled PN with STED microscopy (ϰ-STED). Next, we manually segmented the positively labeled proximal dendrite, including 68 spines. Besides multiple large, branched TEs, I found that the dendrite exhibited many smaller, non-branched spines (Figure 32b). Guided by pSCRs, we segmented all structures that were synaptically connected to the proximal dendrite. From 56 presynaptic structures, I identified 43 as MFBs, based on their structure, the presence of pSCRs, as well as the presence of an axon running parallel to other axons in a mossy fiber tract (Figure 32b).

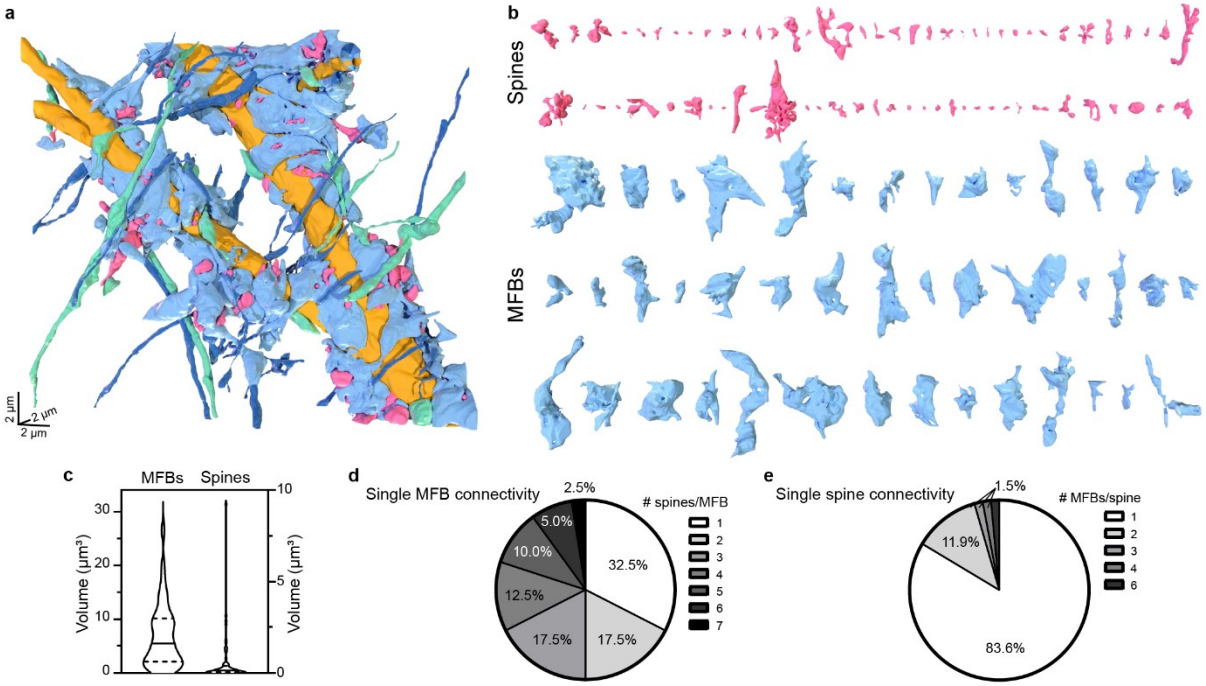


**Figure 32: Analyzing the synaptic input field of a CA3 PN.** A single CA3 PN in a cultured organotypic hippocampal slice was whole-cell patch-clamped and dye-filled, followed by coCATS labeling, immersion fixation and STED-imaging. a) 3D-reconstruction of the CA3 PN proximal dendrite (gold), its spines (magenta), as well as all connected presynaptic, grouped as MFBs (light blue), MFB axons and filopodia (dark blue), and non-MFB structures (turquoise). b) 3D rendering of 68 spines (magenta) and 43 MFBs (light blue) used for DG CG-CA3 PN connectivity analysis. c) Violin plot of MFB (n=43) and spine (n=68) volumes. d) Analysis of connectivity of each d) MFB (n=43) and e) PN spine (n=68). Adapted from Michalska *et al.*, 2022[155].

Upon quantification, I found that the size distribution of PN spines was strongly skewed towards small volumes, indicating that only few postsynaptic structures were in fact TEs (Figure 32c). I analyzed the connectivity pattern between the pre- and postsynaptic structures. Interestingly, I found that only ⅓ of all reconstructed MFBs contacted only a single spine. More commonly, MFBs contacted multiple, up to 7 spines. Often, a MFB would form multiple pSCRs with one or more TEs, and one additional pSCR with a closely located small spine (Figure 32d). On the contrary, most spines (83.6 %) formed a single synaptic connection with their presynaptic partners. Only large spines, which can be classified as TEs, were engulfed by more than one MFB (Figure 32e).

Summarizing, these results show that while MFBs commonly connect with more than one spine on the same postsynaptic cell, most spines are only contacted by single MFBs, with the exception of TEs, which receive input from multiple MFBs.
These results should be validated by *in vivo* studies to ensure that they are not biased by the developmental stage of the slice culture. Further, it would be of interest to determine whether single MFBs form excitatory connections with more than one PN.

# 3.3 Reconstructing the output field of a DG GC

Next, I used coCATS to gain insights into the synaptic output field of the main axon of a DG GC. For this, I used organotypic hippocampal slice cultures. Single DG GCs were whole-cell patch-clamped and biocytin-filled. After that, I introduced extracellular contrast by coCATS labeling, immersion-fixed the sample and visualized the intracellular biocytin by using a STED-compatible fluorophore-conjugated streptavidin. I performed overview imaging of the whole cell to identify conspicuous MFB structures along the main axon projecting through the DG hilus into the CA3 *stratum lucidum* (Figure 33a).

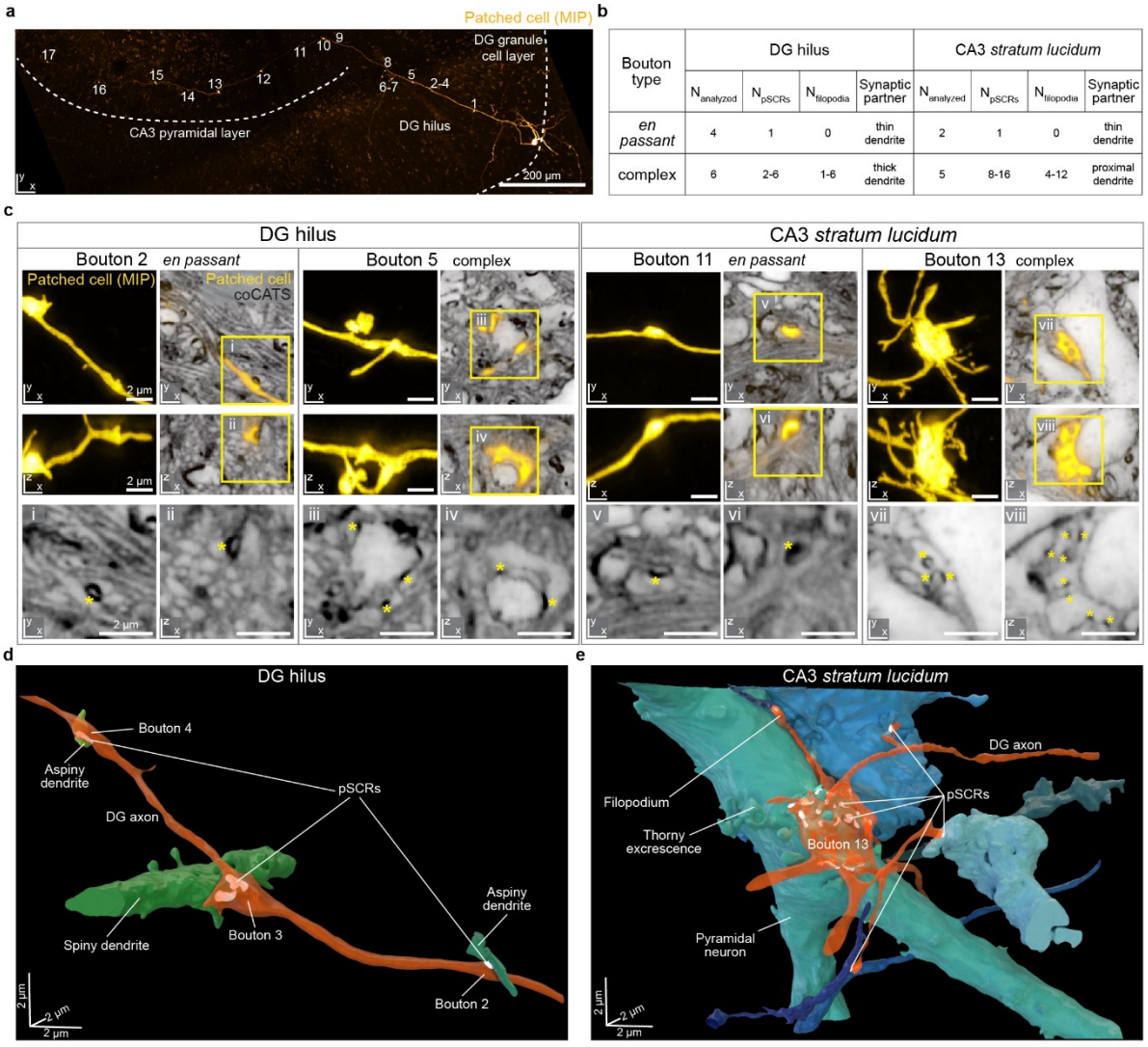


**Figure 33: Synaptic output structure of a DG granule cell mossy fiber.** A single DG GC in a cultured organotypic hippocampal brain slice was whole-cell patch-clamped and biocytin-filled. After coCATS labeling, the sample was immersion-fixed, and the biocytin was read out with a fluorophore-conjugated streptavidin. a) Maximum intensity projection (MIP) of the positively labeled GC projecting through the DG hilus into the CA3, imaged with a spinning disk confocal microscope at low resolution (20x air objective, NA 0.75). 17 identified MFBs are marked. b) Characteristic of the identified MFBs. c) Single *xy*- and *xz*-planes, including zoom-ins of four positively labeled MFBs (yellow) in their local environment elucidated with coCATS (grey). Both channels were super-resolved with z-STED and denoised using N2V (100x silicone objective, NA 1.35). PSCRs are marked with asterisks. Adapted from Michalska *et al.*, 2022[155].

I identified 17 MFBs, which I super-resolved by volumetric z-STED imaging of both the intracellular and the coCATS label. The main structural characteristics of the MFBs in the two different brain areas are summarized in Figure 33b. As previously described, I found two different

types of MFBs both in the DG hilus and the CA3 *stratum lucidum*. *En passant* boutons were small and did not possess filopodia. With the help of coCATS, I found that these boutons were connected to single postsynaptic partners via one pSCR. Complex spines were substantially bigger in size, associated with multiple pSCRs and possessed one or more filopodia (Figure 33b,c). Complex spines exhibited more complex shapes, a higher number of pSCRs and filopodia in the CA3 *stratum lucidum* than in the DG hilus. Using coCATS, I studied the MFBs in their structural context, including their postsynaptic partners. *En passant* boutons exclusively contacted thin dendrites, both in the DG hilus and in the CA3 *stratum lucidum*. Complex spines formed synaptic connections with thick dendrites, likely belonging to mossy cells, in the DG hilus. In the CA3 *stratum lucidum*, they were located in close proximity to PN proximal dendrites (Figure 33c). I reconstructed the local output fields of MFBs in the DG hilus (Figure 33d) and in the CA3 *stratum lucidum* (Figure 33e) from the coCATS data. Bouton 13, a giant MFB located in the CA3 *stratum lucidum*, formed numerous connections with spines on the proximal dendrite of a PN. In addition, numerous filopodia extending from the MFB body targeted 8 additional structures, ranging from long processes to neuronal somata (Figure 33e).

These data show that it is possible to analyze the output circuitry of single neurons with coCATS. Building on this work, the next step would be to reconstruct the postsynaptic partners of all identified MFBs to thoroughly characterize the connectivity of this GC. In addition, it would be beneficial to elucidate the cellular identity of all connected neurons.

# 4 Outlook

For my PhD project, I developed CATS, a toolbox for the interrogation of nervous tissue organization with (super-resolution) light microscopy. CATS involves labeling tools for the fluorescent contrasting of the ECS in fixed brain specimens in combination with molecular markers, protocols for super-resolution imaging with STED and ExM, as well as analysis pipelines for the study of morphological properties and connectivity. It is a versatile technology, as it facilitates the study of diverse brain sample types commonly used in scientific research across various spatial scales, ranging from regional down to single synapse scale.

CATS is the first technology enabling the visualization of the brain ECS with light microscopy in fixed specimens. Compared to previous approaches, which are limited to living tissue, such as SUSHI and LIONESS, this bares multiple advantages. Firstly, CATS is highly compatible with standard molecular labeling techniques. While I mainly focused on staining of protein targets, I expect that it will pair easily with the localization of other molecular entities. Secondly, CATS gives access to extended sample volumes when paired with clearing and/or expansion strategies. Thirdly, CATS provides access to specimens which cannot be visualized by live imaging, for example human clinical tissue. Fourthly, CATS allows the study of brain tissue close to its native state. While SUSHI and LIONESS utilize freely diffusible fluorophores, fluorophores are immobilized in the extracellular compartment in the CATS labeling approach.[29,133] This is of disadvantage, as photobleaching of immobilized fluorophores will degrade image quality and resolution. In addition, the fixation procedure can result in the creation of artifacts, such as cell swelling and ECS loss. These limitations and possible solutions have been described in detail in Section 2.1.1.1. Labeling the ECS creates a natural border between cellular structures that remain free of intracellular complexity, which is advantageous for the study of tissue organization and connectivity analysis. For example, while at confocal resolution a pan-protein stain provides little information on (sub) cellular organization[98], CATS reveals the gross morphology of all cellular constituents in brain tissue by extracellular contrasting. Yet, at higher resolutions, limited signal intensity of the CATS label can become a problem. This is likely due to two factors. Firstly, the initial labeling has to be performed before the expansion procedure and is thus limited by molecular crowding. Secondly, the amount of labeling targets, in this case mainly primary amines on proteins, is substantially lower in the ECS than in the ICS. Thus, when compared to membrane/protein contrasting techniques, such as the pan-protein stain[98,99], an extracellular label will likely provide lower signal, especially in combination with high expansion factors.

CATS is a great tool for studies of brain tissue organization that do not necessitate single-nm resolution, currently only provided by EM. In comparison with EM, the sample preparation is straightforward and the imaging procedure is time-efficient. For example, the hands-on sample-preparation time for obtaining a super-resolved dataset after coCATS *in vivo* microinjection is ~4-5 h, including the injection procedure, transcardial perfusion, tissue slicing and labeling of molecular markers. The acquisition time of a 30 x 30 x 12 µm volumetric dataset containing 3 color channels is ~1.5 h with a commercial STED microscope. As confocal and STED imaging provides optical sectioning, there is no need for data alignment. The resulting datasets are also substantially smaller, mainly due to the bigger voxel sizes, and therefore easier to handle.

While CATS holds great potential for light microscopy-based connectomics, it is of importance to point out that higher resolution is necessary to reach this goal. As previously discussed, this can theoretically be achieved by using higher expansion factors, although this will lead to substantial signal dilution. Using (near-isotropic) light sheet microscopy can solve the problem of imaging throughput. An additional bottleneck for connectomics studies is the segmentation of the data. Automated segmentation pipelines, as well as semi-automated proofreading tools, will need to be implemented to create dense segmentations in a reasonable amount of time (see Section 2.3.2).

There are many other exciting avenues for utilizing the CATS toolbox.
CATS is compatible with functional readouts, for example electrophysiological recordings, such that it is a great tool to study cellular structure-function relationships. I also expect it to pair well with other approaches for studying neuronal activity and connectivity, including calcium imaging and viral tracing.[103,210]
In combination with spatial multi-omics approaches, including transcriptomics[211,212], translatomics[213] and proteomics[214,215], CATS is capable of providing contextual information needed for the profiling of brain tissue across various scales. On a large scale, CATS would allow researchers to unambiguously localize transcripts in their respective cellular compartments to phenotype whole tissues at single-cell resolution.[213,216–219] At high resolution, for example by combining spatial transcriptomics approaches with ExM[220,221], CATS could provide subcellular structural context to study local translation in neuronal compartments, such as dendrites and synapses.[222]
As CATS provides an unbiased readout of brain tissue organization, it could further be used to study changes in brain architecture and synaptic connectivity during development, neuronal activity and disease. For developmental studies, coCATS might be better suited, as it does not depend on the distribution of ECM components. RCATS, on the other hand, may have the potential to shed light on changes in the ECM associated with aging and neurological disease, including epilepsy, dementia and Alzheimer's disease, specifically in human clinical tissue.[174,223]
Another exciting avenue lies in the combination of CATS with live imaging for the study of dynamic processes. For example, we have recently developed LIONESS as a tool to study changes in synapse morphology in organotypic slice cultures.[29] Pairing this approach with coCATS would allow a more in-depth characterization of the synapse, for example by using molecular markers to characterize synaptic composition. This way, one could study structural plasticity in a molecularly informed fashion.
The brain ECS, which surrounds all cellular constituents, takes up ~20 % of the brain volume.[133,162,224] It forms a reservoir for molecules that is essential for cellular signaling, metabolite clearance, as well as electrical activity. Further, it houses the ECM, which plays a major role in scaffolding and cellular homeostasis.[154,225] The ECS is highly dynamic, displaying geometric changes in response to neuronal activity and, as part of the glymphatic system, circadian rhythm and sleep.[225] Despite its evident importance for brain functioning, the ECS is poorly understood, mainly due to limitations in the technologies currently used to probe it. As CATS labels the extracellular compartment, it may serve as a tool to study the organization and function of the ECS itself. For this, it will be necessary to optimize fixation conditions to ensure that the ECS is preserved adequately. Then, CATS could be used to assess the geometry and distribution of the ECS, as well as the ECM, across brain regions, with the aim of understanding how its shape and composition affects the diffusional transport of molecules.
For my thesis, my main interest lay in studying the brain, as it houses some of the most intricate and complex structures in the body. Yet, CATS can also be used to shed light on the organization of tissues other than the brain. Infused into the ECS of mouse organs, including kidney, liver, spleen and thymus, coCATS creates rich extracellular contrast, visualizing the morphology of those tissues from whole region down to subcellular level. In combination with a readout of cellular identities, this approach may prove useful to create in-depth profiles of those organs, for example in the form of a reference atlas.

# 5 Bibliography


1. Hell, S. W. & Wichmann, J. Breaking the diffraction resolution limit by stimulated emission: stimulated-emission-depletion fluorescence microscopy. *Optics Letters* **19**, 780 (1994).
2. Klar, T. A., Jakobs, S., Dyba, M., Egner, A. & Hell, S. W. Fluorescence microscopy with diffraction resolution barrier broken by stimulated emission. *PNAS* **97**, 8206–8210 (2000).
3. Chen, F., Tillberg, P. W. & Boyden, E. S. Expansion microscopy. *Science* **347**, 543–548 (2015).
4. Gallagher, B. R. & Zhao, Y. Expansion microscopy: A powerful nanoscale imaging tool for neuroscientists. *Neurobiology of Disease* **154**, 105362 (2021).
5. Abbe, E. Beiträge zur Theorie des Mikroskops und der mikroskopischen Wahrnehmung. *Archiv f. mikrosk. Anatomie* **9**, 413–418 (1873).
6. Weiss, S. Shattering the diffraction limit of light: A revolution in fluorescence microscopy? *Proceedings of the National Academy of Sciences* **97**, 8747–8749 (2000).
7. Bond, C., Santiago-Ruiz, A. N., Tang, Q. & Lakadamyali, M. Technological advances in super-resolution microscopy to study cellular processes. *Molecular Cell* **82**, 315–332 (2022).
8. Perge, J. A., Niven, J. E., Mugnaini, E., Balasubramanian, V. & Sterling, P. Why Do Axons Differ in Caliber? *Journal of Neuroscience* **32**, 626–638 (2012).
9. Zuber, B., Nikonenko, I., Klauser, P., Muller, D. & Dubochet, J. The mammalian central nervous synaptic cleft contains a high density of periodically organized complexes. *PNAS* **102**, 19192–19197 (2005).
10. Heintzmann, R. & Cremer, C. G. Laterally modulated excitation microscopy: improvement of resolution by using a diffraction grating. in *Optical Biopsies and Microscopic Techniques III* vol. 3568 185–196 (SPIE, 1999).
11. Manton, J. D. Answering some questions about structured illumination microscopy. *Philosophical Transactions of the Royal Society A: Mathematical, Physical and Engineering Sciences* **380**, 20210109 (2022).
12. Weisshart, K. The Basic Principle of Airyscanning. (2014).
13. Wu, X. & Hammer, J. A. ZEISS Airyscan: Optimizing usage for fast, gentle, super-resolution imaging. *Methods Mol Biol* **2304**, 111–130 (2021).
14. Jahr, W., Velicky, P. & Danzl, J. G. Strategies to maximize performance in STimulated Emission Depletion (STED) nanoscopy of biological specimens. *Methods* (2019) doi:10.1016/j.ymeth.2019.07.019.
15. Betzig, E. *et al.* Imaging Intracellular Fluorescent Proteins at Nanometer Resolution. *Science* **313**, 1642–1645 (2006).
16. Hess, S. T., Girirajan, T. P. K. & Mason, M. D. Ultra-High Resolution Imaging by Fluorescence Photoactivation Localization Microscopy. *Biophysical Journal* **91**, 4258–4272 (2006).
17. Rust, M. J., Bates, M. & Zhuang, X. Sub-diffraction-limit imaging by stochastic optical reconstruction microscopy (STORM). *Nature Methods* **3**, 793–796 (2006).
18. Heilemann, M. *et al.* Subdiffraction-Resolution Fluorescence Imaging with Conventional Fluorescent Probes. *Angewandte Chemie International Edition* **47**, 6172–6176 (2008).
19. Testa, I. *et al.* Multicolor Fluorescence Nanoscopy in Fixed and Living Cells by Exciting Conventional Fluorophores with a Single Wavelength. *Biophysical Journal* **99**, 2686–2694 (2010).
20. Sharonov, A. & Hochstrasser, R. M. Wide-field subdiffraction imaging by accumulated binding of diffusing probes. *Proc Natl Acad Sci U S A* **103**, 18911–18916 (2006).
21. Jungmann, R. *et al.* Single-Molecule Kinetics and Super-Resolution Microscopy by Fluorescence Imaging of Transient Binding on DNA Origami. *Nano Letters* **10**, 4756–4761 (2010).
22. Weber, M. *et al.* MINSTED fluorescence localization and nanoscopy. *Nat. Photonics* **15**, 361–366 (2021).
23. Weber, M. *et al.* MINSTED nanoscopy enters the Ångström localization range. *Nat Biotechnol* 1–8 (2022) doi:10.1038/s41587-022-01519-4.
24. Balzarotti, F. *et al.* Nanometer resolution imaging and tracking of fluorescent molecules with minimal photon fluxes. *Science* **355**, 606–612 (2017).
25. Dobrucki, J. W. & Kubitscheck, U. Fluorescence Microscopy. in *Fluorescence Microscopy* 85–132 (John Wiley & Sons, Ltd, 2017). doi:10.1002/9783527687732.ch3.
26. Lenz, M. O. & Tønnesen, J. Considerations for Imaging and Analyzing Neural Structures by STED Microscopy. *Methods Mol. Biol.* **1941**, 29–46 (2019).
27. Keller, J., Schönle, A. & Hell, S. W. Efficient fluorescence inhibition patterns for RESOLFT microscopy. *Opt. Express, OE* **15**, 3361–3371 (2007).
28. Wildanger, D., Medda, R., Kastrup, L. & Hell, S. W. A compact STED microscope providing 3D nanoscale resolution. *Journal of Microscopy* **236**, 35–43 (2009).
29. Velicky, P. *et al.* Saturated reconstruction of living brain tissue. 2022.03.16.484431 Preprint at https://doi.org/10.1101/2022.03.16.484431 (2022).
30. Harke, B. *et al.* Resolution scaling in STED microscopy. *Opt. Express, OE* **16**, 4154–4162 (2008).
31. Kilian, N. *et al.* Assessing photodamage in live-cell STED microscopy. *Nature Methods* **15**, 755–756 (2018).

32. Antonello, J., Burke, D. & Booth, M. J. Aberrations in stimulated emission depletion (STED) microscopy. *Opt Commun* **404**, 203–209 (2017).
33. Deng, S., Liu, L., Cheng, Y., Li, R. & Xu, Z. Effects of primary aberrations on the fluorescence depletion patterns of STED microscopy. *Opt. Express, OE* **18**, 1657–1666 (2010).
34. Heine, J. *et al.* Three dimensional live-cell STED microscopy at increased depth using a water immersion objective. *Review of Scientific Instruments* **89**, 053701 (2018).
35. Velasco, M. G. M. *et al.* 3D super-resolution deep-tissue imaging in living mice. *Optica, OPTICA* **8**, 442–450 (2021).
36. Sun, J., Lee, S. J., Wu, L., Sarntinoranont, M. & Xie, H. Refractive index measurement of acute rat brain tissue slices using optical coherence tomography. *Opt Express* **20**, 1084–1095 (2012).
37. Yang, J. *et al.* Improving the characterization of ex vivo human brain optical properties using high numerical aperture optical coherence tomography by spatially constraining the confocal parameters. *NPh* **7**, 045005 (2020).
38. Lue, N. *et al.* Tissue refractometry using Hilbert phase microscopy. *Opt Lett* **32**, 3522–3524 (2007).
39. Urban, N. T., Willig, K. I., Hell, S. W. & Nägerl, U. V. STED Nanoscopy of Actin Dynamics in Synapses Deep Inside Living Brain Slices. *Biophysical Journal* **101**, 1277–1284 (2011).
40. Gould, T. J., Burke, D., Bewersdorf, J. & Booth, M. J. Adaptive optics enables 3D STED microscopy in aberrating specimens. *Optics Express* **20**, 20998 (2012).
41. Bancelin, S., Mercier, L., Murana, E. & Nägerl, U. V. Aberration correction in stimulated emission depletion microscopy to increase imaging depth in living brain tissue. *NPh* **8**, 035001 (2021).
42. Tillberg, P. W. & Chen, F. Expansion Microscopy: Scalable and Convenient Super-Resolution Microscopy. *Annual Review of Cell and Developmental Biology* **35**, 683–701 (2019).
43. Gao, R. *et al.* Cortical column and whole-brain imaging with molecular contrast and nanoscale resolution. *Science* **363**, eaau8302 (2019).
44. Tillberg, P. W. *et al.* Protein-retention expansion microscopy of cells and tissues labeled using standard fluorescent proteins and antibodies. *Nature Biotechnology* **34**, 987–992 (2016).
45. Chozinski, T. J. *et al.* Expansion microscopy with conventional antibodies and fluorescent proteins. *Nature Methods* **13**, 485–488 (2016).
46. Ku, T. *et al.* Multiplexed and scalable super-resolution imaging of three-dimensional protein localization in size-adjustable tissues. *Nature Biotechnology* **34**, 973–981 (2016).
47. Chang, J.-B. *et al.* Iterative expansion microscopy. *Nature Methods* **14**, 593–599 (2017).
48. Sarkar, D. *et al.* Revealing nanostructures in brain tissue via protein decrowding by iterative expansion microscopy. *Nat. Biomed. Eng* 1–17 (2022) doi:10.1038/s41551-022-00912-3.
49. Truckenbrodt, S. *et al.* X10 expansion microscopy enables 25-nm resolution on conventional microscopes. *EMBO reports* **19**, e45836 (2018).
50. Truckenbrodt, S., Sommer, C., Rizzoli, S. O. & Danzl, J. G. A practical guide to optimization in X10 expansion microscopy. *Nature Protocols* **14**, 832–863 (2019).
51. Klimas, A. *et al.* Magnify is a universal molecular anchoring strategy for expansion microscopy. *Nat Biotechnol* 1–12 (2023) doi:10.1038/s41587-022-01546-1.
52. Park, H.-E. *et al.* Scalable and Isotropic Expansion of Tissues with Simply Tunable Expansion Ratio. *Advanced Science* **0**, 1901673 (2019).
53. Gao, R. *et al.* A highly homogeneous polymer composed of tetrahedron-like monomers for high-isotropy expansion microscopy. *Nature Nanotechnology* 1–10 (2021) doi:10.1038/s41565-021-00875-7.
54. Gambarotto, D. *et al.* Imaging cellular ultrastructures using expansion microscopy (U-ExM). *Nature Methods* **16**, 71 (2019).
55. Sun, D. *et al.* Click-ExM enables expansion microscopy for all biomolecules. *Nature Methods* 1–7 (2020) doi:10.1038/s41592-020-01005-2.
56. Shi, X. *et al.* Label-retention expansion microscopy. *J Cell Biol* **220**, e202105067 (2021).
57. Cui, Y. *et al.* A Multifunctional Anchor for Multimodal Expansion Microscopy. 2022.06.19.496699 Preprint at https://doi.org/10.1101/2022.06.19.496699 (2022).
58. Wen, G. *et al.* Evaluation of Direct Grafting Strategies via Trivalent Anchoring for Enabling Lipid Membrane and Cytoskeleton Staining in Expansion Microscopy. *ACS Nano* (2020) doi:10.1021/acsnano.9b09259.
59. Karagiannis, E. D. *et al.* Expansion Microscopy of Lipid Membranes. *bioRxiv* (2019) doi:10.1101/829903.
60. White, B. M., Kumar, P., Conwell, A. N., Wu, K. & Baskin, J. M. Lipid Expansion Microscopy. *J. Am. Chem. Soc.* jacs.2c03743 (2022) doi:10.1021/jacs.2c03743.
61. Wen, G. *et al.* A Universal Labeling Strategy for Nucleic Acids in Expansion Microscopy. *J. Am. Chem. Soc.* (2021) doi:10.1021/jacs.1c05931.
62. Shim, S.-H., Kim, D., Kim, T., Lee, J. & Kim, N. Amplified Expansion Stimulated Emission Depletion Microscopy. *ChemBioChem* (2019) doi:10.1002/cbic.201800775.
63. Maidorn, M., Olichon, A., Rizzoli, S. O. & Opazo, F. Nanobodies reveal an extra-synaptic population of SNAP-25 and Syntaxin 1A in hippocampal neurons. *mAbs* **11**, 305–321 (2019).

64. Zwettler, F. U. *et al.* Molecular resolution imaging by post-labeling expansion single-molecule localization microscopy (Ex-SMLM). *Nature Communications* **11**, 3388 (2020).
65. Ramon y Cajal, S. Estructura de los centros nerviosos de las aves. *Rev. Trim. Histol. Normal Patol.* 1:1-10 (1888).
66. Loomba, S. *et al.* Connectomic comparison of mouse and human cortex. *Science* **377**, eabo0924 (2022).
67. Montero-Crespo, M. *et al.* Three-dimensional synaptic organization of the human hippocampal CA1 field. *eLife* **9**, e57013 (2020).
68. Shapson-Coe, A. *et al.* A connectomic study of a petascale fragment of human cerebral cortex. *bioRxiv* 2021.05.29.446289 (2021) doi:10.1101/2021.05.29.446289.
69. Kasthuri, N. *et al.* Saturated Reconstruction of a Volume of Neocortex. *Cell* **162**, 648–661 (2015).
70. Motta, A. *et al.* Dense connectomic reconstruction in layer 4 of the somatosensory cortex. *Science* **366**, (2019).
71. Turner, N. L. *et al.* Reconstruction of neocortex: Organelles, compartments, cells, circuits, and activity. *Cell* (2022) doi:10.1016/j.cell.2022.01.023.
72. MICrONS Consortium *et al. Functional connectomics spanning multiple areas of mouse visual cortex*. http://biorxiv.org/lookup/doi/10.1101/2021.07.28.454025 (2021) doi:10.1101/2021.07.28.454025.
73. Svara, F. *et al.* Automated synapse-level reconstruction of neural circuits in the larval zebrafish brain. *Nat Methods* 1–10 (2022) doi:10.1038/s41592-022-01621-0.
74. Hildebrand, D. G. C. *et al.* Whole-brain serial-section electron microscopy in larval zebrafish. *Nature* **545**, 345–349 (2017).
75. Wanner, A. A., Genoud, C., Masudi, T., Siksou, L. & Friedrich, R. W. Dense EM-based reconstruction of the interglomerular projectome in the zebrafish olfactory bulb. *Nat Neurosci* **19**, 816–825 (2016).
76. Witvliet, D. *et al.* Connectomes across development reveal principles of brain maturation. *Nature* **596**, 257–261 (2021).
77. Cook, S. J. *et al.* Whole-animal connectomes of both Caenorhabditis elegans sexes. *Nature* **571**, 63–71 (2019).
78. White, J. G., Southgate, E., Thomson, J. N. & Brenner, S. The structure of the nervous system of the nematode Caenorhabditis elegans. *Philosophical Transactions of the Royal Society of London. B, Biological Sciences* **314**, 1–340 (1986).
79. Scheffer, L. K. *et al.* A connectome and analysis of the adult Drosophila central brain. *eLife* **9**, e57443 (2020).
80. Denk, W. & Horstmann, H. Serial Block-Face Scanning Electron Microscopy to Reconstruct Three-Dimensional Tissue Nanostructure. *PLOS Biology* **2**, e329 (2004).
81. Xu, C. S. *et al.* Enhanced FIB-SEM systems for large-volume 3D imaging. *eLife* **6**, e25916 (2017).
82. Hayworth, K. J. *et al.* Gas cluster ion beam SEM for imaging of large tissue samples with 10 nm isotropic resolution. *Nat Methods* **17**, 68–71 (2020).
83. Bosch, C. *et al.* Functional and multiscale 3D structural investigation of brain tissue through correlative in vivo physiology, synchrotron microtomography and volume electron microscopy. *Nat Commun* **13**, 2923 (2022).
84. Costantini, I. *et al.* A multimodal imaging and analysis pipeline for creating a cellular census of the human cerebral cortex. 2021.10.20.464979 Preprint at https://doi.org/10.1101/2021.10.20.464979 (2021).
85. Foxley, S. *et al.* Multi-modal imaging of a single mouse brain over five orders of magnitude of resolution. *Neuroimage* **238**, 118250 (2021).
86. Simon, A. *et al. Ultrastructural readout of* in vivo *synaptic activity for functional connectomics*. http://biorxiv.org/lookup/doi/10.1101/2021.07.07.451278 (2021) doi:10.1101/2021.07.07.451278.
87. Holler, S., Köstinger, G., Martin, K. A. C., Schuhknecht, G. F. P. & Stratford, K. J. Structure and function of a neocortical synapse. *Nature* 1–6 (2021) doi:10.1038/s41586-020-03134-2.
88. Lee, W.-C. A. *et al.* Anatomy and function of an excitatory network in the visual cortex. *Nature* **532**, 370–374 (2016).
89. Briggman, K. L., Helmstaedter, M. & Denk, W. Wiring specificity in the direction-selectivity circuit of the retina. *Nature* **471**, 183–188 (2011).
90. Bock, D. D. *et al.* Network anatomy and in vivo physiology of visual cortical neurons. *Nature* **471**, 177–182 (2011).
91. Begemann, I. & Galic, M. Correlative Light Electron Microscopy: Connecting Synaptic Structure and Function. *Frontiers in Synaptic Neuroscience* **8**, (2016).
92. Thomas, C. I. *et al.* Cryo-Confocal Imaging for CLEM Mapping in Brain Tissues. *Microscopy Today* **29**, 34–39 (2021).
93. Watson, M. L. Staining of Tissue Sections for Electron Microscopy with Heavy Metals. *J Biophys Biochem Cytol* **4**, 727–730 (1958).
94. Kuchenbrod, M. T., Schubert, U. S., Heintzmann, R. & Hoeppener, S. Revisiting staining of biological samples for electron microscopy: perspectives for recent research. *Mater. Horiz.* **8**, 685–699 (2021).
95. Reynolds, E. S. The use of lead citrate at high pH as an electron-opaque stain in electron microscopy. *J Cell Biol* **17**, 208–212 (1963).
96. Riemersma, J. C. Osmium tetroxide fixation of lipids: nature of the reaction products. *J Histochem Cytochem.* **11**, 436–442 (1963).
97. Kuan, A. T. *et al.* Dense neuronal reconstruction through X-ray holographic nano-tomography. *Nature Neuroscience* 1–7 (2020) doi:10.1038/s41593-020-0704-9.

98. M'Saad, O. & Bewersdorf, J. Light microscopy of proteins in their ultrastructural context. *Nature Communications* **11**, 3850 (2020).
99. Mao, C. *et al.* Feature-rich covalent stains for super-resolution and cleared tissue fluorescence microscopy. *Science Advances* **6**, eaba4542 (2020).
100. Qian, C. *et al.* Super-resolution label-free volumetric vibrational imaging. *Nat Commun* **12**, 3648 (2021).
101. Shi, L. *et al.* Super-Resolution Vibrational Imaging Using Expansion Stimulated Raman Scattering Microscopy. *Advanced Science* **9**, 2200315 (2022).
102. Chalfie, M., Tu, Y., Euskirchen, G., Ward, W. W. & Prasher, D. C. Green Fluorescent Protein as a Marker for Gene Expression. *Science* **263**, 802–805 (1994).
103. Wickersham, I. R., Finke, S., Conzelmann, K.-K. & Callaway, E. M. Retrograde neuronal tracing with a deletion-mutant rabies virus. *Nat Methods* **4**, 47–49 (2007).
104. Light, A. R. & Durkovic, R. G. Horseradish peroxidase: An improvement in intracellular staining of single, electrophysiologically characterized neurons. *Experimental Neurology* **53**, 847–853 (1976).
105. Buhl, E. H. & Schlote, W. Intracellular Lucifer Yellow staining and electron microscopy of neurones in slices of fixed epitumourous human cortical tissue. *Acta Neuropathol* **75**, 140–146 (1987).
106. Livet, J. *et al.* Transgenic strategies for combinatorial expression of fluorescent proteins in the nervous system. *Nature* **450**, 56–62 (2007).
107. Snippert, H. J. *et al.* Intestinal Crypt Homeostasis Results from Neutral Competition between Symmetrically Dividing Lgr5 Stem Cells. *Cell* **143**, 134–144 (2010).
108. Bardehle, S. *et al.* Live imaging of astrocyte responses to acute injury reveals selective juxtavascular proliferation. *Nat Neurosci* **16**, 580–586 (2013).
109. Sakaguchi, R., Leiwe, M. N. & Imai, T. Bright multicolor labeling of neuronal circuits with fluorescent proteins and chemical tags. *eLife* **7**, e40350 (2018).
110. Li, Y. *et al.* Bitbow: a digital format of Brainbow enables highly efficient neuronal lineage tracing and morphology reconstruction in single brains. *bioRxiv* 2020.04.07.030593 (2020) doi:10.1101/2020.04.07.030593.
111. Kitamura, K., Judkewitz, B., Kano, M., Denk, W. & Häusser, M. Targeted patch-clamp recordings and single-cell electroporation of unlabeled neurons in vivo. *Nat Methods* **5**, 61–67 (2008).
112. Gretz, J. E., Norbury, C. C., Anderson, A. O., Proudfoot, A. E. I. & Shaw, S. Lymph-Borne Chemokines and Other Low Molecular Weight Molecules Reach High Endothelial Venules via Specialized Conduits While a Functional Barrier Limits Access to the Lymphocyte Microenvironments in Lymph Node Cortex. *Journal of Experimental Medicine* **192**, 1425–1440 (2000).
113. Whish, S. *et al.* The inner CSF–brain barrier: developmentally controlled access to the brain via intercellular junctions. *Front Neurosci* **9**, (2015).
114. Godin, A. G. *et al.* Single-nanotube tracking reveals the nanoscale organization of the extracellular space in the live brain. *Nature Nanotechnology* **12**, 238–243 (2017).
115. Dani, A., Huang, B., Bergan, J., Dulac, C. & Zhuang, X. Superresolution imaging of chemical synapses in the brain. *Neuron* **68**, 843–856 (2010).
116. Liu, K. S. Y. *et al.* RIM-Binding Protein, a Central Part of the Active Zone, Is Essential for Neurotransmitter Release. *Science* **334**, 1565–1569 (2011).
117. Tang, A.-H. *et al.* A trans-synaptic nanocolumn aligns neurotransmitter release to receptors. *Nature* **536**, 210–214 (2016).
118. Siddig, S. *et al.* Super-resolution imaging reveals the nanoscale organization of metabotropic glutamate receptors at presynaptic active zones. *Science Advances* **6**, eaay7193 (2020).
119. Wilhelm, B. G. *et al.* Composition of isolated synaptic boutons reveals the amounts of vesicle trafficking proteins. *Science* **344**, 1023–1028 (2014).
120. Grabner, C. P. *et al.* Resolving the molecular architecture of the photoreceptor active zone with 3D-MINFLUX. *Science Advances* **8**, eabl7560 (2022).
121. Helm, M. S. *et al.* A large-scale nanoscopy and biochemistry analysis of postsynaptic dendritic spines. *Nat Neurosci* **24**, 1151–1162 (2021).
122. Xu, K., Zhong, G. & Zhuang, X. Actin, Spectrin, and Associated Proteins Form a Periodic Cytoskeletal Structure in Axons. *Science* **339**, 452–456 (2013).
123. Vassilopoulos, S., Gibaud, S., Jimenez, A., Caillol, G. & Leterrier, C. Ultrastructure of the axonal periodic scaffold reveals a braid-like organization of actin rings. *Nature Communications* **10**, 5803 (2019).
124. D'Este, E., Kamin, D., Göttfert, F., El-Hady, A. & Hell, S. W. STED Nanoscopy Reveals the Ubiquity of Subcortical Cytoskeleton Periodicity in Living Neurons. *Cell Reports* **10**, 1246–1251 (2015).
125. Tønnesen, J., Katona, G., Rózsa, B. & Nägerl, U. V. Spine neck plasticity regulates compartmentalization of synapses. *Nature Neuroscience* **17**, 678–685 (2014).
126. Biederer, T., Kaeser, P. S. & Blanpied, T. A. Transcellular Nanoalignment of Synaptic Function. *Neuron* **96**, 680–696 (2017).
127. Hruska, M., Henderson, N., Le Marchand, S. J., Jafri, H. & Dalva, M. B. Synaptic nanomodules underlie the organization and plasticity of spine synapses. *Nature Neuroscience* **21**, 671–682 (2018).

128. Böhme, M. A. *et al.* Rapid active zone remodeling consolidates presynaptic potentiation. *Nature Communications* **10**, 1085 (2019).
129. Wegner, W., Steffens, H., Gregor, C., Wolf, F. & Willig, K. I. Environmental enrichment enhances patterning and remodeling of synaptic nanoarchitecture as revealed by STED nanoscopy. *eLife* **11**, e73603 (2022).
130. Sigal, Y. M., Speer, C. M., Babcock, H. P. & Zhuang, X. Mapping Synaptic Input Fields of Neurons with Super-Resolution Imaging. *Cell* **163**, 493–505 (2015).
131. M'Saad, O. *et al.* All-optical visualization of specific molecules in the ultrastructural context of brain tissue. 2022.04.04.486901 Preprint at https://doi.org/10.1101/2022.04.04.486901 (2022).
132. Shen, F. Y. *et al.* Light microscopy based approach for mapping connectivity with molecular specificity. *Nature Communications* **11**, 4632 (2020).
133. Tønnesen, J., Inavalli, V. V. G. K. & Nägerl, U. V. Super-Resolution Imaging of the Extracellular Space in Living Brain Tissue. *Cell* **172**, 1108-1121.e15 (2018).
134. Arizono, M., Inavalli, V. V. G. K., Bancelin, S., Fernández-Monreal, M. & Nägerl, U. V. Super-resolution shadow imaging reveals local remodeling of astrocytic microstructures and brain extracellular space after osmotic challenge. *Glia* **69**, 1605–1613 (2021).
135. Weigert, M. *et al.* Content-aware image restoration: pushing the limits of fluorescence microscopy. *Nature Methods* **15**, 1090 (2018).
136. Lin, Z., Wei, D., Lichtman, J. & Pfister, H. *PyTorch Connectomics: A Scalable and Flexible Segmentation Framework for EM Connectomics*. http://arxiv.org/abs/2112.05754 (2021) doi:10.48550/arXiv.2112.05754.
137. Dembitskaya, Y. *et al.* Shadow imaging for panoptical visualization of living brain tissue. 2022.11.03.511028 Preprint at https://doi.org/10.1101/2022.11.03.511028 (2022).
138. Lisman, J. E. Relating Hippocampal Circuitry to Function: Recall of Memory Sequences by Reciprocal Dentate–CA3 Interactions. *Neuron* **22**, 233–242 (1999).
139. Rebola, N., Carta, M. & Mulle, C. Operation and plasticity of hippocampal CA3 circuits: implications for memory encoding. *Nat Rev Neurosci* **18**, 208–220 (2017).
140. Johnston, D. & Amaral, D. G. Hippocampus. in *The Synaptic Organization of the Brain* (ed. Shepherd, G. M.) 0 (Oxford University Press, 2004). doi:10.1093/acprof:oso/9780195159561.003.0011.
141. Basu, J. & Siegelbaum, S. A. The Corticohippocampal Circuit, Synaptic Plasticity, and Memory. *Cold Spring Harb Perspect Biol* **7**, a021733 (2015).
142. David, A. & Pierre, L. Hippocampal Neuroanatomy. in *The Hippocampus Book* (eds. Andersen, P., Morris, R., Amaral, D., Bliss, T. & O'Keefe, J.) 0 (Oxford University Press, 2006). doi:10.1093/acprof:oso/9780195100273.003.0003.
143. Schultz, S., Panzeri, S., Rolls, E. & Treves, A. Quantitative Analysis of a Schaffer Collateral Model. in *Information Theory and the Brain* (eds. Földiák, P., Hancock, P. & Baddeley, R.) 257–272 (Cambridge University Press, 2000). doi:10.1017/CBO9780511665516.019.
144. Martin, E. A., Woodruff, D., Rawson, R. L. & Williams, M. E. Examining Hippocampal Mossy Fiber Synapses by 3D Electron Microscopy in Wildtype and Kirrel3 Knockout Mice. *eNeuro* **4**, ENEURO.0088-17.2017 (2017).
145. Ramon y Cajal, S. *Histologie du système nerveux de l'homme et des vertébrés*. (A. Maloine, 1911).
146. Blackstad, T. W. & Kjaerheim, Å. Special axo-dendritic synapses in the hippocampal cortex: Electron and light microscopic studies on the layer of mossy fibers. *Journal of Comparative Neurology* **117**, 133–159 (1961).
147. Hamlyn, L. H. The fine structure of the mossy fibre endings in the hippocampus of the rabbit. *J Anat* **96**, 112-120.6 (1962).
148. Chicurel, M. E. & Harris, K. M. Three-dimensional analysis of the structure and composition of CA3 branched dendritic spines and their synaptic relationships with mossy fiber boutons in the rat hippocampus. *Journal of Comparative Neurology* **325**, 169–182 (1992).
149. Rollenhagen, A. *et al.* Structural Determinants of Transmission at Large Hippocampal Mossy Fiber Synapses. *J. Neurosci.* **27**, 10434–10444 (2007).
150. Wilke, S. A. *et al.* Deconstructing Complexity: Serial Block-Face Electron Microscopic Analysis of the Hippocampal Mossy Fiber Synapse. *J. Neurosci.* **33**, 507–522 (2013).
151. Acsády, L., Kamondi, A., Sı□ k, A., Freund, T. & Buzsáki, G. GABAergic Cells Are the Major Postsynaptic Targets of Mossy Fibers in the Rat Hippocampus. *J. Neurosci.* **18**, 3386–3403 (1998).
152. McBain, C. J. Chapter 13 Differential mechanisms of transmission and plasticity at mossy fiber synapses. in *Progress in Brain Research* (eds. Sossin, W. S., Lacaille, J.-C., Castellucci, V. F. & Belleville, S.) vol. 169 225–240 (Elsevier, 2008).
153. Rollenhagen, A. & Lübke, J. The mossy fiber bouton: the 'common' or the 'unique' synapse? *Frontiers in Synaptic Neuroscience* **2**, 2 (2010).
154. Nicholson, C. & Hrabětová, S. Brain Extracellular Space: The Final Frontier of Neuroscience. *Biophysical Journal* **113**, 2133–2142 (2017).
155. Michalska, J. M. *et al.* Uncovering brain tissue architecture across scales with super-resolution light microscopy. 2022.08.17.504272 Preprint at https://doi.org/10.1101/2022.08.17.504272 (2022).

156. Bogatyreva, N. S., Finkelstein, A. V. & Galzitskaya, O. V. Trend of amino acid composition of proteins of different taxa. *J. Bioinform. Comput. Biol.* **04**, 597–608 (2006).
157. Hermanson, G. T. Chapter 3 - The Reactions of Bioconjugation. in *Bioconjugate Techniques (Third Edition)* (ed. Hermanson, G. T.) 229–258 (Academic Press, 2013). doi:10.1016/B978-0-12-382239-0.00003-0.
158. Kolb, H. C., Finn, M. G. & Sharpless, K. B. Click Chemistry: Diverse Chemical Function from a Few Good Reactions. *Angewandte Chemie International Edition* **40**, 2004–2021 (2001).
159. Maus, L. *et al.* Ultrastructural Correlates of Presynaptic Functional Heterogeneity in Hippocampal Synapses. *Cell Reports* **30**, 3632-3643.e8 (2020).
160. Studer, D. *et al.* Capture of activity-induced ultrastructural changes at synapses by high-pressure freezing of brain tissue. *Nature Protocols* **9**, 1480–1495 (2014).
161. Tanaka, K. A. K. *et al.* Membrane molecules mobile even after chemical fixation. *Nat Methods* **7**, 865–866 (2010).
162. Korogod, N., Petersen, C. C. & Knott, G. W. Ultrastructural analysis of adult mouse neocortex comparing aldehyde perfusion with cryo fixation. *eLife* **4**, e05793 (2015).
163. Tamada, H., Blanc, J., Korogod, N., Petersen, C. C. & Knott, G. W. Ultrastructural comparison of dendritic spine morphology preserved with cryo and chemical fixation. *eLife* **9**, e56384 (2020).
164. Cragg, B. Brain extracellular space fixed for electron microscopy. *Neuroscience Letters* **15**, 301–306 (1979).
165. Fang, T. *et al.* Nanobody immunostaining for correlated light and electron microscopy with preservation of ultrastructure. *Nat Methods* **15**, 1029–1032 (2018).
166. Pallotto, M., Watkins, P. V., Fubara, B., Singer, J. H. & Briggman, K. L. Extracellular space preservation aids the connectomic analysis of neural circuits. *eLife* **4**, e08206 (2015).
167. Borges-Merjane, C., Kim, O. & Jonas, P. Functional Electron Microscopy ("Flash and Freeze") of Identified Cortical Synapses in Acute Brain Slices. *Neuron* (2020) doi:10.1016/j.neuron.2019.12.022.
168. McDonald, K. L. & Auer, M. High-Pressure Freezing, Cellular Tomography, and Structural Cell Biology. *BioTechniques* **41**, 137–143 (2006).
169. Laporte, M. H., Klena, N., Hamel, V. & Guichard, P. Visualizing the native cellular organization by coupling cryofixation with expansion microscopy (Cryo-ExM). *Nat Methods* 1–7 (2022) doi:10.1038/s41592-021-01356-4.
170. Sartori, N., Richter, K. & Dubochet, J. Vitrification depth can be increased more than 10-fold by high-pressure freezing. *Journal of Microscopy* **172**, 55–61 (1993).
171. Walker, R. A. The use of lectins in histopathology. *Pathol Res Pract* **185**, 826–835 (1989).
172. Long, K. R. *et al.* Extracellular Matrix Components HAPLN1, Lumican, and Collagen I Cause Hyaluronic Acid-Dependent Folding of the Developing Human Neocortex. *Neuron* **99**, 702-719.e7 (2018).
173. Bonneh-Barkay, D. & Wiley, C. A. Brain Extracellular Matrix in Neurodegeneration. *Brain Pathol* **19**, 573–585 (2008).
174. Morawski, M., Filippov, M., Tzinia, A., Tsilibary, E. & Vargova, L. Chapter 10 - ECM in brain aging and dementia. in *Progress in Brain Research* (eds. Dityatev, A., Wehrle-Haller, B. & Pitkänen, A.) vol. 214 207–227 (Elsevier, 2014).
175. Bratthauer, G. L. The Avidin–Biotin Complex (ABC) Method and Other Avidin–Biotin Binding Methods. in *Immunocytochemical Methods and Protocols* (eds. Oliver, C. & Jamur, M. C.) 257–270 (Humana Press, 2010). doi:10.1007/978-1-59745-324-0_26.
176. Lin, R. *et al.* A hybridization-chain-reaction-based method for amplifying immunosignals. *Nat Methods* **15**, 275–278 (2018).
177. Faget, L. & Hnasko, T. S. Tyramide Signal Amplification for Immunofluorescent Enhancement. in *ELISA* (ed. Hnasko, R.) vol. 1318 161–172 (Springer New York, 2015).
178. Altman, R. B. *et al.* Cyanine fluorophore derivatives with enhanced photostability. *Nat Methods* **9**, 68–71 (2012).
179. Staudt, T. *et al.* Far-field optical nanoscopy with reduced number of state transition cycles. *Opt. Express, OE* **19**, 5644–5657 (2011).
180. Heine, J. *et al.* Adaptive-illumination STED nanoscopy. *Proceedings of the National Academy of Sciences* **114**, 9797–9802 (2017).
181. Wurm, C. A., Neumann, D., Schmidt, R., Egner, A. & Jakobs, S. Sample Preparation for STED Microscopy. in *Live Cell Imaging* (ed. Papkovsky, D. B.) vol. 591 185–199 (Humana Press, 2010).
182. Tyson, A. L., Akhtar, A. M. & Andreae, L. C. Optimisation and validation of hydrogel-based brain tissue clearing shows uniform expansion across anatomical regions and spatial scales. *Sci Rep* **9**, 12084 (2019).
183. Krull, A., Buchholz, T.-O. & Jug, F. Noise2Void - Learning Denoising from Single Noisy Images. *arXiv:1811.10980 [cs]* (2019).
184. Prakash, M. *et al.* Leveraging Self-supervised Denoising for Image Segmentation. Preprint at http://arxiv.org/abs/1911.12239 (2020).
185. Buchholz, T.-O., Prakash, M., Krull, A. & Jug, F. DenoiSeg: Joint Denoising and Segmentation. Preprint at http://arxiv.org/abs/2005.02987 (2020).

186. Broaddus, C., Krull, A., Weigert, M., Schmidt, U. & Myers, G. Removing Structured Noise with Self-Supervised Blind-Spot Networks. in *2020 IEEE 17th International Symposium on Biomedical Imaging (ISBI)* 159–163 (IEEE, 2020). doi:10.1109/ISBI45749.2020.9098336.
187. Hillman, E. M. C., Voleti, V., Li, W. & Yu, H. Light-Sheet Microscopy in Neuroscience. *Annual Review of Neuroscience* **42**, 295–313 (2019).
188. Chen, B.-C. *et al.* Lattice light-sheet microscopy: Imaging molecules to embryos at high spatiotemporal resolution. *Science* **346**, (2014).
189. Chakraborty, T. *et al.* Light-sheet microscopy of cleared tissues with isotropic, subcellular resolution. *Nature Methods* **16**, 1109–1113 (2019).
190. Glaser, A. K. *et al.* A hybrid open-top light-sheet microscope for versatile multi-scale imaging of cleared tissues. *Nat Methods* **19**, 613–619 (2022).
191. Gao, M. *et al.* Expansion Stimulated Emission Depletion Microscopy (ExSTED). *ACS Nano* **12**, 4178–4185 (2018).
192. Chen, R. *et al.* Expansion tomography for large volume tissue imaging with nanoscale resolution. *Biomed. Opt. Express* **12**, 5614 (2021).
193. Schindelin, J. *et al.* Fiji: an open-source platform for biological-image analysis. *Nature Methods* **9**, 676 (2012).
194. Pietzsch, T., Saalfeld, S., Preibisch, S. & Tomancak, P. BigDataViewer: visualization and processing for large image data sets. *Nat Methods* **12**, 481–483 (2015).
195. Hörl, D. *et al.* BigStitcher: reconstructing high-resolution image datasets of cleared and expanded samples. *Nature Methods* **16**, 870–874 (2019).
196. Bogovic, J. A., Hanslovsky, P., Wong, A. & Saalfeld, S. Robust registration of calcium images by learned contrast synthesis. in *2016 IEEE 13th International Symposium on Biomedical Imaging (ISBI)* 1123–1126 (2016). doi:10.1109/ISBI.2016.7493463.
197. Lillvis, J. L. *et al.* Rapid reconstruction of neural circuits using tissue expansion and light sheet microscopy. *eLife* **11**, e81248 (2022).
198. Boergens, K. M. *et al.* webKnossos: efficient online 3D data annotation for connectomics. *Nat Methods* **14**, 691–694 (2017).
199. Berger, D. R., Seung, H. S. & Lichtman, J. W. VAST (Volume Annotation and Segmentation Tool): Efficient Manual and Semi-Automatic Labeling of Large 3D Image Stacks. *Front. Neural Circuits* **12**, (2018).
200. Lee, K. *et al.* Convolutional nets for reconstructing neural circuits from brain images acquired by serial section electron microscopy. *Current Opinion in Neurobiology* **55**, 188–198 (2019).
201. Lee, K., Zung, J., Li, P., Jain, V. & Seung, H. S. Superhuman Accuracy on the SNEMI3D Connectomics Challenge. Preprint at https://doi.org/10.48550/arXiv.1706.00120 (2017).
202. Januszewski, M. *et al.* High-precision automated reconstruction of neurons with flood-filling networks. *Nat Methods* **15**, 605–610 (2018).
203. Sheridan, A. *et al.* Local Shape Descriptors for Neuron Segmentation. *bioRxiv* 2021.01.18.427039 (2021) doi:10.1101/2021.01.18.427039.
204. Palay, S. L. Synapses in the central nervous system. *The Journal of Biophysical and Biochemical Cytology* **2**, 193–202 (1956).
205. Ounkomol, C., Seshamani, S., Maleckar, M. M., Collman, F. & Johnson, G. R. Label-free prediction of three-dimensional fluorescence images from transmitted-light microscopy. *Nat Methods* **15**, 917–920 (2018).
206. Laine, R. F., Jacquemet, G. & Krull, A. Imaging in Focus: An Introduction to Denoising Bioimages in the Era of Deep Learning. *The International Journal of Biochemistry & Cell Biology* 106077 (2021) doi:10.1016/j.biocel.2021.106077.
207. Pereira, P. M. *et al.* Fix Your Membrane Receptor Imaging: Actin Cytoskeleton and CD4 Membrane Organization Disruption by Chemical Fixation. *Front. Immunol.* **10**, (2019).
208. Schnell, U., Dijk, F., Sjollema, K. A. & Giepmans, B. N. G. Immunolabeling artifacts and the need for live-cell imaging. *Nature Methods* **9**, 152–158 (2012).
209. Galimberti, I. *et al.* Long-Term Rearrangements of Hippocampal Mossy Fiber Terminal Connectivity in the Adult Regulated by Experience. *Neuron* **50**, 749–763 (2006).
210. Ben-Simon, Y. *et al.* A direct excitatory projection from entorhinal layer 6b neurons to the hippocampus contributes to spatial coding and memory. *Nat Commun* **13**, 4826 (2022).
211. Chen, K. H., Boettiger, A. N., Moffitt, J. R., Wang, S. & Zhuang, X. Spatially resolved, highly multiplexed RNA profiling in single cells. *Science* **348**, aaa6090 (2015).
212. Chen, X. *et al.* High-Throughput Mapping of Long-Range Neuronal Projection Using In Situ Sequencing. *Cell* **179**, 772-786.e19 (2019).
213. Zeng, H. *et al.* Spatially Resolved Single-cell Translatomics at Molecular Resolution. 2022.09.27.509605 Preprint at https://doi.org/10.1101/2022.09.27.509605 (2022).
214. Saka, S. K. *et al.* Immuno-SABER enables highly multiplexed and amplified protein imaging in tissues. *Nat Biotechnol* 1–11 (2019) doi:10.1038/s41587-019-0207-y.
215. Goltsev, Y. *et al.* Deep Profiling of Mouse Splenic Architecture with CODEX Multiplexed Imaging. *Cell* **174**, 968-981.e15 (2018).

216. Shah, S., Lubeck, E., Zhou, W. & Cai, L. In situ transcription profiling of single cells reveals spatial organization of cells in the mouse hippocampus. *Neuron* **92**, 342–357 (2016).
217. Moffitt, J. R. *et al.* Molecular, spatial, and functional single-cell profiling of the hypothalamic preoptic region. *Science* **362**, eaau5324 (2018).
218. Zhang, M. *et al.* Spatially resolved cell atlas of the mouse primary motor cortex by MERFISH. *Nature* **598**, 137–143 (2021).
219. Wang, Y. *et al.* EASI-FISH for thick tissue defines lateral hypothalamus spatio-molecular organization. *Cell* **184**, 6361-6377.e24 (2021).
220. Alon, S. *et al.* Expansion sequencing: Spatially precise in situ transcriptomics in intact biological systems. *Science* **371**, (2021).
221. Fang, R. *et al.* Conservation and divergence of cortical cell organization in human and mouse revealed by MERFISH. *Science* **377**, 56–62 (2022).
222. Holt, C. E., Martin, K. C. & Schuman, E. M. Local translation in neurons: visualization and function. *Nat Struct Mol Biol* **26**, 557–566 (2019).
223. Pitkänen, A. *et al.* Chapter 11 - Neural ECM and epilepsy. in *Progress in Brain Research* (eds. Dityatev, A., Wehrle-Haller, B. & Pitkänen, A.) vol. 214 229–262 (Elsevier, 2014).
224. Syková, E. & Nicholson, C. Diffusion in Brain Extracellular Space. *Physiological Reviews* **88**, 1277–1340 (2008).
225. Soria, F. N., Miguelez, C., Peñagarikano, O. & Tønnesen, J. Current Techniques for Investigating the Brain Extracellular Space. *Front. Neurosci.* **14**, (2020).
226. Lu, L., Duong, V. T., Shalash, A. O., Skwarczynski, M. & Toth, I. Chemical Conjugation Strategies for the Development of Protein-Based Subunit Nanovaccines. *Vaccines* **9**, 563 (2021).
227. Bulovaite, E. *et al.* A brain atlas of synapse protein lifetime across the mouse lifespan. *bioRxiv* 2021.12.16.472938 (2021) doi:10.1101/2021.12.16.472938.
228. Masch, J.-M. *et al.* Robust nanoscopy of a synaptic protein in living mice by organic-fluorophore labeling. *Proceedings of the National Academy of Sciences* **115**, E8047–E8056 (2018).
229. Stoppini, L., Buchs, P.-A. & Muller, D. A simple method for organotypic cultures of nervous tissue. *Journal of Neuroscience Methods* **37**, 173–182 (1991).
230. Lancaster, M. A. *et al.* Cerebral organoids model human brain development and microcephaly. *Nature* **501**, 373–379 (2013).
231. Villa, C. E. *et al.* CHD8 haploinsufficiency links autism to transient alterations in excitatory and inhibitory trajectories. *Cell Reports* **39**, (2022).
232. Guzman, S. J., Schlögl, A. & Schmidt-Hieber, C. Stimfit: quantifying electrophysiological data with Python. *Front Neuroinform* **8**, 16 (2014).

# 6 Appendix

**Appendix Table 1: Properties of compounds used for coCATS live labeling.**

| Name | Structure | MW (g/mol) | Δq (-) | $\lambda_{ex}$ (nm) | $\lambda_{em}$ (nm) |
|---|---|---|---|---|---|
| Alexa Fluor 488-NHS[1] | 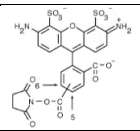 | 643.4 | NA | 494 | 517 |
| Alexa Fluor 546-NHS[1] | 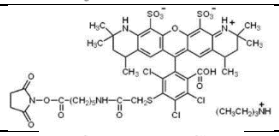 | 1159.6 | NA | 554 | 570 |
| Alexa Fluor 594-NHS | 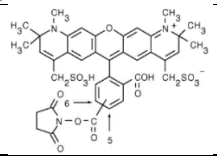 | 819.8 | NA | 590 | 617 |
| Atto 643-NHS[2] | Proprietary | 955.0 | -1 | 643 | 665 |
| Atto 643-maleimide[2] | Proprietary | 1071.0 | -1 | 643 | 664 |
| Maleimide-$PEG_{11}$-$biotin_1$ | 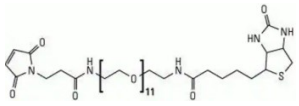 | 921.7 | NA | NA | NA |
| NHS-$PEG_{12}$-biotin[1] | 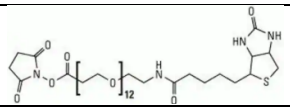 | 922.1 | NA | NA | NA |
| NHS-$PEG_{12}$-BCN[3] | 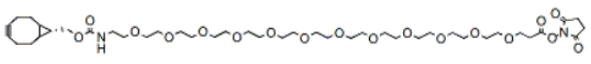 | 891.0 | NA | NA | NA |
| NHS-$PEG_4$-DBCO[3] | 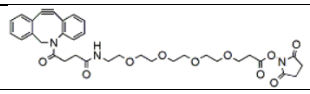 | 649.7 | NA | NA | NA |
| NHS-$PEG_{12}$-DBCO[3] | 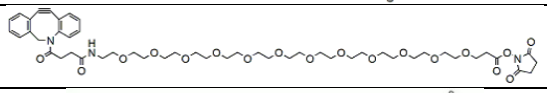 | 1002.1 | NA | NA | NA |
| NHS-sulfo-biotin[1] | 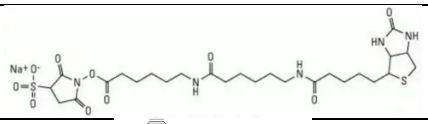 | 669.8 | NA | NA | NA |
| NHS-sulfo-DBCO[4] | 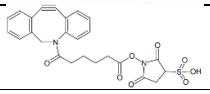 | 509.5 | NA | NA | NA |
| PFP-$PEG_{36}$-biotin[3] | 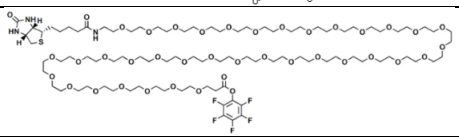 | 2067.4 | NA | NA | NA |
| STAR RED-NHS[5] | Proprietary | 1029.0 | -1 | 638 | 655 |
| TFP-$PEG_{12}$-NHS[6] | 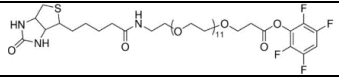 | 992.1 | NA | NA | NA |

MW = molecular weight, Δq = electrical charge, $\lambda_{ex}$ = longest-wavelength absorption maximum, $\lambda_{em}$ = fluorescence maximum, NA = not available

Information and chemical structures from vendor: [1] thermofisher.com; [2] atto-tec.com; [3] broadpharm.com; [4] jenabioscience.com, [5] abberior.shop, [6] sigmaaldrich.com

**Appendix Table 2: Sample preparation parameters during live incubation for coCATS labeling and additional staining steps after fixation (post-processing).**

| | Primary neurons | Cerebral organoid | Organotypic slice culture | Acute slice | Acute retina |
|---|---|---|---|---|---|
| *coCATS label* | Atto 643-NHS | NHS-$PEG_{12}$-biotin | Atto 643-NHS | STAR RED-NHS | Atto 643-NHS |
| *Label concentration (µM)* | 40 | 200 | 50 | 50 | 40 |
| *Buffer* | Carbogen-equilibrated ACSF | Organoid culture medium | Carbogen-equilibrated ACSF | Carbogen-equilibrated ACSF | Carbogen-equilibrated Ames medium |
| *Incubation temperature (°C)* | 22 | 37 | 37 | 37 | 22 |
| *Incubation time (min)* | 20 | 45 | 25 | 40 | 45 |
| *Fixation* | NA | 24 h, 4 °C | 1 h, RT | 2 h, RT | 1 h, RT |
| *Post-processing* | NA | Triton-X permeabilization, 3 µg/ml neutravidin-STAR 635P readout | NA | NA | NA |

NA = not available

# 6.1 Chemical conjugation strategies

1. NHS chemistry

NHS esters mainly react with primary amines ($NH_2$) to form a stable amide bond at pH 7-9 (Appendix Figure 1a). During this reaction, NHS is formed as a byproduct. In addition, they can react with secondary amines, creating imide linkages. Thus, in a reaction with proteins, NHS esters selectively conjugate primary amine-containing lysines. NHS esters are prone to hydrolysis, such that in an aqueous solution the hydrolysis competes with the primary amine reaction. This reaction is dependent on the reaction pH, where a high pH negatively affects the half-life time of the NHS ester. Hence, NHS esters should be stored in organic solvents, such as DMSO, and only diluted in an aqueous solution right before the start of the experiment.[157]
TFP and PFP esters conduct the same reactions as NHS esters, but are more resistant to hydrolysis, resulting in higher labeling efficiency in aqueous solutions.

2. Strain-promoted azide-alkyne cycloaddition

Strain-promoted azide-alkyne cycloaddition is a type of click chemistry that was developed as an alternative to the traditional copper-catalyzed azide-alkyne reaction. Instead of the traditional linear alkyne group, here a cyclic analogue is used. It reacts with the azide with higher efficiency due to the high degree of ring strain of the alkyne (Appendix Figure 1b).[226] The reaction is most efficient at a pH of 7.7.

3. Maleimide-thiol chemistry

The reaction of Maleimide to thiols is highly specific and most efficient at a pH of 6.5-7.5 (Appendix Figure 1c). During the reaction, a stable thioether bond is formed without any byproduct. In proteins, thiol groups are present on cysteines, such that the Maleimide-thiol chemistry specifically targets this amino acid. At a pH above 8.5, maleimides also react with primary amines.

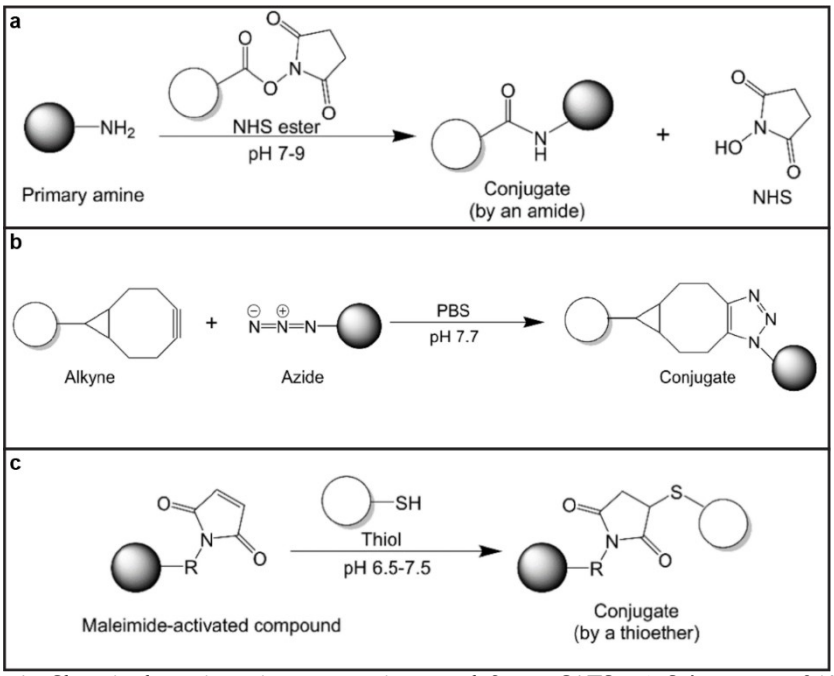


**Appendix Figure 1: Chemical conjugation strategies used for coCATS.** a) Schematic of NHS chemistry. b) Schematic of strain-promoted azide-alkyne cycloaddition. c) Schematic of maleimide-thiol chemistry. Adapted from Lu *et al.*, 2021[226].

# 6.2 Additional material & methods

## 6.2.1 Primary hippocampal neuron culture

**Solutions**

| Borate buffer (100 ml, pH 8.5, sterile filtered) | | |
|---|---|---|
| $Na_2B_4O_7$ | 100 mM | 2.012 g |
| $H_3BO_3$ | 100 mM | 0.618 g |

| Plating medium (123.1 ml, sterile filtered) | | |
|---|---|---|
| Minimal Essential Medium | | 111 ml |
| D-glucose | 3.3 mM | 66 mg |
| Horse serum | 10% (v/v) | 11 ml |
| L-glutamine | 2 mM | 1.1 ml (of 200 mM stock) |

| Enzyme solution (10 ml) | | |
|---|---|---|
| Dulbeccos' Modified Eagle Medium | 10 ml | |
| Cysteine | 20% (w/v) | 2 mg |
| $CaCl_2$ | 1 mM | |
| Ethylenediaminetetraacetic acid | 0.5 mM | |
| Papain | 20-25 unit (U)/ml | |

Add papain freshly before use
Bubble with carbogen for 10-20 min, filter, and keep at 37°C until use

| Inactivation solution (500 ml) | | |
|---|---|---|
| Minimal Essential Medium | | 475 ml |
| Fetal calf serum | 5% (v/v) | 25 ml |
| BSA | 0.25% (w/v) | 1.25 g |
| Penicillin/Streptomycin | 40 U/ml | 2 ml |

| Neurobasal-A culture medium (500 ml) | | |
|---|---|---|
| Neurobasal-A | | 484 ml |
| B27 | 20% (v/v) | 10 ml |
| GlutaMAX | 10% (v/v) | 5 ml |
| Penicillin/Streptomycin | 20 U/ml | 1 ml |

**Coverslip preparation**

1. Clean coverslips in 70-100% ethanol (EtOH) overnight.
2. Place coverslips in wells and let the EtOH evaporate.
3. Sterilize coverslips with ultraviolet light for 30 min.
4. Incubate with 1 mg/ml PLL in borate buffer (or 0.01% PLL from ThermoFisher) in cell culture incubator overnight.
5. Remove PLL (do not reuse, quality decreases dramatically).
6. Wash 4x with sterile $ddH_2O$.
7. Remove $ddH_2O$ thoroughly and add 1 ml of plating medium.
8. Store until use (max. 1 week later).

**Hippocampus extraction & dissociation**

1. Sacrifice P0-P1 rat pups by decapitation.
2. Cut skull along the midline from back to front, and along the bone plate meeting line to both sides.

3. Open skull with scissors.
4. Remove brain with spatula and place in ice-cooled dish with Hank's Balanced Salt Solution (HBSS) (without $MgCl_2$ and $CaCl_2$).
5. Once all brains are extracted, move to dissection microscope.
6. Remove meninges with forceps.
7. Fold cortex to the sides with forceps to reveal hippocampi.
8. Separate brain hemispheres with forceps.
9. Remove hippocampi with dissection scissors.
10. Place hippocampi in separate ice-cooled dish with HBSS (without $MgCl_2$ and $CaCl_2$).
11. Chop up hippocampi with a razor blade.
12. Collect all hippocampi pieces in a 15 ml falcon.
13. Remove HBSS, replace with 4.5 ml fresh HBSS (without $MgCl_2$ and $CaCl_2$) .
14. Remove HBSS, add 10 ml enzyme solution pre-warmed to 37°C.
15. Agitate at 37°C for 60 min.
16. Remove enzyme solution, add 10 ml inactivation solution pre-warmed to 37°C and incubate for 5 min at 37°C.
17. Remove inactivation solution, add 5-10 ml of plating medium, centrifuge at 200 rpm for 5-6 min.
18. Remove supernatant, add 1 ml of plating medium, homogenize with a 5 ml pipette (take care to be gentle and to not cause bubbles). Repeat 4-5 times to a final volume of 4-5 ml.

**Neuron culture**

1. Count cells and plate at desired density (~40,000 cells for 12 mm coverslip, 50,000-80,000 cells for 18 mm coverslip). Culture at 37 °C with 5% carbon dioxide ($CO_2$).
2. 2-4 h after seeding, exchange medium for pre-heated culture medium (well by well, do not leave cells without liquid).
3. Culture for up to 4 weeks without any medium change.

## 6.2.2 Acute retina preparation

**Solutions**

Ames' medium (Sigma Aldrich, A1420)

- Measure 90% of the required volume of dd$H_2O$ (900 ml) into a bottle.
- Gas the dd$H_2O$ with carbogen (95% $O_2$, 5% $CO_2$). Add 1.9 g/l sodium bicarbonate to the liquid while gently stirring it.
- Add the powdered medium to the solution and stir until dissolved completely. Do not heat the solution.
- Rinse the medium vial to remove all traces of powder and transfer it into the solution.
- Add dd$H_2O$ to the solution to a final volume of 1000 ml.
- Continue carbogen-equilibrating the solution until use.

**Eye removal**

1. Place the animal in an airtight chamber and anesthetize it with isoflurane.
2. Take the animal out of the chamber and sacrifice it by cervical dislocation.
3. Remove eyes. Use forceps to push eyes out of the sockets gently, until you can close the forceps underneath the eyes around the optic nerve. Then, pull out the eye including the optic nerve.

**Retinal dissection**

4. Place a droplet of superglue in the middle of a dish and glue the eye onto the bottom of the dish with the optic nerve facing down.
5. Fill the dish with carbogen-equilibrated Ames' medium. Make sure the eye is completely submerged in the solution.
6. Work in carbogen-equilibrated Ames' medium at RT. Make sure to replenish the solution with fresh carbogen-equilibrated medium regularly.
7. Remove as much muscle and connective tissue as possible using two pairs of angled forceps.
8. Use spring scissors to make a small cut into the cornea at the retinal margin (cornea-scleral divide).
9. Carefully cut the cornea in a circle along the cornea-scleral divide while supporting the eye with forceps.
10. Once completely cut, remove the cornea and iris. Use forceps to press gently on the sides of the eye to push out the lens.
11. Carefully tear the sclera and choroid from the retina by using two pairs of forceps, until the retina detaches from the rest of the material.
12. Trim the rim of the retina and clean it from remaining iris.
13. Create a four-petal flower-like structure by creating four incisions towards the center of the retina with scissors. This will hinder the cup-shaped retina from folding up.

**Acute retina coCATS labeling**

14. Transfer the retina into a fresh dish containing carbogen-equilibrated Ames' medium using a Pasteur pipette with a large opening (cut off the tip of the Pasteur pipette to create a larger opening). Let the tissue recover for 15 min in the solution while gently gasing it.
15. Prepare a coCATS labeling solution by diluting a NHS-dye stock solution in Ames' medium just before the start of the incubation (example: 1:250 dilution of 10 mM Atto 643-NHS stock solution in DMSO to achieve a 40 μM Atto 643-NHS working solution in Ames' medium.).
16. Transfer the retina into the coCATS labeling solution with a Pasteur pipette.

17. Incubate the retina in coCATS labeling solution for 45 min at RT while gently gasing the solution with carbogen.
18. Wash the sample twice for 1 min with carbogen-equilibrated Ames' medium.
19. Fix the sample with 4% FA in 1X PBS for 1 h at RT with gentle agitation.
20. Wash the sample 3-times for 30 min with 1X PBS at RT with gentle agitation.
21. Flip the retina onto a coverslip in an imaging chamber with the nerve fiber layer facing the coverslip. Immobilize the sample with a slice anchor and fill the imaging chamber with 1X PBS.
22. Image the sample on an inverted fluorescence microscope.

# 6.3 Publications

## 6.3.1 Uncovering brain tissue architecture across scales with super-resolution microscopy

### 6.3.1.1 Preprint



1 **Uncovering brain tissue architecture across scales with**
2 **super-resolution light microscopy**
3
4 Julia M. Michalska[1], Julia Lyudchik[1], Philipp Velicky[1], Hana Korinkova[1], Jake F. Watson[1],
5 Alban Cenameri[1], Christoph Sommer[1], Alessandro Venturino[1], Karl Roessler[2], Thomas
6 Czech[2], Sandra Siegert[1], Gaia Novarino[1], Peter Jonas[1], Johann G. Danzl[1]
7
8 [1]Institute of Science and Technology Austria, Am Campus 1, 3400 Klosterneuburg, Austria
9 [2]Medical University of Vienna, Department of Neurosurgery, Waehringer Guertel 18-20, 1090
10 Vienna, Austria
11
12 correspondence to: johann.danzl@ist.ac.at
13

14 **Abstract**

15 Mapping the complex and dense arrangement of cells and their connectivity in brain tissue
16 demands nanoscale spatial resolution imaging. Super-resolution optical microscopy excels at
17 visualizing specific molecules and individual cells but fails to provide tissue context. Here we
18 developed Comprehensive Analysis of Tissues across Scales (CATS), a technology to densely
19 map brain tissue architecture from millimeter regional to nanoscopic synaptic scales in diverse
20 chemically fixed brain preparations, including rodent and human. CATS leverages fixation-
21 compatible extracellular labeling and advanced optical readout, in particular stimulated-
22 emission depletion and expansion microscopy, to comprehensively delineate cellular
23 structures. It enables 3D-reconstructing single synapses and mapping synaptic connectivity by
24 identification and tailored analysis of putative synaptic cleft regions. Applying CATS to the
25 hippocampal mossy fiber circuitry, we demonstrate its power to reveal the system's
26 molecularly informed ultrastructure across spatial scales and assess local connectivity by
27 reconstructing and quantifying the synaptic input and output structure of identified neurons.
28

# Introduction

The challenge of illuminating the complex structure of brain tissue has been a major motivating force to advance imaging technologies. Optical super-resolution approaches visualize cells and molecules down to nanoscopic scales, increasing resolution beyond the diffraction limit of a few hundred nanometers either by increasing instrument resolution[1–4] or by physically increasing specimen size and hence distances between features[5–8]. Super-resolution microscopy has generated insights into the molecular organization of synapses[9–11], the neuronal cytoskeleton[12], structure-function relationships in neurons[13], and tissue organization[14]. However, in all these cases, analysis is limited to specific molecular targets or sparse subsets of labeled cells, lacking information about their context within the tissue. Electron microscopy (EM) provides comprehensive structural contrast and exquisite spatial resolution, but 3D-tissue reconstruction is technically challenging, laborious, and difficult to complement with molecular information. Optical technologies that visualize the tissue's architecture and provide contextual meaning to molecules and cellular structures at high resolution would provide major opportunities for discovery.

Extracellular labeling is a powerful tool to delineate all cells in a tissue volume. It has been applied to guide patch clamp experiments[15] and visualize extracellular space[16,17] in living brain tissue, and for early EM-connectomics studies in mouse retina[18]. Reading out freely diffusing, extracellularly applied fluorophores with stimulated emission depletion (STED) microscopy[1,19,20] in living brain tissue in the framework of super-resolution shadow imaging (SUSHI)[17,21–23] casts super-resolved shadows of all cells. We recently showed that extracellular labeling integrated with a specifically engineered 3D-super-resolution/machine learning technology enables dense, synapse-level reconstruction of living brain tissue[24]. However, while live imaging uniquely accesses dynamics, it is constrained by applicable super-resolution modality, molecular labeling options, addressable tissue volumes, and sample type. In fixed tissues, feature-rich representations of cells and various tissues have been achieved by several strategies, including fluorescent[25–29] or Raman[30] contrast for total protein density or other molecule classes in expansion microscopy (ExM). However, none of these approaches has been amenable to *in silico* reconstruction of the brain tissue's architecture or sub-cellular morphology. There is thus an unmet need for an optical technology that is capable of visualizing and quantifying tissue organization from regional to single-synapse level in a technologically straightforward manner.

Here we developed *Comprehensive Analysis of Tissues across Scales* (CATS), an integrated labeling, optical imaging, and analysis platform to decode brain tissue architecture, subcellular morphologies, and molecular arrangements within their structural context. We engineered CATS to visualize all cellular structures in fixed tissue by extracellular labeling with (super-resolution) fluorescence microscopy. Thereby, CATS removes the constraints associated with live imaging and permits analysis from regional to nanoscopic spatial scales for commonly used native and cultured brain tissue preparations. It capitalizes on the full technology base for labeling, optically homogenizing, and 3D-super-resolution imaging available for fixed tissues, building on the pertinent strengths of STED and expansion microscopy, in a widely adoptable approach. With specifically tailored analysis, CATS quantitatively reveals tissue architecture, maps synaptic connectivity, and allows 3D-reconstruction of subcellular morphology down to single-synapse level in a molecularly informed fashion. To demonstrate the power of this approach to quantify synaptic connectivity and structure, we characterized one of the key synapse types in the hippocampal circuitry. We reveal the synaptic input and output structure of identified, functionally recorded neurons across brain regions, and furthermore apply the technique to clinically derived human tissue samples.

# Results

## CATS unravels tissue architecture at super-resolved detail

We developed two strategies for revealing tissue structure by selective labeling of the extracellular domain (**Fig. 1a**): i) "Compartment CATS" (coCATS) applies covalently binding labeling compounds to the *extracellular compartment* in living tissue, with intact membrane boundaries constraining labeling to the extracellular space and cell surfaces. ii) "Resident CATS" (rCATS) labels classes of *extracellularly resident* molecules, in particular extracellular polysaccharides. This makes CATS applicable also to specimens where live labeling is not possible (**Fig. 1b**). Both approaches revealed the cellular architecture of brain tissue, for example in the hippocampal region, across scales (**Fig. 1b,c**).

To analyze brain architecture with coCATS, we screened for molecules providing high extra- to intracellular contrast, high labeling density, and compatibility with downstream super-resolution readout in organotypic hippocampal slice cultures (**Supplementary Fig. 1**). We focused on commercially available compounds for easy adoptability. We ensured cell impermeability either via hydrophilic, anionic fluorophores or additional sulfo- or polyethylene

glycol (PEG) groups. As expected, chemistries targeting primary amines, including N-hydroxysuccinimide (NHS) and tetra- (TFP) and pentafluorophenyl (PFP) esters, effectively mediated homogeneous labeling by covalent attachment to extracellular and cell surface molecules, particularly proteins. For readout, we used either directly conjugated fluorophores or a small molecule reporter (biotin/fluorescent avidin).

For decrypting near-natively preserved brain at super-resolved detail, we performed *in vivo*-stereotactic injection of an NHS-derivative of a hydrophilic, far-red, high-performance STED fluorophore followed by transcardial fixative perfusion. Injection into the brain lateral ventricle labeled areas adjacent to the ventricular system, distant from the lesioned region at the injection site (**Supplementary Fig. 2**). STED microscopy provides direct, "all optical" super-resolved readout by applying a light pattern that confines fluorescence ability to volumes smaller than the diffraction limit. We first focused on hippocampus, a brain region central to spatial navigation and memory with well-characterized fundamental circuitry. As an important component, mossy fibers originating from dentate gyrus (DG) granule cells convey excitatory input to pyramidal neurons in the CA3 *stratum lucidum*, forming key synapses in the hippocampal trisynaptic circuit. These synapses are an established model for functional synapse characterization and contribute to higher order computations[31,32]. STED imaging at the transition between *stratum pyramidale* and *stratum lucidum* of the CA3 region revealed the complex arrangement of cell bodies, dendrites, bundles of thin axons, and synaptic terminals at high signal-to-noise ratio (SNR) (**Fig. 1d**). Diffraction-unlimited resolution, here on the order of 60 nm laterally, was indispensable to resolve the cellular structures in this extremely complex and dense arrangement (**Supplementary Fig. 3**). For example, we were able to resolve the individual unmyelinated axons in mossy fiber bundles, most conspicuous as small circular structures when transversely optically sectioned. When complemented with immunolabelling for the pre-synaptic marker BASSOON and for SHANK2, a scaffolding protein in post-synaptic densities of excitatory synapses, CATS assigned molecularly defined synaptic sites to individual pre-synaptic boutons of mossy fibers and revealed their location within the tissue's ultrastructure (**Fig. 1d-f**). It revealed both pre- and post-synaptic structures, showing the complex arrangement of large mossy fiber boutons (MFBs) containing multiple transmission sites. These contact complex pyramidal neuron spines[33] termed "thorny excrescences". Such contextual structural meaning was missing with immunostainings alone or sparse labeling of a subset of cells by gold-standard cytosolic fluorescent protein expression (**Supplementary Fig. 4**).

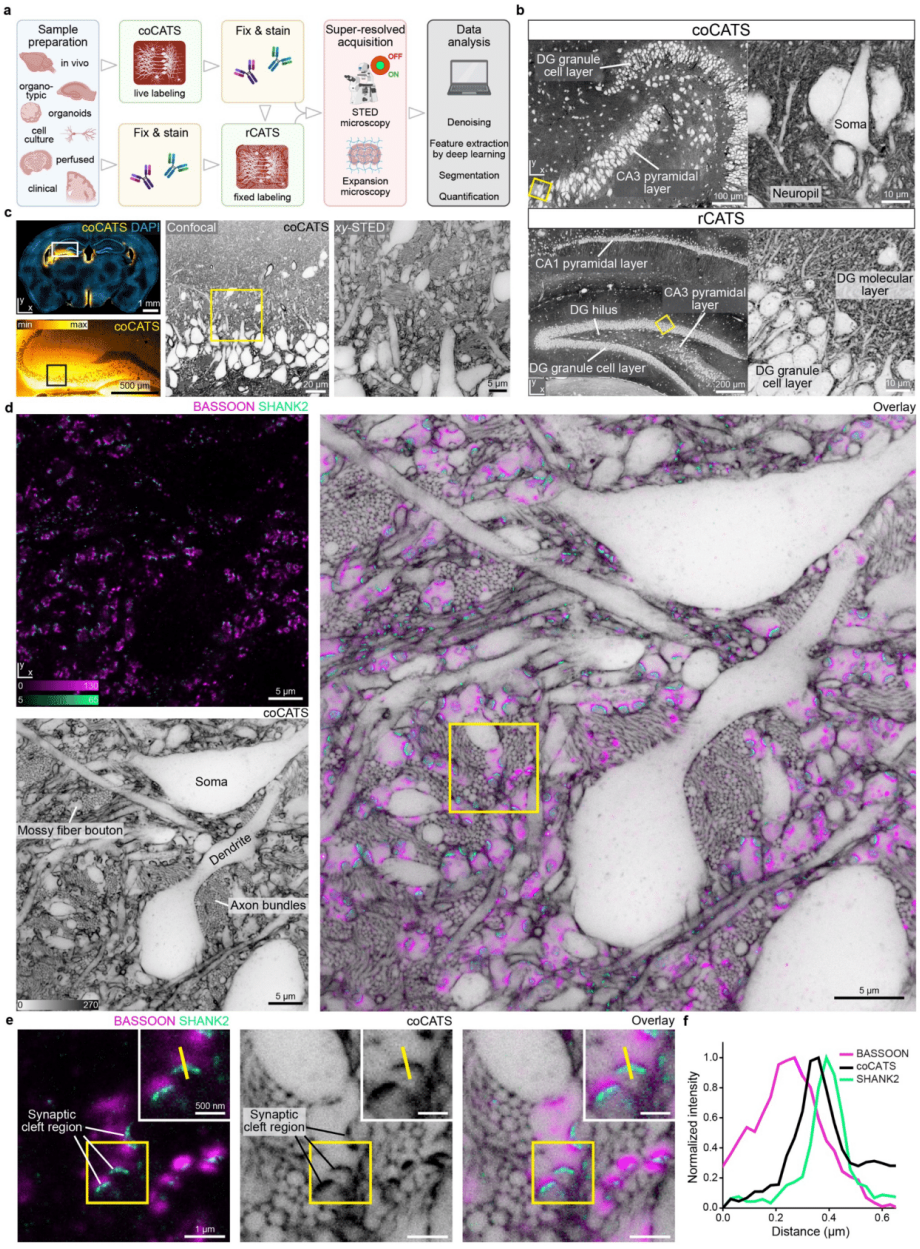


**Fig. 1| Comprehensive analysis of tissue across scales (CATS). a,** Platform for tissue analysis including live extracellular labeling (compartment CATS, coCATS) or extracellular labeling in previously fixed tissue (resident CATS, rCATS), optional molecular staining, super-resolved acquisition, and machine learning/conventional analysis. **b,** (*Top*) CoCATS labeling

in organotypic hippocampal slice, revealing gross architecture of the dentate gyrus (DG) and CA3 region, and zoomed view of boxed region (confocal). (*Bottom*) RCATS labeling in perfusion-fixed adult mouse coronal section, showing hippocampus with zoomed view. Intensity lookup tables (LUTs) for CATS are inverted throughout, i.e. black regions correspond to high labeling intensity, unless otherwise noted. Raw data. **c,** Progressive zoom from hippocampal regional to cellular scale in CA3 *stratum pyramidale* and *stratum lucidum.* CoCATS labeling by *in vivo* stereotactic injection into the lateral ventricle (LV) of adult mouse (*left*: LUT not inverted, *left bottom*: gamma correction applied). *Left, center*: confocal; *right*: STED, lateral resolution increase (*xy*-STED). Raw data. **d,** Super-resolved tissue architecture of mouse CA3 *stratum pyramidale/lucidum*, after *in vivo* coCATS label microinjection into LV. (*Left top*) Immunostaining of pre-synaptic BASSOON (magenta, confocal) and post-synaptic SHANK2 (turquoise, *xy*-STED). (*Left bottom*) coCATS (*xy*-STED) of same region. (*Right*) Overlay placing synaptic markers into structural context, including mossy fiber boutons (MFBs). Raw data. **e,** Magnified view from d (boxed), focusing on a MFB with multiple synaptic sites, amidst bundles of thin mossy fiber axons. Inset: magnification of synaptic transmission site. High-intensity coCATS labeling pinpoints dense/protein-rich features between pre- and post-synapses corresponding to putative synaptic cleft regions (pSCRs). **f,** Line profile as indicated in e, showing sandwich arrangement of BASSOON, high-intensity coCATS (pSCR), and SHANK2 signals.

---

## Quantifying single synapse structure and connectivity

When inspecting the combined structural/molecular data more closely, we discovered that coCATS labeling consistently produced high-intensity features sandwiched between pre- and post-synapses. These correspond to putatively primary amine/protein-rich extracellular regions at apparent synaptic transmission sites, likely reflecting the high protein density of the synaptic cleft[34] (**Fig. 1e,f**). We clarified their spatial relationship with a range of additional synaptic molecules (SYNAPTOPHYSIN1, HOMER1, vesicular GABA transporter (VGAT), vesicular glutamate transporter (VGLUT1), N-CADHERIN) both in excitatory and inhibitory synapses and with sparsely labeled MFBs (**Supplementary Fig. 5**). Taken together, we found their location consistent with synaptic clefts. This prompted us to designate them "putative synaptic cleft regions" (pSCRs) and develop an automated pipeline for segmenting and mapping them (**Fig. 2a**). After enhancing volumetric datasets with a deep-learning-based denoising algorithm (Noise2Void[35], N2V, **Supplementary Fig. 6,7**), we used super-resolved SHANK2 immunostaining as guide to excitatory synapses and performed locally confined thresholding to isolate high-intensity coCATS features. We classified them as pSCRs in case of apposition

with pre-synaptic BASSOON (confocal) and post-synaptic SHANK2 (STED) in a triple-sandwich arrangement. This also eliminated false positive synapse identifications from unavoidable background in immunostainings (**Supplementary Fig. 8**). Finally, we performed instance segmentation of individual pSCRs, applied manual proofreading, and contextualized them by association with manually created volume segmentations of MFBs. Automated analysis substantially reduced human processing time compared to manual pSCR segmentation.

Using this pipeline, we reconstructed individual synaptic boutons with their synaptic transmission topology in 3D. Reconstruction is limited by the least resolved spatial axis, i.e. along the optical (*z*-)axis. We therefore applied a dedicated light pattern for near-isotropic STED-resolution[1] (*z*-STED, **Supplementary Fig. 3**) and recorded 3 volumetric datasets in the CA3 *stratum lucidum* (~30x30x12 $\mu m^3$, 2 brain slices, 1 animal). We selected 10 prominent MFBs from each, manually segmented their 3D-shape from the coCATS channel, and quantified both key geometrical parameters and pSCRs (**Fig. 2b-h, Supplementary Video 1,2, Supplementary Fig. 9**). Individual boutons varied widely in size and shape, with mean volume $\overline{V}_{MFB}$=13.6±5.0 $\mu m^3$ (± s.d., **Fig. 2c**) and mean surface area $\overline{A}_{MFB}$=53.5±16.6 $\mu m^2$ (**Fig. 2d**). These values are consistent with previous EM results from adult mouse[36] ($\overline{V}_{MFB}$=13.5 $\mu m^3$, $\overline{A}_{MFB}$=66.5 $\mu m^2$). Mean surface area was smaller in our case as we did not include filopodial structures extending from the main bouton, as they are at the limit of the resolution used in this measurement. PSCRs were similarly diverse, often forming fenestrated structures (**Fig. 2b**). To identify regions of MFBs occupied by putative active zones, we related pSCRs to MFB segmentations. For this, we identified pSCR voxels that touched voxels of segmented MFBs, extracted the contacting surfaces and turned them into 3D-meshes. The total area of individual boutons occupied by pSCRs ($A_{pSCR/MFB}$) had a mean value of $\overline{A}_{pSCR/MFB}$=4.6±1.6 $\mu m^2$ (**Fig. 2e**). The fraction of MFB surface occupied by pSCRs ($A_{pSCR/MFB}/A_{MFB}$) calculated at individual bouton level displayed smaller spread, hinting towards a correlation between MFB size and the extent of synaptic release sites. Indeed, when plotting $A_{pSCR/MFB}$ as a function of MFB volume (**Fig. 2f**) (Pearson correlation coefficient r=0.844, 95% confidence interval (CI): 0.694-0.923, p<0.0001, $R^2$=0.72, 30 MFBs) or surface area (**Fig. 2g**) (r=0.841, CI: 0.689-0.922, p<0.0001, $R^2$=0.71, 30 MFBs), we found strong correlation, indicating that larger MFBs also engage more extensively in synaptic contacts. This is in accordance with previous studies showing a linear relationship between MFB volume and active zone extent both in organotypic slice cultures and *in vivo*[37]. Interestingly, the fraction of MFB surface area occupied by pSCRs (8.6±1.7 %)

was consistent with previous quantifications of MFB surface area occupied by active zones in serial sectioning EM in adult rat on a smaller number of MFBs (9.7%)[38]. The number of pSCRs showed large variability between individual boutons (3-28, mean 13.03±5.93), similar as in an EM study on adult rat[38], and also correlated with bouton size (**Supplementary Fig. 9**). These data demonstrate that CATS can identify synaptic transmission sites and deliver quantitative biological data at single synapse level. Our data are consistent with EM-reconstructions[36,38,39] but include molecular information and can be obtained without complex sample preparation or serial sectioning procedures and with high experimental throughput (imaging time for 3-channel measurement per volume: ~1.5 h).

## Deep-learning-based prediction of synapse location

Based on the prominence of pSCRs in coCATS data, we hypothesized that coCATS may reveal synapse location based on local tissue structure. We thus trained a convolutional neural network with U-net architecture[40] to predict synapse location purely from CATS structural data using deep-learning-based image translation (**Fig. 2i, Supplementary Fig. 10**). For training, we provided the network with near-isotropically super-resolved coCATS data paired with immunostainings as molecular ground truth. We used the resulting model to predict molecule location in unseen datasets. Indeed, a model trained on coCATS and super-resolved BASSOON, present in excitatory and inhibitory synapses, was capable of guiding segmentation of pSCRs in mossy fiber boutons. The network prediction can replace the immunostainings in the pipeline above for pSCR segmentation. This is remarkable, as thresholding alone, neglecting local context, was insufficient to identify pSCRs among dense CATS features. For validation, we correlated predicted BASSOON signal with immunolabeled BASSOON in datasets not included in the training (**Supplementary Fig. 10**, Pearson correlation, r=0.818). In addition to voxel-based correlation, we evaluated resulting automated pSCR segmentation guided by immunostaining vs. segmentation guided by predicted BASSOON signal using the F1 score, and found a high degree of similarity (F1=0.73 at intersection over union (IOU) threshold 0.5, **Fig. 2j,k, Supplementary Fig. 10**). For this, instance segmentations of our deep-learning-prediction and the corresponding ground-truth dataset were compared by identifying object-pairs and calculating their IOUs (ratio of overlapping volume vs. combined volume). The F1 score as a function of IOU takes into account the precision (number of correctly segmented objects divided by number of all segmented objects) and recall (number of correctly segmented objects divided by number of

all true objects). As expected, network predictions improved with the higher precision of super-resolved compared to confocal molecular signals as input data for training (**Supplementary Fig. 10**). Denoising with Noise2Void had a minor effect on prediction outcome (**Supplementary Fig. 10**). These data demonstrate that deep-learning-based analysis within the CATS framework has the power to reveal synaptic transmission sites, leveraging local context and structural labeling of putative synaptic clefts.

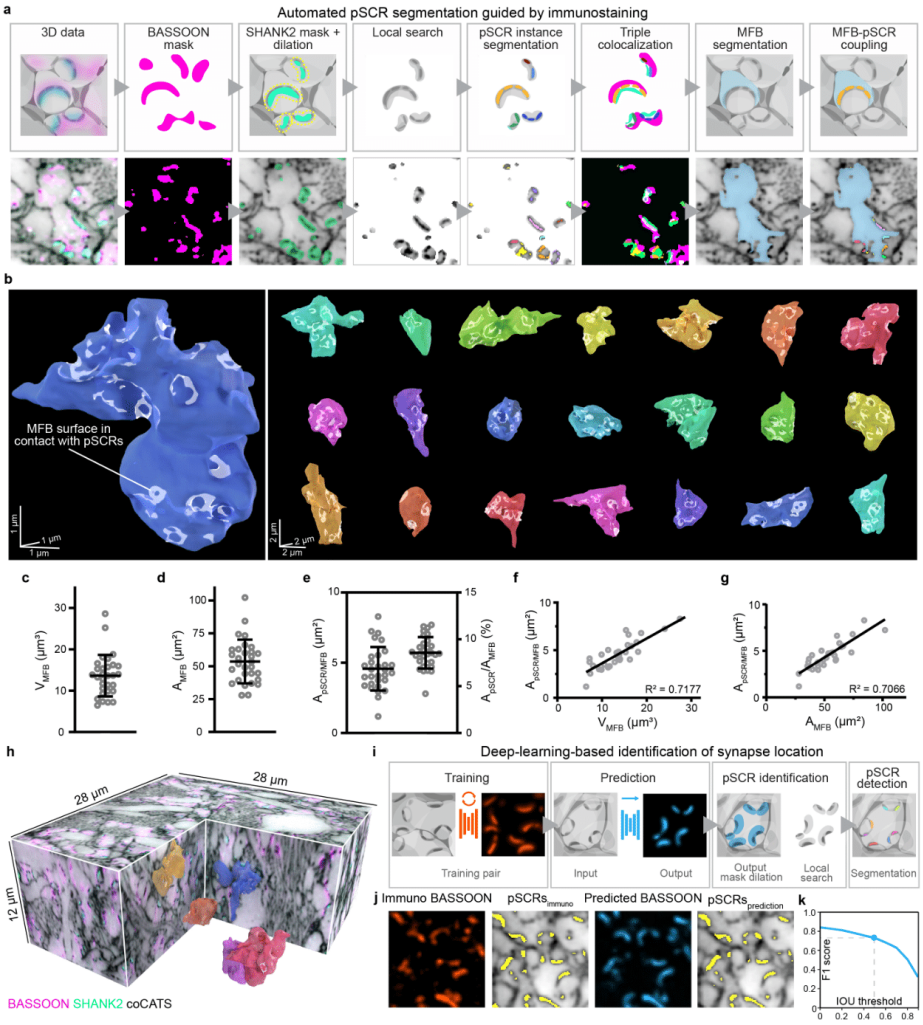


**Fig. 2| Quantifying synaptic connectivity and single-bouton properties.** CoCATS analysis of hippocampal mossy fiber to CA3 pyramidal neuron synapses in adult mouse CA3

*stratum lucidum* by *in vivo* microinjection into the LV. **a,** Automated synapse detection guided by immunostaining for synaptic markers. High-intensity 3D-features in coCATS in proximity to synaptic markers are segmented and classified as pSCRs in case of triple colocalization between a pre-synaptic marker, the dense coCATS feature, and a post-synaptic marker. Detected pSCRs are then associated with manual volume segmentations of individual MFBs. Schematic (*top*) and single *xy*-planes of volumetric data (*bottom*) including coCATS (grey, *z*-STED), BASSOON (magenta, confocal) and SHANK2 (turquoise, *z*-STED) after denoising with Noise2Void (N2V, raw data: **Supplementary Fig. 7**). **b,** 3D-renderings of 22 randomly selected MFBs segmented from volumetric coCATS data at near-isotropic resolution (*z*-STED). MFB surface areas occupied by pSCRs are indicated in white. 3D-scale bars refer to bouton center. **c-e,** Quantification of MFB volume ($V_{MFB}$), MFB surface area ($A_{MFB}$), absolute ($A_{pSCR/MFB}$) and relative area occupied by pSCRs on individual MFBs ($A_{pSCR/MFB}/A_{MFB}$) ($n_{MFB}$=30). **f,g,** $A_{pSCR/MFB}$ as a function of bouton volume and surface area with linear regression ($n_{MFB}$=30). **h,** One of the imaging volumes used for MFB characterization (denoised with N2V, raw data: **Supplementary Fig. 7**) with coCATS (grey, *z*-STED), BASSOON (magenta, confocal) and SHANK2 (turquoise, *z*-STED), including manually segmented MFBs and automatically detected pSCRs. **i,** Deep-learning-based pSCR identification with training on paired structural (coCATS) and molecular (BASSOON immunostaining) super-resolved data. Prediction of synaptic marker location in unseen datasets is based on structural data alone. PSCRs are segmented similarly as in a, but using predicted BASSOON instead of immunostainings as guide to synaptic sites. **j,** Immunostained BASSOON (orange, *z*-STED) and BASSOON distribution predicted (blue) from coCATS structure in a dataset not included in the training. Corresponding pSCRs (yellow) segmented from coCATS data (grey, *z*-STED, N2V), guided by immunostained ($pSCRs_{immuno}$) or predicted BASSOON ($pSCRs_{prediction}$). **k,** Quantification of similarity between $pSCRs_{immuno}$ and $pSCRs_{prediction}$ by F1 score (ranging from 0 to 1, combining precision and recall) as a function of intersection over union (IOU) threshold.

---

## Synaptic input structure of identified, functionally characterized hippocampal neurons

To combine structural and functional readout, we performed coCATS in organotypic hippocampal slice cultures (**Fig. 3a,b, Supplementary Video 3**) after whole-cell patch clamp recordings. CATS revealed pSCRs and provided comprehensive structural context to individual, electrophysiologically characterized neurons, including DG granule cells, CA1 pyramidal neurons, CA3 interneurons, and CA3 pyramidal neurons, which were filled with fluorophores during recording for later identification (**Fig. 3c-e, Supplementary Fig. 11**).

Electrophysiological recordings during and after coCATS label application showed that neuronal activity (induced action potential generation) continued (**Supplementary Fig. 12**), demonstrating that cells were alive and functional at the time of fixation.

CATS visualized electrophysiologically characterized neurons together with surrounding structures at near-isotropic STED resolution, revealing key information missing with sparse positive cellular labeling alone (**Fig. 3c,g**). We set out to determine the complete connectivity structure of a proximal dendrite (**Fig. 3g**). Proximity of pre- and post-synaptic structures is an unreliable predictor of synaptic connectivity[41]. However, with application of deep-learning-based pSCR segmentation followed by manual validation, coCATS allowed us to identify synaptically connected structures (**Supplementary Fig. 13**). We mapped the synaptic input structure of a proximal dendrite in an electrophysiologically characterized CA3 pyramidal neuron (**Fig. 3h, Supplementary Fig. 14**). From the coCATS data, we reconstructed 58 structures (43 MFB- and 14 non-MFB structures synaptically connected to the dendrite of the recorded cell) to clarify the intricate 3D spatial arrangement of individual MFBs and their post-synaptic complex spines (**Fig. 3h,i, Supplementary Video 4**). MFBs contacting the same dendrite displayed a wide range of sizes, with smaller mean volume and larger spread (**Fig. 3j**, 6.85±5.95 $\mu m^3$) than the manually selected MFBs in adult brain in Fig. 2, potentially reflecting an earlier developmental stage[37] in the ~20 days *in vitro* slice cultures. The volume distribution of spines (68 reconstructed) on the pyramidal neuron included large spines with highly complex shapes, i.e. quintessential thorny excrescences. However, the size distribution was strongly skewed towards small spines emanating from the shaft, also in contact with MFBs (**Fig. 3j**). We next evaluated connectivity of individual MFBs (**Fig. 3k**). Interestingly, only ~1/3 of MFBs formed connections with a single spine, whereas synaptic contact with multiple spines was more common, with single boutons connecting to up to 7 different spine structures. Conversely, individual, especially small, spines mostly connected to single MFBs, but some (16.4%), mostly elaborate, complex spines, were synaptically contacted by more than one MFB (e.g. **Fig. 3i)**. We observed a maximum of 6 pre-synaptic boutons for the largest of the post-synaptic structures (**Fig. 3l**). Together, these data shed light on the complex organization of the mossy fiber circuitry, with signal integration at CA3 pyramidal neurons occurring even at the level of individual thorny excrescences. More broadly, it demonstrates the power of CATS to provide quantitative data on structural and functional connectivity.

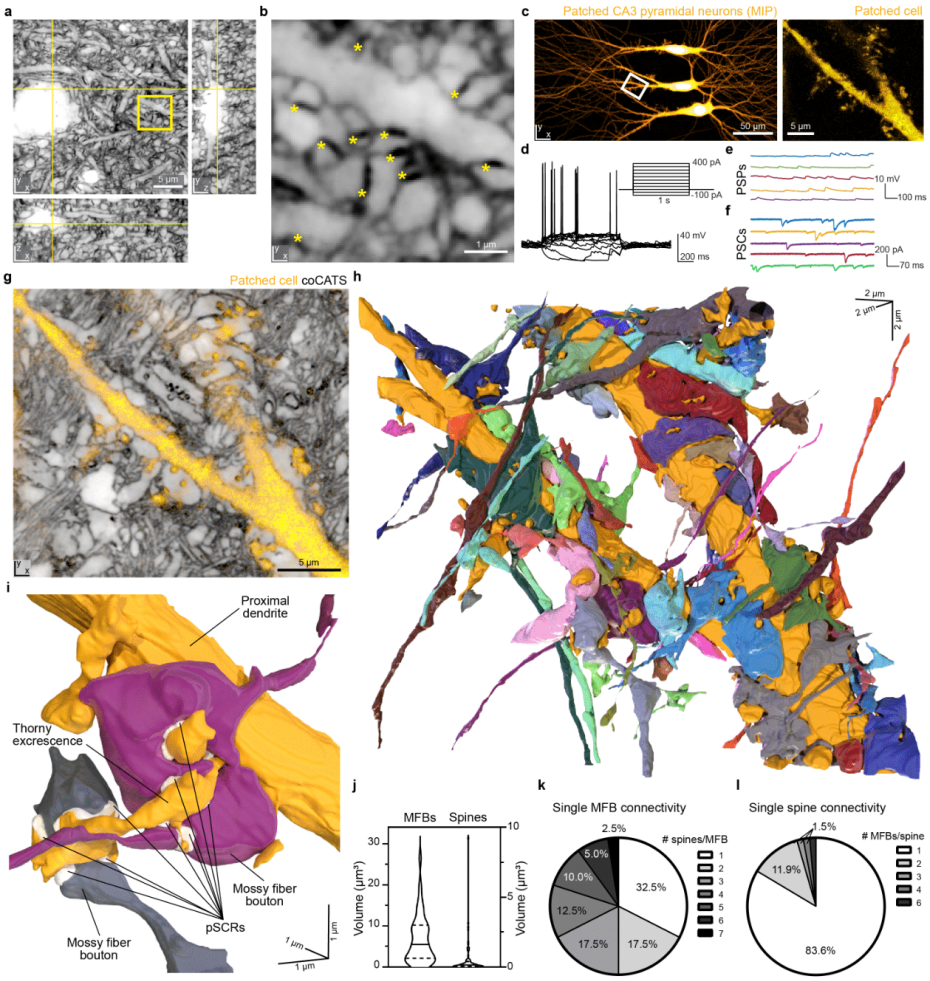


**Fig. 3| Reconstruction of CA3 pyramidal neuron local input field with coCATS. a,** Orthogonal views of a coCATS imaging volume recorded with *z*-STED at near-isotropic resolution (N2V, raw data: **Supplementary Fig. 7**) in neuropil of an organotypic hippocampal brain slice. Yellow lines indicate position of displayed planes. **b,** Magnified view of the boxed region in a. Asterisks: pSCRs. **c,** (*Left*) CA3 pyramidal neurons in an organotypic hippocampal slice whole-cell patch-clamped and filled with fluorescent dye (Lucifer yellow). (*Right*) Magnified view of a piece of proximal dendrite in the boxed region. **d,** Action potential response of the middle pyramidal neuron elicited by current injection (inset). **e,f,** Spontaneous post-synaptic potentials (PSPs) and post-synaptic currents (PSCs) recorded from middle pyramidal neuron. **g,** CoCATS (grey, *z*-STED, N2V) overlaid with the intracellular label (yellow, confocal) of the middle pyramidal neuron provides super-resolved information on its local micro-

environment. **h,** 3D-rendering of the same proximal dendrite (gold) and 57 structures synaptically connected to it, reconstructed from the volumetric coCATS data. Connectivity was inferred by the presence of pSCRs between the positively labeled dendrite and the respective adjacent structures. **i,** 3D-rendering of two MFBs (violet, grey) forming complex connections with one thorny excrescence of the proximal dendrite. PSCRs are indicated in white. **j,** Violin plots with median (line) and quartiles (dashed lines) of the MFB volumes ($n_{MFB}$=40) contacting the recorded pyramidal neuron and its spines ($n_{spine}$=68). **k,l,** Quantification of connectivity pattern of individual MFBs and pyramidal neuron spines.

---

## Synaptic output structure and differential tissue architecture across regions

We next took advantage of CATS' contextual information from single synapse to regional scale, characterizing the synaptic output field of an individual DG granule cell in an organotypic hippocampal slice culture. We performed coCATS labeling after electrophysiological recording (**Supplementary Fig. 15**) and biocytin-filling. We followed the main axon, as it travelled from the cell body in the DG granule cell layer through the hilus to the CA3 *stratum lucidum* (**Fig. 4a**). We performed volumetric, isotropically resolving STED imaging around 17 conspicuous pre-synaptic boutons, focusing mostly on complex boutons (**Fig. 4b,c**). While the axon trajectory and bouton structure could be determined already from the super-resolved positive single-cell label, CATS was required to identify post-synaptic partners via pSCR connectivity, evaluated by deep-learning-based segmentation and manual validation, and to reveal structural context (**Fig. 4c, Supplementary Fig. 15,16**). We analyzed complex mossy fiber boutons, but also smaller *en passant* boutons with identified pSCRs. *En passant* boutons displayed a single synaptic transmission site (one pSCR) to thin dendritic structures and lacked filopodia. In contrast, large boutons featured multiple pSCRs and filopodia in both the hilus (4.0±2.0 filopodia per analyzed bouton) and CA3 *stratum lucidum* (8.5±3.4 filopodia per bouton). These structures formed complex synapses with hilar mossy cells and CA3 pyramidal neurons, respectively, identifiable from their cellular morphology and context in CATS staining. We reconstructed synaptic units in the hilus (**Fig. 4d, Supplementary Video 5**) and the CA3 *stratum lucidum* (**Fig. 4e, Supplementary Video 6**), showing the difference in complexity between *en passant* boutons (boutons 2 and 4) and complex boutons (bouton 13). In CA3, we observed connections between bouton 13 and nine neuronal structures (**Fig. 4e**). These included both engulfment of thorny excrescences by the main bouton, and contacts via filopodial extensions. We also observed pSCRs at synapses

formed by filopodia, which are thought to mainly contact inhibitory interneurons, remarkably enhancing complexity of the circuitry[42].

Seeking to reveal tissue architecture beyond hippocampal circuitry, we returned to *in vivo* coCATS labeling. Microinjection into lateral ventricles or cortex (**Supplementary Fig. 17**) visualized the diversity of cell and tissue architecture in cerebral cortex, different areas of the hippocampus (dentate gyrus, CA1, CA3), striatum, corpus callosum, thalamus, hypothalamus, hindbrain and cerebellum (**Fig. 4f, Supplementary Fig. 18**). Tissue structure was intact beyond ~200 µm of local damage around the injection site (**Supplementary Fig. 17**). STED disclosed rich structural detail of neuronal and glial processes, synapses, axon bundles, blood vessels, and ependyma in all these regions, with e.g. myelinated axons in the corpus callosum standing out by demarcation of the inner border of myelin sheaths (**Fig. 4f**).

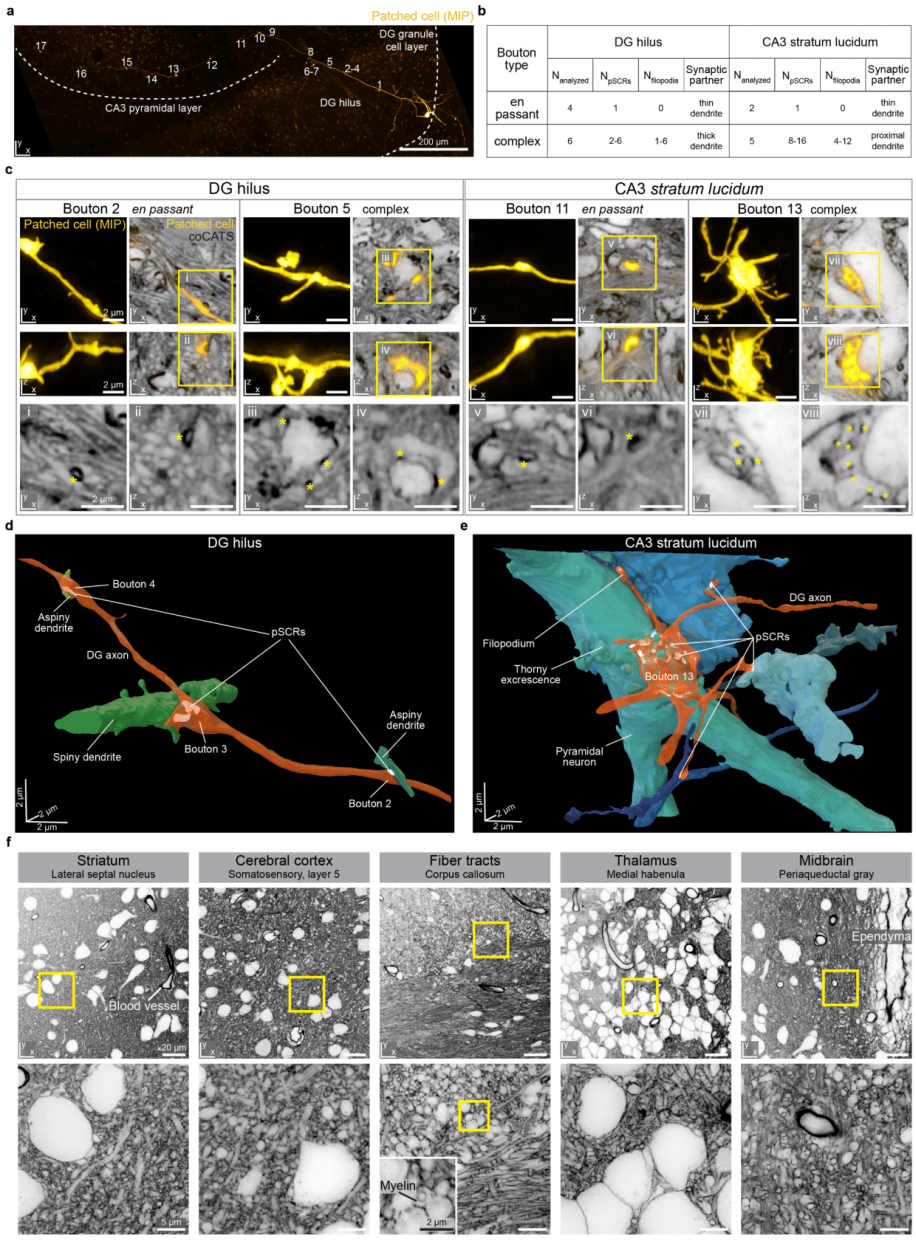


| Bouton type | DG hilus | | | | CA3 stratum lucidum | | | |
|---|---|---|---|---|---|---|---|---|
| | $N_{analyzed}$ | $N_{pSCRs}$ | $N_{filopodia}$ | Synaptic partner | $N_{analyzed}$ | $N_{pSCRs}$ | $N_{filopodia}$ | Synaptic partner |
| en passant | 4 | 1 | 0 | thin dendrite | 2 | 1 | 0 | thin dendrite |
| complex | 6 | 2-6 | 1-6 | thick dendrite | 5 | 8-16 | 4-12 | proximal dendrite |

**Fig. 4| Tissue architecture and single-cell output structure at individual synapse level across brain regions. a,** Maximum intensity projection (MIP) of a whole-cell patch-clamped and biocytin-filled DG granule cell in organotypic hippocampal slice (confocal). 17 conspicuous boutons are marked along the main axon's trajectory, projecting as mossy fiber

from the DG granule cell layer through the hilus to the CA3 *stratum lucidum*. **b,** Characteristics of analyzed synaptic boutons. **c,** Single *xy*- and *xz*-planes of 4 example super-resolved volumes comprising specific synapses as marked in a, with coCATS (grey, *z*-STED, N2V) revealing local microenvironment of the positively labeled mossy fiber (yellow, *z*-STED, N2V) (raw data: **Supplementary Fig. 7**). (*Bottom*) Magnified views of the coCATS channel with asterisks indicating pSCRs used to identify synaptic partners. **d,e,** 3D-renderings of two axon stretches with boutons, pSCRs, and synaptically connected structures in DG hilus and CA3 *stratum lucidum*. **f,** Architecture of various regions in near-natively preserved brain revealed by coCATS with *in vivo* microinjection. Organization of cell bodies, dendrites, axons, synapses, ependyma around liquor spaces, and blood vessels is visible. Myelinated axons can be distinguished by a fine demarcation of the inner border of the myelin sheath (inset, corpus callosum). (*Top*) Confocal, (*bottom*) *xy*-STED. Raw data.

---

## Large-scale tissue analysis with CATS and expansion microscopy

ExM involves hydrogel embedding, disruption of mechanical cohesiveness of the tissue, and subsequent isotropic swelling, while conserving relative spatial arrangements[5]. This provides effective super-resolution with diffraction-limited readout. It reduces autofluorescence and homogenizes sample refractive index to that of water, clearing the tissue and mitigating aberrations and scattering. Together, this facilitates acquisition of axially extended, super-resolved volumes. We therefore sought to combine CATS' capability to decode tissue architecture with the strengths of ExM. Expansion requires a label that is faithfully retained in the hydrogel and is minimally affected by the radical chemistry during gel polymerization and heat/chemical denaturation during preparation. Biotin fulfills these criteria, such that we screened for biotin-containing coCATS labels (**Supplementary Fig. 1**). We found that an additional chemical group was required to ensure sufficient extra-to-intracellular contrast and chose $PEG_{12}$. We live labeled organotypic hippocampal slice cultures with NHS-$PEG_{12}$-biotin, used heat/chemical denaturation (**Fig. 5a,b, Supplementary Fig. 19**) or enzymatic digestion (**Supplementary Fig. 19**) to disrupt tissue cohesiveness. We expanded ~4-fold with the magnified analysis of proteomes (MAP)[6] and protein-retention ExM[8] approaches, respectively, followed by application of fluorophore-conjugated streptavidin to visualize the extracellular label. This provided signal amplification and flexibility with downstream processing. We recorded confocal stacks of ~400 µm axial range, showing that it is straightforward to obtain super-resolved context over 100 µm depth at native tissue scale.

For several important preparations, in particular previously fixed brain, it is not possible to perform extracellular labeling while the tissue is alive. We therefore screened binders to ECS-resident molecules that were widely and homogeneously distributed in mouse brain (resident CATS, rCATS). Different polysaccharide-binding proteins showed distinct labeling patterns, highlighting the molecular diversity in the ECS (**Supplementary Fig. 20**). Wheat germ agglutinin (WGA) binds to N-acetyl-D-glucosamine and sialic acid and has been used in different organs to outline blood vessels or cell bodies[43,44]. Labeling fixed mouse brain tissue with fluorescently marked WGA revealed hippocampal architecture clearly (**Fig. 1b**). Myelinated axons were distinguishable in STED mode, as validated by specific staining (**Supplementary Fig. 21**), as well as carbohydrate-rich nuclear pores. However, WGA features few lysines for hydrogel anchoring, resulting in poor retention upon expansion (**Supplementary Fig. 22**). To make rCATS compatible with ExM, we developed a dedicated signal retention strategy (**Supplementary Fig. 22**), transferring information from biotinylated WGA to acrylamide-modified streptavidin copolymerizing with the gel. Large-scale readout of expanded samples with spinning disc confocal microscopy allowed high resolution visualization of tissue architecture (**Fig. 5c, Supplementary Fig. 23**). To illustrate the rich information contained in this type of data, we imaged a 1.4x1.7x0.32 $mm^3$ (post-expansion; expansion factor 4.5; 303x371x70 $\mu m^3$ pre-expansion; ~1 TB) volume of the DG crest and enclosed hilus, wherein rCATS provided structural context to sparse Thy1-EGFP labeled neurons and excitatory synapses labeled for SHANK2 (**Fig. 5d-f**). Given the large scale of the data, we skeletonized the major dendritic arborizations of an unlabeled example neuron from the rCATS signal. This cell, identified as a mossy cell by its morphology and the presence of multiple MFBs in contact with its dendrites, can be studied amidst its 3D-context, demonstrating the utility of rCATS for unbiased imaging and analysis of any neuronal population in the tissue (**Fig. 5f,g**).

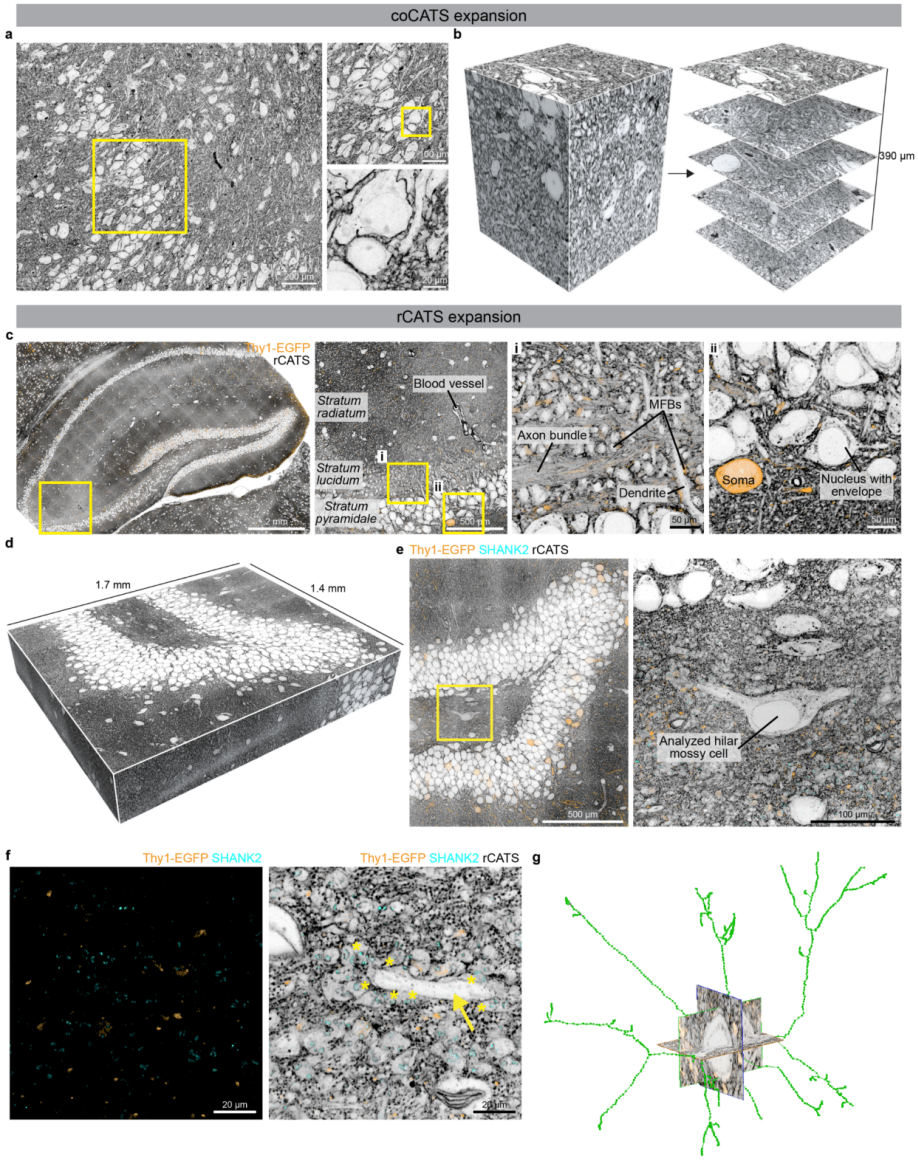


**Fig. 5| Large-scale imaging of tissue context with expansion microscopy. a,** Organotypic hippocampal brain slice live labeled with coCATS (NHS-$PEG_{12}$-biotin probe) and ~4-fold expanded with MAP[6]. Confocal image with two progressive zoom-ins (raw data). Scale bars refer to tissue size after expansion throughout. **b,** Extended depth imaging in ~4-fold expanded organotypic hippocampal brain slice after live coCATS labeling, showing the imaging volume (*left*) and five single planes at progressively larger depths (*right*). Axial imaging range in

confocal readout (N2V) was ~400 µm, corresponding to ~100 µm in the original tissue. **c,** Brain tissue section from previously perfusion-fixed Thy1-EGFP+ adult mouse with sparse neuronal labeling by cytosolic EGFP expression (visualized with immunostaining, orange), labeled with rCATS and ~4-fold expanded by protein-retention ExM[8], showing full hippocampal area. Zoomed views in the CA3 at two different magnifications show that rCATS delineates tissue context from gross organization down to sub-cellular morphology (confocal, raw data). Zoom i shows mossy fiber boutons as globular structures among axon (mossy fiber) bundles in the *stratum lucidum*, zoom ii shows the arrangement of cell bodies and neuropil at the outer border of the *stratum pyramidale*. **d,** 3D-representation of a volume of the DG crest of a previously perfusion-fixed Thy1-EGFP+ adult mouse. After rCATS labeling (grey, N2V), immunostaining for SHANK2 (cyan, N2V) and EGFP (orange, N2V), the sample was 4.5-fold expanded and imaged with high-speed spinning disc microscopy. The displayed volume corresponds to 303x371x70 µm$^3$ in original tissue volume. **e**, Single *xy*-plane of the data represented in d with zoom-in on the soma of a hilar mossy cell. **f,** Different plane from the same volume showing immunostainings alone and overlaid with rCATS at higher magnification. The yellow arrow indicates a dendrite belonging to the mossy cell displayed in e, lined by MFBs with SHANK2 located at the synaptic transmission sites. Yellow asterisks highlight a subset of MFBs in contact with the mossy cell dendrite. **g,** Skeletonization of the major branches of the hilar mossy cell in e,f from rCATS data.

---

## CATS in human brain tissue

Analysis of human clinical brain samples largely relies on conventional histology stainings, such as hematoxylin and eosin, that coarsely represent tissue architecture. To test whether CATS can be adopted to human samples, we obtained fixed hippocampal tissue extracted from a 36 year-old male patient undergoing epilepsy surgery. We applied rCATS at confocal resolution together with immunolabeling of neuronal processes (microtubule-associated protein 2, MAP2) and excitatory synapses (HOMER1). Also in the human samples, rCATS labeling revealed contextual information and differential architecture in the layers of the DG (**Fig. 6a,b**). In addition, comprehensive visualization by rCATS allowed detailed, yet straightforward, assessment of tissue preservation, the major quality determinant for microanatomical studies of clinical brain material. In contrast, immunostainings alone without rCATS made it challenging to distinguish effects of tissue degradation due to the sparse distribution patterns of target molecules. RCATS is thus a valuable resource for studying tissue structure and single-cell morphology in clinical specimens of healthy and diseased individuals.

Finally, we sought to demonstrate the applicability of CATS to human cerebral organoids. Organoids are emerging as an experimentally tractable human system for studying brain development and disease mechanisms[45]. We asked whether CATS could be extended to densely reconstruct the cellular constituents of an organoid volume. We chose coCATS, as it is independent of the deposition of extracellular matrix molecules in this early development model system. Using STED at near-isotropic resolution allowed dense cellular segmentation (**Fig. 6c-e, Supplementary Video 7**), making CATS useful for cell and tissue phenotyping also in this sample type. The organoid showed lower complexity than the other sample types analyzed. However, this proof-of-principle experiment paves the way towards large-scale dense reconstruction of complex tissue samples with light microscopy.

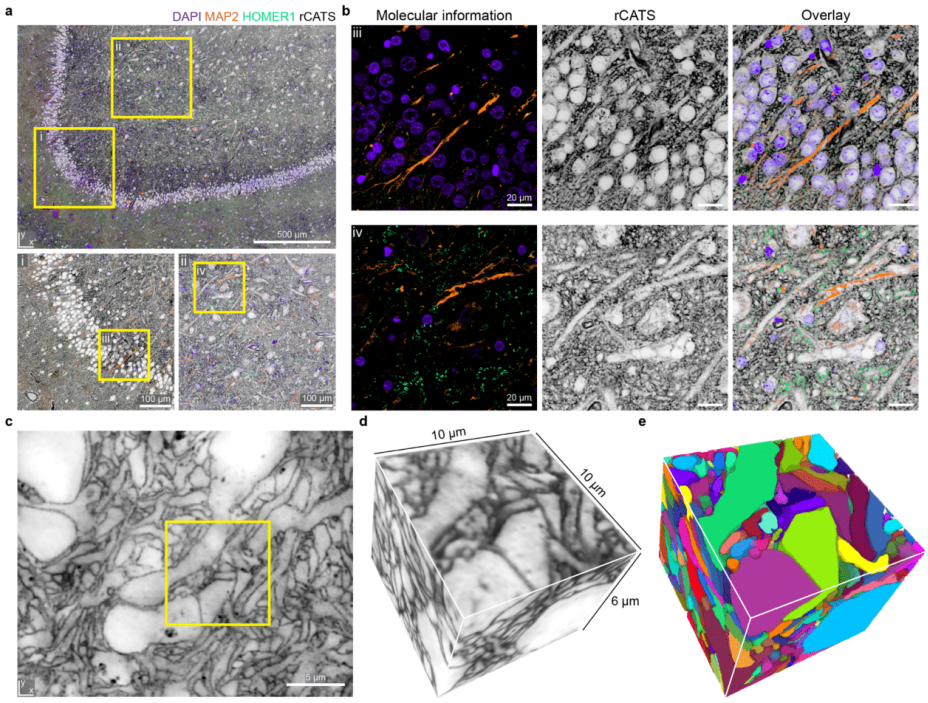


**Fig. 6| Tissue architecture in human nervous tissue. a,** RCATS (grey) in the DG-region of a human hippocampal surgery specimen with additional staining for dendrites (MAP2, orange), excitatory synapses (HOMER1, green) and nuclei (DAPI, purple). (*Top*) Confocal, with magnified views of boxed regions (*bottom*). **b,** Magnified views of the boxed regions iii and iv in a. (*Left*) Molecular stainings alone, (*middle*) tissue architecture revealed by rCATS, (*right*) overlay. Raw data. **c,** CoCATS in human cerebral organoid. Single plane of super-

resolved volume (*z*-STED, N2V, adaptive histogram equalization). **d,** Subvolume of the same dataset, as indicated in c. **e,** Dense tissue reconstruction with coCATS via manual segmentation of the volume in d.

## Discussion

Here we developed CATS, a labeling, imaging, and analysis platform to map brain tissue architecture across spatial scales with light microscopy. CATS places cells and specific molecules into their tissue context, and allows quantifying neuronal connectivity and reconstructing tissue structure down to subcellular nano-morphology, including single synapses. Designed for fixed rather than living tissues, it facilitates analysis of diverse specimens and extended volumes, using readily available super-resolution approaches, specifically STED and expansion microscopy. Contrary to the selective representation with positive cellular labeling, CATS displays the tissue with all its cellular structures in an unbiased fashion. CATS labels molecules in extracellular space and on cell surfaces, with the structural imaging channel remaining free from intracellular complexity. This creates a clear boundary between cells and allows distinguishing cellular structures at high contrast in extremely dense brain tissue, even when read out at diffraction-limited resolution or comparatively moderate resolution increase over the diffraction limit. Together with broad compatibility with standard molecular labeling techniques, this property will facilitate widespread incorporation into tissue analysis workflows, dramatically advancing their information content.

We employed two labeling strategies, coCATS and rCATS, to cater for diverse brain tissue preparations, including native rodent brain, organotypic slice cultures, previously fixed mouse and human brain tissue, and human cerebral organoids. Broad labeling of extracellular molecules in coCATS and the resulting high labeling density enabled reconstruction of single synapse morphology, whereas rCATS extended usefulness to sample types that do not allow live labeling. CATS is a technologically straightforward approach to 3D tissue reconstruction in the vast number of applications where EM resolution is not essential and adds super-resolved molecular information to 3D reconstruction. By directly bridging spatial scales (mm–nm), it avoids complex correlative workflows that require reconciling different sample preparation and imaging modalities.

Obvious improvements include specifically engineering labels for enhanced hydrogel retention[46] or signal amplification and, in rCATS, multi-component labeling of extracellular molecules, as well as increasing readout speed with light-sheet microscopy[14]. CATS paves the

way towards development of molecularly informed, light-microscopy based connectomics. For this, specifically increasing optical resolution or expansion factors[47–50,29,28] should allow tracing also the thinnest of neuronal structures, finer than the resolution employed here.

We used the hippocampal mossy fiber circuitry as first application target. Quantifications of single-bouton geometry and connectivity are in line with benchmark EM data[36,38,39]. However, in contrast to EM, CATS enabled straightforward incorporation of specific molecular information in 3D-reconstructions and massively reduced requirements in time, personnel and equipment over classical serial-sectioning EM studies. For example, imaging the three volumes used to reconstruct the 30 MFBs in **Fig. 2** required only ~4h hands-on sample preparation and 3x1.5 h total imaging time for the 3-channel measurement.

Taking advantage of comprehensive tissue visualization, we addressed a long-standing challenge in brain tissue imaging by applying CATS to decode synaptic connectivity. A surprising, but powerful discovery is that coCATS unveils putative synaptic cleft regions (pSCRs) by a prominent labeling pattern within its structural context. These are detectable with specifically tailored machine learning analysis even in absence of molecular staining. Accordingly, pSCRs can be leveraged to infer and quantify synaptic connections, and identify synaptic partners among neighboring structures. We used this to reconstruct the local synaptic input structure of an identified CA3 pyramidal neuron and to characterize the synaptic output structure of a DG granule cell when following its main axon across the hippocampus. In both cases our analysis revealed stunning complexity, showing CATS' power to unravel the structural correlates of diverging and converging signal integration in the central nervous system.

Our analysis presents one of the largest datasets of local mossy fiber connectivity reconstruction to date. Throughput of 3D reconstruction was limited by manual volume segmentation. Overall throughput will substantially benefit from replacing manual cell shape segmentation with deep-learning-based approaches adopted from EM connectomics[51–53], as already employed in super-resolution reconstruction of living brain tissue[24]. This will make large-scale studies of local connectivity, complete neuronal synaptic input or output fields, and neuron-glia interplay[21] feasible. We furthermore expect CATS to seamlessly integrate with complementary technologies, such as calcium imaging or viral circuit tracing[54,55], similar to the combined structural and functional characterization demonstrated here with whole-cell patch clamp recordings. CATS will be an important tool to clarify how tissue architecture and synaptic connectivity are remodeled in response to neuronal activity, during development, or in neurodevelopmental or neurodegenerative disease models. CATS furthermore opens the

door to unbiased phenotyping of cell and tissue structure of rodent and patient-derived human samples, shedding new light on tissue architecture, cell-cell interactions, and subcellular morphology both in healthy and diseased brain. High throughput, easy adoptability, and seamless pairing of structural data with molecular and functional information puts CATS in an excellent position to clarify structure-function or genotype-to-tissue-phenotype relationships. Taken together, CATS is a powerful tool for phenotyping brain and provides unprecedented views into cellular microenvironments both in health and disease.

# References

1. Klar, T. A., Jakobs, S., Dyba, M., Egner, A. & Hell, S. W. Fluorescence microscopy with diffraction resolution barrier broken by stimulated emission. *PNAS* **97,** 8206–8210 (2000).

2. Betzig, E., Patterson, G. H., Sougrat, R., Lindwasser, O. W., Olenych, S., Bonifacino, J. S., Davidson, M. W., Lippincott-Schwartz, J. & Hess, H. F. Imaging Intracellular Fluorescent Proteins at Nanometer Resolution. *Science* **313,** 1642–1645 (2006).

3. Rust, M. J., Bates, M. & Zhuang, X. Sub-diffraction-limit imaging by stochastic optical reconstruction microscopy (STORM). *Nature Methods* **3,** 793–796 (2006).

4. Hess, S. T., Girirajan, T. P. K. & Mason, M. D. Ultra-High Resolution Imaging by Fluorescence Photoactivation Localization Microscopy. *Biophysical Journal* **91,** 4258–4272 (2006).

5. Chen, F., Tillberg, P. W. & Boyden, E. S. Expansion microscopy. *Science* **347,** 543–548 (2015).

6. Ku, T., Swaney, J., Park, J.-Y., Albanese, A., Murray, E., Cho, J. H., Park, Y.-G., Mangena, V., Chen, J. & Chung, K. Multiplexed and scalable super-resolution imaging of three-dimensional protein localization in size-adjustable tissues. *Nature Biotechnology* **34,** 973–981 (2016).

7. Chozinski, T. J., Halpern, A. R., Okawa, H., Kim, H.-J., Tremel, G. J., Wong, R. O. L. & Vaughan, J. C. Expansion microscopy with conventional antibodies and fluorescent proteins. *Nature Methods* **13,** 485–488 (2016).

8. Tillberg, P. W., Chen, F., Piatkevich, K. D., Zhao, Y., Yu, C.-C., English, B. P., Gao, L., Martorell, A., Suk, H.-J., Yoshida, F., DeGennaro, E. M., Roossien, D. H., Gong, G., Seneviratne, U., Tannenbaum, S. R., Desimone, R., Cai, D. & Boyden, E. S. Protein-retention expansion microscopy of cells and tissues labeled using standard fluorescent proteins and antibodies. *Nature Biotechnology* **34,** 987–992 (2016).

9. Dani, A., Huang, B., Bergan, J., Dulac, C. & Zhuang, X. Superresolution imaging of chemical synapses in the brain. *Neuron* **68,** 843–856 (2010).

10. Liu, K. S. Y., Siebert, M., Mertel, S., Knoche, E., Wegener, S., Wichmann, C., Matkovic, T., Muhammad, K., Depner, H., Mettke, C., Bückers, J., Hell, S. W., Müller, M., Davis, G. W., Schmitz, D. & Sigrist, S. J. RIM-Binding Protein, a Central Part of the Active Zone, Is Essential for Neurotransmitter Release. *Science* **334,** 1565–1569 (2011).

11. Tang, A.-H., Chen, H., Li, T. P., Metzbower, S. R., MacGillavry, H. D. & Blanpied, T. A. A trans-synaptic nanocolumn aligns neurotransmitter release to receptors. *Nature* **536,** 210–214 (2016).

12. Xu, K., Zhong, G. & Zhuang, X. Actin, Spectrin, and Associated Proteins Form a Periodic Cytoskeletal Structure in Axons. *Science* **339,** 452–456 (2013).

13. Tønnesen, J., Katona, G., Rózsa, B. & Nägerl, U. V. Spine neck plasticity regulates compartmentalization of synapses. *Nature Neuroscience* **17,** 678–685 (2014).

14. Gao, R., Asano, S. M., Upadhyayula, S., Pisarev, I., Milkie, D. E., Liu, T.-L., Singh, V., Graves, A., Huynh, G. H., Zhao, Y., Bogovic, J., Colonell, J., Ott, C. M., Zugates, C., Tappan, S., Rodriguez, A., Mosaliganti, K. R., Sheu, S.-H., Pasolli, H. A., Pang, S., Xu, C. S., Megason, S. G., Hess, H., Lippincott-Schwartz, J., Hantman, A., Rubin, G. M., Kirchhausen, T., Saalfeld, S., Aso, Y., Boyden, E. S. & Betzig, E. Cortical column and whole-brain imaging with molecular contrast and nanoscale resolution. *Science* **363,** eaau8302 (2019).

15. Kitamura, K., Judkewitz, B., Kano, M., Denk, W. & Häusser, M. Targeted patch-clamp recordings and single-cell electroporation of unlabeled neurons in vivo. *Nat Methods* **5,** 61–67 (2008).

16. Godin, A. G., Varela, J. A., Gao, Z., Danné, N., Dupuis, J. P., Lounis, B., Groc, L. & Cognet, L. Single-nanotube tracking reveals the nanoscale organization of the extracellular space in the live brain. *Nature Nanotech* **12,** 238–243 (2017).

17. Tønnesen, J., Inavalli, V. V. G. K. & Nägerl, U. V. Super-Resolution Imaging of the Extracellular Space in Living Brain Tissue. *Cell* **172,** 1108-1121.e15 (2018).

18. Briggman, K. L., Helmstaedter, M. & Denk, W. Wiring specificity in the direction-selectivity circuit of the retina. *Nature* **471,** 183–188 (2011).

19. Hell, S. W. & Wichmann, J. Breaking the diffraction resolution limit by stimulated emission: stimulated-emission-depletion fluorescence microscopy. *Optics Letters* **19,** 780–782 (1994).

20. Jahr, W., Velicky, P. & Danzl, J. G. Strategies to maximize performance in STimulated Emission Depletion (STED) nanoscopy of biological specimens. *Methods* **174,** 27–41 (2020).

21. Arizono, M., Inavalli, V. V. G. K., Panatier, A., Pfeiffer, T., Angibaud, J., Levet, F., Ter Veer, M. J. T., Stobart, J., Bellocchio, L., Mikoshiba, K., Marsicano, G., Weber, B., Oliet, S. H. R. & Nägerl, U. V. Structural basis of astrocytic Ca 2+ signals at tripartite synapses. *Nature Communications* **11,** 1–15 (2020).

22. Arizono, M., Inavalli, V. V. G. K., Bancelin, S., Fernández-Monreal, M. & Nägerl, U. V. Super-resolution shadow imaging reveals local remodeling of astrocytic microstructures and brain extracellular space after osmotic challenge. *Glia* **69,** 1605–1613 (2021).

23. Inavalli, V. V. G. K., Lenz, M. O., Butler, C., Angibaud, J., Compans, B., Levet, F., Tønnesen, J., Rossier, O., Giannone, G., Thoumine, O., Hosy, E., Choquet, D., Sibarita, J.-B. & Nägerl, U. V. A super-resolution platform for correlative live single-molecule imaging and STED microscopy. *Nat Methods* **16,** 1263–1268 (2019).

24. Velicky, P., Miguel, E., Michalska, J. M., Wei, D., Lin, Z., Watson, J. F., Troidl, J., Beyer, J., Ben-Simon, Y., Sommer, C., Jahr, W., Cenameri, A., Broichhagen, J., Grant, S. G. N., Jonas, P., Novarino, G., Pfister, H., Bickel, B. & Danzl, J. G. Saturated reconstruction of living brain tissue. 2022.03.16.484431 Preprint at https://doi.org/10.1101/2022.03.16.484431 (2022)

25. M'Saad, O. & Bewersdorf, J. Light microscopy of proteins in their ultrastructural context. *Nature Communications* **11,** 3850 (2020).

26. Mao, C., Lee, M. Y., Jhan, J.-R., Halpern, A. R., Woodworth, M. A., Glaser, A. K., Chozinski, T. J., Shin, L., Pippin, J. W., Shankland, S. J., Liu, J. T. C. & Vaughan, J. C. Feature-rich covalent stains for super-resolution and cleared tissue fluorescence microscopy. *Science Advances* **6,** eaba4542 (2020).

27. Klimas, A., Gallagher, B., Wijesekara, P., Fekir, S., Stolz, D., Cambi, F., Watkins, S., Barth, A., Moore, C., Ren, X. & Zhao, Y. *Nanoscale Imaging of Biomolecules using Molecule Anchorable Gel-enabled Nanoscale In-situ Fluorescence Microscopy*. (In Review, 2021). doi:10.21203/rs.3.rs-858006/v1

28. Damstra, H. G., Mohar, B., Eddison, M., Akhmanova, A., Kapitein, L. C. & Tillberg, P. W. Visualizing cellular and tissue ultrastructure using Ten-fold Robust Expansion Microscopy (TREx). *eLife* **11,** e73775 (2022).

29. M'Saad, O., Kasula, R., Kondratiuk, I., Kidd, P., Falahati, H., Gentile, J. E., Niescier, R. F., Watters, K., Sterner, R. C., Lee, S., Liu, X., Camilli, P. D., Rothman, J. E., Koleske, A. J., Biederer, T. & Bewersdorf, J. All-optical visualization of specific molecules in the ultrastructural context of brain tissue. 2022.04.04.486901 Preprint at https://doi.org/10.1101/2022.04.04.486901 (2022)

30. Qian, C., Miao, K., Lin, L.-E., Chen, X., Du, J. & Wei, L. Super-resolution label-free volumetric vibrational imaging. *Nat Commun* **12,** 3648 (2021).

31. Mori, M., Abegg, M. H., Gähwiler, B. H. & Gerber, U. A frequency-dependent switch from inhibition to excitation in a hippocampal unitary circuit. *Nature* **431,** 453–456 (2004).

32. Vandael, D., Borges-Merjane, C., Zhang, X. & Jonas, P. Short-Term Plasticity at Hippocampal Mossy Fiber Synapses Is Induced by Natural Activity Patterns and Associated with Vesicle Pool Engram Formation. *Neuron* **107,** 509-521.e7 (2020).

33. Chicurel, M. E. & Harris, K. M. Three-dimensional analysis of the structure and composition of CA3 branched dendritic spines and their synaptic relationships with mossy fiber boutons in the rat hippocampus. *Journal of Comparative Neurology* **325,** 169–182 (1992).

34. Perez de Arce, K., Schrod, N., Metzbower, S. W. R., Allgeyer, E., Kong, G. K.-W., Tang, A.-H., Krupp, A. J., Stein, V., Liu, X., Bewersdorf, J., Blanpied, T. A., Lucić, V. & Biederer, T. Topographic Mapping of the Synaptic Cleft into Adhesive Nanodomains. *Neuron* **88,** 1165–1172 (2015).

35. Krull, A., Buchholz, T.-O. & Jug, F. Noise2Void - Learning Denoising from Single Noisy Images. *arXiv:1811.10980 [cs]* (2019). at <http://arxiv.org/abs/1811.10980>

36. Wilke, S. A., Antonios, J. K., Bushong, E. A., Badkoobehi, A., Malek, E., Hwang, M., Terada, M., Ellisman, M. H. & Ghosh, A. Deconstructing Complexity: Serial Block-Face Electron Microscopic Analysis of the Hippocampal Mossy Fiber Synapse. *J. Neurosci.* **33,** 507–522 (2013).

37. Galimberti, I., Gogolla, N., Alberi, S., Santos, A. F., Muller, D. & Caroni, P. Long-Term Rearrangements of Hippocampal Mossy Fiber Terminal Connectivity in the Adult Regulated by Experience. *Neuron* **50,** 749–763 (2006).

38. Rollenhagen, A., Sätzler, K., Rodríguez, E. P., Jonas, P., Frotscher, M. & Lübke, J. H. R. Structural Determinants of Transmission at Large Hippocampal Mossy Fiber Synapses. *J. Neurosci.* **27,** 10434–10444 (2007).

39. Martin, E. A., Woodruff, D., Rawson, R. L. & Williams, M. E. Examining Hippocampal Mossy Fiber Synapses by 3D Electron Microscopy in Wildtype and Kirrel3 Knockout Mice. *eNeuro* **4,** ENEURO.0088-17.2017 (2017).

40. Ounkomol, C., Seshamani, S., Maleckar, M. M., Collman, F. & Johnson, G. R. Label-free prediction of three-dimensional fluorescence images from transmitted-light microscopy. *Nat Methods* **15,** 917–920 (2018).

41. Kasthuri, N., Hayworth, K. J., Berger, D. R., Schalek, R. L., Conchello, J. A., Knowles-Barley, S., Lee, D., Vázquez-Reina, A., Kaynig, V., Jones, T. R., Roberts, M., Morgan, J. L., Tapia, J. C., Seung, H. S., Roncal, W. G., Vogelstein, J. T., Burns, R., Sussman, D. L., Priebe, C. E., Pfister, H. & Lichtman, J. W. Saturated Reconstruction of a Volume of Neocortex. *Cell* **162,** 648–661 (2015).

42. Acsády, L., Kamondi, A., Sík, A., Freund, T. & Buzsáki, G. GABAergic Cells Are the Major Postsynaptic Targets of Mossy Fibers in the Rat Hippocampus. *Journal of Neuroscience* **18,** 3386–3403 (1998).

43. Kishi, J. Y., Lapan, S. W., Beliveau, B. J., West, E. R., Zhu, A., Sasaki, H. M., Saka, S. K., Wang, Y., Cepko, C. L. & Yin, P. SABER amplifies FISH: enhanced multiplexed imaging of RNA and DNA in cells and tissues. *Nat Methods* **16,** 533–544 (2019).

44. Todorov, M. I., Paetzold, J. C., Schoppe, O., Tetteh, G., Shit, S., Efremov, V., Todorov-Völgyi, K., Düring, M., Dichgans, M., Piraud, M., Menze, B. & Ertürk, A. Machine learning analysis of whole mouse brain vasculature. *Nat Methods* **17,** 442–449 (2020).

45. Lancaster, M. A., Renner, M., Martin, C.-A., Wenzel, D., Bicknell, L. S., Hurles, M. E., Homfray, T., Penninger, J. M., Jackson, A. P. & Knoblich, J. A. Cerebral organoids model human brain development and microcephaly. *Nature* **501,** 373–379 (2013).

46. Wen, G., Vanheusden, M., Acke, A., Valli, D., Neely, R. K., Leen, V. & Hofkens, J. Evaluation of Direct Grafting Strategies via Trivalent Anchoring for Enabling Lipid Membrane and Cytoskeleton Staining in Expansion Microscopy. *ACS Nano* (2020). doi:10.1021/acsnano.9b09259

47. Chang, J.-B., Chen, F., Yoon, Y.-G., Jung, E. E., Babcock, H., Kang, J. S., Asano, S., Suk, H.-J., Pak, N., Tillberg, P. W., Wassie, A. T., Cai, D. & Boyden, E. S. Iterative expansion microscopy. *Nature Methods* **14,** 593–599 (2017).

48. Truckenbrodt, S., Maidorn, M., Crzan, D., Wildhagen, H., Kabatas, S. & Rizzoli, S. O. X10 Expansion Microscopy Enables 25 nm Resolution on Conventional Microscopes. *EMBO Reports* (2018). doi:10.1101/172130

49. Truckenbrodt, S., Sommer, C., Rizzoli, S. O. & Danzl, J. G. A practical guide to optimization in X10 expansion microscopy. *Nature Protocols* **14,** 832–863 (2019).

50. Park, H. E., Choi, D., Park, J. S., Sim, C., Park, S., Kang, S., Yim, H., Lee, M., Kim, J., Pac, J., Rhee, K., Lee, J., Lee, Y., Lee, Y. & Kim, S. Y. Scalable and Isotropic Expansion of Tissues with Simply Tunable Expansion Ratio. *Advanced Science* **6,** (2019).

51. Lin, Z., Wei, D., Lichtman, J. & Pfister, H. *PyTorch Connectomics: A Scalable and Flexible Segmentation Framework for EM Connectomics*. (arXiv, 2021). doi:10.48550/arXiv.2112.05754

52. Lee, K., Zung, J., Li, P., Jain, V. & Seung, H. S. Superhuman Accuracy on the SNEMI3D Connectomics Challenge. *arXiv preprint arXiv:1706.00120* (2017).

53. Januszewski, M., Kornfeld, J., Li, P. H., Pope, A., Blakely, T., Lindsey, L., Maitin-Shepard, J., Tyka, M., Denk, W. & Jain, V. High-precision automated reconstruction of neurons with flood-filling networks. *Nature Methods* **15,** 605–610 (2018).

54. Wickersham, I. R., Finke, S., Conzelmann, K.-K. & Callaway, E. M. Retrograde neuronal tracing with a deletion-mutant rabies virus. *Nat Methods* **4,** 47–49 (2007).

55. Ben-Simon, Y., Kaefer, K., Velicky, P., Csicsvari, J., Danzl, J. G. & Jonas, P. Entorhinal layer 6b subplate neurons govern spatial learning and memory. *bioRxiv* 2022.01.26.477814 (2022). doi:10.1101/2022.01.26.477814

## Acknowledgements

We thank Jakob Vorlaufer, Nathalie Agudelo-Dueñas, Wiebke Jahr and Andreas Wartak for microscope maintenance and troubleshooting, as well as Caroline Kreuzinger and Anna Freeman for technical assistance. We gratefully acknowledge Eder Miguel for setting up webKnossos and Marek Šuplata for computational support and hardware control. We are grateful to Ryuichi Shigemoto and Bernd Bickel for generous support, and Michael Sixt and Scott Boyd (Stanford University) for discussions and critical reading of the manuscript. PSD95-HaloTag mice were kindly provided by Seth Grant (University of Edinburgh). We acknowledge expert support by the scientific service units of the Institute of Science and Technology Austria, including scientific computing, imaging and optics, preclinical, and life science facilities, and by the Miba machine shop.

We gratefully acknowledge funding by the following sources:
Austrian Science Fund (FWF) grant I3600-B27 (JGD)
Austrian Science Fund (FWF) grant DK W1232 (JGD)
Austrian Science Fund (FWF) grant Z 312-B27, Wittgenstein award (PJ)
Gesellschaft für Forschungsförderung NÖ (NFB) grant LSC18-022 (JGD)
European Union's Horizon 2020 research and innovation programme, European Research Council (ERC) grant 715508 – REVERSEAUTISM (GN)
European Union's Horizon 2020 research and innovation programme, European Research Council (ERC) grant 692692 – GIANTSYN (PJ)
Marie Skłodowska-Curie Actions Individual Fellowship 101026635 under the EU Horizon 2020 program (JFW)

## Author contributions

JMM and JGD designed the study, experiments, and analysis and interpreted data. JMM performed experiments, analysis, proofreading, and visualization, prepared figures and contributed to manuscript writing. JL designed and performed analysis, visualized and interpreted data, prepared figures and contributed to manuscript writing. PV supported experiments. HK performed stereotactic injections. JFW performed patch-clamp experiments. AC performed manual segmentations. CS supported image analysis. AV, KR, TC, and SS provided human brain surgery specimens. GN advised on and provided human cerebral organoids. PJ supervised patch clamp experiments and advised on synaptic neuroscience and hippocampal circuitry. JGD initiated and supervised the study. JGD wrote the manuscript with critical input from all authors.

### 6.3.1.2 Material & methods

Below are the detailed methods used for the publication: Michalska et al., 2022[155].

# I Reagents

## I.1 Chemicals & solutions

**Appendix Table 3: List of chemicals.**

| Reagent | Abbr. | Source | Identifier |
|---|---|---|---|
| 2-Mercaptoethanol (50 mM) | - | ThermoFisher Scientific/ Gibco | 31350010 |
| 2-(N-morpholino)ethanesulfonic acid | MES | Sigma Aldrich/ Merck | M3671 |
| 4-(2-hydroxyethyl)-1-piperazineethanesulfonic acid | HEPES | Sigma Aldrich/ Merck | H3375 |
| 4-(2-hydroxyethyl)-1-piperazineethanesulfonic acid 1 M | HEPES 1 M | ThermoFisher Scientific/ Gibco | 15630056 |
| 4-hydroxy-2,2,6,6-tetramethylpiperidine- | TEMPO | Sigma Aldrich/ Merck | 176141 |
| 6-((acryloyl)amino)hexanoic acid, succinimidyl ester | AcX | ThermoFisher Scientific | A20770 |
| Accutase | - | Sigma Aldrich/ Merck | A6964 |
| Acrylamide | AA | Sigma Aldrich/ Merck | A9099 |
| Acrylic acid N-hydroxysuccinimide ester | NAS | Sigma Aldrich/ Merck | A8060 |
| Adenosine-5'-triphosphate-disodium salt hydrate | $Na_2ATP$ | Sigma Aldrich/Merck | A3377 |
| Agarose | - | Sigma Aldrich/ Merck | #A9539 |
| Ammonium persulfate | APS | Sigma Aldrich/ Merck | A3678 |
| Ascorbic acid | - | Sigma Aldrich/ Merck | A5960 |
| B-27 supplement (50X) serum free | B27 | ThermoFisher Scientific/ Gibco | 17504044 |
| B-27 supplement (50X) (-vitamin A) | B27 (-vitA) | ThermoFisher Scientific/ Gibco | 12587010 |
| Biocytin | - | ThermoFisher Scientific/ Invitrogen | B1592 |
| Bovine serum albumin, albumin fraction V (pH 7.0) | BSA | PanReac AppliChem | A1391,0500 |
| Calcium chloride dihydrate | $CaCl_2$ | Sigma Aldrich/ Merck | C3881 |
| Crimson microspheres 40 nm | - | Abberior | NA |
| D-glucose | - | Sigma Aldrich/ Merck | G8270 |
| DMEM/F-12, HEPES | DMEM/F-12 | ThermoFisher Sientific/ Gibco | 11330057 |
| Ethylenediaminetetraacetic acid (0.5 M), pH 8.0, RNase-free | EDTA | ThermoFisher Scientific/ Invitrogen | AM9261 |
| Ethylene glycol-bis(2-aminoethylether-N,N,N',N'-tetraacetic acid | EGTA | Sigma Aldrich/Merck | E0396 |
| Fetal bovine serum | FBS | ThermoFisher Scientific | 10270106 |
| Glutamax | - | ThermoFisher Scientific/ Gibco | 35050038/ 35050061 |
| Glycerol Bioxtra | - | Sigma Aldrich/ Merck | G6279 |
| Guanidine hydrochloride | HCl | Sigma Aldrich/ Merck | G3272 |
| Guanosine 5'-triphosphate sodium salt hydrate | GTP | Sigma Aldrich/ Merck | G8877 |
| Hank's Balanced Salt Solution (without calcium and magnesium) | HBSS (-/-) | ThermoFisher Scientific/ Gibco | 14175053 |
| Hank's Balanced Salt Solution (calcium, magnesium) | HBSS (+/+) | ThermoFisher Scientific/ Gibco | 24020091 |
| Heparin sodium salt from porcine intestinal mucosa | Heparin | Sigma Aldrich/ Merck | H3149 |
| Horse serum | HS | ThermoFisher Scientific/ Gibco | 26050088 |
| Insulin solution human | Insulin | Sigma Aldrich/ Merck | I9278 |
| Isoflurane | - | Virbac/ Vetflurane | NA |
| Ketaminol 100 mg/ml | Ketamine | MSD Tiergesundheit | NA |
| L-Ascorbic acid | Vitamin C | Sigma Aldrich/ Merck | A4544 |

| | | | |
|---|---|---|---|
| Magnesium chloride | $MgCl_2$ | Sigma Aldrich/ Merck | M8266 |
| Magnesium sulfate | $MgSO_4$ | Sigma Aldrich/ Merck | M2643 |
| Corning® Matrigel® Matrix | - | Corning | 356235 |
| Mc Coy's 5A (Adapted) medium | Mc Coy's | ThermoFisher Scientific/ Gibco | 26600023 |
| Minimum Essentials Medium, Earl's salts w/o glutamine | MEM | ThermoFisher Scientific/ Gibco | 11095080 |
| Minimum Essentials Medium, Non-Essential Amino Acids Solution (100X) | MEM-NEAA | ThermoFisher Scientific/ Gibco | 11140050 |
| mTeSR1 medium | - | StemCell Technologies | 85850 |
| N-2 Supplement (100x) | N-2 | ThermoFisher Scientific/ Gibco | 17502048 |
| Neurobasal medium | Neurobasal | ThermoFisher Scientific/ Gibco | 21103049 |
| Normal goat serum | NGS | ThermoFisher Scientific/ Invitrogen | 31872 |
| Novalgin 0.5 g/ml | Metamizol | Sanofi | NA |
| N,N-dimethylacrylamide | DMAA | Sigma Aldrich/ Merck | 274135 |
| N,N' methyleneis-acrylamide | BIS | Sigma Aldrich/ Merck | M7279 |
| N,N,N',N'-tetramethyl-ethyelenediamine | TEMED | Sigma Aldrich/ Merck | T9281 |
| OleoVital eye ointment (Dexpanthenol 2%) | - | Fresenius Kabi | NA |
| Paraformaldehyde | PFA | Sigma Aldrich/ Merck | 158127 |
| Formaldehyde EM grade | PFA EM grade | TAAB Laboratory & Microscopy | P026 |
| Penicillin-Streptomycin (10,000 U/ml) | PenStrep | ThermoFisher Scientific/ Gibco | 15140122 |
| Potassium chloride | KCl | Sigma Aldrich/ Merck | P5405 |
| Potassium gluconate | K-gluconate | Sigma Aldrich/ Merck | G4500 |
| Potassium persulfate | KPS | Sigma Aldrich/ Merck | 379824 |
| Proteinase K | - | New England Biolabs (NEB) | P8107S |
| Sodium azide | $NaN_3$ | Sigma Aldrich/ Merck | 71289 |
| Sodium bicarbonate | $NaHCO_3$ | Sigma Aldrich/ Merck | S5761 |
| Sodium acrylate | SA | Sigma Aldrich/ Merck | 408220 |
| Sodium chloride BioXtra | NaCl | Sigma Aldrich/ Merck | S7653 |
| Sodium chloride (human tissue) | NaCl | Braun | 3570160 |
| Sodium dodecyl sulfate | SDS | | 436143 |
| Sodium hydrogencarbonate | $NaHCO_3$ | Millipore | 106329 |
| Sodium hydroxide | NaOH | Sigma Aldrick/ Merck | S5881 |
| Sodium phosphate monobasic monohydrate | $NaHPO_4*H_2O$ | Sigma Aldrick/ Merck | 71504-MM |
| Sucrose/ D-(+)saccharose | Sucrose | Sigma Aldrick/ Merck | 84097 |
| Tris 1 M, pH 8.0, RNase-free | - | ThermoFisher Scientific/ Invitrogen | AM9856 |
| Triton X-100 | TX | Sigma Aldrich/ Merck | X100 |
| Xylasol 20 mg/ml | Xylazine | Livisto | NA |
| Y-27632 dihydrochloride | Y-27632 | StemCell Technologies | 72302 |

Abbr.=abbreviation

**Appendix Table 4: List of solutions.**

| Solution | Abbr. | pH | Component | Molarity (mM) |
|---|---|---|---|---|
| 0.2 M phosphate buffer | 0.2 M PB | 7.4 | Sodium phosphate dibasic heptahydrate ($Na_2HPO_4*7H_2O$) | 150.82 |
| | | | Sodium phosphate monobasic monohydrate ($NaH_2PO_4*H_2O$) | 49.18 |
| 10X phosphate buffered saline | 10X PBS | 7.4 | Sodium Phosphate dibasic ($Na_2HPO_4$) | 100.00 |
| | | | Potassium Phosphate Monobasic ($KH_2PO_4$) | 19.84 |
| | | | Potassium chloride (KCl) | 26.83 |
| | | | Sodium chloride (NaCl) | 1368.90 |
| 1X phosphate buffered saline | 1X PBS | 7.4 | Sodium Phosphate dibasic ($Na_2HPO_4$) | 10.00 |
| | | | Potassium Phosphate Monobasic ($KH_2PO_4$) | 1.98 |
| | | | Potassium chloride (KCl) | 2.68 |
| | | | Sodium chloride (NaCl) | 136.89 |

## 1.2 Probes & antibodies

**Appendix Table 5: List of probes and antibodies.**

| Reagent | Abbr. | Working c. | Source | Identifier |
|---|---|---|---|---|
| 4'6-diamidino-2-phenylindole | DAPI | 2.5-5 µg/ml | Sigma Aldrich/ Merck | D9542 |
| Alexa Fluor 488-avidin | AF488-avidin | 20 µg/ml | ThermoFisher Scientific/ Invitrogen | A21370 |
| Alexa Fluor 488 donkey anti-rabbit IgG (H+L) | AF488 anti-rb | 5 µg/ml | Jackson ImmunoResearch | 711-545-152 |
| Alexa Fluor 488 donkey anti-guinea pig IgG (H+L) | AF488 anti-gp | 1-2 µg/ml | Jackson ImmunoResearch | 706-545-148 |
| Alexa Fluor 488 goat anti-mouse IgG (H+L) | AF488 anti-m | 6-20 µg/ml | Thermo Fisher Scientific/ Invitrogen | A11001 |
| Alexa Fluor 488 plus goat anti-rabbit IgG (H+L) | AF488 + anti-rb | 4 µg/ml | Thermo Fisher Scientific/ Invitrogen | A32731 |
| Alexa Fluor 488-N-hydroxysuccinimide | AF488-NHS | 40-50 µM | Jena Bioscience | APC-002-1 |
| Alexa Fluor 546 goat anti-guinea pig IgG (H+L) | AF546 anti-gp | 5 µg/ml | Thermo Fisher Scientific/ Invitrogen | A11076 |
| Alexa Fluor 546-N-hydroxysuccinimide | AF546-NHS | 40-50 µM | Thermo Fisher Scientific/ Invitrogen | A20002 |
| Alexa Fluor 594 goat anti-guinea pig IgG (H+L) | AF594 anti-gp | 4-8 µg/ml | Thermo Fisher Scientific/ Invitrogen | A11076 |
| Alexa Fluor 594 goat anti-mouse IgG (H+L) | AF594 anti-m | 4-8 µg/ml | Thermo Fisher Scientific/ Invitrogen | A11005 |
| Alexa Fluor 594 goat anti-rabbit IgG (H+L) | AF594 anti-rb | 8 µg/ml | ThermoFisher Scientific/ Invitrogen | A11037 |
| Alexa Fluor 594-N-hydroxysuccinimide | AF594-NHS | 40-50 µM | Jena Bioscience | APC-004-1 |
| Alexa Fluor 594-streptavidin | - | 4 µg/ml | Thermo Fisher Scientific/ Invitrogen | S32356 |
| Alexa Fluor 647 donkey anti-sheep IgG (H+L) | AF 647 anti-sh | 4 µg/ml | Thermo Fisher Scientific/ Invitrogen | A21448 |
| Anti-Bassoon monoclonal mouse (SAP7F407) | Anti-Bassoon, m | 2-4 µg/ml | Abcam | ab82958 |
| Anti-green fluorescent protein monoclonal, mouse (3E6) | Anti-GFP, m | 4 µg/ml | ThermoFisher Scientific/ Invitrogen | A11120 |
| Anti-green fluorescent protein polyclonal, rabbit | Anti-GFP, rb | 5 µg/ml | ThermoFisher Scientific/ Invitrogen | A11122 |
| Anti-Homer1 polyclonal, rabbit | Anti-Homer1, rb | 2 µg/ml | Synaptic Systems | 160003 |
| Anti-hyaluronic acid 1 polyclonal, sheep | Anti-HA1, sh | 50 µg/ml | Abcam | ab53842 |
| Anti-microtubule associated protein 2 polyclonal, guinea pig | Anti-MAP2, gp | 1 µg/ml | Synaptic Systems | 188004 |
| Anti-N-cadherin monoclonal (D-4), mouse | Anti-N-cadherin, m | 0.7 µg/ml | Santa Cruz | sc-8424 |
| Anti-Shank2 polyclonal, guinea pig | Anti-Shank2, gp | 2-4 µg/ml | Synaptic Systems | 162204 |
| Anti-Synaptophysin 1 monoclonal, mouse | Anti-Syph 1, m | 2 µg/ml | Synaptic Systems | 101011 |
| Anti-Synaptophysin 1 polyclonal, guinea pig | Anti-Syph1, gp | 2 µg/ml | Synaptic Systems | 101004 |
| Anti-vesicular gamma-aminobutyric acid transporter polyclonal, rabbit | Anti-VGAT, rb | 3 µg/ml | Synaptic Systems | 131003 |
| Anti-vesicular glutamate transporter 1 polyclonal, rabbit | Anti-VGLUT 1, rb | 10 µg/ml | Synaptic Systems | 135302 |

| | | | | |
|---|---|---|---|---|
| Atto 643-azide | - | 20-33 µM | Atto-Tec | AD643-101 |
| Atto 643-biotin | - | 4-8 µg/ml | Atto-Tec | AD 643-71 |
| Atto 643-maleimide | - | 10 µM | Atto-Tec | AD 643-41 |
| Atto 643-N-hydroxysuccinimidyl ester | Atto 643-NHS | 40-50 µM | Atto-Tec | AD 643-31 |
| Atto 643-streptavidin | - | 4 µg/ml | Atto-Tec | AD 643-61 |
| Concanavalin A | - | 5 µg/ml | Vectorlabs/ Szabo Scandic | VECB-1005 |
| Dibenzocyclooctyne-PEG4-N-hydroxysuccinimidyl ester | NHS-$PEG_4$-DBCO | 50 µM | Sigma Aldrich/ Merck | 764019 |
| Endo-bicyclononyne-PEG12-N-hydroxysuccinimidyl ester | NHS-$PEG_{12}$-BCN | 250 µM | Tebu-bio | BP-23766 |
| FluoroMyelin™ Green Fluorescent Myelin Stain | FluoroMyelin | 1:300 (concentration NA) | ThermoFisher Scientific/ Invitrogen | F34651 |
| Hyaluronic acid binding protein, biotinylated | HABP-biotin | 10 µg/ml | Merck | 385911 |
| Jacalin biotin | - | 5 µg/ml | Vectorlabs/ Szabo Scandic | VECB-1155 |
| Lucifer Yellow CH lithium salt | Lucifer Yellow | 0.2% (w/v) | Sigma Aldrich/ Merck | L0259 |
| Lycopersicon esculentum (tomato) lectin DyLight 594 | LEL DyLight 594 | 2.5 µg/ml | ThermoFisher Scientific | L32471 |
| Maleimide-PEG11-biotin | Maleimide-$PEG_{11}$-biotin | 200 µM | ThermoFisher Scientific | 21911 |
| N-hydroxysuccinimidyl ester-PEG12 –dibenzylcyclooctyne | NHS-$PEG_{12}$-DBCO | 200 µM | Tebu-bio | BP-24149 |
| N-hydroxysuccinimidyl ester – PEG12-biotin, EZ-Link™ | NHS-$PEG_{12}$-biotin | 250-1000 µM | ThermoFisher Scientific | A35389 |
| Pentafluorophenyl ester-dPEG36-biotin | PFP-$PEG_{36}$-biotin | 250 µM | Broadpharm | BP-24318 |
| Phaseolus vulgaris erythro-agglutinin biotin | PHA-E biotin | 5 µg/ml | Vectorlabs/ Szabo Scandic | VECB-1125 |
| Phaseolus vulgaris leuco-agglutinin biotin | PHA-L biotin | 5 µg/ml | Vectorlabs/ Szabo Scandic | VECB-1115 |
| STAR 580-azide | - | 10-20 µM | Abberior | ST580-004 |
| STAR 580 goat anti-mouse IgG | STAR 580 anti-m | 10-15 µg/ml | Abberior | ST580-1001 |
| STAR 580 goat anti-rabbit IgG | STAR 580 anti-rb | 10-15 µg/ml | Abberior | ST580-1002 |
| STAR 635P-neutravidin | - | 5-6 µg/ml | Abberior | ST635P-0121 |
| STAR RED-N-hydroxysuccinimidyl ester | STAR RED-NHS | 40-50 µM | Abberior | STRED-0002 |
| STAR RED-streptavidin | - | 3-4 µg/ml | Abberior | STRED-0120 |
| Streptavidin-acrylamide | Strept-acrylamide | 4-20 µg/ml | ThermoFisher Scientific | S21379 |
| Sulfo-dibenzylcyclooctyne-N-hydroxysuccinimidyl ester | NHS-sulfo-DBCO | 200 µM | Jena Bioscience | CLK-A124-10 |
| Sulfo- N-hydroxysuccinimidyl ester-biotin, long chain, EZ Link™ | NHS-sulfo-biotin | 1000 µM | ThermoFisher Scientific | 21338 |
| Tetrafluorophenyl ester-dPEG12-biotin | TFP-$PEG_{12}$-biotin | 250 µM | Sigma Aldrich/ Merck | QBD10008 |
| Vicia villosa lectin biotin | VVL biotin | 5 µg/ml | Vectorlabs/ Szabo Scandic | VECB-1235 |
| Wheat germ agglutinin, biotinylated | WGA biotin | 15-20 µg/ml | Vectorlabs/ Szabo Scandic | VECB-1025 |
| Wheat germ agglutinin CF633 | WGA CF633 | 5-10 µg/ml | Biotium | 29024-1 |
| Wisteria floribunda lectin biotinylated | WFL biotin | 8 µg/ml | Vectorlabs/ Szabo Scandic | VECB-1355 |

c.=concentration

# II Samples

## II.1 Animals

Experiments were performed on male and female mice used interchangeably. Adult (3-5 months) C57BL/6J and STOCK Tg(Thy1-EGFP)MJrs/J (Thy1-EGFP, Jackson #007788, hemizygous) mice were used for *in vivo* microinjection and/or perfusion experiments. 5-7 day old C57BL/6J, Thy1-EGFP, or PSD95-HaloTag mice[227,228] (homo- or heterozygous) (courtesy of Seth Grant, University of Edinburgh) were used to prepare organotypic hippocampal slice cultures. Available PSD95-HaloTag positive slices were used interchangeably in screening experiments in Supplementary Fig. 1 to reduce total number of animals, but the HaloTag was not used for labeling/readout.
All animal experiments were carried out according to national and institutional regulations and were approved by the Austrian Federal Ministry for Education, Science and Research (authorization BMBWF-V/Sb: 2020-0.363.126 and 2021-0.547.215). All animals used in this study were housed with a 12/12 h light/dark cycle in an environment with controlled temperature (21-23 °C) and relative humidity (45-65 %) and had access to food and water *ad libitum*.

## II.2 Human surgery specimens

Samples of human hippocampus were obtained from patients undergoing surgery of the temporal lobe for epilepsy treatment after obtaining informed consent. Procedures were approved by the Ethics Committee of the Medical University Vienna (authorization 1188/2019).

# III Experimental methods

## III.1 Fixative perfusion

Adult mice were briefly anaesthetized with isoflurane (1-2 % (volume/volume, v/v)) and then deeply anesthetized with Ketamine (80-100 mg/kg of body weight) and Xylazine (10 mg/kg) intraperitoneally, combined with Metamizol (200 mg/kg) subcutaneously for analgesia. After ensuring that the animals were deeply anesthetized by toe pinch, they were transcardially perfused with 10 ml ice-cold 1X PBS, followed by 80 ml ice-cold fixative solution (4 % (weight/volume, w/v) PFA EM grade, 0.1 M PB, 0.1 M NaOH, pH 7.4) at a flow rate of 7-8 ml/min. The brains were dissected and post-fixed in 5 ml fixative solution overnight (ON) at 4 °C on an orbital shaker.

## III.2 Tissue processing

Perfused mouse brains were washed three times for 1 h each with 1X PBS on an orbital shaker at room temperature (RT). Serial coronal sections of 50-100 µm thickness were prepared with a vibratome (Leica VT 1200S). The sections were kept in 0.02 % (w/v) $NaN_3$ in 1X PBS at 4 °C for short-term storage (1-2 weeks) or in cryo-protectant solution (60 % (v/v) glycerol in 0.1 M PB) at -20 °C for long-term storage.

## III.3 Tissue culture

### III.3.1 Organotypic hippocampal slice culture

Organotypic hippocampal slice cultures were prepared according to the membrane interface method with slight modifications[229]. 5-7 day old mice were rapidly decapitated with surgical scissors. The brain was dissected from the skull and placed in ice-cold HBSS (-/-) supplemented with 10 mM D-glucose. Hippocampi including entorhinal cortex were dissected from the brain and transverse slices were obtained perpendicular to the longitudinal axis of the hippocampus at 350 µm thickness with a tissue chopper (McIllwain). Microporous cell culture inserts (pore size 0.4 µm, PICM0RG50, Millicell) were placed in culture dishes filled with 1 ml culture medium (MEM supplemented with 15 % (v/v) heat-inactivated HS; 2 % (v/v) B-27; 25 mM HEPES; 3 mM Glutamax; 2.8 mM $CaCl_2$; 1.8 mM $MgSO_4$; 0.25 mM ascorbic acid; 6.5 g/l D-glucose) and equilibrated in an incubator at 37 °C with 5 % $CO_2$. The sliced hippocampi were transferred into a new dish filled with ice-cold HBSS (-/-) supplemented with 10 mM D-glucose. The slices were inspected with a widefield microscope and 6-7 slices per brain were transferred onto the cell culture inserts, 3-4 slices per insert. Excess HBSS-solution was withdrawn with a filter paper. The slices were cultured in an incubator at 37 °C with 5 % $CO_2$. Medium was exchanged twice a week. Fresh medium was pH- and temperature-equilibrated in the incubator for at least 30 min before medium change. Slices were typically used for experiments 14-30 days after culture start (days in vitro, DIV).
The sample presented in Fig. 5a,b was cultured as described previously[29].

### III.3.2 Human cerebral organoids

Human cerebral organoids were generated with a Adapted protocol from Lancaster *et al.*[230] as described previously[231]. Briefly, human embryonic stem cells were dissociated with Accutase and seeded in ultra-low-binding 96-well plates (Corning) containing mTeSR1 medium supplemented with 50 µM Y-27632. Cells were fed every two days, and supplements were removed from the media after three days of culture. After the cells aggregated to embryoid bodies (EBs), the EBs were transferred into low-adhesion 24-well plates containing neural induction medium (50 ml DMEM/F-12, 0.5 ml N-2, 0.5 ml Glutamax supplement, 0.5 ml MEM-NEAA, 1µg/ml heparin). Day 0 of cerebral organoid formation was defined at the start of neuroepithelial tissue formation. The organoids were embedded in Corning® Matrigel® Matrix droplets. Growth medium was first

exchanged to cerebral organoid medium without vitamin A (125 ml DMEM/F-12, 125 ml Neurobasal, 1.25 N-2, 5 ml B-27 without vitamin A, 2.5 μg/ml insulin, 50 μM 2-Mercaptoethanol, 2.5 ml Glutamax, 1.25 ml MEM-NEAA, 2.5 ml PenStrep), followed by cerebral organoid medium with vitamin A (250 ml DMEM/F-12, 250 ml Neurobasal, 2.5 ml N-2, 10 ml B-27, 2.5 μg/ml insulin, 50 μM 2-Mercaptoethanol, 5 ml Glutamax, 2.5 ml MEM-NEAA, 500 μM ascorbic acid, 5 ml PenStrep, 0.2 % (w/v) $NaHCO_3$) four days later. The organoids were placed on a horizontal shaker at 70-100 rounds per minute (rpm) and fed twice a week.

## III.4 Electrophysiological recordings

Electrophysiological recordings were obtained from hippocampal organotypic slice cultures at 10-21 DIV. The slices were submerged in artificial cerebrospinal fluid (ACSF: 125 mM NaCl, 25 mM $NaHCO_3$, 25 mM glucose, 2.5 mM KCl, 1.25 mM $NaH_2PO_4$, 2 mM $CaCl_2$, and 1 mM $MgCl_2$, with pH maintained at 7.3, equilibrated with carbogen (95 % $O_2$/5 % $CO_2$)) at ~22 °C. Glass micropipettes were pulled from thick-walled borosilicate glass (2 mm outer diameter, 1 mm inner diameter) and filled with intracellular solution containing 135 mM K-gluconate, 20 mM KCl, 0.1 mM EGTA, 2 mM $MgCl_2$, 4 mM $Na_2ATP$, 0.3 mM GTP, 10 mM HEPES, with the addition of 1 mg/ml Lucifer Yellow or 0.2 % (w/v) biocytin as required. Pipettes were positioned using up to four LN mini 25 micromanipulators (Luigs and Neumann) under visual control on a Adapted Olympus BX51 microscope equipped with a 60x -immersion objective (Olympus LUMPlan FI/IR, 60x, NA = 0.90, working distance (WD) 2.05 mm). Up to four neurons were simultaneously recorded in the whole-cell patch-clamp configuration, with signals acquired on Multiclamp 700B amplifiers (Molecular Devices), low-pass filtered at 6 kHz and digitized at 20 kHz with a Cambridge Electronic Design 1401 mkII AD/DA converter. Signals were acquired using Signal 6.0 software (CED). Action potential phenotypes were recorded on sequential current pulse injections (-100 pA to +400 pA) in the current clamp configuration. Neurons were identified based on morphological properties and spike frequency upon current injection. In current-clamp recordings, pipette capacitance was 70 % compensated. Recordings were analyzed using Stimfit[232] and MATLAB-based scripts.

## III.5 Stainings

### III.5.1 Immunostaining

Brain slices were permeabilized with 0.2-0.5 % (v/v) TX in 1X PBS ON at 4 °C with gentle agitation and washed three times for 30 min each with 1X PBS, unless otherwise noted. Brain slices were blocked with blocking solution (5% BSA (w/v), 1 % (v/v) NGS in 1X PBS) for 4 h at RT with gentle agitation. Brain slices were incubated with primary antibodies (ABs) in 5 % (w/v) BSA in 1X PBS ON at 4 °C with gentle agitation. They were washed three times for 30 min each with 5 % (w/v) BSA in 1X PBS at RT with gentle agitation. Secondary AB incubation was performed in 5 % (w/v) BSA in 1X PBS either ON at 4 °C or for 4 h at RT with gentle agitation. The samples were washed thoroughly with 1X PBS.

### III.5.2 Other stainings

III.5.2.1 Positive labeling of single cells by dye-filling

To achieve positive labeling of single cells in organotypic hippocampal slice cultures, cells were whole-cell patch-clamped as described in section 3.4. For direct fluorescent labeling for confocal imaging, the cells were filled with 1 mg/ml Lucifer yellow during recording (Fig. 3, Extended Data Fig. 6).
To achieve a super-resolution compatible read-out, cells were filled with 0.2 % (w/v) biocytin during recording (Fig. 4, Supplementary Fig. 7). After fixation, the slices was permeabilized with 0.2 % (v/v) TX in 1X PBS for 7 h at 4 °C with gentle agitation. The slices were washed three times

for 30 min each with 1X PBS at RT with gentle agitation, followed by a 2 h blocking step in 5 % (w/v) BSA and 1 % (v/v) NGS in 1X PBS at RT with gentle agitation. The slices were incubated with 4 µg/ml Alexa Fluor 594-streptavidin 1X PBS ON at 4 °C with gentle agitation. They were then washed three times for 30 min each with 1X PBS at RT with gentle agitation.

III.5.2.2 Additional lectin stainings

For lectin stainings other than WGA, perfusion-fixed mouse brain sections were permeabilized with 0.5 % (v/v) TX in 1X PBS ON at 4 °C with gentle agitation. The samples were washed three times for 30 min each with 1X PBS at RT with gentle agitation.
For LEL labeling, the samples were incubated with 2.5 µg/ml LEL Dylight 594 in 1X PBS for 2 h at RT with gentle agitation. The samples were washed three times for 30 min each with 1X PBS at RT with gentle agitation before imaging.
For the remaining, biotin-conjugated lectins, the samples were incubated with 5-8 µg/ml biotinylated lectin in 1X PBS with 2 mM $CaCl_2$ for 20 h at 4 °C with gentle agitation. The samples were washed three times for 30 min each with 1X PBS at RT with gentle agitation. Lectin signal was read out by incubation with 4 µg/ml Alexa Fluor 594-streptavidin for 2 h at RT or 4 °C ON on an orbital shaker. The samples were washed again three times for 30 min each with 1X PBS.

III.5.2.3 Hyaluronic acid binding protein

Adult mouse PFA-perfusion fixed coronal brain sections of 100 µm thickness were washed three times for 30 min each with 1X PBS at RT with gentle agitation. The sections were incubated with 10 % (w/v) BSA and 0.2 % (v/v) TX in 1X PBS ON at 4 °C on an orbital shaker. The samples were then incubated with 10 µg/ml HABP-biotin in 10 % (w/v) BSA and 0.2 % (v/v) TX in 1X PBS for 48 h at 4 °C with gentle agitation. The sections were washed three times 30 min each with 1X PBS at RT with gentle agitation.

III.5.2.4 FluoroMyelin stain

Adult mouse (Thy1-EGFP+) PFA-perfused fixed coronal brain sections of 100 µm thickness were washed three times for 30 min each with 1X PBS at RT on an orbital shaker. The sections were permeabilized with 0.5 % (v/v) TX in 1X PBS ON at 4 °C with gentle agitation. The next day, the samples were washed three times for 30 min each with 1X PBS at RT with gentle agitation, followed by rCATS staining. The sections were then incubated with FluoroMyelin (1:300 dilution of a 300x stock in water) diluted in 1X PBS for 2 h at RT with gentle agitation. The samples were washed again three times for 30 min each with 1X PBS on an orbital shaker.

III.5.2.5 Nuclear stain

Nuclear stains were performed by incubating samples with 0.5-1 µg/ml DAPI (1:5,000-10,000 dilution of a 5 mg/ml stock in $ddH_2O$) for 15-30 min at RT with gentle agitation. DAPI incubation was performed in 1X PBS for all samples, except for expanded hydrogels, which were incubated in $ddH_2O$. After the staining, samples were washed two times for 15 min each with 1X PBS or $ddH_2O$ (expanded hydrogels). Nuclear stains were always performed as the last step before imaging.

## III.6 coCATS

### III.6.1 Stereotactic surgery for *in vivo* microinjection of coCATS labeling compounds

Adult mice were briefly anesthetized with isoflurane (1-2 %) and then deeply anesthetized with Ketamine (80-100 mg/kg of body weight) and Xylazine (10 mg/kg) intraperitoneally, combined with Metamizol (200 mg/kg) subcutaneously for analgesia. The head was shaved, OleoVital was

applied to the eyes and the animals were head-fixed in a stereotactic frame (David Kopf Instruments). To ensure that the skull was centered and leveled in the stereotactic frame, bregma and lambda were aligned to the same height. A small hole was drilled at the injection coordinate, the injection pipette was lowered to the brain surface (used as vertical reference point) and advanced into the tissue. Using a microinjection pump (Nanoliter 2010, World Precision Instruments, Sarasota, FL, USA), a highly concentrated coCATS labeling solution (20 mM amine-reactive compound in DMSO) was injected over a time span of 10 min using the following coordinates (measured from bregma):

- LV: 1.25 mm caudally, +/-2 mm laterally and 2 mm vertically, for injections into the right or left LV. A total volume of 500 nl was injected at 50 nl/min.
- Cortex: 0.71 mm caudally, 1.65 mm laterally and 1 mm vertically, for injections into the right primary somatosensory cortex. A total volume of 100 nl was injected at 10 nl/min.

After each injection, the pipette was left for 5 min *in situ* before slowly retracting it to prevent backflow. Mice were placed on a heating pad during and after surgery until transcardial perfusion. The level of anesthesia was confirmed by toe pinch. If necessary, additional Ketamine/Xylazine was administered. The procedure was followed by transcardial perfusion 40-45 min after the onset of dye delivery.

### III.6.2 coCATS labeling of organotypic hippocampal slice cultures

14-25 DIV cultured organotypic hippocampal slices were used for experiments. A piece of underlying membrane including a slice was cut out of the cell culture insert. The slice was immersed in carbogen-equilibrated, pre-warmed ACSF with HEPES (20 mM D-glucose, 4.8 mM KCl, 125 mM NaCl, 26 mM $NaHCO_3$, 1.25 mM $NaHPO_4*H_2O$, 2 mM $CaCl_2$, 1.3 mM $MgCl_2$, 7.5 mM HEPES in dd$H_2O$, pH 7.4). CoCATS labeling compound was freshly prepared in carbogen-equilibrated ACSF with HEPES from a highly concentrated stock (typically 20-100 mM in DMSO). For direct fluorophore labeling, 40-50 µM STAR RED-NHS (Fig. 3e, 4c) or 50 µM Atto 643-NHS (Fig. 4a,b) were used. For expansion experiments, 250 µM NHS-$PEG_{12}$-biotin was used (Fig. 5a,b). The slice was immersed in coCATS labeling solution and incubated at 37 °C for 20-25 min (direct labeling with fluorophore) or 45 min (biotin labeling for expansion) with gentle agitation. The sample was washed twice for 1 min with carbogen-equilibrated ACSF with HEPES. If not otherwise stated, the sample was immersion-fixed with fixative solution (4 % (w/v) PFA EM grade, 0.1 M PB, 0.1 M NaOH in dd$H_2O$, pH 7.4) for 1 h at RT, followed by ON incubation at 4 °C in the same solution with gentle agitation.

For the screening experiments in Supplementary Fig. 1, cultured organotypic hippocampal slices were incubated with 40-50 µM of the various NHS-conjugated fluorophores for 25-30 min at 37 °C in carbogen-equilibrated ACSF with HEPES with gentle agitation.

For screening of biotin or click chemistry derivatives, live labeling with the respective biotin probes was performed in carbogen-equilibrated ACSF with HEPES for 45 min at 37 °C with gentle agitation, using concentrations as indicated in Supplementary Table 1. After washing and fixation, samples were washed three times for 30 min each with 1X PBS at RT with gentle agitation and permeabilized with 0.2 % (v/v) TX in 1X PBS ON at 4 °C with gentle agitation. Samples were washed three times for 30 min each with 1X PBS at RT with gentle agitation and incubated with a readout probe in 1X PBS ON at 4 °C with gentle agitation.

The samples were washed three times for 30 min each in 1X PBS with gentle agitation, followed by confocal imaging. Information about probes and concentrations is detailed in Supplementary Table 1.

### III.6.3 Expansion of organotypic slice cultures with coCATS labeling

III.6.3.1 Expansion with the magnified analysis of the proteome (MAP) approach

After coCATS labeling with an amine-reactive biotin derivative, the sample was ~4-fold expanded according to the MAP protocol[46] with slight modifications. The sample was immersed in fixative solution (4 % (w/v) PFA in 1X PBS) for 10 min at RT with gentle agitation. It was then carefully dissociated from the cell culture insert with a brush, placed into MAP solution (30 % (w/v) AA, 10 % (w/v) PFA, 7 % (w/v) SA, 0.1 % (w/v) BIS, 0.1 % (w/v) VA-044 in $ddH_2O$) and incubated ON at RT with gentle agitation. The sample was washed three times for 30 min each with 1X PBS. It was then transferred to a gelation chamber[50] consisting of a coverslip and two 100 µm thick spacers placed on a Superfrost slide. The sample was immersed in fresh MAP solution and a second coverslip was placed on top of the spacers. The gelation chamber was placed in a humidified chamber and gelation was performed for 1 h at 45 °C. The sample was removed from the gelation chamber and immersed in MAP denaturation solution (200 mM SDS, 200 mM NaCl, 50 mM Tris in $ddH_2O$, pH 9). The sample was denatured ON at 37 °C in a humidified environment. The next day, fresh MAP denaturation solution was pre-heated to 70 °C. The sample was immersed in the solution and incubated for 1 h at 70 °C in a water bath. The temperature of the water bath was then increased to 95 °C over a time course of 30 min. The sample was then incubated for another 1 h at 95 °C. It was expanded ~4-fold by immersing in $ddH_2O$ with 3 fluid exchanges at 30 min intervals. The gel was trimmed, removing portions not containing biological sample. It was blocked in 5 % (w/v) BSA in 1X PBS for 30 min at RT with gentle agitation and the CATS signal was read out after incubation with 5 µg/ml STAR 635P neutravidin in 0.1X PBS ON at RT with gentle agitation and re-expansion by incubating it three times for 30 min each in $ddH_2O$.

III.6.3.2 Expansion with protein retention expansion microscopy (proExM)

CoCATS labeled organotypic hippocampal slice cultures were ~4-fold expanded with protein retention expansion microscopy (proExM)[44]. After coCATS labeling with an amine-reactive biotin derivative, the sample was immersion-fixed with fixative solution (4 % (w/v) PFA in 1X PBS) for 1 h at RT with gentle agitation. The sample was carefully dissociated from the cell culture insert with a brush. It was washed three times for 30 min each with 1X PBS and permeabilized with 0.5 % (v/v) TX in 1X PBS ON at 4 °C with gentle agitation. The next morning, the sample was washed three times for 30 min with 1X PBS on an orbital shaker. It was then incubated with 100 µg/ml AcX in MES buffer (100 mM MES, 150 mM NaCl in $ddH_2O$, pH 6) ON at RT with gentle agitation. It was washed three times for 30 min each in 1X PBS and pre-incubated in ice-cold proExM gelation solution (8.6 % (w/v) SA, 2.5 % (w/v) AA, 0.15 % (w/v) BIS, 11.7 % (w/v) NaCl, 0.2 % (w/v) TEMED, 0.2 % (w/v) APS, 0.01 % (w/v) TEMPO in 1X PBS) for 1 h on ice with gentle agitation. The sample was transferred to a gelation chamber consisting of a coverslip and two 100 µm thick spacers placed on a Superfrost slide. Excess gelation solution was carefully removed with a Kimwipe. A second larger coverslip was placed on top of the spacers. Fresh gelation solution was pipetted into the gap between the coverslips, until it was filled. The gelation chamber was placed in a humidified chamber and the sample was incubated for 2 h at 37 °C until gelation was complete. The gelation chamber was carefully disassembled and the sample stuck to the bottom coverslip was washed once with 1X PBS. The sample was immersed in digestion solution (8 U/ml proteinase K, 0.8 M guanidine HCl, 50 mM Tris, 2 mM $CaCl_2$, 0.5 % (v/v) TX in $ddH_2O$, pH 8) and incubated for 14-17 h at 50 °C in a humidified environment with gentle agitation. The sample was expanded ~4-fold by immersing in $ddH_2O$ with 3 fluid exchanges at 30 min intervals. The sample was trimmed to remove gel portions not containing biological sample. It was then incubated with 5 µg/ml STAR 635P neutravidin in 0.1X PBS ON at RT with gentle agitation. The sample was re-expanded by incubating it three times for 30 min each in ddH2O.

### III.6.4 coCATS viability test

To obtain electrophysiological traces after coCATS labeling, 14-16 DIV slice cultures were first incubated in 0.25 % (v/v) DMSO (control) or 50 µM STAR RED-NHS (dye incubation) in carbogen-equilibrated ACSF with HEPES for 25 min at 37 °C with gentle agitation. Then, the slices were briefly washed with carbogen-equilibrated ACSF with HEPES and 3-4 CA1 pyramidal neurons per slice were recorded as described in section 3.4.
To obtain functional recordings during coCATS labeling incubation (Supplementary Fig. 6b), CA3 pyramidal neurons from a 16 DIV organotypic hippocampal slice culture were first recorded as described in section 3.4 for 10 min. ACSF was then exchanged with dye solution (50 µM STAR RED-NHS in ACSF) and the recording was continued for another 20 min without constant flow of solution to reproduce the coCATS labeling procedure.

### III.6.5 coCATS labeling of cerebral organoids

Cerebral organoids were incubated in 40 µM STAR RED-NHS in pre-warmed carbogen-equilibrated ACSF containing HEPES for 30 min at 37 °C with gentle agitation. The samples were briefly washed with fresh ACSF solution and fixed with 4 % (w/v) PFA in 0.1 M PB and 0.1 M NaOH, pH 7.4 for 1 h at RT with gentle agitation. The samples were washed three times for 30 min each in 1X PBS before imaging.

## III.7 rCATS

### III.7.1 rCATS labeling of fixed brain tissue

III.7.1.1 Mouse brain tissue

Coronal brain sections of 100-200 µm thickness obtained from PFA-fixative perfused animals were permeabilized by repeated freeze-thaw cycles. For this, they were washed three times for 30 min each with 1X PBS and incubated with 30 % (w/v) sucrose in 1X PBS ON at 4 °C with gentle agitation. The sections were placed on a Superfrost slide, immersed in sucrose solution and positioned on dry ice until the solution was completely frozen, then removed and left to thaw at RT. Freeze-thawing was repeated 4-5 times. The sections were then washed three times for 30 min and immunostained as described in section 3.5.1. To achieve rCATS labeling, the primary AB solution was complemented with 8 µg/ml WGA CF633. Alternatively to the freeze-thaw method, we used permeabilization by an ON incubation with 0.5 % TX (v/v) in 1X PBS at 4 °C with gentle agitation as indicated for specific experiments.

III.7.1.2 Human brain tissue

We obtained surgery specimens from 4 individuals and applied rCATS. The data shown in Fig. 6a,b is from a hippocampal brain section from a 36 year old male patient diagnosed with epilepsy with sclerosis of the hippocampus. Previously to the temporal lobe surgery during which tissue was extracted for the experiments described here, a brain tumor had been removed. Histology of the hippocampus showed no presence of neoplastic tissue. Immediately after resection, the tissue was transferred to physiological saline (0.9 % (v/v) NaCl in $H_2O$). The tissue was immersed in 4 % (w/v) PFA within 5 min and post-fixed on an orbital shaker at 4 °C ON. After PFA fixation, the tissue was washed with 1X PBS three times for at least 15 min each. The samples were embedded in 3 % (w/v) agarose and sliced with a vibratome (Leica VT 1200) at a thickness of 100-200 µm. The vibratome slices were then cryoprotected with 30 % (w/v) sterile-filtered sucrose until they sunk in the solution. The samples were stored at -80 °C until further use. The tissue was brought to RT and thoroughly washed with 1X PBS and permeabilized with 0.5 % (v/v) TX in 1X PBS ON at RT with gentle agitation. The samples were briefly washed with 1X PBS and blocked with 5 % (w/v) BSA, 1 % (v/v) NGS and 0.5 % (v/v) TX in 1X PBS for 2 h at RT with

gentle agitation. They were then incubated with primary ABs in 5 % (w/v) BSA, 1 % (v/v) NGS and 0.5 % (v/v) TX in 1X PBS for 72 h at RT with gentle agitation. They were washed three times for 30 min each with 5 % BSA in 1X PBS with gentle agitation and incubated with secondary ABs in 5 % (w/v) BSA, 1 % (v/v) NGS and 0.5 % (v/v) TX in 1X PBS for 4 h at RT with gentle agitation. The samples were washed three times for 30 min each with 1X PBS with gentle agitation, then incubated with 6 μg/ml WGA CF633 in 1X PBS ON at RT with gentle agitation. The samples were washed three times for 30 min each with 1X PBS.

### III.7.2 rCATS labeling with expansion in previously fixed mouse brain

RCATS labeled brain tissue was ~4-fold expanded with proExM[44]. After pre-expansion imaging of EGFP signal on a spinning disk confocal microscope, 100 μm thick brain sections from PFA-fixative perfused adult mouse were immunostained as described in section 3.5.1. They were then incubated with 16.7 μg/ml WGA-biotin in 1X PBS for 20 h at RT with gentle agitation. Samples were washed three times for 30 min each with 1X PBS and then incubated with 20 μg/ml streptavidin acrylamide for 20 h at RT with gentle agitation. Samples were washed three times for 30 min each with 1X PBS, followed by an anchoring step with 100 μg/ml AcX in MES buffer (100 mM MES, 150 mM NaCl in $ddH_2O$, pH 6) ON at RT with gentle agitation. They were washed three times for 30 min each in 1X PBS with gentle agitation and pre-incubated in ice-cold proExM gelation solution (8.6 % (w/v) SA, 2.5 % (w/v) AA, 0.15 % (w/v) BIS, 11.7 % (w/v) NaCl, 0.2 % (w/v) TEMED, 0.2 % (w/v) APS, 0.01 % (w/v) TEMPO in 1X PBS) for 1 h on ice with gentle agitation. Samples were transferred to a gelation chamber consisting of a coverslip and two 100 μm thick spacers placed on a Superfrost slide. Excess gelation solution was carefully removed with a Kimwipe. A second larger coverslip was placed on top of the spacers. Fresh gelation solution was pipetted into the gap between the coverslips, until it was filled. The gelation chamber was placed in a humidified chamber and incubated for 2 h at 37 °C until gelation was complete. The gelation chamber was carefully disassembled and the samples were washed once with 1X PBS. Samples were immersed in digestion solution (8 U/ml proteinase K, 0.8 M guanidine HCl, 50 mM Tris, 2 mM $CaCl_2$, 0.5 % (v/v) TX in $ddH_2O$, pH 8) and incubated for 14-17 h at 50 °C in a humidified environment with gentle agitation. The samples were washed three times for 1 h each in 1X PBS at RT with gentle agitation. They were incubated with 6 μg/ml Atto 643 biotin in 0.1 % (v/v) TX in 1X PBS ON at RT with gentle agitation. Samples were washed once with 1X PBS and expanded ~4-fold by immersing in $ddH_2O$ with three fluid exchanges at 30 min intervals.

## III.8 Imaging

Data was acquired on three different microscope setups described below. A detailed summary of the labeling and imaging parameters for each dataset can be found in Supplementary Table 1. Power values refer to the power at the sample determined with a slide powermeter head (Thorlabs, S170C).

### III.8.1 Confocal imaging

Single point scanning confocal imaging was performed for volumetric imaging of expanded organotypic slice cultures and overview imaging of expanded brain slices from fixative perfused animals. A Leica Sp8 inverted microscope equipped with a supercontinuum pulsed white light laser (for excitation at 490 nm and 630 nm) and a 405 nm continuous wave diode laser, and HyD GaAaP detectors was used. Imaging was performed with a 40x water objective (Leica HC PL APO 40x/numerical aperture (NA) 1.10 W CORR CS2, WD 0.65 mm). The Leica LAS X software version 2.5.7.23225 was used for data acquisition.

### III.8.2 Spinning disk confocal microscopy

Spinning disk confocal microscopy was performed on an Andor Dragonfly imaging platform consisting of a Nikon Ti2E inverted microscope with a motorized stage, a spinning disk with two pinhole disc patterns (25 µm and 40 µm hole diameter) and four continuous-wave excitation lasers (405 nm, 488 nm, 561 nm and 637 nm). The signal was detected with an Andor Zyla 4.2 Megapixel sCMOS camera. Overview images of brain sections from fixative-perfused animals were acquired with a 10x air objective (Nikon CFI P-Apo 10x λ/NA 0.45/WD 4.0 mm). Overview images of organotypic slice cultures were acquired with a 20x air objective (Nikon CFI P-Apo 20x λ /NA 0.75/WD 1.00 mm). Volumetric data of expanded rCATS specimens was acquired with a long-working distance 20x water objective (Nikon CFI P-Apochromat 20x/NA 0.95/WD 0.95) or a 40x water immersion objective (Nikon Apochromat LWD 40x lambda S/NA 1.15/Water/ WD 0.6 mm) for high-resolution imaging. Andor Fusion software version 2.2 was used for data acquisition and stitching of tiles, unless otherwise stated.

### III.8.3 STED imaging

Confocal and STED imaging were performed on an inverted STED microscope (Abberior Instruments Expert Line) using a 60x water objective (Olympus UPLSAPO60XW 60x/NA 1.20 /WD 0.28) or a 100x silicone oil objective (Olympus UPLSAPO100XS 100x/NA 1.35/WD 0.20 mm), both equipped with a correction collar. Pulsed lasers (488 nm, 561 nm, 640 nm) were used for excitation and a pulsed 775 nm laser was used for stimulated emission. The pulse repetition rate was 40 MHz and fluorescence detection was time gated. Fluorescence was detected by photon counting avalanche photodiodes (APDs) using bandpass filters at 525/50 nm (Semrock, #F37-516), 605/50 nm (Chroma, #F49-605), and 685/70 nm (Chroma, #F49-686). Galvanometric mirrors were used for lateral scanning and a sample piezo stage (Physik Instrumente GmbH & Co, KG, #P-735.ZRO) was used for axial scanning.

For confocal imaging, a pinhole size of 0.5-1.0 Airy units was used. Typical imaging parameters for acquiring confocal data were 10-20 µs dwell time and 1-2 line accumulations.

Typical imaging parameters for acquiring single plane STED data with lateral resolution enhancement were: 10-20 µs dwell time, 3-5 line accumulations, 0.8-6.0 µW (561 nm) and 0.5-5.0 µW (640 nm) excitation laser power and 24-100 mW STED laser power. The 488 nm excitation channel was used in confocal mode with 0.5-5.0 µW excitation power. Pixel size was 30 nm x 30 nm or 50 nm x 50 nm. A spatial light modulator (SLM) was used for 2π-helical phase modulation to generate the *xy*-STED pattern and to partially compensate for aberrations.
Typical imaging parameters for acquiring volumetric $z$-STED data were: 10-15 µs dwell time, 2-3 line accumulations, 1-2 µW (561 nm) and 0.3-2.6 µW (640 nm) excitation laser power and 43-88 mW STED laser power. The 405 nm and 488 nm excitation channels were used in confocal mode with 6.8-16.0 µW (405 nm) and 0.2-5.0 µW (488 nm) excitation power, respectively. The voxel size was 50 nm x 50 nm x 50 nm. The SLM was used to create a π-top-hat phase modulation ($z$-STED) with the aim of predominantly increasing axial resolution. In Supplementary Fig. 12, combined $z$-STED (80% power) and *xy*-STED (20% power) patterns were used, with panel e acquired with the same parameters as Velicky *et al.*[29].
Volumetric imaging data was typically created with all power assigned to the $z$-STED pattern. The acquisition scan mode was set to $xzy$, with $y$ being the slowest scan axis. For STED imaging, the pinhole was adjusted to 0.5-0.9 Airy units.
The software Imspector version 14.0.3052 was used for data acquisition. Tiling at the STED microscope was implemented with a custom-written python script to control the position of the sample stage. The acquired tiles were stitched using the Fiji plugin 'Grid/Collection stitching'.

# IV Data analysis

## IV.1 Colormap inversion for CATS data

The lookup table (LUT) of all CATS images was inverted using ImageJ/Fiji[193] v1.53f51, unless otherwise stated. Display ranges were adjusted for visualization purposes. Intensity LUTs were linear, unless stated otherwise.

## IV.2 Visualization of multi-channel data

For displaying combined CATS plus immunostaining images, all channels were saved separately in RGB format and imported into GIMP v2.10.30. An alpha channel was added to the immunostaining channels and black was set to transparent (alpha=black). The resulting images were overlaid with the CATS data.

## IV.3 Denoising

Volumetric datasets were denoised with Noise2Void v0.2.1 (N2V)[183] with the following parameters, unless otherwise stated: noise2void 3Dmode, patch size 16 x 32 x 32 or 32 x 32 x 32 (*zyx*); number of patches per image: all; each patch augmented 8-times by rotation and axis-mirroring; neighborhood radius: 5; percent pixel manipulation: 1.5; number of epochs: 75-80; number of steps per epoch: 100; batch size: 8-16. Software was installed from GitHub (https://github.com/juglab/n2v). A workstation with the following specifications was used: Intel® Xeon® W "Skylake" W-2145, 3.60 GHz processor, 128 GB RAM, NVIDA GeForce RTX 2080Ti graphics card. The results were visually inspected for artifacts from denoising before further processing. For comparison with denoised data, raw data is displayed in corresponding supplementary figures 4 and 10.

## IV.4 Manual segmentation

Datasets for 3D-rendering in Fig. 2 and 3 were 5-fold upsampled in the lateral dimensions with nearest-neighbor interpolation using ImageJ/Fiji to ease manual segmentation, resulting in 10 nm x 10 nm x 50 nm voxel size. Manual segmentation was performed in VAST[199] v1.4.0, downloaded from https://lichtman.rc.fas.harvard.edu/vast/.

## IV.5 Identification and segmentation of pSCRs guided by immunostaining for synaptic markers

Analysis of coCATS data after *in vivo* stereotactic injection (Fig. 2, analysis of 3 imaging volumes) involved the following steps using custom written Python v3.7.12 pipelines implemented with Jupyter lab v3.2.4. For visual inspection, Napari v0.4.12 (https://doi.org/10.5281/ZENODO.3555620) was used.

### IV.5.1 BASSOON and SHANK2 segmentation

For background removal and smoothing, datasets for immunostained BASSOON (confocal) and SHANK2 (STED) were smoothed with two different Gaussian filters using *scipy.ndimage.gaussian_filter* with sigma of 15 and 1 voxels, corresponding to background and signal, respectively. The background was then subtracted from the signal and negative values were clipped to zero. Resulting images were then transformed into binary masks by global Otsu thresholding.

### IV.5.2 PSCR segmentation

After denoising of 3D-CATS data with N2V, contrast stretching with the *skimage.exposure.rescale_intensity* function was performed using the 1st and 99th intensity percentile (imaging volumes 1 and 2) or the 1st and 98th percentile (imaging volume 3) as limits. Next, the SHANK2 mask was dilated using *skimage.morphology.binary_dilation* with a ball of 2 voxels radius. Volumetric CATS data were then multiplied with the corresponding dilated binary SHANK2 mask to isolate regions containing pSCRs. Then, a global threshold was applied to the resulting image to create a binary CATS mask. The global threshold (*thr*) was computed individually for each dataset, and was set between the 95th (*p95*) and 100th percentile (*p100*) of voxel brightness, as judged by visual inspection using $thr = p95 + s * (p100 - p95)$, with $s = 0.65$ for imaging volumes 1, 2 and $s = 0.6$ for imaging volume 3. To obtain instance segmentations, the connected components of the CATS mask were labeled using the *skimage.label* function. Objects smaller than 8 voxels were discarded.

### IV.5.3 Colocalization

We classified segments obtained from the CATS channel as pSCRs when there was spatial overlap with both SHANK2 and BASSOON. For this, we first defined the overlap region between the BASSOON and non-dilated SHANK2 masks and retained CATS segments as pSCRs that had at least one voxel overlap with this intersection region.

### IV.5.4 Association of pSCRs with MFBs

We next associated pSCRs with individual mossy fiber boutons (MFBs). MFB volume segmentations were performed manually as described above and scaled back to the original voxel size (5-times downscaling in lateral dimensions). MFB masks were dilated using *skimage.morphology.binary_dilation* with a ball of 2 voxel radius. Then, pSCRs that overlapped with dilated MFBs (at least one voxel) were extracted and assigned to that bouton.

### IV.5.5 Manual proofreading

PSCR segments were manually proofread and corrected in VAST. For processing in VAST, MFB and pSCR segmentations were combined into the same layer, conserving manually segmented MFB shape. PSCRs were subsequently proofread. During proofreading empty voxels between pSCR segments and the manually created MFB segments were filled in.

## IV.6 MFB quantification

Single bouton quantification in Fig. 2c-g comprised the following steps. From each of the 3 volumetric datasets containing coCATS, BASSOON and SHANK2 labeling, 10 MFBs were randomly selected based on their characteristic shape and the presence of pSCRs sandwiched between BASSOON and SHANK2 staining.

### IV.6.1 Manual volume segmentation of MFBs

MFBs were manually segmented as described in section 4.4.

### IV.6.2 3D-mesh creation

The Scikit-image implementation of the marching cubes algorithm was used to create 3D-meshes of individual MFBs from the volume segmentation.

### IV.6.3 Volume and area

Bouton surface area $A_{MFB}$ and volume $V_{MFB}$ were computed using a custom-written script in Blender 2.92 (blender.org). Bouton volumes were computed with *bmesh.calc_volume* and areas were computed as the sum of mesh face areas.

### IV.6.4 MFB surface area occupied by pSCRs

The area of MFBs occupied by pSCRs were extracted using a custom Python script. For each 3D-segmented pSCR, voxels that touched the bouton segment and thus defined the contact area between pSCR and MFB were extracted. The coordinates of those voxels were converted into point cloud data (pcd) format using the open3d library in Python. The ball-pivoting algorithm from the open3d library with two radii (1 and 1.5 voxel) was used to create a triangle mesh from the point cloud. All surfaces were manually checked and minor corrections were made in Blender where necessary. The area of contact between a pSCR and an MFB was computed as sum of the corresponding mesh face areas. The total area of individual boutons occupied by pSCRs ($A_{pSCR/MFB}$) is the sum of the pSCR/MFB contact areas of all pSCRs connected to one bouton.

## IV.7 Deep-learning-based prediction of synapse location

To predict synapse location purely from coCATS data, immunostained synaptic markers in the pSCR segmentation pipeline described in section 4.5 were replaced by a deep-learning-based prediction of molecule location. Here, instead of using super-resolved images of immunostained SHANK2 to guide pSCR segmentation, we used super-resolved BASSOON location predicted from the CATS channel. To predict BASSOON location, we used image translation with a U-Net convolutional neural network (CNN)[205] trained with super-resolved coCATS and BASSOON immunostaining data. Code was adapted from Qian et al., 2021 (https://github.com/Li-En-Good/VISTA)[100].

### IV.7.1 Data pre-processing

13 pairs of STED volumes including coCATS plus immunostaining for BASSOON were used for training (~85000 $\mu m^3$). CATS volumes were denoised with N2V and converted into 16-bit format. For background subtraction and denoising of the BASSOON channel, two different Gaussian filters using *scipy.ndimage.gaussian_filter* with sigma of 15 and 1 voxels were applied, corresponding to background and signal channels, respectively. The background channel was subtracted from the signal channel and any negative values were set to zero.

### IV.7.2 Training

The image translation network was trained for 10,000 iterations with batch size 8, buffer size 5 and patch size 64 x 64 x 32 (*xyz*). Training was performed on a single node of a high performance computing cluster available at the Institute of Science and Technology Austria, with a Intel(R) Xeon(R) CPU E5-2680 v4 @ 2.40GHz CPU and 256 GB RAM, assigning up to 64 GB RAM and one CPU according to availability. Training took ~2 h using acceleration with a single GPU (GeForce RTX 2080 Ti). Prediction took ~3.5 min.

### IV.7.3 Segmentation

The predicted super-resolved BASSOON signal was thresholded to obtain a binary mask, dilated as described in section 4.5.2 and multiplied with the corresponding coCATS data to isolate regions containing pSCRs. CATS data was contrast-stretched and thresholded at *thr* = p93 + 0.4 * (p100 - p93), with p93 being the 93$^{rd}$ intensity percentile for binarization.

### IV.7.4 Validation of deep-learning-based synapse prediction

IV.7.4.1 Validation metrics

Voxel- and object-based metrics were used to assess the performance of the trained synapse prediction model, using a test dataset (224 x 224 x 96 voxels) not included in the training, whose size was chosen to account for the specific model architecture.
For voxel-based evaluation, the Pearson correlation coefficient r between BASSOON location predicted from CATS images and BASSOON immunostaining was computed using the *numpy.corrcoef* function in Python.
For object-based evaluation, pSCR segments based on predicted BASSOON location ($pSCRs_{prediction}$) and pSCR segments based on immunostaining for BASSOON ($pSCRs_{immuno}$) of the same region were compared using the *F1* score (Fig. 2k, Supplementary Fig. 5). First, corresponding objects from immunostaining-derived and prediction-derived segmentations were found based on spatial overlap of at least one voxel. For each pair, the intersection over union (IOU, ratio of overlapping volume vs. combined volume) was computed. If a segment from the immunostaining pipeline overlapped with more than one segment from the deep learning pipeline, the immunostaining/deep learning segment pair with the larger IOU was retained. The number of true positives ($N_{TP}$) was determined as the number of $pSCRs_{immuno}$ segments with an IOU above threshold. Conversely, if the IOU was below this threshold, they were considered as false negatives ($N_{FN}$). For calculating *F1*, the threshold was set to 0.5. The number of false positives ($N_{FP}$) was determined as the number of $pSCRs_{prediciton}$ segments that did not have a corresponding $pSCRs_{immuno}$ segment (i.e. their associated IOU value was lower than the threshold). Precision (*P*), recall (*R*), and *F1* (ranging from 0 to 1) were calculated as a function of IOU threshold according to:

$$\mathrm{F1} = 2 \cdot \frac{P \cdot R}{P + R}$$

$$P = \frac{N_{\mathrm{TP}}}{N_{\mathrm{TP}} + N_{\mathrm{FP}}}$$

$$R = \frac{N_{\mathrm{TP}}}{N_{\mathrm{TP}} + N_{\mathrm{FN}}}.$$

IV.7.4.2 Effect of denoising on deep-learning-based synapse prediction

To study the effect of the N2V algorithm on performance of deep-learning-based synapse prediction (Supplementary Fig. 5b), a network was trained with raw instead of N2V-denoised CATS data and super-resolved BASSOON, using raw versions of the same datasets. Processing for the BASSOON immunostaining channel was identical as before whereas pSCR segmentation was done after contrast stretching and Gaussian smoothing of the CATS data using a kernel of 0.5 x 0.5 x 0.5 voxels. The threshold for pSCR segmentation of CATS data was set to *thr* = p85 + 0.4 * (p100 - p85), with p85 being the 85$^{th}$ intensity percentile.

IV.7.4.3 Effect of super-resolution imaging on deep-learning-based synapse prediction

To compare performance of deep-learning-based synapse prediction for super-resolution vs. diffraction-limited acquisition of the molecular ground truth channel (Supplementary Fig. 5e,f), we trained a model with super-resolved coCATS data using either super-resolved or confocal data of immunostained BASSOON as molecular ground truth. Overall training volume was ~65,000 $\mu m^3$ for each. Thresholds for binarizing coCATS data were set to *thr* = p93 + 0.4 * (p100 - p93) for the test dataset using super-resolved BASSOON and *thr* = p96 + 0.4 * (p100 – p96) for the test dataset using confocal BASSOON.

## IV.8 Reconstruction of a local synaptic input field

Reconstruction of synaptic input onto a CA3 pyramidal neuron (PN) proximal dendrite in Fig. 3 was performed according to the following steps.

### IV.8.1 Denoising

The coCATS data was denoised with N2V according to section 4.3. The intracellular channel (Lucifer yellow) was not denoised.

### IV.8.2 Manual segmentation

The positively labeled structure (proximal dendrite of CA3 PN filled with Lucifer yellow during patch-clamp recording) was manually segmented based on the super-resolved coCATS data as described in section 4.4. Then, all structures forming synaptic connections with the proximal dendrite were identified via existence of pSCRs in the CATS data and segmented as well.

### IV.8.3 Visualization

3D-meshes were created as described in section 4.6.2. To account for the lateral upsampling for manual segmentation, the resulting meshes were 5-times upsampled in the axial dimension in Blender to preserve the original proportions.

### IV.8.4 Complex spine extraction and quantification

To extract complex spines, the PN segment was morphologically opened (erosion followed by dilation) with *skimage.morphology.binary*_opening (ball with 3-voxel radius) to detach spines from the main branch. The largest fragment (main branch) was dilated with *skimage.morphology.binary_dilation* by 1 voxel and subtracted from the original PN segment, yielding a binary mask containing all complex spines. *Skimage.measure.label* was used to generate an instance segmentation of complex spines. Minor manual corrections to the resulting objects were done in VAST. Spine meshes were generated with the marching cubes algorithm and imported into Blender to determine their volumes as described above.

### IV.8.5 MFB extraction and quantification

MFBs were identified by the following characteristics: 1. Bulbous enlargement in close proximity to the PN proximal dendrite, 2. One or multiple contacts (pSCRs, typically wrapping postsynaptic structures) with the spines of the PN proximal dendrite, 3. An axon running alongside other axons in a mossy fiber bundle, typically roughly perpendicular to the PN proximal dendrite. All segmented structures that did not fulfill these characteristics were classified as non-MFB structures. Only structures which were situated completely or near-completely (roughly >80 % as judged from lower resolution overview images) in the imaging volume were included in the quantification.
To measure volume of MFBs (Fig. 3j), axons and filopodia were detached from the main bouton bodies by erosion and dilation adapted for each object, followed by manual corrections in VAST. 3D-meshes were constructed for each bouton. Volumes were computed as described above.

### IV.8.6 Deep-learning-based pSCR segmentation

We used the image translation model trained on super-resolved CATS and BASSOON in Fig. 2j for pSCR segmentation (Extended Data Fig. 7). For the prediction of BASSOON location, the CATS dataset in Fig. 3 (456 x 530 x 160 voxels) was denoised with N2V and cut into overlapping 3D patches (224 x 224 x 96 voxels). Predictions of BASSOON location for individual patches were combined and fed into the pSCR segmentation pipeline, during which contrast stretching (1$^{st}$

and 98$^{th}$ intensity percentile) and thresholding at *thr* = p96 + 0.65 * (p100 - p96) was applied to CATS data.

### IV.8.7 Quantification of MFBs-spine interactions

An interaction between an MFB and a complex spine (Fig. 3h,i) was identified if one or more pSCRs connected these two structures. PSCR masks were dilated with a ball structure with a radius of 1 voxel. For each pSCR, a list of both MFBs and spines having at least 1 voxel spatial overlap with the pSCR was generated. If a pSCR displayed overlap with more than one MFB, the one with the largest overlap was retained. These lists were used to determine the number of MFBs interacting with each spine and number of spines interacting with each MFB.

## IV.9 Reconstruction of synaptic output field

Reconstruction of the synaptic output field of a DG granule cell Fig. 4d,e was performed according to the following steps.

### IV.9.1 Segmentation of the positively labeled neuron

The positively labeled DG granule cell axon was segmented from the super-resolved intracellular channel using the Otsu thresholding method. In Fig. 4d, the resulting binary mask was additionally eroded with *skimage.morphology.binary_erosion* by 1 voxel.

### IV.9.2 Manual segmentation of postsynaptic structures

All structures forming synaptic connections with the boutons of the positively labeled DG granule cell were identified via existence of pSCRs in the coCATS data and segmented as described in section 4.4 without upsampling.

### IV.9.3 Deep-learning-based pSCR segmentation

PSCR segmentation was performed as described in section 4.8.6, where CATS channels were contrast-stretched using the 1$^{st}$ and 99$^{th}$ intensity percentile and binarized using *thr* = p95 + 0.65 * (p100 - p95).

### IV.9.4 Association

Next, pSCRs associated with the positively labeled DG granule cell were identified. First, the segmentation masks obtained from the positively labeled neuron in the individual imaging volumes were dilated using *skimage.morphology.binary_dilation* with a ball with a 2-voxel radius. Then, only pSCRs that overlapped (at least one voxel) with dilated masks were retained.

### IV.9.5 Visualization

3D-meshes of the segmented positively labeled DG granule cell axon, associated postsynaptic structures, and pSCRs were created as described in section 4.6.2 and imported into Blender for visualization.

## IV.10 Expanded rCATS data

### IV.10.1 Pre-processing

Before stitching pre- and post-expansion volumes with the Fiji plugin BigStitcher version 0.8.3[195], we created a new BigStitcher dataset using the *Automatic Loader (Bioformats)* option. Tiles were initially arranged with the *Move Tiles to Regular Grid* option with a 12 x 10 tile arrangement (pre-expansion) and 5 x 6 tiles arrangement (post-expansion) both with 10 % overlap in each

dimension. For efficient alignment and visualization in BigDataViewer[194], both volumes were resaved (using default options) to the chunked, pyramidal image format *N5* with 6 pre-computed resolutions levels.

### IV.10.2 Alignment

Tiles were stitched using BigStitcher version 0.8.3. For the *Pairwise shift calculation* we averaged over the raw channels in the post-expansion volume. The pairwise shifts between all adjacent tiles were computed at 2x sub-sampled resolution. Resulting shifts were filtered based on their Pearson correlation coefficient r. Only shifts exceeding a corresponding r-value of 0.7 were used in the global optimization. We used the option *Identify wrong links and handle unconnected Tiles, STRICT* as the global optimization strategy. Once datasets were aligned, we fused and exported aligned tiles into new HDF5/BigDataViewer files. We chose 16-bit unsigned integer as pixel type, tri-linear interpolation and smooth image blending for the fusion operation. To not exceed the available computer memory of 128 GB we used the *Cached* image option. For HDF5 creation, we used BigStitcher's default parameters.
For denoising the post-expansion image, we developed custom training and prediction Python scripts based on the BigDataViewer/N5 data-set and Noise2Void (version 0.2.1). For training, 6000 patches of size 64 x 64 x 64 (*xyz*) were randomly sampled across the entire volume per channel. We trained for 60 epochs with 256 steps per epoch. Each channel was trained independently of the other channels and yielded a N2V model file per channel. We predicted the denoised output for each N5 chunk in parallel with SLURM on a high-performance cluster with GPU-acceleration using a custom Python script.
Manual alignment of the pre- with the post-expansion volume was performed with BigWarp[196] by matching landmarks in the Thy1-EGFP channels in 3D. The effective expansion factor was extracted from BigWarp's landmark file using a custom Fiji/Groovy script.
For manual annotations of objects skeletons, the denoised multi-channel post-expansion volume was converted from BigDataViewer/HDF5 format to the webKnossos file data structure. Since the volumes exceeded available main memory of 128 GB, we created custom Python scripts based on the webKnossos Python library (version 0.10.5) to convert the binary image data block-wise.

### IV.10.3 Skeletonization

The skeletonization of a mossy cell in the DG hilus was performed with webKnossos (version 22.05.1)[198]. WebKnossos was installed on a local server following the instructions in the webKnossos documentation (https://docs.webknossos.org/webknossos/installation.html, section: Installation on your Server) with slight modifications. Specifically, we explicitly attached the ports for both the datastore (9000) and tracingstore (9000) and started *Docker* through *Docker-compose* specifying the *Docker* tag 22.05,1. Due to the large size of the dataset, we used file-system transfer. The local server ran on a 2x AMD EPIC™ MILAN 75F3 processor, 32-core 32C/64T, 2.95 GHz with 512 GB of memory, 2 TB Intel NVMe-SSD and 4x NVIDIA A6000 GPUs. To create a skeleton, a cell soma situated in the center of the volumetric dataset was chosen and skeletonized with the webKnossos-skeleton tool with orthogonal views.

## IV.11 Dense reconstruction of human cerebral organoid volume

### IV.11.1 Intensity homogenization

The 3D-dataset was denoised using N2V and intensity was normalized to the maximum value. To account for a slight gradient in image intensity with depth, adaptive histogram equalization was implemented with a custom Python script based on the *skimage.exposure.equalize_adapthist* function. The clip limit was set to 0.02 and the kernel size to 1/5 of the stack size in each dimension.

### IV.11.2 Manual segmentation

Manual segmentation was performed as described in section 4.4.

### IV.11.3 Visualization

The segmented volume was visualized using the 3D viewer in VAST.

# V Statistics and reproducibility

## V.1 Experimental reproducibility

In all images, representative data from single experiments are shown. *In vivo* microinjections of different coCATS labeling compounds into multiple brain areas were performed at least 10 times. MFB segmentation and MFB and pSCR quantifications (Fig. 2c-i) were performed on three volumetric imaging datasets from two brain sections coming from the same animal. Deep-learning-based prediction of synapse location based on super-resolved BASSOON immunostaining was performed on 13 volumetric imaging datasets from five brain sections coming from three animals (Fig. 2j-l). Deep-learning-based prediction of synapse location from confocal BASSOON immunostaining (Fig. 2j-l, Supplementary Fig. 5) was performed on 8 volumetric imaging datasets from five brain sections coming from two animals (Supplementary Fig. 5e). Whole-cell patch-clamping experiments combined with coCATS labeling as seen in Fig. 3 and 4 were performed at least 20 times with various cell types being patched. Reconstructions (Fig. 3h,i and Fig. 4d,e) were created from individual volumetric imaging datasets. CoCATS labeling of organotypic slice cultures in combination with expansion microscopy (Fig. 5a,b) was performed at least 3 times. CoCATS viability experiments (Supplementary Fig. 6a) were performed in cultures prepared at three different time points, and for each condition (control, STAR RED-NHS) at least three samples were used per condition. CoCATS labeling of cerebral organoids (Fig. 6c-e) was performed at least 3 times.
RCATS labeling of PFA perfusion-fixed mouse brain tissue was performed at least 20 times. RCATS labeling of PFA perfusion-fixed mouse brain tissue in combination with expansion microscopy (Fig. 5c-f) was performed at least 5 times. RCATS labeling of human brain tissue (Fig. 6a,b) was performed on samples from four individuals.

## V.2 Statistics

Graphs, except for line profile graphs, were created with GraphPad Prism (version 9.0.2). Graphs of line profiles, created with ImageJ/Fiji, were generated with Excel 2016. All statistical tests were performed with GraphPad Prism.
Graphs in Fig. 2c-e show individual data points (grey circles), as well as mean and standard deviation (s.d.). Graphs in Fig. 2f,g and Extended Data Fig. 5b,c show individual data points (grey circles) and linear regression lines with their corresponding R-squared values ($R^2$). Pearson correlation was performed to test the extent of linear correlation in these datasets and is reported in form of Pearson correlation coefficient (r) with 95% confidence intervals (CI), and two-tailed p-value (p). Volume distributions in Fig. 3j are displayed as violin plots with medians (lines) and quartiles (dashed line). Single MFB and single spine connectivities in Fig. 3k,l are displayed as pie charts including percentage of all instances. The graph in Supplementary Fig. 6a shows mean and s.d. of 11 (control) and 9 (STAR RED-NHS) data points per current. Unpaired t-test was used to compare whether the difference between the two experimental groups (control; STAR RED-NHS) for each current was significant (s, $p<0.05$) or not significant (ns, $p>0.05$).

## V.3 Creation of figures

Schematics in Fig. 1a, Supplementary Fig. 2a and Supplementary Fig. 13a were created with BioRender (biorender.com).

# 6.3.2 Saturated reconstruction of living brain tissue



1 # Saturated reconstruction of living brain tissue

2

3 Philipp Velicky[1], Eder Miguel[1], Julia M. Michalska[1], Donglai Wei[2,3], Zudi Lin[2], Jake F. Watson[1],
4 Jakob Troidl[2], Johanna Beyer[2], Yoav Ben-Simon[1,4], Christoph Sommer[1], Wiebke Jahr[1,5], Alban
5 Cenameri[1], Johannes Broichhagen[6], Seth G. N. Grant[7,8], Peter Jonas[1], Gaia Novarino[1], Hanspeter
6 Pfister[2], Bernd Bickel[1], Johann G. Danzl[1*]

7

8 [1]Institute of Science and Technology Austria (ISTA), Klosterneuburg, Austria.
9 [2]School of Engineering and Applied Sciences, Harvard University, Cambridge, MA, USA.
10 [3]present address: Department of Computer Science, Boston College, Boston, MA, USA.
11 [4]present address: Dept. of Neurophysiology and Pharmacology, Vienna Medical University,
12 Vienna, Austria.
13 [5]present address: In-Vision Technologies AG, Guntramsdorf, Austria.
14 [6]Leibniz-Forschungsinstitut für Molekulare Pharmakologie, Berlin, Germany.
15 [7]Genes to Cognition Program, Centre for Clinical Brain Sciences, University of Edinburgh,
16 Edinburgh, UK.
17 [8]Simons Initiative for the Developing Brain (SIDB), Centre for Discovery Brain Sciences,
18 University of Edinburgh, Edinburgh, UK.

19

20 *correspondence to: johann.danzl@ist.ac.at
21

# Abstract

Complex wiring between neurons underlies the information-processing network enabling all brain functions, including cognition and memory. For understanding how the network is structured, processes information, and changes over time, comprehensive visualization of the architecture of living brain tissue with its cellular and molecular components would open up major opportunities. However, electron microscopy (EM) provides nanometre-scale resolution required for full *in-silico* reconstruction[1–5], yet is limited to fixed specimens and static representations. Light microscopy allows live observation, with super-resolution approaches[6–12] facilitating nanoscale visualization, but comprehensive 3D-reconstruction of living brain tissue has been hindered by tissue photo-burden, photobleaching, insufficient 3D-resolution, and inadequate signal-to-noise ratio (SNR). Here we demonstrate saturated reconstruction of living brain tissue. We developed an integrated imaging and analysis technology, adapting stimulated emission depletion (STED) microscopy[6,13] in extracellularly labelled tissue[14] for high SNR and near-isotropic resolution. Centrally, a two-stage deep-learning approach leveraged previously obtained information on sample structure to drastically reduce photo-burden and enable automated volumetric reconstruction down to single synapse level. Live reconstruction provides unbiased analysis of tissue architecture across time in relation to functional activity and targeted activation, and contextual understanding of molecular labelling. This adoptable technology will facilitate novel insights into the dynamic functional architecture of living brain tissue.


# Introduction

Brain computation and information storage are intimately linked to the structure of a network of ~86 billion neurons[15] in humans. Each is typically connected by thousands of information-transmitting synapses to other neurons and interacts with glial support cells. To address how this incredibly crowded and complex tissue's architecture, connectivity, and functional activity evolve over time and interrelate, one would ideally employ a technology that enables imaging and *in-silico* reconstruction of *living* brain tissue. This would allow mapping of how neuronal and non-neuronal cells and their delicate, functionally paramount subcellular specializations, such as synapses, relate to each other in the 3D tissue environment, and how this changes over time or in response to specific intervention. Combining connectivity information with the location of specific molecules could then further define cellular and subcellular identities, and provide a molecular ground truth for synapse location and type.

EM reconstruction[1–5] offers the most detailed insights into brain architecture. However, it is limited to fixed specimens, static tissue representations, and sample preparation that impedes molecular labelling. A light microscopy-based technology for tissue reconstruction, in contrast, could enable observation of living systems, together with visualization of specific molecules and cellular signaling. The intricate cellular arrangements in brain tissue call for a super-resolution approach[6–9] with resolution improvement in all three spatial dimensions, because reconstruction is limited by the lowest-resolution direction (typically along the optical axis, *z*-direction). Conventional (diffraction-limited) microscopy is unsuitable, as it has a best-case lateral resolution of about half the wavelength of employed light and axial resolution as poor as ~1000 nm for tissue-compatible high-numerical aperture objective lenses and far red excitation. The ongoing revolution in machine learning is transforming not only image analysis, including for connectomics, but brings about new concepts for how to amalgamate data acquisition and analysis in microscopy.

Here we introduce saturated reconstruction of living brain tissue. To achieve dense reconstruction of the cellular components in tissue volumes, we developed an integrated optical /machine learning technology for tissue imaging that breaks the intertwined limitations for 3D-resolving power, signal-to-noise ratio (SNR), speed, and light burden in classical super-resolution imaging of living systems. We started from the realization that this would require specifically adapting and melding the three key elements factoring into overall information yield, i.e. biological preparation, in-tissue 3D-super-resolution imaging technology, and analysis. We based our technology on stimulated emission depletion[6,13] (STED) microscopy. Here, a light pattern turns off fluorophores at sub-nanosecond timescales except those located near its intensity minimum and positions are queried sequentially. STED is thus compatible with freely diffusing fluorophores and relatively robust against movement in living samples. Unlike visualization of protein distributions or tracing the morphology of sparse cells[16], saturated tissue reconstruction requires comprehensive delineation of all cells. We therefore employed super-resolution shadow imaging[14], where extracellularly applied fluorophores[17] define cellular structures more comprehensively than in single-molecule approaches for extracellular space imaging (ECS)[18], and which has proven powerful for visualizing cellular arrangements and neuronal interactions[19–21]. Here, photobleached fluorophores are replenished by diffusion, and radicals generated from extracellular fluorophore bleaching are less able to damage the specimen than intracellular radicals. Despite these advantages, synapse-level reconstruction of living brain tissue has been elusive. The square-root dependence of resolution on applied STED laser power[22] and the need for Nyquist sampling in 3D with low tens of nanometers

step sizes impose a heavy cost of tissue light-burden to increase 3D-resolution[23]. Together with in-tissue optical imperfections leading to progressive signal loss at higher resolution, these factors ultimately limit achievable 3D-resolution and signal-to-noise ratio (SNR)[24].

We therefore specifically modified STED for improved SNR and near isotropically super-resolved tissue imaging, coupled with a custom-designed, two-stage deep-learning strategy. Stage one leveraged information on sample structure from numerous separate, prior measurements allowing to drastically reduce light burden and imaging time without sacrificing resolution, and hence enabled live-tissue compatible volumetric super-resolution imaging. Counterintuitively, SNR was improved even beyond ground-truth high-SNR training data, which was key for subsequent automated segmentation tasks. Stage two was adapted from EM-connectomics algorithms and trained to automatically translate our volumetric live-imaging data into a saturated instance segmentation at single synapse level. We termed this technology LIONESS for *Live Information-Optimized Nanoscopy Enabling Saturated Segmentation* (**Fig. 1A**). LIONESS allows dynamic brain tissue reconstruction paired with molecular and functional information.

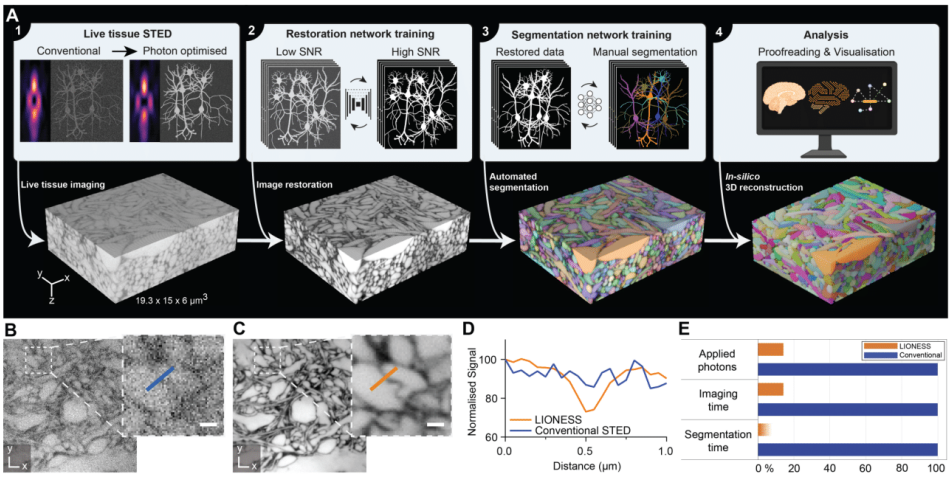


**Fig. 1. LIONESS enables saturated reconstruction of living brain tissue.** (**A**) LIONESS technology exemplified in living human cerebral organoid. Optical improvements, deep-learning training, and analysis (top) flow into individual processing steps (bottom): (1) Near-infrared STED with light patterns for improved effective point-spread-function in tissue. (2) Deep neural network training on paired low-exposure, low-SNR and high-exposure, high-SNR 3D-super-resolved volumes. (3) Deep 3D-segmentation network training with manually annotated data. (4) Postprocessing. (**B**) Conventional STED imaging in CA1 neuropil of organotypic hippocampal

slice culture with phase modulation patterns for lateral (*xy*)- plus axial (*z*)-resolution increase. (**C**) Same region imaged with tissue-adapted STED patterns (4π-helical plus π-top-hat phase modulation), improved detector dynamic range, and deep-learning based SNR-restoration. STED power and dwell time were identical in panels B and C. Scale bars: 500 nm. (**D**) Line profiles across a synaptic cleft as indicated in (B) and (C). (**E**) Light exposure and imaging time were reduced by 86% with LIONESS compared to conventional high-photon load ground truth in network training, in addition to optical improvements of SNR. Deep-learning accelerates segmentation by orders of magnitude, also depending on sample complexity. LIONESS lookup tables are linear and inverted throughout, ranging from black (maximum photon counts extracellularly) to white.

# Results

### *Achieving near-isotropic high-SNR STED in tissue*

We opted for near-infrared STED (775 nm), to deliver highest STED performance coupled with reduced tissue absorption and scattering over visible light[23,25]. We screened for cell-impermeant fluorophores to label ECS and delineate cellular structures with maximized extra- vs. intracellular contrast, and identified suitable hydrophilic, anionic high-performance STED labels, including both unmodified commercial and custom sulfonated variants (**Suppl. Fig. 1**). We aimed for near-isotropic STED resolution and first incoherently overlapped classical 2π-helical and π-top-hat phase modulation patterns to achieve lateral (*xy*) and predominantly axial (*z*) STED resolution increase[24], respectively, and mitigated spherical aberrations on the sensitive *z*-STED pattern using a silicone immersion objective with correction collar. However, the resulting intensity minimum of the combined light patterns was highly susceptible to aberrations and imperfect spatial overlap in tissue. We therefore replaced the 2π(*xy*)-pattern with a helicity-2 mode generated by 4π-helical phase modulation[26]. The shallower intensity rise and broader overall distribution of the 4π(*xy*)-STED pattern allowed more robust in-tissue alignment and improved quenching of "sidelobe" fluorescence insufficiently silenced by the *z*-STED pattern alone (**Suppl. Fig. 2A-C**). This led to substantially enhanced definition of cellular structures (**Suppl. Fig. 2D**). Increasing detector dynamic range further improved SNR (**Suppl. Fig. 3**). To delineate narrow spaces between cells with the extracellular label in 3D and detect the fluorescence modulation produced by thin cellular processes with sufficient SNR for segmentation, we integrated photons for 70µs per 50 x 50 x 50 $nm^3$ voxel and dialed in near-isotropic resolution of ~130 nm. However, this approach was too harsh and too slow for volumetric imaging of living tissue, causing dramatic photodamage in the tissue sample (**Suppl. Fig. 4A)**.

***Low-exposure, high-speed STED***

We thus sought for strategies to simultaneously reduce both the light burden and imaging time while augmenting SNR. To achieve this, we recorded low-exposure STED data at high speed and deployed deep-learning-based restoration to computationally increase SNR, retrieving information on sample structure from prior measurements. We trained a convolutional neural network[27] (**Suppl. Fig. 5A)** on paired low- and high-SNR imaging volumes from mouse organotypic slice cultures and the alveus region of acutely prepared mouse hippocampus. These contained diverse structures that were sampled at high SNR with 70 µs voxel dwell time, from which we set aside photon counts of the first 10 µs as low-SNR training input data. This ensured that both corresponded to voxel-exact equivalent sample structures. We could then apply this trained neural network to previously unseen data to predict high-SNR images from low-exposure input data. To evaluate the accuracy of this prediction in the context of cellular segmentation, per-voxel probabilistic uncertainty measures and ensemble disagreement between independently trained networks[27] were of limited utility (**Suppl. Fig. 5B**). Therefore, we compared prediction outcome with corresponding sparse, positively labelled cellular structures (**Suppl. Fig. 6A**) and with paired high-SNR measurements, with both not included in the training (**Suppl. Fig. 6B**). This indicated that inaccuracies at the voxel level did not negatively impact delineation of cellular structures.

Repeated volumetric imaging in this low-exposure mode left cells intact, whereas they disintegrated when aiming to achieve similar resolution and SNR with the conventional high-photon load STED mode (**Suppl**. **Fig. 4**). Development of this scheme further reduced photon load by 86%. In contrast to current techniques[24] for reducing STED exposure[28,29] and photobleaching[30,31], it also correspondingly sped up acquisition 7-fold and additionally denoised the data. Integrating labelling, optimizations for in-tissue isotropically resolving super-resolution imaging, low-exposure data collection, and computational SNR restoration resulted in a substantial gain in image quality over conventional STED imaging for given live-tissue compatible STED light exposure (**Fig. 1B-E**). For example, when applied to dense neuropil in organotypic hippocampal slice cultures, this LIONESS imaging regime revealed synaptic clefts at STED light exposure far too low to do so in conventional STED mode (**Fig. 1B-D**). Together, this resulted in volumetric light-microscopy data suitable for comprehensive segmentation of living neuronal tissue.

***In-silico saturated reconstruction***

Manual annotation of all cellular structures in a small volume of such LIONESS imaging data showed that saturated live tissue reconstruction was feasible. However, it was time consuming and therefore poorly scalable. Segmentation of a ~400 µm$^3$ volume of living brain tissue, selected from a highly interwoven region of neuropil in an organotypic hippocampal slice, took a trained segmenter ~450 hours **(Suppl. Fig. 7)**. We therefore implemented a second deep neural network for automated segmentation, adapting algorithms and software from EM-connectomics[32,33], and employed an iterative training scheme. We initially trained the network on a subvolume of the manually annotated LIONESS imaging volume (~285 µm$^3$, the other part was used for validation) and applied it together with watershed postprocessing to larger imaging volumes that harbored additional structural diversity (CA1 and dentate gyrus (DG) neuropil in organotypic hippocampal slice cultures and alveus in acutely prepared hippocampi). We then manually proofread the output and fed it back into training, thus extending the training volume to ~800 µm$^3$, yielding an improved segmentation neural network with enhanced prediction quality.

We chose living human cerebral organoids[34] as first specimen for automated reconstruction, as these have emerged as powerful model systems for studying human brain development and disease mechanisms at cell to tissue level. When applied to a living cerebral organoid, our pipeline enabled saturated tissue reconstruction (**Fig. 1A)**. Such samples with moderately complex tissue structure required minor intervention by manual proofreading. Reconstruction yielded contextual information not available with imaging of sparsely labelled specimens. For example, we observed the interaction of an axonal growth cone with neighboring structures in the living organoid (**Suppl. Fig. 8**). The gain in throughput from automated over manual segmentation was substantial, with our whole pipeline including microscopic data acquisition (140 seconds), image restoration (10 seconds) and automated saturated segmentation (~40 minutes) taking less than 45 minutes excluding data inspection and proofreading (**Fig. 1E**). Manual segmentation would require an estimated ~860 person-hours for this organoid dataset (1,737 µm$^3$). Extracting the space not occupied by cellular segments additionally allowed us to reconstruct the ECS, which amounted to 225 µm$^3$ or 13% in this organoid subvolume (**Suppl. Fig. 9**).

In the next step, we chose the alveus of intact, acutely dissected mouse hippocampi, a region that is extremely densely packed with thin neuronal processes transmitting signals to other regions. Automated reconstruction highlighted the thin, individually resolved axons running in various orientations and interacting with glial cells (**Suppl. Fig. 10A-C and Suppl. Videos 1 and 2**). Such

dense but structurally comparatively homogeneous regions also required little intervention during proofreading. Approximately 45 corrections per mm axon length were necessary in such data, with false splits being the dominant type of error (**Suppl. Fig. 10D**). These data showed that a comprehensive structural segmentation of living nervous tissue is feasible. Furthermore, deep-learning models for segmentation were applicable across brain tissue preparations.

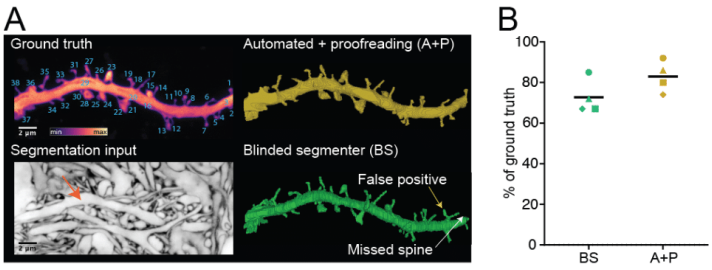


**Fig. 2. Validation of segmentation. (A)** *Top left*: Maximum intensity projection of a dendrite in organotypic hippocampal slice culture labelled by cytosolic EGFP expression. The positive label serves as ground truth for segmentation, with individual spines numbered. *Bottom left*: Plane from volumetric LIONESS acquisition with arrow indicating the same dendrite (maximum intensity projection spanning 150 nm). *Top right*: 3D-reconstruction after automated segmentation and proofreading of LIONESS imaging data by the experimenter who recorded the data (A+P). As this person was not blinded to the EGFP-channel, this indicates which spines can be retrieved from LIONESS but does not serve as independent control. *Bottom right*: Fully manual spine detection from LIONESS imaging data by a segmenter blinded to the EGFP-channel (BS). Exemplary missed and false positive spines are indicated by white and yellow arrows, respectively. **(B)** Percentage of correctly assigned spines from the automated plus proofread (A+P, orange) and manual (BS, green) segmentations relative to the total number of spines in the positively labelled ground truth for 4 different datasets from three independent samples **(Suppl. Fig. 11)**. Correctly identified spines were counted as +1, false positives as -1. Black bars: mean of the 4 datasets.

### *Validation of segmentation*

To test the potential of this technology for saturated reconstruction and analysis of complex nervous tissue specimens, we collected imaging volumes from the highly interwoven neuropil in organotypic hippocampal slices. These volumes contained diverse neuronal structures from spiny dendrites, to axons and their boutons, and astrocytic processes. We focused on assignment of dendritic spines to dendrite branches, as the fine connecting spine necks are among the thinnest of neuronal structures. We tested our reconstruction capability against sparse structural ground truth from cytosolic EGFP expression, which revealed all dendritic spines on a given dendrite. From

LIONESS imaging data alone, without automated segmentation, a neuroscientist blinded to EGFP ground truth data correctly assigned 73% (±8.3%, mean ± standard deviation, s.d.) of spines in four different example dendrite stretches (from three independent biological replicates; 129 spines in total, 34 missed, 2 false positive). When applied to the same datasets, the artificial network often segmented and correctly connected spines to the respective dendrite or classified spines as separate (orphan) segments which could then be unambiguously assigned to a dendrite. The experimenter who collected the data performed proofreading of the segmentation output and correctly attached 83% (±8.0%, mean ± s.d.; 129 spines in total, 20 missed, 0 false positive) of dendritic spines (**Fig. 2, Suppl. Fig. 11**). This showed that both manual and automated reconstruction can retrieve a large percentage of dendritic spines and demonstrated applicability of LIONESS for analysis of neuropil architecture.

***Connectivity reconstruction***

We now applied our technology to living hippocampal neuropil in the dentate gyrus (DG) to unbiasedly visualize the architecture of this complex region. We identified and reconstructed diverse cellular constituents like myelinated and unmyelinated axons, spiny dendrites, and glial cells in the densely packed tissue volume (**Fig. 3A,B, Suppl. Fig. 12A, and Suppl. Video 3**). Similar as with EM, proofreading of automated segmentation remains a time-limiting factor, such that it is often preferable to selectively apply it to the specific structures of interest. We focused reconstruction on an individual dendrite, revealing 38 spines that showed various morphologies, including thin, branched, mushroom-shaped, and filopodial (**Fig. 3C**). Spine heads were of diverse 3D-shapes, some hand-like engulfing part of the presynaptic bouton. Spine lengths ranged from 0.54 µm to 3.96 µm (1.77 µm ± 0.69 µm, mean ± s.d.) and showed a unimodal distribution (**Fig. 3D**). We identified 28 axons where a bouton directly contacted a spine head, resulting in a total of 39 putative synapses along these 22 µm of reconstructed dendrite (**Fig. 3C, Suppl. Fig 12B)**. Most axons made single (20) or double (6) connections, however triple and quadruple spine contacting axons were also observed. We did not observe a preferred angular orientation of contacting axons with respect to the dendritic shaft, further demonstrating the complex arrangement of the DG neuropil. The mean density of spines was 1.7/µm dendrite length. Both length and density quantifications are in-keeping with previous data[35]. **Fig. 3E** details spine length and position along the dendrite for each spine, together with exemplary volumetric renderings of pre- and postsynaptic structures.

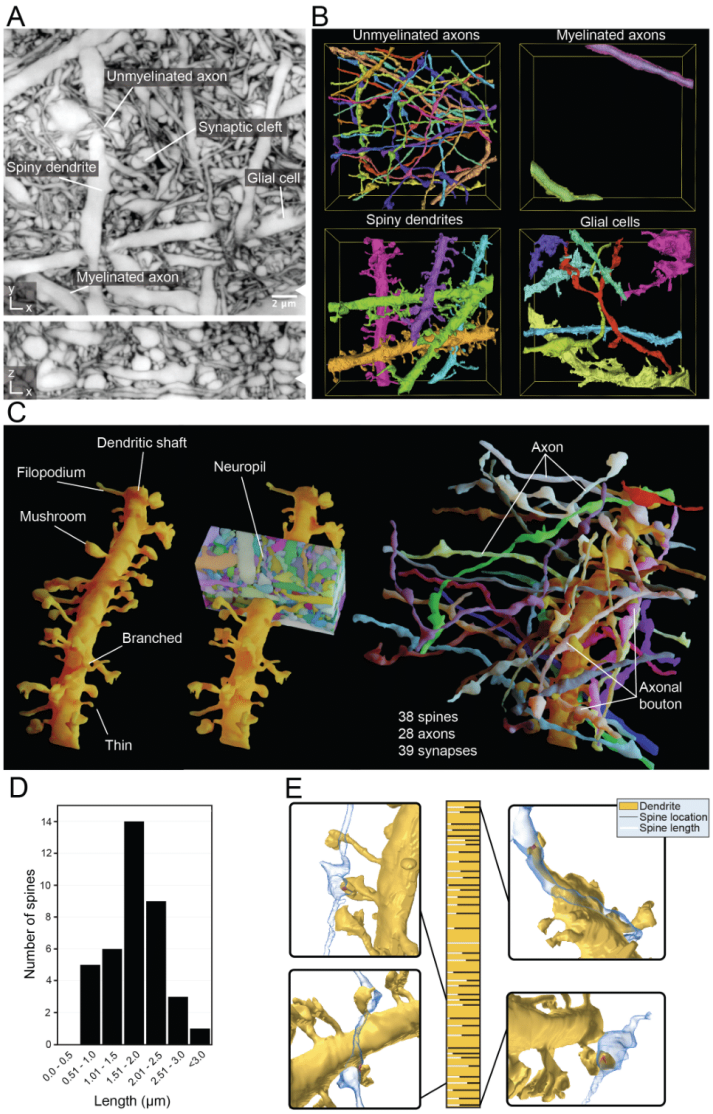


**Fig. 3. Connectivity reconstruction in live hippocampus.** (**A**) Orthogonal planes from a LIONESS volume in *xy*- and *xz*-directions in neuropil of the dentate gyrus in organotypic hippocampal slice cultures. White arrowheads at image edges indicate position of corresponding orthogonal planes. Scale bar: 2 µm. LIONESS images are maximum intensity projections spanning 150 nm. (**B**) 3D-reconstructions of exemplary cellular structures extracted from (A). (**C**) 3D-reconstruction of a spiny dendrite from (A), showing various spine shapes (left), its embedding in dense neuropil (middle) and the 28 axons making a total of 39 synaptic connections at 38

spines (right). (**D**) Distribution of spine lengths for the dendrite in (C). (**E**) Spine location (bars) and relative spine lengths (white portion of bars) along the dendrite (gold) with 3D-renderings of exemplary synaptic connections.

***Molecularly informed reconstruction***

We next sought to integrate key methods for live molecular labelling into tissue reconstruction. Live affinity labels proved useful for corroborating identity of specific structures, like myelinated axons (**Suppl. Fig. 13**). Most importantly, light microscopy is unrivalled at visualizing the location of specific proteins. As mere proximity of spines and boutons can be a poor predictor of synaptic connectivity between neurons[1], we complemented it with a molecular definition of synaptic sites. We used a mouse line expressing a HaloTag fused to endogenous PSD95 protein[36,37], an abundant protein located in the postsynaptic densities of excitatory synapses. Irreversible binding of applied HaloTag ligands coupled to a fluorescent dye visualized all excitatory postsynapses. In addition, we applied a combination of adeno-associated virus (AAV) and pseudotyped rabies particles[38] to induce expression of EGFP-coupled synaptophysin, visualizing pre-synaptic terminals (**Fig. 4A, Suppl. Fig. 14, Suppl. Video 4**). These pre- and postsynaptic markers were combined with 3D-structural LIONESS imaging in the CA1 neuropil, providing cellular context lacking with conventional molecular labelling and imaging. Combined structural and molecular information unambiguously revealed various types of connections between pre- and postsynaptic partners: boutons of two separate axons converging on a single spine, single boutons contacting two neighboring spines of the same dendrite, and textbook-like single bouton to single spine connections (**Fig. 4B**). Excitatory synapses are preferentially located at dendritic spines, however also occur on dendritic shafts, in particular on aspiny interneurons. We also used the combined molecular and structural information to determine the fraction of excitatory synapses with dendritic shaft location in our imaging volumes, equaling 8.3% in **Fig. 4** and 14.7% in **Suppl. Fig. 14**. Of note, comparison with diffraction-limited readout of synaptic molecules further illustrated the gain in 3D-definition with LIONESS (**Fig. 4A**, **bottom**, **Suppl. Fig. 14B, bottom**).

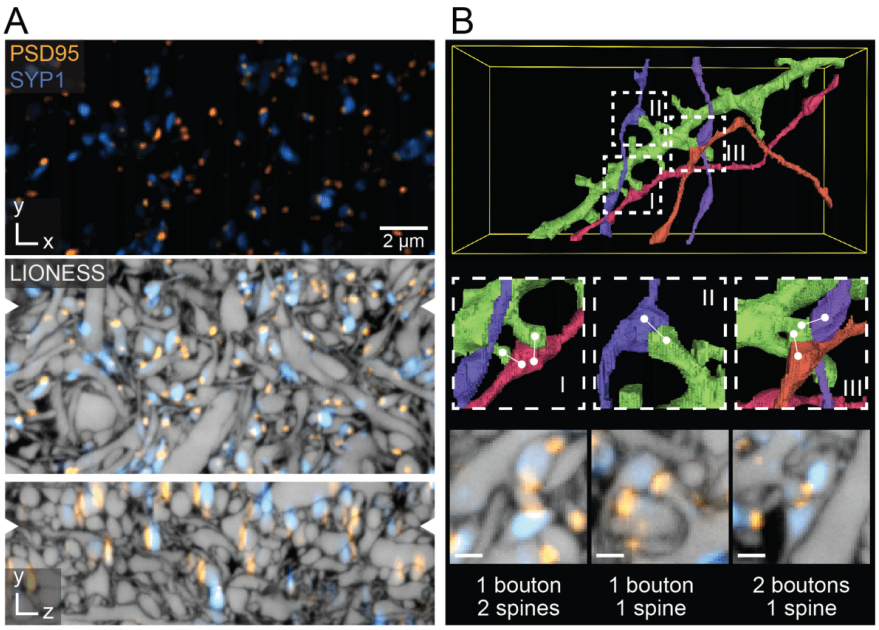


**Fig. 4. Molecularly informed reconstruction of living brain tissue.** (**A**) *Top*: Confocal image of CA1 neuropil in organotypic hippocampal slice culture, with virus-assisted delivery of synaptophysin 1-EGFP (SYP1, blue) highlighting a subset of presynaptic terminals, and PSD95-HaloTag knock-in labelling all excitatory postsynapses. Denoising applied. Scale bar: 2 µm. *Middle* and *bottom*: Overlay with near-isotropically super-resolved volumetric LIONESS data. Orthogonal planes in *xy*- and *xz*-directions represented as maximum intensity projections spanning 150 nm, with positions of corresponding planes indicated by arrowheads at image edges. Diffraction-limited SYP1 and PSD95 signals extend beyond the cellular structures defined by LIONESS. (**B**) *Top*: 3D-reconstruction of a selected dendrite (green) from the same LIONESS volume with 4 synaptically connected axons. *Middle*: Magnified views as indicated by the dashed boxes in the top panel, highlighting diverse geometric arrangements of boutons and spines. White lines indicate synaptic connections retrieved from the molecular information. *Bottom*: LIONESS planes from the corresponding subvolumes together with molecular information. Maximum intensity projections spanning 150 nm. Scale bars: 500 nm.

### *Morphodynamics and activity*

Our low-exposure approach allowed repeated reconstruction of the same tissue volume, revealing how subcellular morphologies and the neuronal network evolved over time, while pairing this directly with optical readout of activity. We first used LIONESS to repeatedly image the same

volume of hippocampal neuropil over 3 days. This allowed us to observe morphology changes and movement of neuronal and non-neuronal subcellular structures in their context (**Suppl. Fig. 15**), rather than being limited to sparse, positively labelled cells[16].

We now devised an all-optical approach to correlate 3D-structure and signaling activity in the same living cellular network. We focused on the hippocampal circuitry, where mossy fibers originating from dentate gyrus (DG) granule cells deliver excitatory input to the proximal dendrites of pyramidal neurons in the CA3 region, forming boutons on complex spines often termed thorny excrescences[39] (**Suppl. Fig. 16A,B**). Using organotypic slices from mice where all DG granule cells expressed the calcium indicator[40] GCaMP6f (Ai95/Prox1-cre) we recorded calcium transients in individual mossy fiber boutons with sub-second resolution, applying pharmacological manipulation with the $GABA_A$ receptor antagonist gabazine to enhance network activity. LIONESS revealed the underlying 3D-cellular organization (**Suppl. Fig. 16C,D, Suppl. Video 5, 6**). When we repeated volumetric LIONESS imaging, both mossy fiber boutons and their postsynaptic complex spines showed structural dynamics on the minutes timescale. Signaling activity continued during LIONESS acquisition (**Suppl**. **Fig. 16B,E**).

We next developed a more refined approach for investigating activity and dynamics within the tissue, combining chemogenetically targeted cell activation with $Ca^{2+}$-imaging and dynamic reconstruction in the same living specimen. We expressed the virally encoded DREADD (designer receptor exclusively activated by designer drugs)[41] hM3Dq in a subset of DG granule cells, which enhanced neuronal excitation upon application of the bio-orthogonal drug clozapine N-oxide (CNO). This allowed us to control and image the activity of a large mossy fiber bouton in the DG hilus, before structurally reconstructing it together with the complex spines on the postsynaptic hilar mossy cell (**Fig. 5A, Suppl. Video 7**). Comprehensive automated segmentation additionally clarified the relationship with neighboring mossy fiber boutons **(Suppl. Video 8)**. We visualized the structural evolution after 19.5h (**Fig. 5B**), which revealed dramatic rearrangements in synaptic architecture, mirrored in a bouton volume change from 11.8 $\mu m^3$ to 8.3 $\mu m^3$. These values are comparable to volumes of large mossy fiber boutons on CA3 pyramidal cells determined by serial sectioning EM in rat hippocampus[39]. However, with its applicability to living tissue, LIONESS has the unique capacity to repeatedly retrieve both activity and dynamic structural information directly in the living state. It has thus the capability to follow structural plasticity and determine structure-function relationships in neuronal tissue.

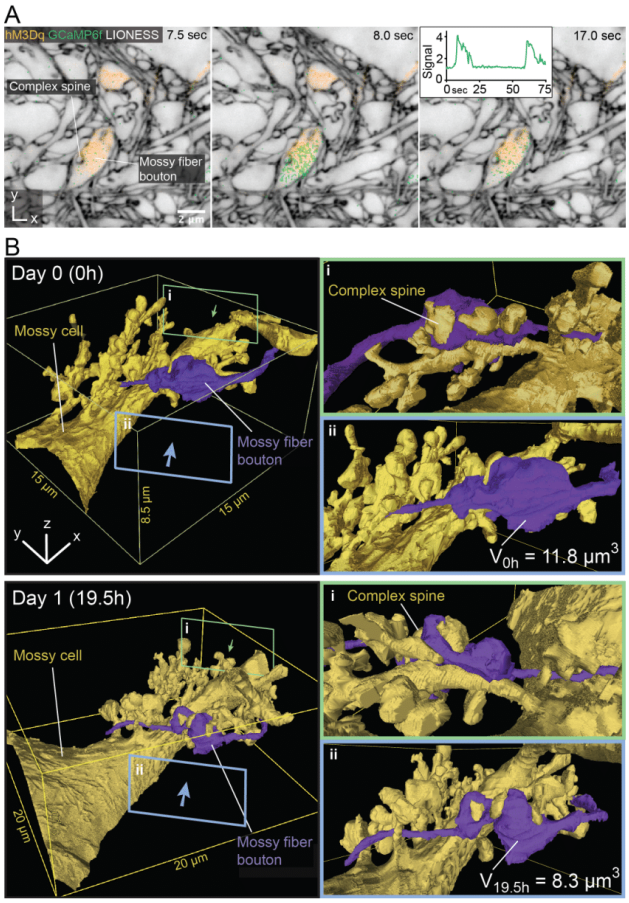


**Fig. 5. 3D-morphodynamics and chemogenetically induced $Ca^{2+}$-activity in hippocampal mossy fiber-hilar mossy cell synapses.** (**A**) Single plane of a LIONESS volume in the hilus of the dentate gyrus in an organotypic hippocampal slice culture where a subset of mossy fiber boutons expressed both the excitatory DREADD hM3Dq (together with cytosolic dTomato, orange) and the calcium indicator GCaMP6f (green). LIONESS and dTomato images are identical replicates placing the overlaid time-varying $Ca^{2+}$-signals after stimulation with the DREADD ligand CNO into structural context, with 3 exemplary points from a time series. Insert: GCaMP signal (averaged pixel value normalized to first frame) as a function of time. LIONESS image is a maximum intensity projection spanning 150 nm. Scale bar: 2 µm. (**B**) 3D-reconstructions of a hM3Dq-expressing mossy fiber bouton (purple) and its postsynaptic partner, a hilar mossy cell (gold) with complex spines at two timepoints (top: day 0 (0h), bottom: day 1 (19.5h)). $V_{0h}$ and $V_{19.5h}$ are bouton volumes at the respective time points. Green (i) and blue (ii) frames indicate the viewing angles from opposite directions for the magnified views on the right. The structures designated by the lettering in both panels refer to the same bouton and complex spine.

***Electrophysiology***

We reasoned that with LIONESS, light microscopy may not only be used for visual guidance of electrophysiology experiments, but to correlate electrical properties of single and synaptically connected pairs of neurons with the underlying neuronal architecture in the living state. We performed whole-cell patch-clamp recordings of two neighboring pyramidal neurons in the hippocampal CA1 region, taking advantage of the fact that these cells often form monosynaptic connections in organotypic culture[42]. Cells with confirmed synaptic connectivity were imaged post-recording (**Suppl**. **Fig. 17)**, first in diffraction-limited mode with fluorophores intracellularly applied during recording, and then with LIONESS. Zooming in on a region of putative contact, diffraction-limited readout indicated that this was the site of electrophysiologically confirmed communication. Only comprehensive 3D-super-resolved delineation in the LIONESS volume revealed the deception by disclosing an intervening, unlabeled neuronal process missed in diffraction-limited mode. This corroborated that LIONESS was suitable for a multimodal approach to simultaneously retrieve and correlate structural with functional aspects of tissue architecture in living specimens, and more powerful in doing so than diffraction-limited imaging.

***Bridging scales***

Analysis of tissue architecture was not limited to single LIONESS volumes. For extending analysis volumes and embedding them into meso-scale context, we followed two straight-forward approaches. Firstly, recording multiple partially overlapping subvolumes in the living tissue allowed automatically 3D-registering them with sufficient accuracy, such that segments from automated reconstruction smoothly extended over the borders. For example, we reconstructed a 70 µm-long stretch of mostly parallel axon fibers in acutely prepared mouse alveus from four image volumes – thus capturing ~3 mm of cumulative axon length in this continuous region (**Suppl. Fig. 18**). Secondly, we guided selection of LIONESS volumes by recording larger volumes with diffraction-limited resolution, which provided further context to reconstructed regions. As one example, imaging a 650,000 $\mu m^3$ volume in the DG crest of the hippocampus gave positional context and allowed identification of larger objects like cell somata and major dendritic branches, whereas LIONESS reconstruction revealed how DG granule cell and other cellular processes were embedded in the invaginations of a glial cell (**Suppl. Fig. 19, Suppl. Video 9, 10**).

Imaging across spatial scales thus yields information on cell position and identity to extend the interpretation of connectivity analysis made possible by LIONESS.

## Discussion

Here we demonstrate saturated reconstruction of living mammalian brain tissue. This allowed tracking the time evolution of its structure, direct pairing with information on molecule location, and with simultaneous manipulation and readout of activity. Together, these elements constitute a fundamentally new quality of information for the study of brain structure and function, overcoming limitations of both static EM representations and reconstruction of positively labelled, incomplete subsets of tissue constituents in light microscopy.

To achieve this, we developed a technology for imaging and segmenting living brain tissue, integrating optimization of optical nanoscopy for tissue imaging with a two-step deep-learning strategy. It may come as a surprise that a moderate ~130 nm isotropic 3D-resolution, chosen to limit burden on the living specimen, was sufficient for brain tissue reconstruction. This contrasts with ~4x better resolution in the worst-resolved direction in typical EM reconstructions[1,2], relying on physical sectioning at ~30 nm steps. Four factors aided segmentation: 1) Extracellular labelling[14,17] selectively highlighted the space separating cellular structures. The presence of a separating fluorophore layer was detectable also at resolution worse than the thickness of this layer. ECS labelling eclipsed complexity from intracellular organelles in the cell segmentation channel, whereas specific labelling revealed intracellular structures and molecules in spectrally distinct detection channels. 2) Also cellular structures smaller than the effective point-spread-function of the microscope led to modulation of fluorescence counts by volume exclusion of extracellular label, aiding in their detection. 3) Live imaging lacks alterations of tissue structure from chemical fixation, including shrinkage[43] of the space filled with label in between cells. 4) Optical sectioning yields inherently aligned volumetric stacks, avoiding potential technical challenges with alignment after physical sectioning.

Our parameter search for image acquisition, processing, and segmentation was in no way exhaustive, opening possibilities for future improvements. For example, beyond brute-force further extension of the training bases for both deep-learning networks, the first network may be trained on paired low/high-exposure volumes where the high-exposure ground truth also features increased resolution. LIONESS will likely benefit from specifically engineered fluorophores for high performance extracellular labelling, which we have only started to explore by attaching hydrophilicity-enhancing sulfonate groups.

The capacity of LIONESS to bridge to the wider tissue context will benefit biological studies. Our chosen LIONESS volumes of up to ~4,500 $\mu m^3$ reflect best optical performance within a few tens of µm depth and in the central region of the objective's field of view. We increased these laterally via volumetric tiling whereas adaptive optics[44] may be used to enhance axial range. Rather than maximizing imaging volumes, one may also bridge scales with complementary methods, such as viral tracing. While we used rabies virus for live labelling of synapses, this approach may be extended to retrogradely trace[38,45] the cellular origins of synaptic input identified in LIONESS. Application of LIONESS in living animals harbors engineering challenges due to movement[46] that may be addressed by developing motion-compensating algorithms. We envision that correlating live information from LIONESS with light microscopy measurements of the same specimen after fixation will be useful, as this opens up further possibilities for molecular characterization and large-scale super-resolution tissue imaging[47]. Such all-optical correlative measurements will be considerably less complex than correlative approaches with EM. As expected, optimum sample and imaging conditions were required for full reconstruction. However, STED imaging was performed on a commercial microscope with minor adaptations, which underscores adoptability of this technology. The simplified workflow and lower demands in equipment or personnel of LIONESS compared to serial-sectioning or block-face imaging EM should enable analysis of multiple specimens as a function of genotype, developmental stage, disease, or specific intervention.

More fundamentally though, LIONESS is unique in that it allows repeated reconstruction of brain tissue over time, capturing single-synapse to network-level structural plasticity together with location of specific molecules and neuronal activity directly in the living state. For determining structure-function relationships, this sets it apart also from functional EM studies of brain tissue, including in correlative $Ca^{2+}$ imaging[3,4] and "flash and freeze" EM[48]. Taking advantage of extracellular rather than sparse cellular labelling, LIONESS resolves structures with their interacting partners. This provides resolution of both neuronal input and output, as well as tissue microenvironment, and facilitates observation of how activity and plasticity of one component translates to surrounding structures. Likewise, it offers new opportunities for studying synaptic heterogeneity, which underlies much of the complexity of the brain. Our results demonstrate that LIONESS is a powerful tool that can provide new biological insights into the function of neuronal circuits. As LIONESS can be applied to live tissue, it is possible to monitor synaptic connectivity over time, permitting real-time analysis of the dynamics of the connectome. Furthermore, since

LIONESS can be applied in conjunction with molecular labels (such as PSD95), structural and functional connectivity can be analyzed in parallel. Thus, LIONESS may contribute to the identification of structural and functional components of synaptic engrams in neuronal circuits. Finally, because LIONESS is fully compatible with $Ca^{2+}$-imaging, it allows to correlate synaptic plasticity with the pre- and postsynaptic activity history of the synapse, allowing future users to define the precise induction rules of synaptic plasticity and engram formation.

LIONESS has the capability to analyze the structure of living brain tissue in a comprehensive, and thus unbiased way. This provides rich opportunities for unexpected discoveries that may ultimately challenge the way we think about the extent and significance of plasticity in the central nervous system. We extracted exemplary quantitative data on neuronal connectivity and structure to showcase that LIONESS provides quantitative, dynamical biological information. We thus expect it to facilitate addressing biological questions related to stability and rewiring of network structure[49], the dynamics of neuron-glia interactions and ECS[19,20], and structure-function relationships[48]. LIONESS opens up new avenues for decoding complex, dynamic tissue architecture in living mammalian brain and other organs.

# References

1. Kasthuri, N. *et al.* Saturated Reconstruction of a Volume of Neocortex. *Cell* **162**, 648–661 (2015).
2. Motta, A. *et al.* Dense connectomic reconstruction in layer 4 of the somatosensory cortex. *Science* **366**, eaay3134 (2019).
3. Turner, N. L. *et al.* Reconstruction of neocortex: Organelles, compartments, cells, circuits, and activity. *Cell* **185**, 1082–1100 (2022).
4. Briggman, K. L., Helmstaedter, M. & Denk, W. Wiring specificity in the direction-selectivity circuit of the retina. *Nature* **471**, 183–188 (2011).
5. Shapson-Coe, A. *et al.* A connectomic study of a petascale fragment of human cerebral cortex. *bioRxiv* 2021.05.29.446289 (2021) doi:10.1101/2021.05.29.446289.
6. Klar, T. A., Jakobs, S., Dyba, M., Egner, A. & Hell, S. W. Fluorescence microscopy with diffraction resolution barrier broken by stimulated emission. *Proceedings of the National Academy of Sciences* **97**, 8206–8210 (2000).
7. Rust, M. J., Bates, M. & Zhuang, X. Sub-diffraction-limit imaging by stochastic optical reconstruction microscopy (STORM). *Nature Methods* **3**, 793–796 (2006).

8. Betzig, E. *et al.* Imaging Intracellular Fluorescent Proteins at Nanometer Resolution. *Science* **313**, 1642–1645 (2006).
9. Hess, S. T., Girirajan, T. P. K. & Mason, M. D. Ultra-high resolution imaging by fluorescence photoactivation localization microscopy. *Biophysical Journal* **91**, 4258–4272 (2006).
10. Giannone, G. *et al.* Dynamic Superresolution Imaging of Endogenous Proteins on Living Cells at Ultra-High Density. *Biophysical Journal* **99**, 1303–1310 (2010).
11. Heilemann, M. *et al.* Subdiffraction-resolution fluorescence imaging with conventional fluorescent probes. *Angewandte Chemie - International Edition* **47**, 6172–6176 (2008).
12. Chen, F., Tillberg, P. W. & Boyden, E. S. Expansion microscopy. *Science* **347**, 543–548 (2015).
13. Hell, S. W. & Wichmann, J. Breaking the diffraction resolution limit by stimulated emission: stimulated-emission-depletion fluorescence microscopy. *Optics Letters* **19**, 780–782 (1994).
14. Tønnesen, J., Inavalli, V. V. G. K. & Nägerl, U. V. Super-Resolution Imaging of the Extracellular Space in Living Brain Tissue. *Cell* **172**, 1108-1121.e15 (2018).
15. Azevedo, F. A. C. *et al.* Equal numbers of neuronal and nonneuronal cells make the human brain an isometrically scaled-up primate brain. *J. Comp. Neurol.* **513**, 532–541 (2009).
16. Nägerl, U. V., Willig, K. I., Hein, B., Hell, S. W. & Bonhoeffer, T. Live-cell imaging of dendritic spines by STED microscopy. *Proceedings of the National Academy of Sciences* **105**, 18982–18987 (2008).
17. Kitamura, K., Judkewitz, B., Kano, M., Denk, W. & Häusser, M. Targeted patch-clamp recordings and single-cell electroporation of unlabeled neurons in vivo. *Nature Methods* **5**, 61–67 (2008).
18. Godin, A. G. *et al.* Single-nanotube tracking reveals the nanoscale organization of the extracellular space in the live brain. *Nature Nanotech* **12**, 238–243 (2017).
19. Arizono, M. *et al.* Structural basis of astrocytic Ca 2+ signals at tripartite synapses. *Nature Communications* **11**, 1–15 (2020).
20. Arizono, M., Inavalli, V. V. G. K., Bancelin, S., Fernández-Monreal, M. & Nägerl, U. V. Super-resolution shadow imaging reveals local remodeling of astrocytic microstructures and brain extracellular space after osmotic challenge. *Glia* **69**, 1605–1613 (2021).
21. Inavalli, V. V. G. K. *et al.* A super-resolution platform for correlative live single-molecule imaging and STED microscopy. *Nat Methods* **16**, 1263–1268 (2019).
22. Harke, B. *et al.* Resolution scaling in STED microscopy. *Optics Express* **16**, 4154–4162 (2008).

23. Kilian, N. *et al.* Assessing photodamage in live-cell STED microscopy. *Nat Methods* **15**, 755–756 (2018).
24. Jahr, W., Velicky, P. & Danzl, J. G. Strategies to maximize performance in STimulated Emission Depletion (STED) nanoscopy of biological specimens. *Methods* **174**, 27–41 (2020).
25. Göttfert, F. *et al.* Coaligned Dual-Channel STED Nanoscopy and Molecular Diffusion Analysis at 20 nm Resolution. *Biophysical Journal* **105**, L01–L03 (2013).
26. Saleh, B. E. A. & Teich, M. C. *Fundamentals of Photonics*. (John Wiley & Sons, 2007). doi:10.1002/0471213748.
27. Weigert, M. *et al.* Content-aware image restoration: pushing the limits of fluorescence microscopy. *Nat Methods* **15**, 1090–1097 (2018).
28. Staudt, T. *et al.* Far-field optical nanoscopy with reduced number of state transition cycles. *Optics Express* **19**, 5644–5657 (2011).
29. Heine, J. *et al.* Adaptive-illumination STED nanoscopy. *Proceedings of the National Academy of Sciences* **114**, 9797–9802 (2017).
30. Danzl, J. G. *et al.* Coordinate-targeted fluorescence nanoscopy with multiple off states. *Nature Photonics* **10**, 122–128 (2016).
31. Donnert, G. *et al.* Macromolecular-scale resolution in biological fluorescence microscopy. *Proceedings of the National Academy of Sciences* **103**, 11440–11445 (2006).
32. Lin, Z., Wei, D., Lichtman, J. & Pfister, H. PyTorch Connectomics: A Scalable and Flexible Segmentation Framework for EM Connectomics. *arXiv preprint arXiv:2112.05754* (2021).
33. Lee, K., Zung, J., Li, P., Jain, V. & Seung, H. S. Superhuman Accuracy on the SNEMI3D Connectomics Challenge. *arXiv preprint arXiv:1706.00120* (2017).
34. Lancaster, M. A. *et al.* Cerebral organoids model human brain development and microcephaly. *Nature* **501**, 373–379 (2013).
35. Barón-Mendoza, I. *et al.* Changes in the Number and Morphology of Dendritic Spines in the Hippocampus and Prefrontal Cortex of the C58/J Mouse Model of Autism. *Front. Cell. Neurosci.* **15**, 726501 (2021).
36. Bulovaite, E. *et al.* A brain atlas of synapse protein lifetime across the mouse lifespan. *bioRxiv* 2021.12.16.472938 (2021) doi:10.1101/2021.12.16.472938.
37. Masch, J.-M. *et al.* Robust nanoscopy of a synaptic protein in living mice by organic-fluorophore labeling. *Proceedings of the National Academy of Sciences* **115**, E8047–E8056 (2018).

38. Sumser, A., Joesch, M., Jonas, P. & Ben-Simon, Y. An extended toolkit for production and use of RVdG-CVS-N2c rabies viral vectors uncovers hidden hippocampal connections. *bioRxiv* 2021.12.23.474014 (2021) doi:10.1101/2021.12.23.474014.

39. Rollenhagen, A. *et al.* Structural Determinants of Transmission at Large Hippocampal Mossy Fiber Synapses. *Journal of Neuroscience* **27**, 10434–10444 (2007).

40. Chen, T.-W. *et al.* Ultrasensitive fluorescent proteins for imaging neuronal activity. *Nature* **499**, 295–300 (2013).

41. Alexander, G. M. *et al.* Remote Control of Neuronal Activity in Transgenic Mice Expressing Evolved G Protein-Coupled Receptors. *Neuron* **63**, 27–39 (2009).

42. Debanne, D., Guerineau, N. C., Gahwiler, B. H. & Thompson, S. M. Physiology and pharmacology of unitary synaptic connections between pairs of cells in areas CA3 and CA1 of rat hippocampal slice cultures. *Journal of Neurophysiology* **73**, 1282–1294 (1995).

43. Korogod, N., Petersen, C. C. & Knott, G. W. Ultrastructural analysis of adult mouse neocortex comparing aldehyde perfusion with cryo fixation. *eLife* **4**, e05793 (2015).

44. Velasco, M. G. M. *et al.* 3D super-resolution deep-tissue imaging in living mice. *Optica* **8**, 442–450 (2021).

45. Wickersham, I. R., Finke, S., Conzelmann, K.-K. & Callaway, E. M. Retrograde neuronal tracing with a deletion-mutant rabies virus. *Nat Methods* **4**, 47–49 (2007).

46. Berning, S., Willig, K. I., Steffens, H., Dibaj, P. & Hell, S. W. Nanoscopy in a Living Mouse Brain. *Science* **335**, 551–551 (2012).

47. Gao, R. *et al.* Cortical column and whole-brain imaging with molecular contrast and nanoscale resolution. *Science* **363**, eaau8302 (2019).

48. Borges-Merjane, C., Kim, O. & Jonas, P. Functional Electron Microscopy ("Flash and Freeze") of Identified Cortical Synapses in Acute Brain Slices. *Neuron* **105**, 992–1006 (2020).

49. Attardo, A., Fitzgerald, J. E. & Schnitzer, M. J. Impermanence of dendritic spines in live adult CA1 hippocampus. *Nature* **523**, 592–596 (2015).

**Supplementary References for Methods Section:**

50. Feng, G. P. *et al.* Imaging neuronal subsets in transgenic mice expressing multiple spectral variants of GFP. *Neuron* **28**, 41–51 (2000).

51. Schindelin, J. *et al.* Fiji: an open-source platform for biological-image analysis. *Nat Methods* **9**, 676–682 (2012).
52. Encell, L. P. *et al.* Development of a dehalogenase-based protein fusion tag capable of rapid, selective and covalent attachment to customizable ligands. *Curr Chem Genomics* **6**, 55–71 (2012).
53. Ben-Simon, Y. *et al.* Entorhinal layer 6b subplate neurons govern spatial learning and memory. *bioRxiv* 2022.01.26.477814 (2022) doi:10.1101/2022.01.26.477814.
54. Armbruster, B. N., Li, X., Pausch, M. H., Herlitze, S. & Roth, B. L. Evolving the lock to fit the key to create a family of G protein-coupled receptors potently activated by an inert ligand. *Proceedings of the National Academy of Sciences* **104**, 5163–5168 (2007).
55. Guzman, S. J., Schlögl, A. & Schmidt-Hieber, C. Stimfit: quantifying electrophysiological data with Python. *Front Neuroinform* **8**, 16 (2014).
56. Krull, A., Buchholz, T.-O. & Jug, F. Noise2Void - Learning Denoising from Single Noisy Images. *arXiv:1811.10980 [cs]* (2019).
57. Berger, D. R., Seung, H. S. & Lichtman, J. W. VAST (Volume Annotation and Segmentation Tool): Efficient Manual and Semi-Automatic Labeling of Large 3D Image Stacks. *Front. Neural Circuits* **12**, 88 (2018).
58. Zlateski, A. & Seung, H. S. Image Segmentation by Size-Dependent Single Linkage Clustering of a Watershed Basin Graph. *CoRR* **abs/1505.00249**, (2015).
59. Jorstad, A., Blanc, J. & Knott, G. NeuroMorph: A Software Toolset for 3D Analysis of Neurite Morphology and Connectivity. *Frontiers in Neuroanatomy* **12**, 59 (2018).
60. Troidl, J. *et al.* Barrio: Customizable Spatial Neighborhood Analysis and Comparison for Nanoscale Brain Structures. *Computer Graphics Forum (Proceedings Eurographics/IEEE Symposium on Visualization, Eurovis 2022* **41**, to appear (2022).

# Author contributions

P.V. designed and performed experiments, analysed, proofread, visualized and interpreted data, and prepared figures. E.M. set up and performed automated segmentation, data analysis, and visualization. J.M.M. supported experiments. D.W. and Z.L. supported automated segmentation. J.F.W. performed patch-clamp experiments and segmentation for validation. J.T. performed visualization, advised by J.Be.. Y.B.-S. provided viral constructs. C.S. supported image analysis. W.J. supported setting up imaging and troubleshooting. A.C. performed manual segmentations. J.Br. synthesized SulfoAtto 643. S.G.N.G. provided PSD95-HaloTag mouse. P.J. supervised patch clamp experiments and

virus generation. G.N. advised on and provided human cerebral organoids. H.P. advised on automated segmentation. B.B. supervised computer vision. J.G.D. conceived and supervised the study, designed experiments, and interpreted data. J.G.D. wrote the paper together with P.V. with critical input from all authors.

# Acknowledgements

We thank J. Vorlaufer, N. Agudelo, A. Wartak for microscope maintenance and troubleshooting, C. Kreuzinger and A. Freeman for technical assistance, and J. Lyudchik and M. Šuplata for computational support and hardware control and Márcia Cunha dos Santos for initial exploration of software. We thank Paul Henderson for advice on deep-learning training and Michael Sixt, Scott Boyd, and Tamara Weiss for discussions and critical reading of the manuscript. Luke Lavis (Janelia Research Campus) generously provided JF585-HaloTag ligand. We acknowledge expert support by IST Austria's scientific computing, bioimaging, preclinical, and life science facilities, and by the Miba machine shop. This work was supported with funding by the Austrian Science Fund (FWF) (I3600-B27 and DK W1232) to J.G.D. and (Z 312-B27, Wittgenstein award) to P.J., by the Gesellschaft für Forschungsförderung NÖ (NFB) to J.G.D. (LSC18-022), an institutional (ISTA) Interdisciplinary Project grant to J.G.D. and B.B., the European Research Council (ERC) under the European Union's Horizon 2020 research and innovation programme to B.B. (715767 – MATERIALIZABLE), to G.N. (715508 – REVERSEAUTISM), to S.G. (695568 – SYNNOVATE), and to P.J. (692692 – GIANTSYN), the Simons Foundation Autism Research Initiative to S.G. (529085), and the Wellcome Trust to S.G. (Technology Development Grant 202932). It was further supported by a MSCA Individual Fellowship under the EU Horizon 2020 program to J.F.W. (101026635) and a postdoctoral fellowship from the Human Frontier Science Program (HFSP) to W.J. (LT000557/2018). This work was also partially supported by NSF grants IIS-1835231 and NCS-FO-2124179 to H.P..

# Methods

## Animals

Animals were housed in groups of 3–4 animals per cage and kept on a 12 h light/dark cycle (lights on at 7:00 am), with food and water available ad libitum. If not stated otherwise, we used wild-type C57BL/6J mice. All transgenic lines (see Table 1) used in this study have been previously characterized. For experimental use, we crossed Ai95 (GCaMP6f)[40] and Prox1-cre. For experiments with PSD95-HaloTag mice[36,37], both homozygous and heterozygous animals were used. For all experiments, male and female mice were used interchangeably. Experiments and procedures were performed in strict accordance with institutional, national, and European guidelines for animal experimentation.

| Transgenic line | Full name | Source (deposited by) | Cat# |
|---|---|---|---|
| Ai95 | B6;129S-Gt(ROSA)26Sortm95.1(CAG-GCaMP6f)Hze/J | Jackson labs (H. Zeng) | 024105 |
| Prox1-cre | Tg(Prox1-cre)SJ32Gsat/Mmucd | MMRRC (N. Heintz) | 036644-UCD |
| PSD95-HaloTag | PSD95-HaloTag | Seth G. N. Grant, Edinburgh | - |
| Thy1-EGFP[50] | STOCK Tg(Thy1-EGFP)MJrs/J | Jackson labs (J. Sanes) | 007788 |

*Table 1*

## Organotypic hippocampal slice cultures

Hippocampal slices were obtained from 5-7 days old mice of either sex and cultured on cell culture inserts with porous membranes. Mouse pups were decapitated and the hippocampus was isolated while the brain was submerged in ice cold sterile filtered HBSS without $Ca^{2+}$ and $Mg^{2+}$ (Gibco, #14175-053) supplemented with 10 mM glucose, using a stereo microscope. Hippocampi were cut into 350 µm thick slices and placed on round porous membranes with 4 mm diameter (PTFE membrane, Merck, #FHLC01300), which have been placed on cell culture inserts with a porous membrane (Millicell, #PICM0RG50) for interface culture. The inserts with the slices were placed in dishes (Greiner, #627161) with 1 ml of culture media. We adapted the media recipe during the course of experiments, as quality of cultures deteriorated with the same nominal composition. We found 78.5% Minimum Essential Medium (MEM, Gibco, #11095-080), 15% heat-inactivated horse serum (Gibco, #26050070), 2% B27 supplement (Gibco, #0080085SA), 2.5% 1 M HEPES (Sigma, #M3375-100G), 1.5% 0.2 M GlutaMax supplement (Gibco, #35050-061), 0.5% 0.05 M ascorbic acid (Sigma, #A5960-25G), with additional 1 mM $CaCl_2$ and 1 mM $MgSO_4$ to produce

satisfactory results, and incubated at 37 °C and 5% $CO_2$. The medium was changed the day after preparation and then every 3-4 days.

## ECS labelling

For ECS labelling, artificial cerebrospinal fluid (ACSF) was prepared from a 10x stock solution with $MgCl_2$ and $CaCl_2$ added freshly before carbogen bubbling, whereas ascorbic acid and Trolox were added after bubbling. Finally, ACSF consisted of 125 mM NaCl, 2 mM $CaCl_2$, 1.3 mM $MgCl_2$, 4.8 mM KCl, 26 mM $NaHCO_3$, 1.25 mM $NaH_2PO_4$, 7.5 mM HEPES (Gibco, #15630056), 20 mM D-glucose (Sigma, #G8270-1kg), 1 mM Trolox (Sigma, #238813), 1 mM ascorbic acid (Sigma, #A5960-25G); pH 7.4. Thereafter, fluorescent dye (Atto 643 (Atto-Tec GmbH, #AD 643-25), SulfoAtto 643, or Abberior STAR 635P (Abberior, #ST635P)) was added from 5 mM stocks (dissolved in ACSF) to a final concentration of 150 µM. A 2 µl droplet of the dye-containing imaging solution was put on a #1.5H coverslip (Bartelt, #6.259 995) that had been placed in an imaging chamber (RC-41, Warner Instruments). Using fine forceps, brain slices with the membrane attached were then carefully put onto the droplet, such that the slice was oriented towards the coverslip. A slice anchor gently kept the sample in place. Immediately afterwards, further imaging solution at room temperature (RT) was added. The imaging chamber was then placed onto the stage adapter of the STED microscope (see below). The data in the manuscript were acquired using Atto 643, except for **Fig. 5** and **Suppl. Fig. 11** (left panel) where SulfoAtto 643 was used.

## Acute preparation of whole hippocampus and labelling

Hippocampi were extracted from 5-7 days old mice of either sex. Mouse pups were decapitated and the hippocampus isolated while the brain was submerged in ice cold sterile filtered HBSS without $Ca^{2+}$ and $Mg^{2+}$ (Gibco, #14175-053) supplemented with 10 mM glucose, using a stereo microscope. The whole hippocampus was then submerged in freshly carbogenized ACSF with 150 µM Atto 643 dye and incubated for 10 min at RT with gentle agitation. Afterwards, entire hippocampi were placed on a #1.5H coverslip that had been placed in an imaging chamber (RC-41, Warner Instruments) with the alveus region facing the coverslip. A slice anchor gently kept the sample in place when freshly carbogenized ACSF with 150 µM Atto 643 dye was added for imaging. The imaging chamber was then placed onto the stage adapter of the STED microscope.

## Generation of cerebral organoids

Human embryonic stem cells were dissociated to single cells using Accutase (Gibco). A total of 2500 cells was transferred to each well of an ultra-low-binding-96-well plate (Corning) in mTeSR1 media supplemented with 50 µM Y-27632 (Stemcell Technologies). Cells were allowed to aggregate to EBs and fed every second day. At day 3 supplements were removed and from day 6 the generation of cerebral organoids was performed according to Lancaster and Knoblich[34]. Briefly, EBs were transferred to neural induction medium (NIM) in low-adhesion 24-well plates (Corning), and fed every second day for 5 days until formation of neuroepithelial tissue (day 0 of cerebral organoid formation). Neuroepithelial tissue-displaying organoids were embedded in Matrigel droplets (Corning, #356234) and grown in cerebral organoid medium (COM) supplemented with B27 without vitamin A (Gibco) and fed every other day. After 4 days tissues were transferred to COM supplemented with B27 containing vitamin A and placed on a horizontal shaker at 70-100rpm. Cerebral organoids were fed twice a week.

## LIONESS imaging

STED microscopy was performed at room temperature on an inverted Expert Line STED microscope (Abberior Instruments) with pulsed excitation and STED lasers. A 640 nm laser was used for excitation and a 775 nm laser for stimulated emission. A silicone oil immersion objective with 1.35 NA and a correction collar (Olympus, UPLSAPS 100XS) was used for image acquisition. The fluorescence signal was collected in a confocal arrangement with a pinhole size of 0.6 or 0.8 airy units. For detection a 685/70 nm bandpass filter (Chroma, #F49-686) was used and a 50:50 beam splitter (Thorlabs, #BSW29R) distributed the signal onto two photon counting avalanche photodiodes, allowing for stronger excitation without saturating detectors. Both detection channels were added up using Fiji[51] Version: 2.3.0/1.53f (Fiji/process/calculator plus/add), photon counts inverted, and data saved in 16-bit TIFF format. The pulse repetition rate was 40 MHz and fluorescence detection was time-gated. LIONESS volumes were acquired with 10 µs pixel dwell time, 2.9 µW (640 nm) excitation laser power and 90 mW STED laser power. A spatial light modulator (SLM) imprinted incoherently overlapped phase patterns for predominantly axial resolution increase (π-top-hat phase modulation, z-STED), and for predominantly improved fluorescence quenching outside the central minimum (4π-helical phase modulation, 4π(*xy*)-STED) onto the STED beam. The SLM was also used to perform alignment directly in the sample,

ensuring that the intensity minima of the two STED patterns spatially coincided and to optionally adjust low-order Zernicke polynomials for empirical aberration correction. Power ratio of *z*-STED/xy(4π)-STED/ was 80/20. Voxel size was 50 x 50 x 50 $nm^3$ for all images. Acquisition scan mode was typically *xzy*, with the *y*-direction being the slowest scan axis, using galvanometric mirrors for lateral (*xy*)-scanning and a sample piezo stage (Physik Instrumente (PI) GmbH & Co. KG, #P-736.ZRO) for axial (*z*)-scanning. Image acquisition and microscope control were performed with Imspector software version 14.0.3052.

For samples with additional positive labels (HaloTag ligand JF585, Synaptophysin-EGFP, Thy-1-EGFP, GCaMP6f), additional color channels with diffraction-limited resolution using a 488 nm or 560 nm laser with 10 µs dwell time and 1.1- 3.9 µW (488 nm) and 2- 2.6 µW (560 nm) excitation power were used for recordings. These signals were collected using a photon counting avalanche photodiode with a 525/50 nm (Semrock, #F37-516) and 605/50 nm (Chroma, #F49-605) bandpass filters for EGFP and JF585 detection, respectively. The 488 nm and 640 nm excitations were done simultaneously, for 560 nm excitation a second line step was used to avoid spectral bleed-through into the far-red channel. Voxel size was again 50 x 50 x 50 $nm^3$ for all images with *xzy*-scan mode. The power values refer to the power at the sample, measured with a slide powermeter head (Thorlabs, S170C).

## Repeated volumetric live imaging

For evaluation of tissue photo-burden with LIONESS vs. conventional high-exposure STED (**Suppl. Fig. 4**) a 70 x 70 µm confocal overview scan was performed in a region of neuropil in the CA1 region of an organotypic hippocampal slice. Next, the central 5 x 5 x 2.5 $µm^3$ volume was exposed to STED in 20 consecutive volumetric scans in *xyz*-scan mode with 70 µs voxel dwell time for long-exposure STED and 10 µs for LIONESS datasets. Excitation and STED power were identical and corresponded to the parameters used in LIONESS imaging, with 90 mW STED power at 80/20 distribution between phase patterns. 10 min after the last volume was acquired, a second 70 x 70 µm confocal overview scan was done of the same region and plane as in the initial measurement.

For long-term repeated imaging of hippocampal neuropil (**Suppl. Fig. 15**), the sample was mounted and placed on the microscope as described in the section on LIONESS imaging. For the first 4 acquisitions within 1h, the sample was kept in place, with the imaging media (carbogenized

ACSF with 150 µM Atto 643) exchanged after 30 min. After that, the sample was placed back onto cell culture inserts and into the tissue culture incubator at 37 °C and 5% $CO_2$ until the next imaging session one day later. The same procedure was repeated for the last imaging time point after 3 days.

For long-term repeated imaging of chemogenetically activated mossy fiber boutons (**Fig. 5**), the sample was placed back after the first imaging session onto cell culture inserts and incubated at 37 °C and 5% $CO_2$. Media was changed after 45 min to wash out residual CNO, and the sample was placed into the tissue culture incubator until the second imaging session on the next day.

## PSD95-HaloTag labelling

Organotypic hippocampal brain slices of PSD95-HaloTag[36,37,52] mice were live labelled using Janelia Fluor (JF)585-HaloTag ligand (Janelia Research Campus). The fluorescent ligand was dissolved in anhydrous DMSO to a stock concentration of 500 µM, aliquoted and stored at -20°C. Before imaging, the fluorescent ligand was added to the culture medium to a final concentration of 500 nM (1:1000) and incubated for at least 45 min at 37 °C.

## Viral vector assembly and synaptophysin labelling

Preparation of AAV and $RVdG_{envA}$-CVS-N2c vectors has previously been described[38,53]. Briefly, AAV2-CaMKIIa-TVA-2A-N2cG (Addgene #172363) vectors were pseudotyped with the AAVdj capsid protein by co-transfection of HEK293T cells. Three days later, the cells were harvested and lysed, and the viral stock was purified using heparin-agarose affinity binding. $RVdG_{envA}$-CVS-N2c-nl. EGFP-SypEGFP (Addgene #172380) were rescued using HEK-GT cells and then amplified and pseudotyped using BHK-eT cells. Viral vectors were purified and concentrated from the supernatant using ultracentrifugation and resuspended in PBS.

For live labelling of synaptic vesicles, first AAV-CaMKIIa-TVA-2A-N2cG was added to organotypic hippocampal slice cultures at 7-10 days in vitro (DIV) for dual expression of the TVA avian receptor and the rabies N2c glycoprotein (N2cG). 14 days later, envA-pseudotyped, G-deleted CVS-N2c rabies viral particles were added for expression of a synaptophysin-EGFP fusion protein and additional EGFP expression in the cell nucleus (RVdG(envA)-CVS-N2c-nlGFP-

sypGFP). 4-5 days after addition of the rabies vectors, EGFP expression was strong enough for imaging.

## Myelin labelling

Live labelling of myelin was performed using FluoroMyelin™ Green (ThermoFisher Scientific, #F34651). The dye was diluted 1:300 in culture media for organotypic hippocampal slices and incubated with the sample at 37 °C for at least 30 min before imaging.

## Calcium imaging

Cultured organotypic hippocampal slices of Prox1-cre/Ai95 (GCaMP6f)[40] mice shown in **Suppl. Fig. 16** were ECS labelled for LIONESS imaging as described above. To reduce level of inhibition, 10 µM GABAA receptor antagonist gabazine were added to the imaging media at the start of the imaging session. A region of interest was first repeatedly imaged via confocal scanning (488 nm excitation, 1.1 µW) of an individual plane with 50 x 50 nm2 pixel size and 5 µs pixel dwell time (frame rate ~1.25 Hz) to detect GCaMP signals. After recording, the enclosing volume was scanned in LIONESS mode. The GCaMP recording was overlaid with a corresponding plane of the volumetric LIONESS acquisition in **Suppl. Fig. 16C**. The same volume was imaged a second time 10 min after the first acquisition. The sample was kept in place in between the two recordings.

## Chemogenetic activation with calcium imaging

Chemically targeted activation with simultaneous calcium imaging of neurons was done using AAVs containing a Cre-dependent DREADD[54] construct (AAV-DIO-CAG-hM3Dq-2A-dTomato; plasmid available from the authors upon request) added to organotypic hippocampal slice cultures of Prox1-cre/Ai95 (GCaMP6f) mice at DIV 4-6. Each transduced cell expressed both cytoplasmic dTomato and the excitatory designer receptor hM3Dq. Concentrated viral stock ($7x10^{11}$ GC/ml) was first diluted 1:10 in culture medium, and subsequently 5 µl were carefully placed on top of each slice. Weak fluorescence was already detectable ~3 days after transfection and live-imaging was performed from day 9 onwards after viral transduction. To activate the designer receptor, Clozapine-N-oxide (CNO) was added (3 µM final concentration) to the imaging medium (fluorophore containing ACSF). The GCaMP signal was recorded via confocal scanning

(488 nm excitation, 3.9 µW) of an individual plane using a pixel size of 100 x 100 $nm^2$ and dwell time of 20 µs, which resulted in a frame rate of ~ 2 Hz. The GCaMP recording together with the dTomato signal were overlaid with a corresponding plane of the LIONESS acquisition for representation. For the inset in **Fig. 5A**, a square region of interest around the CNO activated mossy fiber bouton was defined, GCaMP signal averaged over this region, and normalized to the value in the first frame.

## Electrophysiology

Organotypic slice cultures were submerged in artificial cerebrospinal fluid (ACSF) containing 125 mM NaCl, 25 mM $NaHCO_3$, 25 mM D-glucose, 2.5 mM KCl, 1.25 mM $NaH_2PO_4$, 2 mM $CaCl_2$, and 1 mM $MgCl_2$, with pH maintained at 7.3, equilibrated with a 95% $O_2$/5% $CO_2$ gas mixture at ~22 °C (room temperature). Glass micropipettes were pulled from thick-walled borosilicate glass (2 mm O.D., 1 mm I.D.) and filled with intracellular solution containing 135 mM K-gluconate (Sigma, #G4500), 20 mM KCl, 0.1 mM EGTA (Sigma, #E0396), 2 mM $MgCl_2$, 4 mM $Na_2ATP$ (Sigma, #A3377), 0.3 mM GTP (Sigma, #G8877), 10 mM HEPES (Gibco, #15630056), with the addition of 20 µM AlexaFluor488 hydrazide (Invitrogen, #A10436) and 0.2 % (w/v) biocytin (Invitrogen, #B1592) as required. Pipettes were positioned using two LN mini 25 micromanipulators (Luigs and Neumann) under visual control on a modified Olympus BX51 microscope equipped with a 60x water-immersion objective (LUMPlan FI/IR, NA = 0.90, Olympus, 2.05 mm working distance). Two neurons were simultaneously recorded in the whole-cell patch-clamp configuration, with signals acquired on a Multiclamp 700B amplifier (Molecular Devices), low pass filtered at 6 kHz and digitized at 20 kHz with a Cambridge Electronic Design 1401 mkII AD/DA converter. Signals were acquired using Signal 6.0 software (CED). Action potential phenotypes were recorded on sequential current pulse injections (-100 to +400 pA) in the current clamp configuration. Neurons were identified based on morphological and action potential phenotypes. In current clamp recordings, pipette capacitance was 70 % compensated.

Synaptic connectivity was assessed by sequential current injection into either recorded cell in the current-clamp configuration, while recording EPSCs (Excitatory Postsynaptic Currents) from the other in the voltage-clamp configuration. Presynaptic action potentials were elicited by five 1-2 nA current injection pulses for 2-3 ms at 20 Hz. Putative monosynaptic connections were identified by EPSC generation (peak current > 2.5 times the standard deviation of baseline noise) in the

postsynaptic cell with short latency (< 4 ms) from the presynaptic action potential peak. Recordings were analysed using Stimfit[55] and MATLAB-based scripts.

After recording, neurons were resealed by forming an outside-out patch on pipette retraction, before immersion in solutions for live imaging.

## SulfoAtto 643 synthesis and characterization

In a 5 mL round bottom flask equipped with a magnetic stir bar, Atto 643 NHS-ester (ATTO-TEC: #AD 643-35; 5.0 mg, 5.23 µmol, 1.0 equiv.) was dissolved in a mixture of 700 µL *N*,*N*-dimethylformamide (Fisher Scientific: #D/3846/17) and 300 µL $dH_2O$. *N*,*N*-Di*iso*propylethylamine (Carl Roth: #2474.1) (6.9 mg, 53.8 µmol, 9.3 µL, 10 equiv.) and taurine (Carl Roth: #4721.1) (3.4 mg, 26.8 µmol, 5.1 equiv.) were added successively and the reaction mixture was allowed to incubate under stirring for 60 min before it was quenched by the addition of glacial acetic acid (Carl Roth: #6755.1) (10 µL). Semi-preparative reverse phase-high pressure liquid chromatography was performed on an Agilent 1260 Infinity II LC System equipped with a Reprospher 100 C18 column (5 µm: 250 x 10 mm at 4 mL/min flow rate). Eluents A (0.1% trifluoroacetic acid (TCI: #T0431) in $dH_2O$) and B (0.1% trifluoroacetic acid in acetonitrile (Honeywell: #34851-2.5L)) were used. The gradient was from 10% B for 5 min → gradient to 90% B over 35 min → 90% B for 5 min with 4.0 mL/min flow. Peak detection and collection were performed at $\lambda$ = 650 nm and provided 4.5 mg (4.7 µmol) of the desired product as a blue powder after lyophilization with 91% yield. Characterization was performed using high pressure liquid chromatography mass spectrometry (**Suppl. Fig. 20, left**) on an Agilent 1260 Infinity II LC System equipped with Agilent SB-C18 column (1.8 µm, 2.1 × 50 mm). Buffer A: 0.1% formic acid (Fisher Scientific: A117-50) in $dH_2O$ Buffer B: 0.1% formic acid in acetonitrile. The gradient was from 10% B for 0.5 min → gradient to 95% B over 5 min → 95% B for 0.5 min → gradient to 99% B over 1 min with 0.8 mL/min flow. Retention time $t_R$ = 3.03 min. Low resolution mass spectrometry: calculated: 943 Da, found: 943 Da. Excitation and emission spectra were recorded on a TECAN INFINITE M PLEX plate reader ($\lambda_{Ex}$ = 580±10 nm; $\lambda_{Em}$ = 620–800±20 nm; 10 flashes; 40 µs integration time; $\lambda_{Ex}$ = 300–660±10 nm; $\lambda_{Em}$ = 700±20 nm; 10 flashes; 40 µs integration time) with

200 nM solutions of SulfoAtto 643 in PBS (Carl Roth: #9143.2) in Greiner black flat bottom 96 well plates (Carl Roth: #CEK8.1) (**Suppl. Fig. 20, right**).

## Restoration network training

Volumetric paired low-exposure, low-SNR training input data and high-exposure, high-SNR "ground truth" data were recorded in a voxel-exact mode by collecting low-SNR data during the first 10 µs voxel dwell time and additional photons during the remaining 60 µs dwell time. High-SNR ground truth for network training were thus generated by adding up counts from the total 70 µs dwell time in FIJI Version: 2.3.0/1.53f (Fiji/process/calculator plus/add). Other imaging parameters were as described in the section "LIONESS imaging" (2.9 µW (640 nm) excitation laser power, 90 mW STED laser power with power ratio of *z*-STED/*xy*(4π)-STED of 80/20, voxel size 50 x 50 x 50 $nm^3$). 76 volume pairs of 12.5 x 12.5 x 5 µm each were used for training. Volumes were taken from organotypic hippocampal and cerebellar slice cultures and the alveus region of acutely dissected hippocampi. Network training (Version: CSBDeep 0.6.1)[27] parameters were as follows: 3D mode, 32 x 32 x 32 pixel patch size, 190 patches per volume, 150 steps per epoch, 150 epochs, batch size 32, and training data was loaded as 16-bit TIFF files. Software was installed from GitHub (https://github.com/CSBDeep/CSBDeep). A workstation with the following hardware components was used: Intel® Xeon® W "Skylake" W-2145, 3.60 GHz processor, 128 GB RAM, NVIDA GeForce RTX 2080Ti graphics card.

## Denoising

To denoise confocal images recorded simultaneously with the LIONESS data in **Fig. 4** and **Suppl. Fig. 6** and **14B**, Noise2void[56] (Version 0.2.1) was applied to individual channels with the following parameters: noise2void 3D mode, patch size 32 x 32 x 32 pixels, each patch augmented with rotations and axis-mirroring, training steps per epoch 150, number of epochs 75 (SYP1-EGFP) or 100 (PSD95-HaloTag), batch size 16 (SYP1-EGFP) or 32 (PSD95-HaloTag). Software was installed from GitHub (https://github.com/juglab/n2v). A workstation with the following hardware components was used: Intel® Xeon® W "Skylake" W-2145, 3.60 GHz processor, 128 GB RAM, NVIDA GeForce RTX 2080Ti graphics card.

## Image analysis and processing

All used LUTs were linear except for **Fig. 2**, **Suppl. Figs. 2A-C, 5**, and **11**, where a color calibration bar is provided. Threshold adjustments for display purposes were applied linearly and to the whole image. Line profiles (**Fig. 1D** and **Suppl. Figs. 2C and 3**) were created using Fiji, line width was 2 pixels.

## Volume extension

For stitching of volumetric images, the Fiji 3D stitcher was used (Fiji/Plugins/deprecated/3D Stitching; linear blending, fusion alpha 2.0).

## Manual segmentation and proofreading

Planes for manual segmentation were first upscaled 5-fold without interpolation (plane depth was kept at original 50 nm spacing). Segmentation itself was done using VAST[57] 1.3.0. and 1.4.0. Software was downloaded from https://lichtman.rc.fas.harvard.edu/vast/. For proofreading of automated segmentations data was visualized using Neuroglancer (https://github.com/google/neuroglancer) and corrected using VAST 1.4.0.

## Segmentation

We based our implementation of the automatic segmentation pipeline on the *pytorch_connectomics*[32,33] framework. We used a U-Net architecture and trained the neural network to produce affinity maps which were then processed by a watershed algorithm to obtain the final segmentations.

During training, the U-Net required volume data and the corresponding manual ground-truth segmentation. First, in order to adapt the input datasets to the framework requirements and maximize its performance, we applied a pre-processing step converting the volume data to 8-bit format and stretching the intensity to cover the whole intensity range. Then, the pre-processed volumes together with the corresponding ground-truth segmentations were passed into the U-Net. Three key parameters during training were the sample size, the number of training iterations and the data augmentation. Given the anisotropic step size (5-fold upsampling in the *xz*- or *yz*-plane for manual segmentation) of the input volume we noticed that using a sample size of [128 x 128 x

64], with the lowest number corresponding to the non-upsampled axis, significantly improved the performance of the neural network over smaller sizes. We increased the number of training iterations from the default 100k to 500k which further helped reduce segmentation errors. We found this number of iterations to be a reasonable compromise between training time and inference performance. Finally, we enabled all available data-augmentation techniques.

During inference, we passed the pre-processed volume data into the U-Net and obtained the affinity map as output. At inference time we used the same sample size used during training, with appropriate padding if the input volume was small, and test-time augmentation via axis-mirroring. The values in the final affinity map corresponded to the mean of the values obtained for each augmented case. The output affinity map was processed using the watershed algorithm to produce the labelled automatic segmentation. Our pipeline combined two different watershed implementations. First, we applied the image-based watershed method[58] (https://github.com/zudi-lin/zwatershed) on each slice to compute fragment masks. These were then passed to a volume-based implementation (https://github.com/zudi-lin/waterz), which was applied on the affinity map, producing the final segmentation. We used watershed thresholds in the range [0.2-0.4] to minimize oversegmentation but also avoid merges, which tend to be more tedious to fix during proof-reading. The resulting segmentations contained spurious segments, which we cleaned during a final post-processing step by removing those that consisted of too few voxels (fewer than 10) or slices (fewer that 2). This last step significantly facilitated later proof-reading. The resulting segmentations were then analyzed visually, using Neuroglancer, and quantitatively, using metrics such as segment size distribution and split ratio of ground truth segments with respect to automatic segmentations.

We trained the U-Net on a 8-GPU (NVIDIA 3090s) node, using 32 CPUs and 128 GB RAM during 500k iterations, which took 6 days. Inference time falls in the 10 to 40 minutes range, depending on the size of the input volume, and can be performed on a more modest compute node. In our case, we used a 2-GPU (NVIDIA 3090s) node using 8 CPUs. The post-inference watershed and segmentation cleaning operations were performed on the inference node and took 10 minutes to 20 minutes to complete.

## Visualization

3D visualizations were done either using VAST[57] 1.4.0. (**Fig.1A, 2A** and **Suppl. Figs. 7, 8A, 11, 12, 19A**), Neuroglancer (**Fig. 3B , 4B, 5B, Suppl. Figs. 9, 10, 18, 19B**), Blender 2.93.4 (**Fig 1A,**

**3C, Suppl Fig. 8B**) or Neuromorph[59] 2.8 (**Fig. 3E**). Blender-generated visualizations were produced based on 3D meshes extracted from segmentations using marching cubes (as implemented in Scikit-Image). These 3D meshes were first smoothed in Blender using a vertex-based smoothing operation that flattens angles of mesh vertices and finally the scene was rendered using Blender's Cycles rendering engine. The schematics in the upper row of **Fig. 1A** were created with Biorender.com.

## Dendrite abstraction

For representing dendrite synaptic connectivity in **Fig. 3E**, we developed a visual spine analysis approach inspired by Barrio[60], a software for visual neighborhood analysis of nanoscale neuronal structures. We computed surface meshes for all axons and dendrites based on the segmented neuronal structures. Next, we used Neuromorph[59] to compute spine lengths by specifying the base and tip of each spine and plotted spine positions and relative spine length according to position on the dendrite. Spine lengths were computed between the base and tip of each spine, following the spine's central axis (skeleton). We abstracted the complex 3D morphology and connectivity of a dendrite from 3D to 2D to reduce visual clutter, while preserving relative spine positions and spine lengths. To do so, we mapped a dendrite's 3D skeleton structure to a simplified, but topologically correct, 2D representation. We preserved all relative distance relations within a dendrite (i.e., distances between spines), and encoded spine length at each spine location. Spine lengths were represented as bars, scaled relatively to the largest spine length of the dendrite.

## Statistics and reproducibility

In all images, representative data from single experiments are shown. LIONESS imaging of cerebral organoids as depicted in **Fig. 1A** and **Suppl. Fig. 8** was additionally repeated on similar specimens twice. Acute preparation of hippocampus and LIONESS imaging of the alveus region as shown in **Suppl. Figs. 10 and 18** was repeated 4 times, neuropil of wild type organotypic hippocampal slice cultures as in **Fig. 3** and **Suppl. Figs. 1, 2, 5, 12** and **19** was repeated at least 20 times. LIONESS imaging paired with PSD95-HalTag/SYP1-EGFP live labelling as in **Fig. 4** and **Suppl. Fig. 14** was repeated 4 times. Repeated imaging of the same region using LIONESS as in **Fig. 5** and **Suppl. Figs. 4b, 15 and 16** was performed at least 4 times. Repeated imaging of the same region with conventional, high photon load STED as shown in **Suppl. Fig. 4A** was repeated

with performing *xy*-scanning only, showing the same negative effect. Comparison of single versus split detection (**Suppl. Fig. 3**) and 2π- and 4π-helical phase modulation (**Suppl. Fig. 2**) were repeated at least 3 times each, the comparison between single detection and 2π-helical phase modulation with split detection and 4π-helical phase modulation (**Fig. 1B, C**) was repeated 3 times. Fluoromyelin labelling as shown in **Suppl. Fig. 13** was performed 3 times.

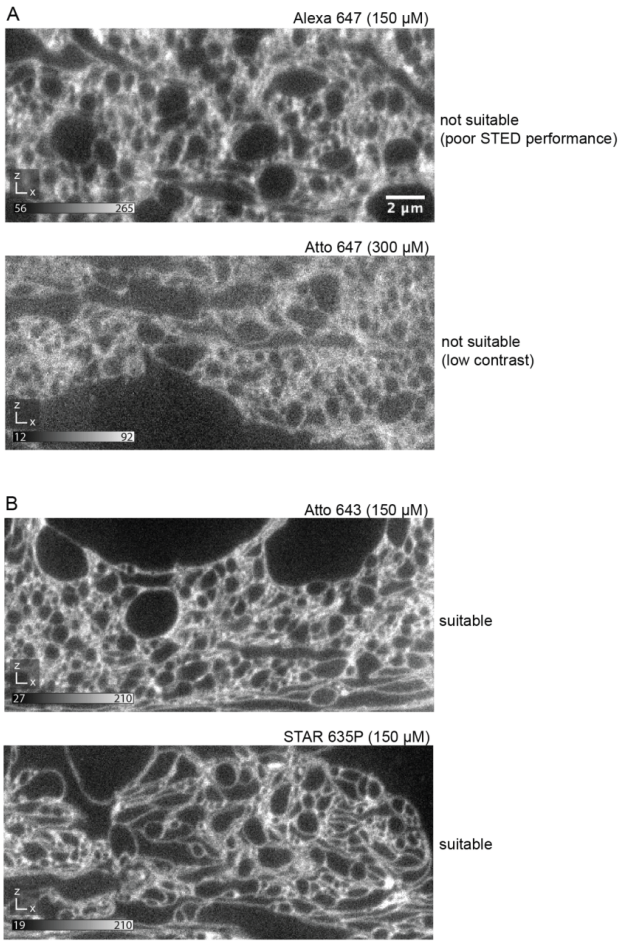


**Suppl. Fig. 1. Fluorophore screening.** (**A**) Two examples of fluorophores yielding insufficient delineation of fine cellular structures, due to suboptimal STED performance (top) or poor extra- vs. intracellular contrast (bottom). (**B**) Two examples of fluorophores with high STED performance and high extra- vs. intracellular contrast (Atto 643, Abberior STAR 635P), yielding adequate delineation of fine cellular structures. All images show raw *xz*-planes recorded with tissue-optimized STED patterns at near-isotropic resolution. Fluorophores applied at indicated concentrations to ECS in organotypic hippocampal slice cultures. The custom synthesized sulfonated variant of Atto 643 (SulfoAtto 643) was equally suited and used interchangeably with Atto 643. Scale bar: 2 µm, valid for all images. Numbers in greyscale bars refer to raw photon counts.

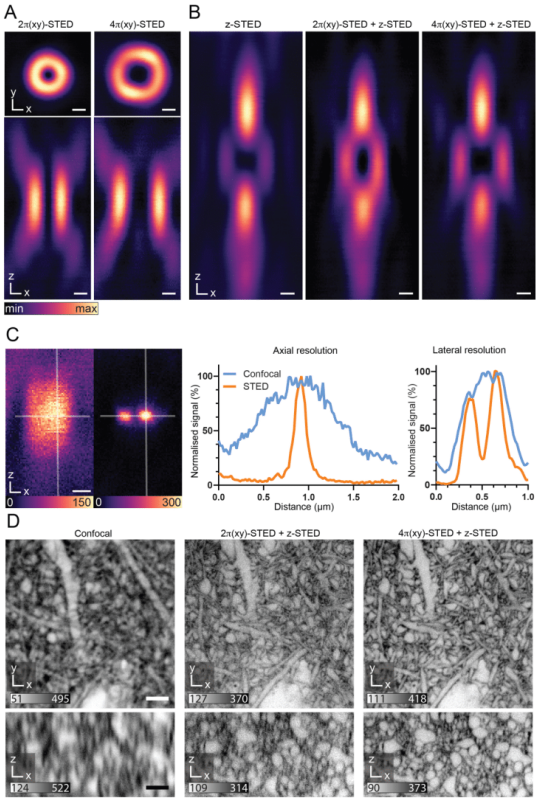


**Suppl. Fig. 2. Tissue-optimized STED.** (**A,B**) STED light intensity distributions in the focal region. (**A**) Lateral (top) and axial (bottom) sections for 2π- and 4π-helical phase modulation. Scale bars: 250 nm. (**B**) Axial sections of the π-top-hat phase modulated *z*-STED pattern (left), an incoherent superposition of 2π(*xy*)- and *z*-STED patterns (middle), and of 4π(*xy*)- and *z*-STED patterns (right). Power distribution between the *z*- and *xy*-STED patterns in the superpositions was 80% vs. 20%. Scale bars: 250 nm. (**C**) Axial scan of 40 nm diameter fluorescent beads in confocal mode (left) and with STED employing combined 4π(*xy*)- and *z*-STED patterns (right). Scale bar: 250 nm. Profiles along the lines in lateral and axial directions as indicated in the images. (**D**) Extracellularly labelled neuropil in organotypic hippocampal slices. Orthogonal planes in *xy*- and *xz*-direction for diffraction-limited confocal (left), classical 2π-helical and π-top-hat phase modulation (middle), and combination of 4π-helical plus π-top-hat modulation for near-isotropic resolution with improved quenching of excitation outside the central STED intensity minimum. The 4π-helical pattern also facilitated robust in-tissue co-alignment of intensity minima. Scale bar: 2 µm. Raw data with linear, inverted color scale. Numbers in greyscale bars refer to raw photon counts.

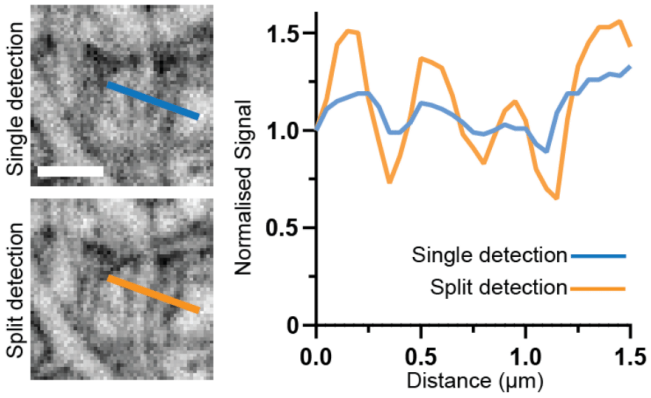


**Suppl. Fig. 3. Detector dynamic range.** Same region in organotypic hippocampal slice culture imaged with a single detector (top) or with a split detection path and two single-photon counting avalanche photodiodes as detectors (bottom). Line profiles over corresponding structures for single (blue) and split (orange) detection, normalized to first data point. STED power and pixel dwell times were identical, and STED patterns for near-isotropic resolution were used. Increased detector dynamic range allowed doubled excitation power within the linear detection regime, improving signal-to-noise ratio. Single imaging planes in organotypic hippocampal slice cultures. Scale bar: 1 µm.

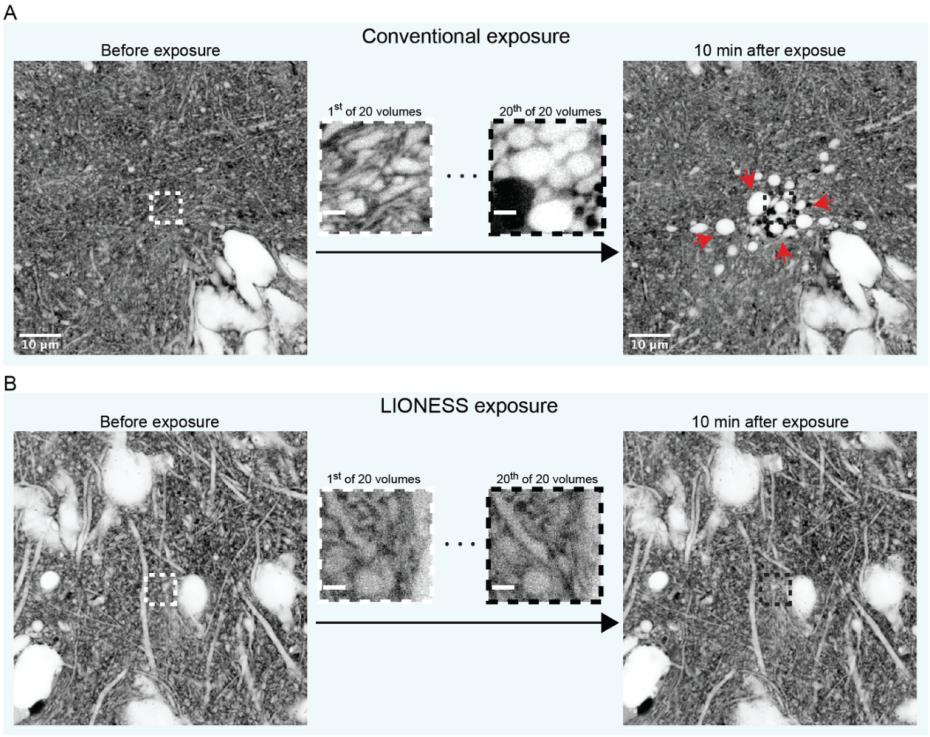


**Suppl. Fig. 4. Live-tissue compatibility.** (**A**) Confocal overview images in an organotypic hippocampal slice culture before (left) and 10 minutes after (right) scanning a volume in the centre (5 x 5 x 2.5 µm$^3$) 20 times in high-photon load STED mode (70 µs voxel integration time). Central images are single planes of the first and last STED volume acquired. Red arrows indicate blebbing and disintegrating cells. (**B**) Confocal overview images of a different region before (left) and 10 minutes after (right) scanning a volume in the centre (5 x 5 x 2.5 µm$^3$) 20 times using LIONESS parameters (10 µs voxel integration time). Central images are single planes of the first and last LIONESS volume acquired. Scale bars: confocal: 10 µm, STED: 1 µm.

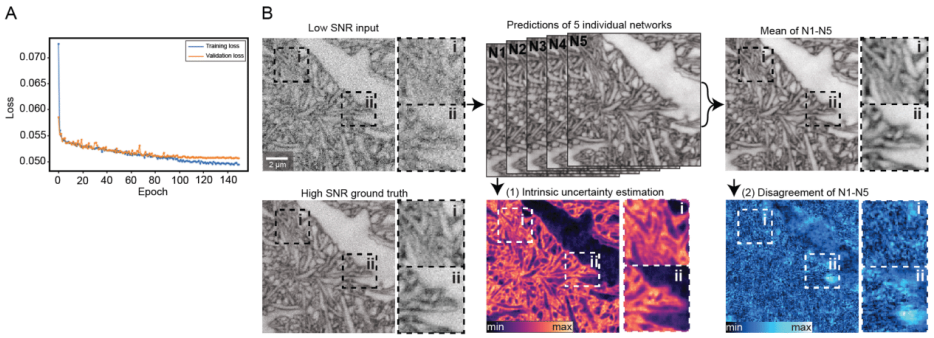


**Suppl. Fig. 5. SNR restoration training.** (**A**) Training and validation loss as a function of epoch number of the SNR-restoring deep artificial network. (**B**) Validation of artificial network predictions on paired low- and high-SNR data that were not part of the network training, recorded with tissue-optimized STED in extracellularly labelled organotypic hippocampal slice cultures. (1) Intrinsic probabilistic estimation of uncertainty for individual predictions (lower panel, middle) and (2) standard deviation of the mean (disagreement) of 5 trained networks N1-N5 for each voxel (lower panel, right). Raw data and network predictions are maximum intensity projections spanning 150 nm. Scale bar: 2 µm.

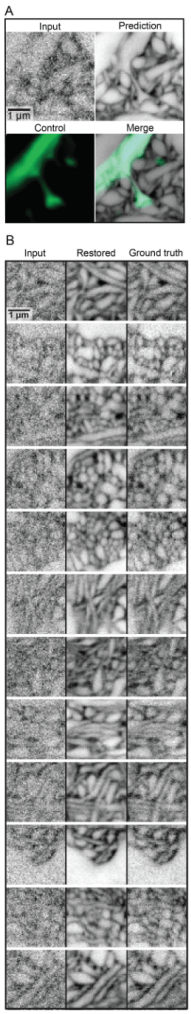


**Suppl. Fig. 6. Validation of SNR restoration.** (**A**) Raw low-exposure input, SNR-restored artificial neural network prediction, positively labelled (Thy1-EGFP[50], diffraction limited) control, and overlay of prediction and control in extracellularly labelled organotypic hippocampal slice culture. (**B**) Twelve exemplary areas of raw input, SNR-restored network prediction, and high-SNR ground truth from an imaging volume not included in the network training data. Neuropil in organotypic hippocampal slice culture. Scale bars: 1 µm. Images except for positively labelled control displayed with inverted look-up table. Maximum intensity projections spanning 150 nm. Data used in validation were not part of restoration network training.

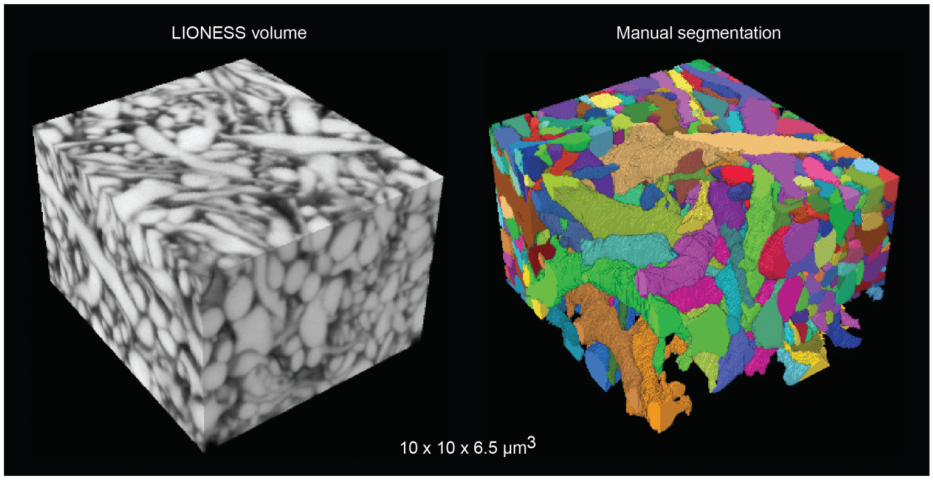


**Suppl. Fig. 7. Manual segmentation.** *Left*: LIONESS tissue volume in neuropil of organotypic hippocampal slice culture. *Right*: Manual segmentation using VAST Lite 1.3.0 and 1.4.0. The region in the foreground shows a partial segmentation.

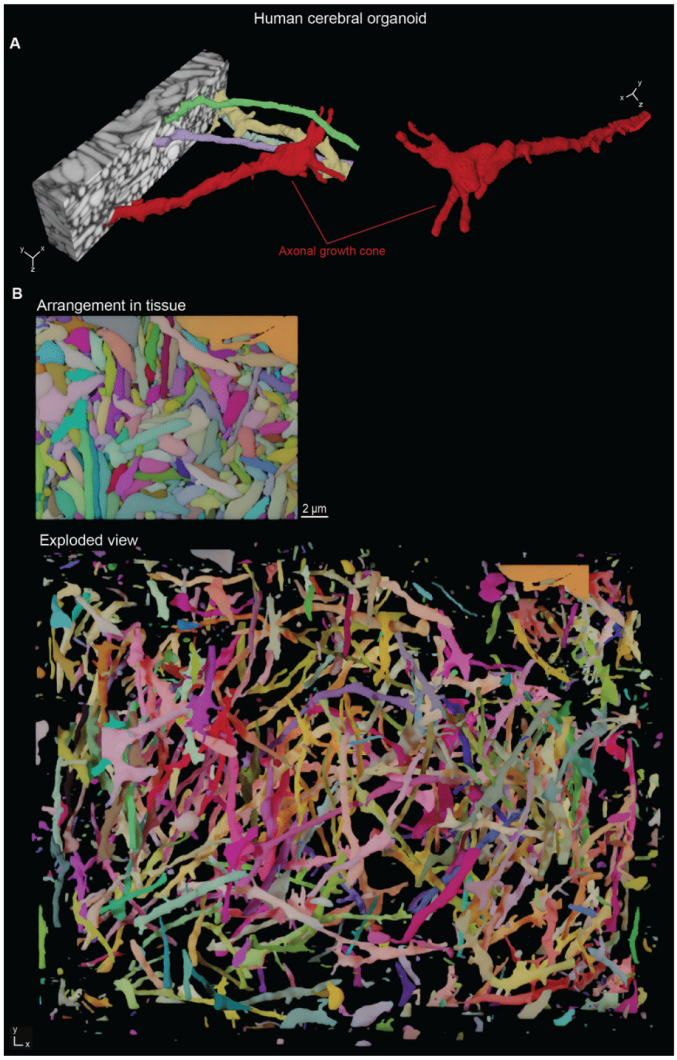


**Suppl. Fig. 8. Reconstruction of living human cerebral organoid.** (**A**) *Left*: LIONESS volume of the human cerebral organoid in Fig. 1A, eroded to reveal an axonal growth cone transmigrating the dense tissue and a selection of the structures it interacts with. *Right*: The same growth cone viewed from a different angle. (**B**) Top view of the saturated organoid reconstruction in Fig. 1. (Top), and exploded view of the same saturated reconstruction (Bottom). Scale bar: 2 µm.

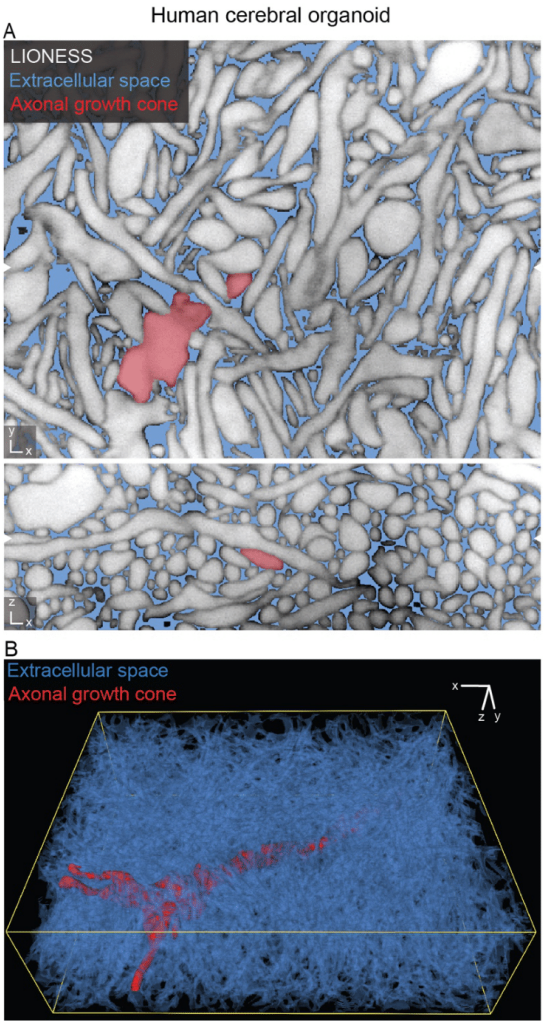


**Suppl. Fig. 9. 3D-segmentation of extracellular space in a human cerebral organoid.** (**A**) Orthogonal views from the human cerebral organoid dataset in Fig. 1A. Extracellular space is highlighted in blue, LIONESS data is shown in grey, and the same axonal growth cone as in Suppl Fig. 8 is indicated in red. White arrowheads at image edges indicate corresponding orthogonal planes. Extracellular space was obtained as the space not occupied by cellular segments. (**B**) 3D-reconstruction of the extracellular space (blue) with the axonal growth cone (red).

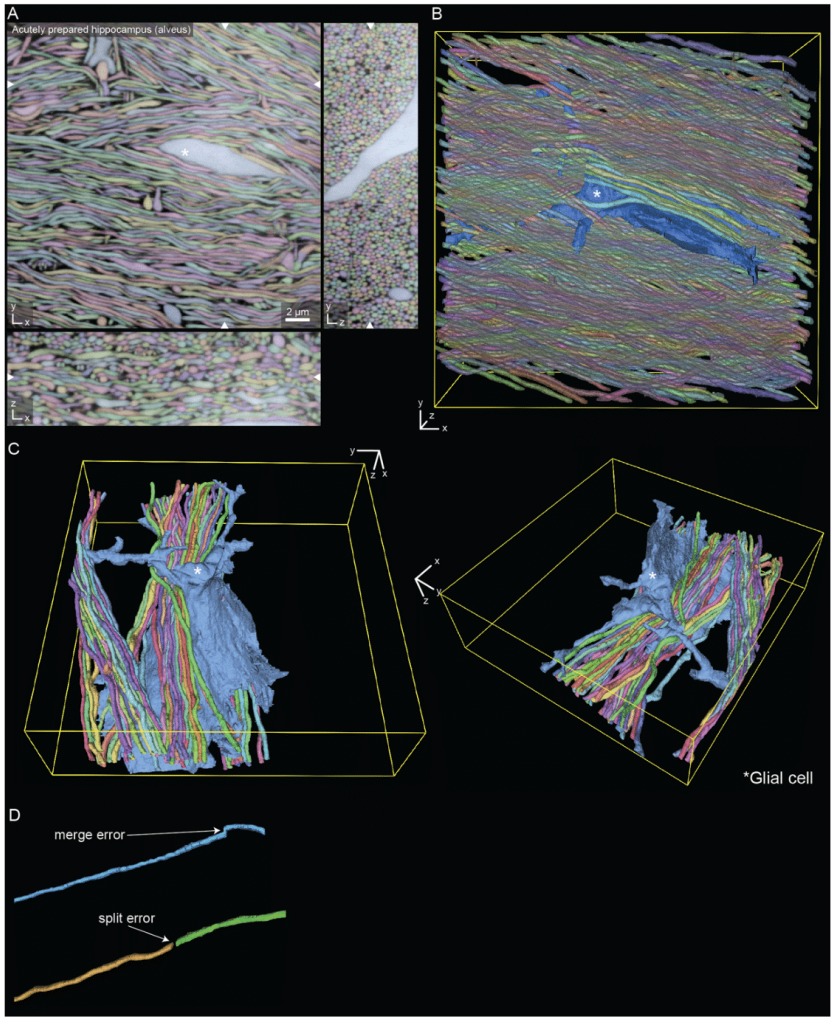


**Suppl. Fig. 10. Reconstruction in living hippocampal alveus.** (**A**) Three orthogonal planes from a fully segmented LIONESS volume in the alveus region of an acutely prepared mouse hippocampus. The white asterisk indicates a glial cell stretching through dense axons. White arrowheads at image edges indicate the position of orthogonal *xy*-, *yz*- or *xz*-views. Scale bar: 2 µm. (**B**) 3D-rendering of a subset of structures from the same dataset as shown in panel A. (**C**) 3D-reconstruction of the glial cell marked in panel A and selected axons, viewed from two different angles. (**D**) Examples of error types after automated segmentation.

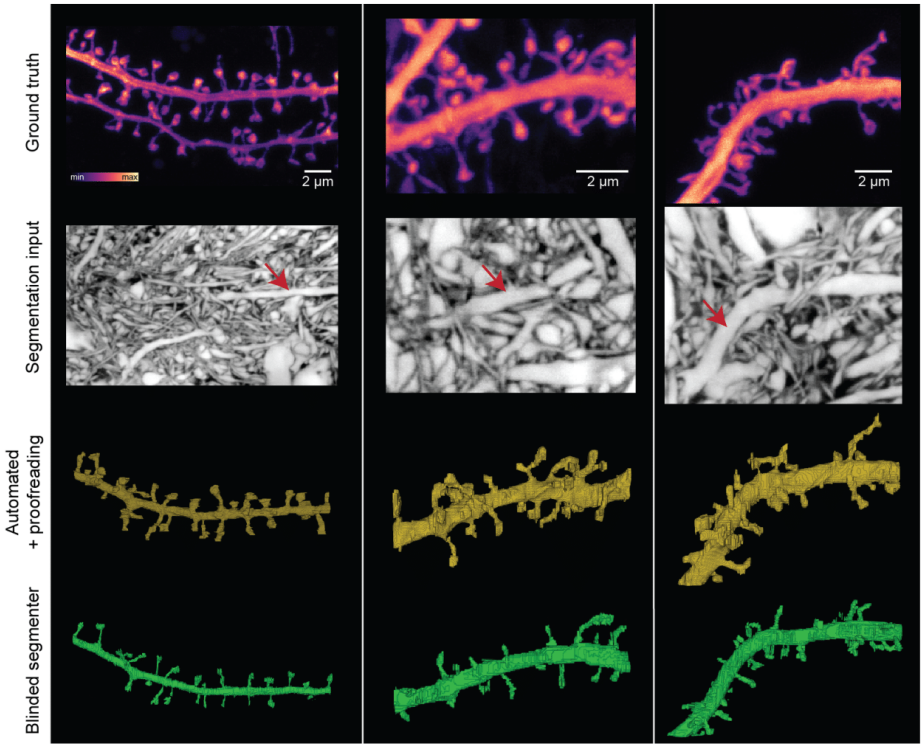


**Suppl. Fig. 11. Validation of LIONESS segmentation.** *Top row*: Maximum intensity projections of positively labeled (Thy1-EGFP) dendrites from neuropil in 3 different samples of organotypic hippocampal slice cultures, serving as sparse ground truth for LIONESS segmentations. Scale bars: 2 µm. *Second from top*: Volumetric LIONESS acquisitions used as source data for segmentation. Red arrows indicate the dendrites corresponding to the positively labelled structure above. *Third from top*: 3D-reconstructions of LIONESS data with automated segmentation and additional proofreading by the experimenter who recorded the data (i.e. non-blinded to the EGFP channel). *Bottom*: Fully manual spine detection from LIONESS data by a segmenter blinded to the EGFP-channel.

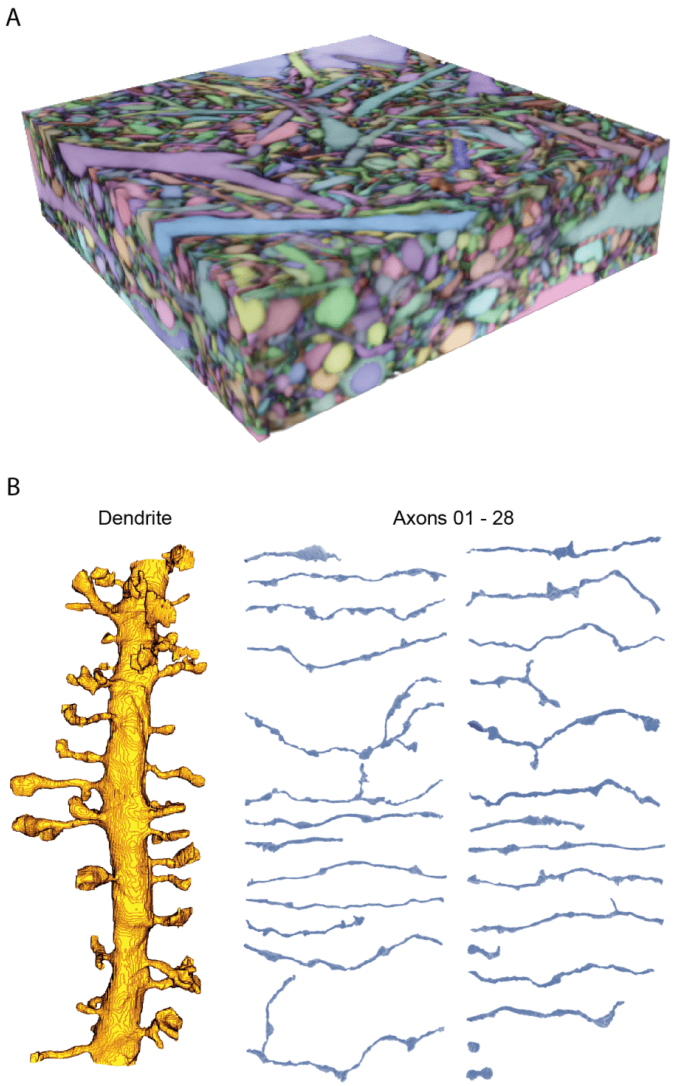


**Suppl. Fig. 12. Reconstruction of spiny dendrites and connected axons.** (**A**) The entire, automatically segmented dataset from Fig. 3, partially proofread. Volume dimensions: 23.2 x 22 x 6 µm$^3$. (**B**) Spiny dendrite and the 28 individual connected axons from Fig. 3 without surface smoothing. The two short segments in the bottom right correspond to one bouton right at the edge of the imaging volume and one bouton which could not be unambiguously assigned to an axon.

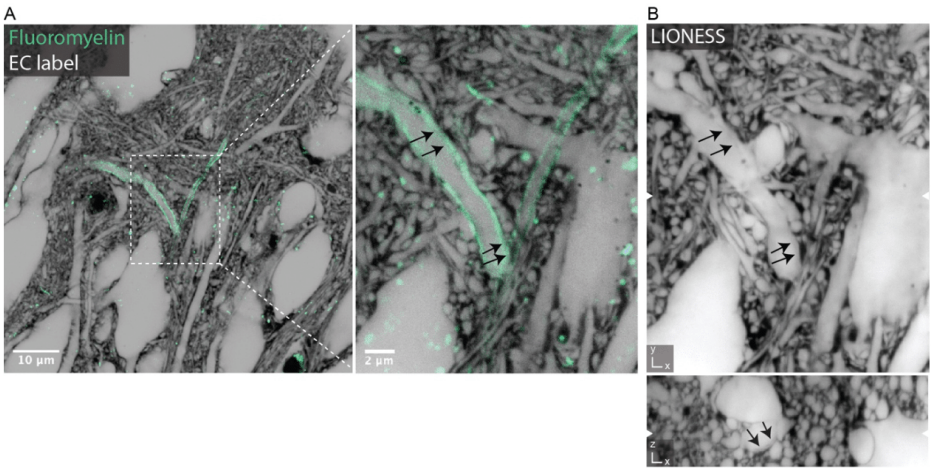


**Suppl. Fig. 13. Identification of myelinated axons.** (**A**) *Left*: Confocal overview image in organotypic hippocampal slice culture with extracellular (grey, inverted LUT) and additional myelin labelling (Fluoromyelin, green). *Right*: Magnified view highlighting a myelinated axon. Single plane in near-isotropically resolving STED mode for extracellular label and confocal mode for the myelin stain. Scale bars: 10 µm (left), 2 µm (right). (**B**)Volumetric LIONESS acquisition of the same region. Black arrows indicate the border between axon and myelin sheath visible in the LIONESS data. White arrowheads at image edges indicate the corresponding position of *xy*- and *xz*-views. LIONESS images are maximum intensity projections spanning 150 nm.

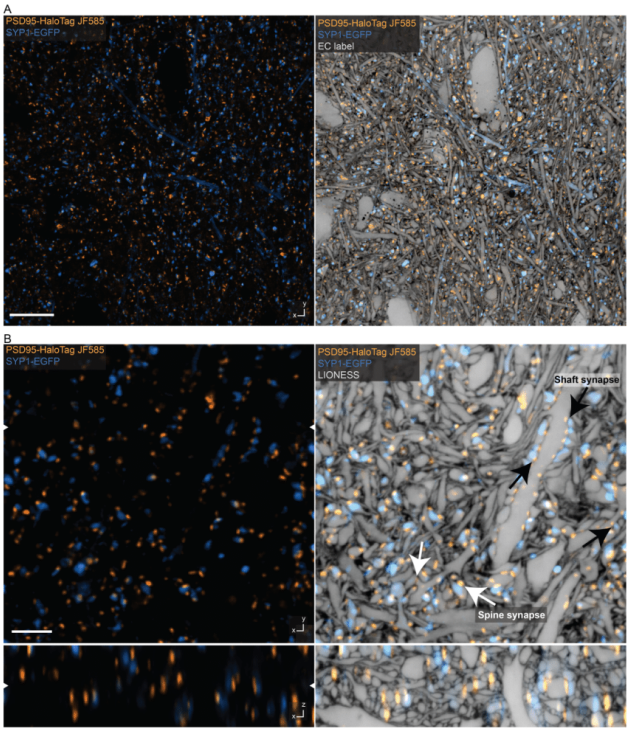


**Suppl. Fig. 14. Structural and molecular information.** (**A**) Overview image of CA1 hippocampal neuropil in living organotypic slice culture from a transgenic mouse line expressing post synaptic density protein 95 (PSD95)-HaloTag to label excitatory postsynapses (orange, STED). A subset of presynaptic terminals were labelled with a synaptophysin 1 (SYP1)-EGFP fusion protein, encoded by a pseudotyped rabies virus (blue, confocal). *Left*: Molecular markers. HaloTag labelled with JF585. *Right*: Same region with structural context from additional extracellular labeling (STED). Scale bar: 10 µm. (**B**) Orthogonal planes in *xy*- and *xz*-direction of an imaging volume in CA1 from a different sample. Labeling and color coding as in panel A. *Left*: Confocal imaging after denoising[56]. *Right*: Additional overlay with near-isotropically super-resolved LIONESS data, clarifying the relationship of molecularly defined entities (pre- and postsynapses) with cell- and tissue-structure. Diffraction-limited signals extend beyond corresponding structures recorded in LIONESS mode, particularly evident in the *xz*-view. White arrows indicate excitatory spine synapses, black arrows indicate excitatory shaft synapses. White arrowheads at image edges indicate the position of corresponding orthogonal planes (left image). LIONESS images correspond to maximum intensity projections spanning 150 nm. Scale bar: 3 µm.

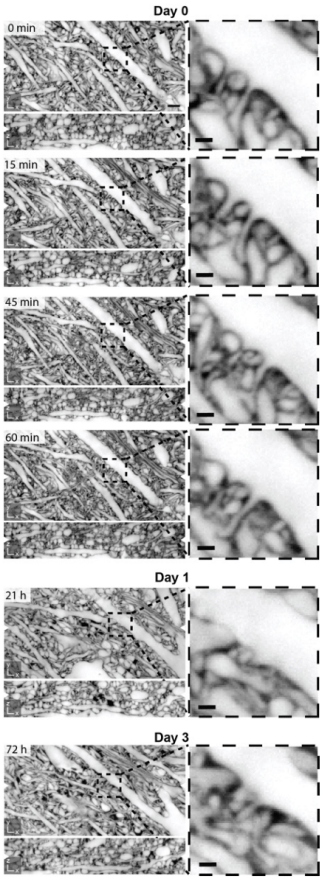


**Suppl. Fig. 15. Structural dynamics in repeated volumetric LIONESS acquisition over 3 days.** Corresponding orthogonal planes in *xy*- and *xz*-direction from 6 consecutive LIONESS measurements of the same volume in the neuropil of an organotypic hippocampal slice culture. The volume was initially imaged 4 times within one hour and then again after one day and after three days. This indicates tissue viability after repeated volumetric LIONESS imaging. Magnified views: Subregion with dendritic spines revealing morphodynamics. Scale bars, overview: 2 µm, magnified views: 500 nm. White arrowheads at image edges indicate the position of corresponding orthogonal planes. Maximum intensity projections spanning 150 nm. Additional dark regions on day 1 and day 3 likely represent branched processes of a damaged cell that took up dye after repeated manual mounting of the sample (supported by a membrane for interface tissue culture), transfer to the microscope, volumetric imaging, unmounting, and transfer back to the tissue culture incubator.

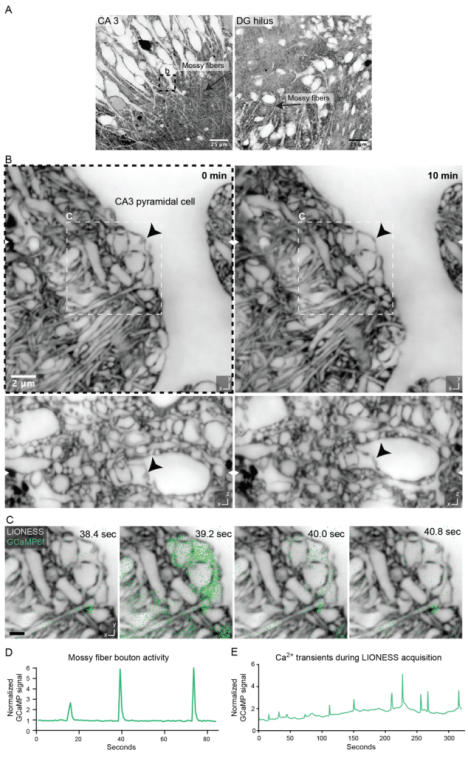


**Suppl. Fig. 16. Correlating structure and morphodynamics with $Ca^{2+}$-activity.** (**A**) Overview images in organotypic hippocampal slice culture with mossy fibers conveying excitatory input from DG granule cells (right) to CA3 pyramidal neurons (left). Scale bar: 25 µm. (**B**) Volumetric LIONESS acquisitions in the stratum lucidum of CA3 at two timepoints (left: 0 minutes, right: 10 minutes) revealed morphodynamics of the complex interface between pre- and post-synaptic structures at mossy fiber to CA3 pyramidal neuron synapses. The black arrowhead marks a structure changing over time. White arrowheads at image edges indicate the corresponding positions of *xy*- and *xz*- views. Scale bar: 2 µm. (**C**) Plane from the LIONESS volume overlaid with diffraction-limited signal from the calcium indicator GCaMP6f (green). LIONESS images are identical replicates providing structural context to the time-varying $Ca^{2+}$-signals. Scale bar: 1 µm. (**D**) GCaMP signal of the mossy fiber bouton shown in (C) as a function of time. Total signal from a rectangular region enclosing the mossy fiber bouton was integrated and normalized to the first frame. (**E**) GCaMP signal as a function of time (and position) recorded as an additional color channel during the volumetric LIONESS acquisition for timepoint 0 min in (B), indicating that $Ca^{2+}$-activity continued during LIONESS acquisition. LIONESS images are maximum intensity projections spanning 150 nm.

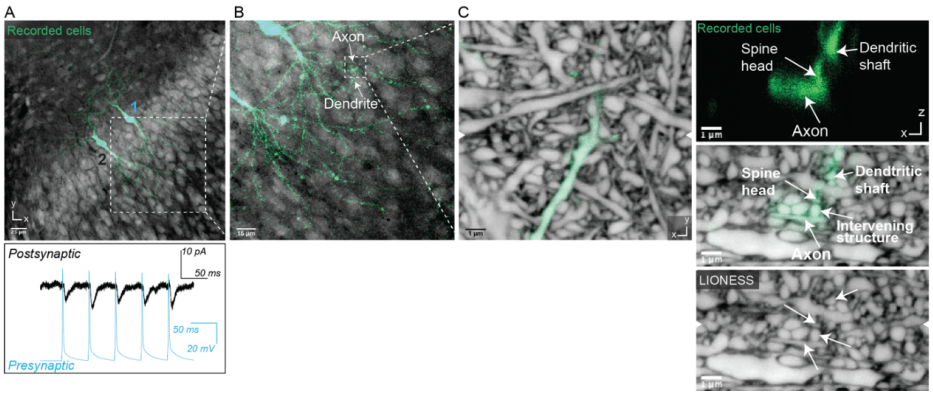


**Suppl. Fig. 17. Correlating structural with electrophysiological information.** (**A**) Two CA1 pyramidal neurons after patch clamp recording and filling with fluorescent dye in living organotypic hippocampal slice culture. Currents in neuron (2, black trace in bottom panel) elicited by triggered action potentials in neuron (1, blue trace in bottom panel) reveal a monosynaptic connection in the paired recording. Scale bar: 25 µm. Confocal image of positively labelled neurons (green) and extracellular label (grey) with low-numerical aperture objective. (**B**) Region where axon of neuron 1 overlaps with a dendrite of neuron 2, suggesting a synaptic connection in confocal imaging. Scale bar: 15 µm. (**C**) Detailed view of overlap region with positively labelled structures (green) read out at diffraction-limited resolution with a high-numerical aperture objective, embedded in surrounding volume recorded with LIONESS. Orthogonal views in *xy*- and *xz*-directions, with arrowheads at image edges indicating the position of the corresponding orthogonal sections. The diffraction-limited *xz*-view of the positively labelled structures indicated a synaptic connection (top). The increased resolution and comprehensive labelling of all cellular structures in the LIONESS xz-view disclosed an intervening structure unrelated to the two patch-clamped neurons. Scale bars: 1 µm. Maximum intensity projections spanning 150 nm.

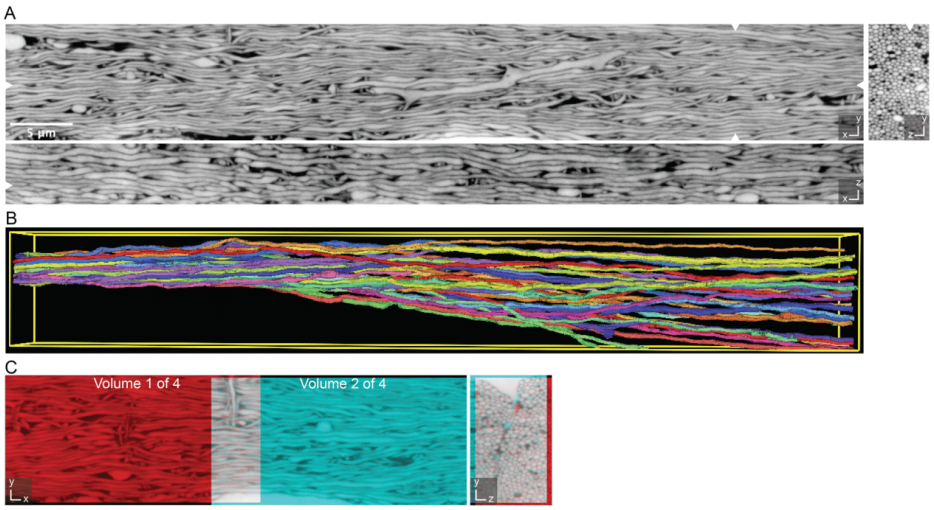


**Suppl. Fig. 18. Extending LIONESS tissue volumes.** (**A**) Orthogonal planes in *xy*-, *xz*-, and *yz*-directions from a LIONESS volume in the alveus region of an acutely prepared mouse hippocampus. Data were registered from 4 consecutive, partially overlapping acquisitions. White arrowheads at image edges indicate position of corresponding orthogonal planes. Maximum intensity projections spanning 150 nm. Scale bar: 5 µm. (**B**) 3D-rendering of selected axons from (A), forming a tight bundle in the left and progressively fanning out. (**C**) Example of alignment between two of the partially overlapping subvolumes in *xy*- and *yz*-views. Individual subvolumes are shown in red and cyan, such that overlapping regions add up to white color, indicating the degree of overlap.

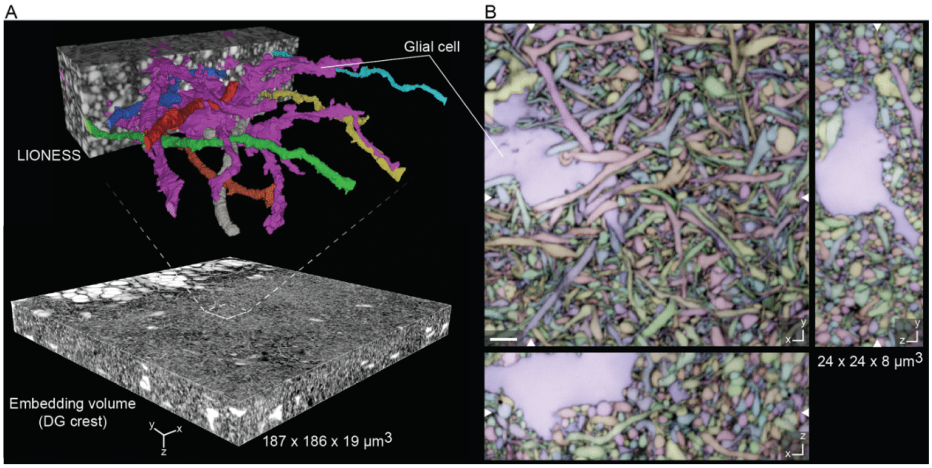


**Suppl. Fig. 19. Meso-scale tissue context.** (**A**) Meso-scale overview volume acquired in diffraction-limited mode with select subvolume acquired and reconstructed using LIONESS in an organotypic hippocampal slice culture. A glial cell is 3D-rendered together with exemplary neuronal processes, showing their mutual arrangement. (**B**) Three orthogonal planes from the automated segmentation of the LIONESS volume in (A). Segmentation (color) and LIONESS data are overlaid. No proofreading was applied. White arrowheads at image edges indicate corresponding orthogonal planes. The same glial cell is indicated in both panels. Scale bar: 2 µm.

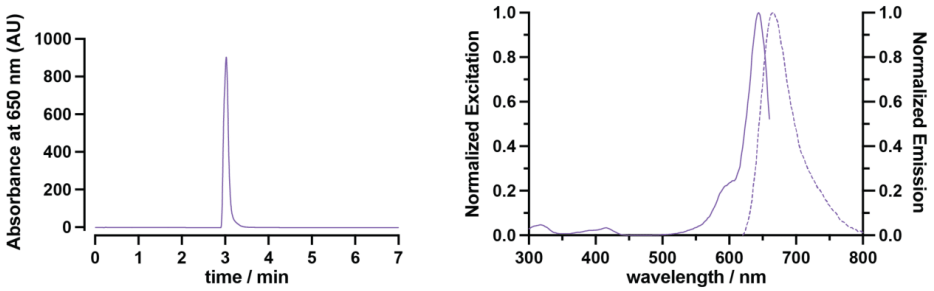


**Suppl. Fig. 20. Characterization of SulfoAtto 643.** *Left*: Absorbance as a function of elution time acquired by liquid chromatography low resolution mass spectrometry. *Right*: Normalized excitation and emission spectra of SulfoAtto 643.

**Supplementary Video 1.**

**LIONESS volume in living hippocampal alveus - 1 (*xy* view).** Full LIONESS stack (*xy*-view) in the alveus region of an acutely prepared mouse hippocampus, corresponding to the dataset in Suppl. Fig. 10. A glial cell embedded in dense axonal structures oriented in various direction can be appreciated. Step size: 50 nm (160 optical sections).

**Supplementary Video 2.**

**LIONESS volume in living hippocampal alveus - 2 (*yz* view).** Full LIONESS stack (*yz*-view) in the alveus region of an acutely prepared mouse hippocampus, corresponding to the dataset in Suppl. Fig. 10. A glial cell embedded in dense axonal structures can be appreciated. Of note, axons are organized in layers with different main orientation, apparent from the differential movement of axonal cross sections in the fly through. Step size: 50 nm (500 optical sections).

**Supplementary Video 3.**

**LIONESS volume in living hippocampal neuropil.** Full LIONESS stack (x*y*-view, followed by *xz*-view) of a volume of dentate gyrus in organotypic hippocampal slice culture, corresponding to the dataset in Fig. 3. Various neuronal and non-neuronal structures are visible. Step size: 50 nm (xy-view: 120 optical sections, xz-view: 440 optical sections).

**Supplementary Video 4.**

**Molecularly informed LIONESS volume in living hippocampal neuropil.** Full LIONESS stack (*xy*-view) of the entire PSD95 (orange) and synaptophysin (blue) labelled dataset shown cropped in Fig. 4. Molecular information confirms synapse location in relation to the structural LIONESS measurement. Step size: 50 nm (120 optical sections).

**Supplementary Video 5.**

**GCaMP recording, overview.** Diffraction limited recording of calcium transients using Ai95/Prox1-cre mouse organotypic hippocampal slice cultures extracellularly labelled with Atto 643. The time series corresponds to a single plane of a region in the DG during application of the $GABA_A$ receptor antagonist gabazine. Acquisition frame rate was 1.25 Hz.

**Supplementary Video 6.**

**GCaMP recording, single synapse.** Full time series of the GCaMP recording after gabazine application in Ai95/Prox1-cre mouse organotypic hippocampal slice cultures shown in Suppl. Fig. 16C. $Ca^{2+}$ transients of a mossy fiber bouton attached to a CA3 pyramidal neuron are visible. LIONESS images are identical

replicates providing structural context to the time-varying $Ca^{2+}$-signals (green). Acquisition frame rate of the GCaMP signal was 1.25 Hz.

**Supplementary Video 7.**

**GCaMP recording, chemogenetically activated single synapse.** Full series of the GCaMP recording shown in Fig. 5A. $Ca^{2+}$ transients of a mossy fiber bouton attached to a hilar mossy cell in Ai95/Prox1-cre mouse organotypic hippocampal slice cultures are visible. LIONESS and dTomato (orange, coexpressed with the DREADD hM3Dq) images are identical replicates placing the overlaid time-varying $Ca^{2+}$-signals (green) after stimulation with the DREADD ligand CNO into structural context. Acquisition frame rate of the GCaMP signal was 2 Hz.

**Supplementary Video 8.**

**3D reconstruction of mossy fiber bouton on hilar mossy cell, including neighboring boutons.** Same reconstruction as in Fig. 5B, but including additional, hM3Dq-negative mossy fiber boutons from automated segmentation (left), and the thorny excrescences alone (right). Additional boutons are not proof-read.

**Supplementary Video 9.**

**LIONESS volume in living hippocampal dentate gyrus - 1 (*xy* view).** Full LIONESS stack (x*y*-view) of a volume of dentate gyrus in organotypic hippocampal slice culture, corresponding to the dataset in Suppl. Fig. 19. Step size: 50 nm (160 optical sections).

**Supplementary Video 10.**

**LIONESS volume in living hippocampal dentate gyrus - 2 (*xz* view).** Full LIONESS stack (x*z*-view) of a volume of dentate gyrus in organotypic hippocampal slice culture, corresponding to the dataset in Suppl. Fig. 19. Step size: 50 nm (480 optical sections).